



Universität
Zürich^{UZH}

Physik-Institut
Wissenschaftlicher Jahresbericht
April 2011 - März 2012

Front picture: after many years of preparations, LHC started to produce physics results; Nicola Chiapolini and Marco Tresch of our *LHCb* group (see Sec. 10) so far find good agreement with the Standard Model predictions.

Sekretariat	044 635 5721	secret@physik.uzh.ch
Prof. C. Amsler	044 635 5784 022 767 2914	amsler@cern.ch
Prof. L. Baudis	044 635 5777	lbaudis@physik.uzh.ch
Prof. H.-W. Fink	044 635 5801	hwfink@physik.uzh.ch
Prof. H. Keller	044 635 5748	keller@physik.uzh.ch
Prof. J. Osterwalder	044 635 5827	osterwal@physik.uzh.ch
Prof. A. Schilling	044 635 5791	schilling@physik.uzh.ch
Prof. U.D. Straumann	044 635 5768	strauman@physik.uzh.ch

The annual reports are available on the internet: <http://www.physik.uzh.ch/reports.shtml>.

Begleitwort

Die Grundlagenforschung am Physik-Institut der Universität Zürich zeigt eine eindrückliche Vielfalt. So werden physikalische Aspekte biologischer Systeme ebenso intensiv untersucht, wie der Frage nachgegangen wird, wo wohl die Grenzen des Standardmodells der Teilchenphysik liegen mögen. Das Jahr 2011 hat erstmals eine relevante Zahl von Kollisionsereignissen am *Large Hadron Collider* hervorgebracht: drei Gruppen am Physik-Institut konzentrieren sich auf den Betrieb der Detektoren und die Analyse der gewonnenen Daten. Weitere Forschungsgruppen widmen sich quantenmechanischen Effekten an Oberflächen kondensierter Materie oder vertiefen das physikalische Verständnis der Supraleitung. Neuartige bildgebende Techniken mit Hilfe von niederenergetischen kohärenten Elektronen werden entwickelt. Damit sollen einzelne biologische Moleküle abgebildet werden. Bei den Untersuchungen der Zusammensetzung der dunklen Materie wurden neue Rekorde in der Sensitivität erreicht.

Neben dem Aufbau und Betrieb der experimentellen Apparaturen in unserem Institut nutzen die Gruppen intensiv die zur Verfügung stehende internationale Forschungsinfrastruktur. Zum Beispiel werden Untersuchungen der magnetischen Eigenschaften kondensierter Materie und der Struktur der Oberflächen am Paul-Scherrer-Institut (PSI) durchgeführt (MuSR, SLS). Ebenfalls liefern wir Beiträge zu zwei Teilchenphysik-Experimenten am PSI. Am Cern in Genf werden zwei Experimente am LHC unterstützt, aber auch verschiedene kleinere Aktivitäten. Ein Experiment zum neutrinolosen Doppelbetazerfall findet im untergrundarmen Labor Gran Sasso bei Rom statt, wo ebenfalls die erwähnte Forschung an dunkler Materie durchgeführt wird.

Die tägliche Forschungsarbeit wird hauptsächlich von den 35 Doktorierenden, 19 Post-Docs und 20 wissenschaftlichen Mitarbeitenden geleistet. Ihre Forschungsergebnisse wurden im Berichtsjahr in über 170 Publikationen veröffentlicht und in mehr als 100 Beiträgen an internationalen Konferenzen vorgestellt. Diese experimentellen Forschungsarbeiten sind nur möglich dank der Unterstützung der Gruppentechniker und der Mitarbeiter der sehr gut ausgerüsteten mechanischen und elektronischen Werkstätten und der Informatik. Dank deren grosser Initiative und der hervorragenden Zusammenarbeit auf allen Stufen können Apparaturen von höchster Qualität entwickelt, konstruiert und betrieben werden.

Die klassische Verknüpfung von Forschung und Lehre ist an unserem Institut sehr ausgeprägt. Fast alle der 103 Angestellten unseres Instituts sind in direkter oder indirekter Form an der Lehre beteiligt. Neben den etwa 140 Studierenden im Hauptfach Physik betreuen wir noch den elementaren Physikunterricht für Studierende der Medizin (292), Veterinärmedizin (87), Biologie (152), Chemie (90) und anderer Studienrichtungen (39) in Form von Vorlesungen, Demonstrationsexperimenten, Übungen und Praktika.

Des Weiteren leisten verschiedene Mitarbeitende einen grossen Einsatz für die Öffentlichkeitsarbeit. In gesamthafter 21 Veranstaltungen im Rahmen von *Scientifica*, *European masterclass for particle physics*, Technikwochen, *TecDays* an Gymnasien, Kinder-Universität, Führungen von Schulklassen und verschiedenen Studieninformationstagen wurden fast 900 Arbeitsstunden eingesetzt, um den entsprechenden Personenkreisen die Faszination der Physik und ihrer Forschungsergebnisse zu vermitteln.

Allen Mitarbeitenden möchte ich an dieser Stelle für ihren uneigennütigen Einsatz, ihre Eigeninitiative und die gute Arbeitsstimmung am Institut herzlich danken.

Zürich, im Mai 2012

Prof. Dr. Ulrich Straumann

Mitarbeiter

Wissenschaftliches Personal

Prof. Christof	Aegerter	Phys. Systembiologie
Dr. Ernest	Aguiló	CMS
Dr. Yves	Allkofer	AEGIS, DARWIN
Prof. Claude	Amsler	AEGIS, DARWIN, DIRAC, CMS
Dr. Jonathan	Anderson	LHCb
Daniel	Assmann	Phys. Systembiologie
Prof. Laura	Baudis	DARWIN, GERDA, XENON
Annika	Behrens	DARWIN, XENON
Giovanni	Benato	GERDA
Markus	Bendele	Supraleitung & Magnetismus
Dr. Angela	Benelli	DIRAC
Dr. Roland	Bernet	LHCb
Saskia	Bosma	Supraleitung & Magnetismus
Olaf	Bossen	PTM
Dr. Angela	Büchler	LHCb
Albert	Bursche	LHCb
Dr. Carlo	Canali	AEGIS
Dr. Luca	Castiglioni	Oberflächenphysik
Nicola	Chiapolini	LHCb
Prof. Vincenzo	Chiochia	CMS
William	Creus	DARWIN
Dr. Huanyao	Cun	Oberflächenphysik
Michel	De Cian	LHCb
Dr. Simon Marie	de Visscher	CMS
Dr. Jan-Hugo	Dil	Oberflächenphysik
Eveline	Eisenring	Oberflächenphysik
Christian	Elsasser	LHCb
Dr. Andreas	Engel	PTM
Dr. Conrad	Escher	Bio-Physik
Carlotta	Favaro	CMS
Dr. Alfredo	Ferella	DARWIN, GERDA, XENON
Prof. Hans-Werner	Fink	Bio-Physik
Dr. Francis	Froborg	GERDA
Arno	Gadola	CTA
Giulia	Ghielmetti	Phys. Systembiologie
Prof. Thomas	Greber	Oberflächenphysik
Roman	Gredig	CTA, Mu3e
Michael	Greif	Oberflächenphysik
Henrik	Grundmann	PTM
Zurab	Guguchia	Supraleitung & Magnetismus
Dr. Kiran K.	Guthikonda	GERDA

Wissenschaftliches Personal (cont)

	Patrick Helfenstein	Bio-Physik
	Adrian Hemmi	Oberflächenphysik
Dr. Matthias	Hengsberger	Oberflächenphysik
Dr. Ludovic	Howald	Supraleitung & Magnetismus
	Ben Huber	CTA
	Kevin Inderbitzin	PTM
Dr. Lars	Jörgensen	AEgIS
Prof. Hugo	Keller	Supraleitung & Magnetismus
	Gaudenz Kessler	XENON
	Mitsuhiro Kimura	AEgIS
Dr. Alexander	Kish	DARWIN, XENON
	Gabriel Landolt	Oberflächenphysik
Dr. Tatiana	Latychevskaia	Bio-Physik
	Dominik Leuenberger	Oberflächenphysik
Dr. Jean-Nicolas	Longchamp	Bio-Physik
	Dr. Haifeng Ma	Oberflächenphysik
Dr. Alexander	Maisuradze	Supraleitung & Magnetismus
	Dr. Aaron Manalaysay	CTA, DARWIN, XENON
	Dr. Teresa Marrodan-Undagoitia	DARWIN, XENON
Prof. Fumihiko	Matsui	Oberflächenphysik
	Barbara Millán Mejías	CMS
Dr. Katharina	Müller	H1, LHCb
	Ulrike Nienhaus	Phys. Systembiologie
Prof. Jürg	Osterwalder	Oberflächenphysik
Dr. Polina	Otyugova	CMS
	Francesco Piastra	XENON
Dr. Christian	Regenfus	AEgIS, DARWIN
Mirena Ivova	Rikova	CMS
	Dr. Peter Robmann	CMS, H1, $\pi \rightarrow e\nu$, Mu3e
	Silvan Roth	Oberflächenphysik
	Mirna Saliba	Bio-Physik
	Christophe Salzmann	LHCb
Prof. Andreas	Schilling	PTM
	Michael Schindlberger	Phys. Systembiologie
	Thomas Schluck	Phys. Systembiologie
Dr. Alexander	Schmidt	CMS
	Dr. Marc Schumann	DARWIN, XENON
Dr. Nicola	Serra	LHCb
	Bartosz Slomski	Oberflächenphysik
Dr. Hella	Snoek	CMS
	Dr. Olaf Steinkamp	LHCb
	Evelyn Stilp	Supraleitung & Magnetismus

Wissenschaftliches Personal (cont)

Dr. James	Storey	AEGIS, CMS
Prof. Ulrich	Straumann	H1, LHCb, CTA, Mu3e
	Michal Tarka	GERDA
Dr. Mark	Tobin	LHCb
Dr. Salvatore	Tupputi	CMS
Dr. Andries	van der Schaaf	$\pi \rightarrow e\nu$
	Mauro Verzetti	CMS
Dr. Achim	Vollhardt	Elektronik, LHCb, CTA
	Fabian von Rohr	PTM
	Manuel Walter	DARWIN, GERDA
Dr. Rasmus	Westerström	Oberflächenphysik
Dr. Stephen	Weyeneth	Supraleitung & Magnetismus
	Flavio Wicki	Bio-Physik

Technisches und administratives Personal

	Renata Bernasconi	Sekretariat
	Kurt Bösiger	Werkstatt
	Tiziano Crudeli	Zeichnen
	Denis Dürst	Werkstatt
	Daniel Florin	Elektronik
	Dario Gabrielli	Werkstatt
	Carmelina Genovese	Sekretariat
	Ruth Halter	Sekretariat
	Alina Horwege	Bio-Physik
	Andreas James	GERDA, XENON
	Thomas Kälin	Oberflächenphysik
	Hanspeter Koch	Vorlesungsbetrieb
	Bruno Lussi	Werkstatt
	Reto Maier	Werkstatt
	Tizian Naterop	Werkstatt
	Lucien Pauli	Vorlesungsbetrieb
	Jacky Rochet	AEGIS, CMS, DIRAC, DARWIN
	Monika Röllin	Sekretariat
Dr. Jean-Pierre	Ruder	CHIPP
	Sandra Saornil Gamarra	LHCb
	Marcel Schaffner	Werkstatt
	Silvio Scherr	Werkstatt
	Stefan Siegrist	PTM, Supraleitung & Magnetismus
	Peter Soland	Elektronik
	Stefan Steiner	CAD, LHCb, CTA

Contents

	Physics of Fundamental Interactions and Particles	1
1	Towards a dark matter experiment	1
2	Test of the equivalence principle with antihydrogen	5
3	GERDA: Neutrinoless Double Beta Decay in Germanium	9
4	Cold Dark Matter Search with XENON	12
5	DARWIN: dark matter WIMP search with noble liquids	16
6	Very High Energy Gamma Ray Astronomy with CTA	20
7	Testing lepton universality: the $\pi \rightarrow e\bar{\nu} / \pi \rightarrow \mu\bar{\nu}$ branching ratio	23
8	Study of Coulomb-bound πK pairs	27
9	Particle Physics at DESY/HERA (H1)	30
10	Particle Physics with LHCb	33
	10.1 The LHCb detector	33
	10.2 Physics Results	34
	10.3 Summary and Outlook	39
11	Particle physics with CMS	41
	11.1 Study of Λ_b and Σ_b	41
	11.2 Observation of a new strange bottom baryon	42
	11.3 Lifetime of the B_s -meson	44
	11.4 Searches for the Higgs boson in $\tau^+\tau^-$ decays	44
	11.5 Improvements to the pixel hit reconstruction	46
	11.6 Studies of B hadron correlations associated to Z^0 bosons	46

Condensed Matter Physics	49
12 Superconductivity and Magnetism	49
12.1 Pressure Effects in Iron-Chalcogenides	49
12.2 Magnetic torque study of single-crystal $\text{Rb}_x\text{Fe}_{2-y}\text{Se}_2$	50
12.3 Anisotropic magnetic order in $\text{EuFe}_{2-x}\text{Co}_x\text{As}_2$ single crystals	52
12.4 μSR study of the magnetoelectric coupling in Cu_2OSeO_3	54
13 Phase transitions and superconducting photon detectors	56
13.1 Superconducting nanowire single-photon detectors	56
13.2 Experiments on $\text{Ba}_{3-x}\text{Sr}_x\text{Cr}_2\text{O}_8$	58
13.3 LC -circuit calorimetry	59
14 Surface Physics	62
14.1 The unit cell of graphene on ruthenium	63
14.2 Rashba effect in Pb quantum well states	65
14.3 Electron dynamics in a quasi-one-dimensional topological metal: $\text{Bi}(114)$	67
15 Physics of Biological Systems	69
16 Physical Systems Biology and non-equilibrium Soft Matter	74
16.1 Localization of light	74
16.2 Three dimensional microscopy in turbid media	77
Infrastructure and Publications	81
17 Mechanical Workshop	81
18 Electronics Workshop	85
19 Publications	88
19.1 Elementary particles and their interactions	88
19.2 Condensed matter	107

1 Towards a dark matter experiment

Y. Allkofer, C. Amsler, W. Creus, A. Ferella, C. Regenfus, J. Rochet, and M. Walter.

We report on our research progress on liquid argon (LAr) which is part of the DARWIN design study [1] for a next generation dark matter facility using noble liquids. More details and references to earlier work can be found in a recent publication [2]. LAr has the potential to be used as a large and sensitive target to detect nuclear recoils from Weak Interacting Massive Particles (WIMP) interactions. WIMPs would produce nuclear recoils which can be detected and isolated in noble liquids through their characteristic excitation and ionization patterns. The uncertainty in the signal calibration of nuclear recoils in LAr is large since only scarce information on the scintillation efficiency can be found in literature. In fact, the complex microscopic processes which lead to the scintillation and charge signals are not well understood at low energies.

The energy dependent light yield Y_{nr} of nuclear recoils is described by the relative scintillation efficiency \mathcal{L}_{eff} which compares the light yield of electrons to that of nuclear recoils (by convention \mathcal{L}_{eff} is measured at zero electric field). Its value is determined by the product of two quenching processes. Towards low energies, an increasing fraction of the recoil energy is lost to heat (nuclear quenching). The density of the excited or ionized states produced during the stopping process depends on their interaction (luminescence quenching). The light yield of electrons is not affected by nuclear effects and is proportional to the energy deposit above some tens of keV. The relative scintillation efficiency is expressed as $\mathcal{L}_{\text{eff}} = E_{ee}/E_r$, where E_{ee} stands for the energy of an electron producing the same amount of light as a recoiling nucleus with energy E_r . In contrast to xenon, a separation of the scintillation signal in fast ($\tau_1 = 6$ ns) and slow ($\tau_2 = 1.6$ μ s) components is possible in LAr. This effect is exploited to reduce background in LAr dark matter detectors.

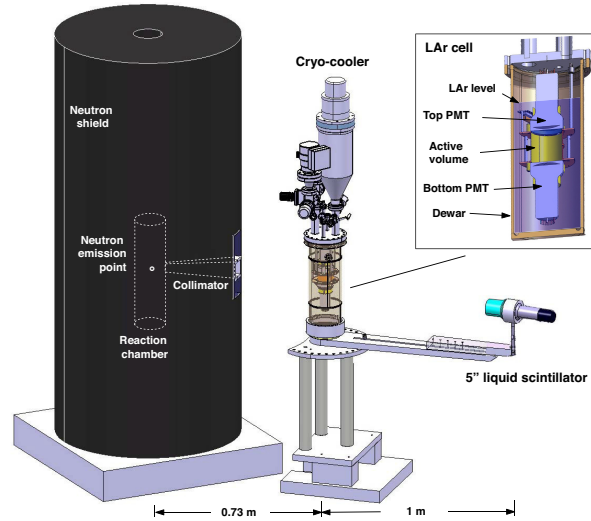


FIG. 1.1 – $n - n - Ar$ scattering experiment with neutron generator, shield and zoom on the LAr cell.

We present an overview of the experimental method to determine \mathcal{L}_{eff} and show first results from data recorded under neutron, α and γ -irradiation in LAr at zero electric field. The experimental setup is shown in Fig. 1.1. We induce nuclear recoils in the LAr cell by 2.45 MeV neutrons from a deuterium-fusion-generator (from NSD-Fusion, Germany). It delivers up to 2×10^6 isotropically emitted monoenergetic neutrons from the two-body reaction $dd \rightarrow {}^3\text{He} + n$. The fusion rate in the deuterium plasma is controlled by an electrical DC field generated by an adjustable constant current HV supply. The environment is shielded from neutron and X-ray radiation by a 1600 kg polyester cylinder with 2 mm Pb cladding. A polyethylene collimator with square cross section restricts the emission of neutrons in a solid angle of about 0.2% of 4π . Liquid scintillator counters (LSC) detect the scattered neutrons at various angles.

The cryogenic cell is shown in the inset. Two tetraphenyl-butadiene (TPB) coated 3" PMTs (Hama-

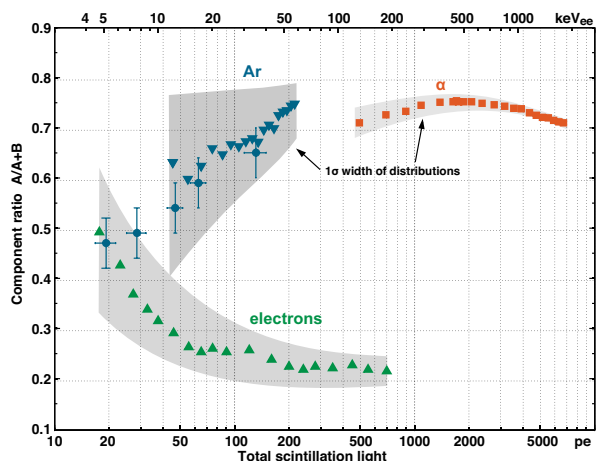


FIG. 1.2 – CR vs. light yield for Ar-, α -recoils and electrons. The grey zones indicate the 1σ spread.

matsu R6091-MOD) with bialkali photo cathodes and Pt underlay ($QE \approx 15\%$) are arranged face to face, forming a cylindrical sensitive volume of roughly 0.2ℓ . The cell walls are covered with a TPB coated reflector foil [3, 4] to shift the VUV scintillation light (128 nm) to ~ 420 nm. A ^{210}Po α -source is installed in the center of the cell. A turbopump is used to evacuate the chamber to typically 10^{-6} mbar prior to filling with argon gas class 60. A membrane pump provides for recirculation via OXISORB cartridges which reduce the O_2 and H_2O contamination. The gas is condensed on top of the chamber by a (Sumitomo CH210) cryocooler. A LabView slow control regulates the cold head temperature and records temperatures, pressures and liquid levels.

The analogue signals from the two PMTs are each split into two inputs (for a larger dynamic range) and sampled with an oscilloscope with 5000 points at 1 GS/s. LAr signals are integrated numerically from the digitized currents of the PMTs, normalised to their mean single photon charges. Light yield calibrations were performed regularly with an external ^{241}Am source producing a prominent 60 keV photopeak.

In LAr VUV fluorescence from the so-called second continuum is the dominant mechanism for light emission. The light pulse shape is described by the sum of two exponentials with amplitudes describing the radiative decays of two fundamental

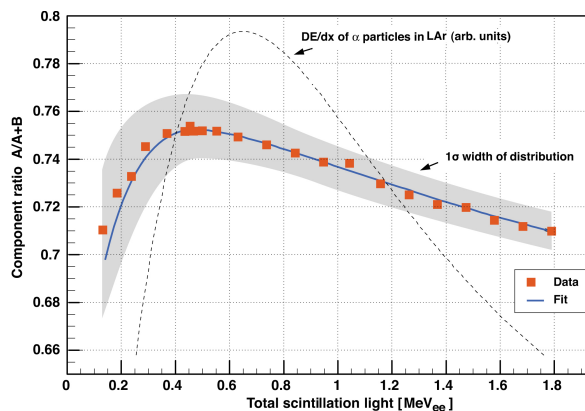


FIG. 1.3 – CR for α s in LAr and fit versus total scintillation light in MeV (electron equivalent).

excimer states (singlet and triplet, with lifetimes τ_1 and τ_2 , respectively). Due to their long lifetime triplet states undergo collisions with neighbouring particles before decaying. Interactions with impurities can cause their (non-radiative) destruction, inducing losses in the slow scintillation light and a reduction in τ_2 . In the following our component ratio (CR) – the relative strength of the fast component of the scintillation light – is corrected for this effect by extrapolation to pure LAr [2, 5].

The CR s are determined for recoiling Ar nuclei (induced by neutrons), α -particles (from the ^{210}Po source) and electrons (induced by 511 keV γ s from an external ^{22}Na source). A coincidence with an external detector was required for the photon data to tag the emission of two 511 keV γ s. This data was also used to determine the time-of-flight calibration. Figure 1.2 shows the CR distribution versus total amount of scintillation light. The two prominent bands from electrons and nuclear recoils merge for energies below about 10 keV $_{ee}$. The values at low energies for argon recoils are also shown (circles). There is a correlation between CR and the stopping power. Large ionisation densities lead to strong interaction between particles and produce a larger fraction of singlet states. For electrons CR is equal to ~ 0.25 at the minimum ionisation densities, close to the statistical weights of 1 : 3 for the isolated production of singlet and triplet states (no interaction between them).

The relation between population of excimer states at various energy losses can be unfolded by taking

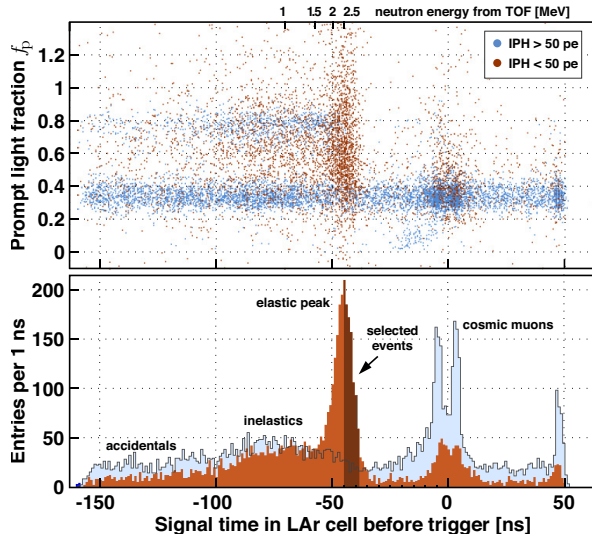


FIG. 1.4 – Prompt light fraction f_p vs. signal time in LAr and projection on the time axis for neutrons triggering the liquid scintillator counter.

into account the integral over the stopping range. We have determined the energy scale for α -particles by assuming a linear relation between CR and the energy transfer [2]. A value of $\mathcal{L}_{\text{eff}}^\alpha = 0.74 \pm 0.04$ was found for the mean relative scintillation efficiency for α -particles in LAr in the range 0.18 – 2.5 MeV (Fig. 1.3). The light loss of $\simeq 25\%$ is entirely due to luminescence quenching.

We now present the data taken with the neutron generator. A 5" liquid scintillator (LSC) was positioned at 30, 40, 50, 60 and 90°, at 1 m from the target, corresponding to 16, 28, 43, 60 and 120 keV recoil energies, respectively. The neutron flux (typically 2×10^5 n/s into 4π) was chosen so that accidental background induced by bremsstrahlung was kept at an acceptable level. About 1 n/min scattered off an argon nucleus in the active volume and was detected in the LSC. The direct line of sight between the exit of the collimator and the LSC was obstructed by a 20 cm thick sheet of polyethylene. Background rates were around 5/min, originating mainly from cosmic muons saturating the LSC, and accidental coincidences between diffusively scattered neutrons and bremsstrahlung. Events in the LAr cell were accepted whenever both PMTs showed signals above 0.2 photoelectrons (pe) in a 50 ns time coincidence. A trigger was generated by a LAr signal within a window of [-150, +50] ns

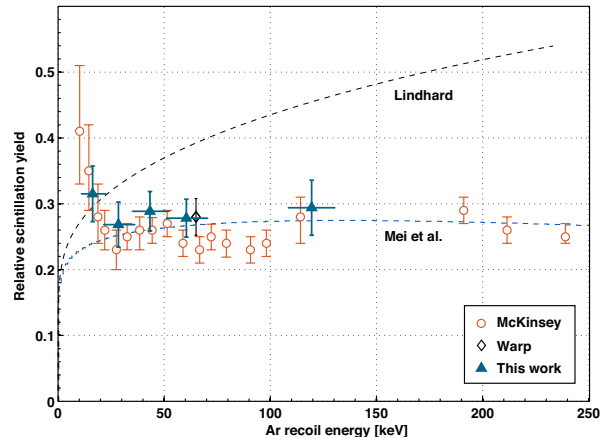


FIG. 1.5 – \mathcal{L}_{eff} from this work compared to theory and previous data.

around the arrival time of a neutron in the LSC.

Figure 1.4 shows the prompt light fraction f_p vs. the time difference between the signals in the LAr cell and the LSC for the 30° data (19k events). Here f_p is the ratio of the scintillation light yield in the first 50 ns to the total light. The time projection is shown in Fig. 1.5. The distribution of signals (< 50 pe) is dominated by elastically scattered neutrons around the nominal flight time at -45 ns (brown histogram). Also visible are inelastic scatters from neutrons and a small background from accidental coincidences of diffusely scattered neutrons with bremsstrahlung in the outer LAr volume. Requiring at most 50 pe removes many of these events and also cosmic muons (blue histogram). A 5 ns wide TOF cut then selects elastic scatters ($\sim 1'000$ events, black area). Figure 1.5 shows our measurements at the five angles, together with the data from refs. [6, 7]. Our measurements lead to the average $\langle \mathcal{L}_{\text{eff}} \rangle = 0.29 \pm 0.03$ for nuclear recoils above 20 keV (or 6 keV electron equivalent). The data are consistent with a constant value for \mathcal{L}_{eff} , in accord with a simple saturation law combined with the Lindhard model [8].

Summarizing, we confirm that scintillation light quenching in LAr by impurities is similar to that in gaseous argon [5]. As in the latter work we use measured lifetimes and component ratios to reconstruct purity independent results. We confirm values for CR monotonically increasing with energy transfer.

A CR value of 0.25 close to the one expected from statistically populated singlet and triplet states is observed for electrons in the region of lowest ionization densities. For nuclear recoils we find CR rising from 50% to 75% between 20 and 200 keV. For α -particles in the MeV range we determine a relative scintillation yield $\mathcal{L}_{\text{eff}}^{\alpha} = 0.74 \pm 0.04$. Within present errors our value of the relative scintillation yield \mathcal{L}_{eff} is constant for nuclear recoils at energies between 16 and 120 keV, with a mean value of 0.29 ± 0.03 . A refined analysis is in progress [9].

4

No conclusive results below 16 keV can be drawn from the present analysis. We are upgrading the cell with PMTs of larger quantum efficiency and are improving the cleaning system. An internal electric field will be added to extract the ionization charge from the liquid and to determine field and energy dependences of both light and charge yields in LAr, at working points relevant to dark matter searches.

- [1] L. Baudis, arXiv:1012.4764v1 [astro-ph.IM] (2010) and <http://darwin.physik.uzh.ch/>
- [2] C. Regenfus *et al.*, arXiv:1203.0849v1 [astro-ph.IM] (2012).
- [3] V. Boccone *et al.*, J. of Instrumentation **4** (2009) P06001; V. Boccone, PhD-thesis, Universität Zürich, 2010.
- [4] M. Walter, Diploma-Thesis, Universität Konstanz, 2011.
- [5] C. Amsler *et al.*, J. of Instrumentation **3** (2008) P02001.
- [6] R. Brunetti *et al.*, New Astr. Rev. **49** (2005) 265.
- [7] D. Gastler *et al.*, arXiv:1004.0373v2 [physics.ins-det] (2011).
- [8] D. Mei *et al.*, Astropart. Phys. **30** (2008) 12.
- [9] W. Creus, PhD-Thesis, Universität Zürich (in preparation).

2 Test of the equivalence principle with antihydrogen

Y. Allkofer, C. Amsler, C. Canali, L. Jörgensen, M. Kimura, C. Regenfus, J. Rochet, and J. Storey

in collaboration with:

INFN Bescia - Firenze - Genova - Milano - Padova - Pavia - Trento, CERN, MPI-K (Heidelberg), Kirchoff Inst. of Phys (Heidelberg), INR (Moscow), ITEP (Moscow), Univ. Claude Bernard (Lyon), Univ. of Oslo, Univ. of Bergen, Czech Tech. Univ (Prague), ETH-Zurich, Politecnico Milano, Laboratoire Aimé Cotton (Orsay).

(AEgIS Collaboration)

The AEGIS experiment [1] will measure for the first time the gravitational acceleration of antimatter \bar{g} using a beam of antihydrogen (\bar{H}) atoms. Previous attempts to measure \bar{g} with positrons and antiprotons failed due to stray electric or magnetic fields. From attempts to unify gravity with the other forces the possibility that $\bar{g} \neq g = 9.81 \text{ m s}^{-2}$ cannot be excluded [2]. Many arguments have been put forward to rule out any difference between g and \bar{g} , and correspondingly many rebuttals have been published [3]. The validity of the weak equivalence principle (WEP) for antimatter thus rests on experimental evidence.

The goal of AEGIS is to measure \bar{g} with an initial precision of 1%. First we need to produce \bar{H} -atoms at $\sim 100 \text{ mK}$. A promising technique [4] uses the

interaction between the antiproton and the highly excited Rydberg state positronium (Ps^*) in which the bound positron is captured by the antiproton and an electron is released ($\text{Ps}^* + \bar{p} \rightarrow \bar{H}^* + e^-$). Figure 2.1 shows a sketch of the apparatus. The process begins with the production of positronium (Ps) by accelerating 10^8 positrons from a Surko type accumulator onto a nanoporous material. The ortho- Ps emitted from the target is then brought to the Rydberg state Ps^* by two-step laser excitation. Some of the Ps^* atoms diffuse across a Penning trap in which 10^5 antiprotons from the CERN antiproton decelerator (AD) have been stored, producing \bar{H} through the charge exchange reaction. An electric field is then applied along the beam axis to accelerate the \bar{H} -atoms to $\sim 400 \text{ m/s}$. This

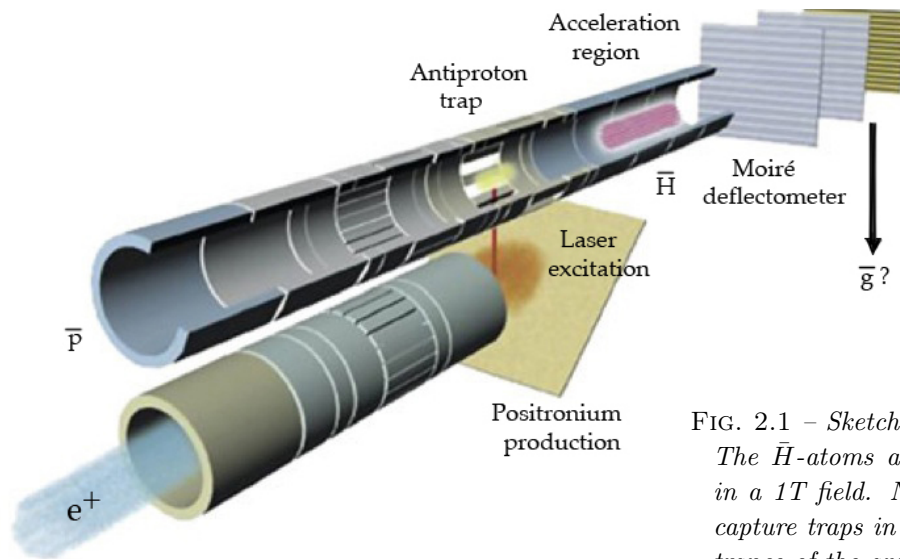


FIG. 2.1 – Sketch of the AEGIS apparatus. The \bar{H} -atoms are produced in the \bar{p} -trap in a 1T field. Not shown are \bar{p} - and e^+ -capture traps in the 5T magnet at the entrance of the apparatus.

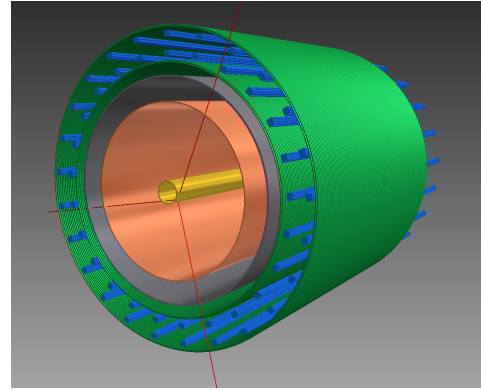
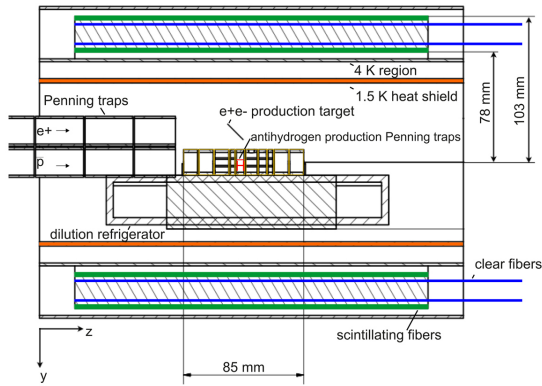


FIG. 2.2 – Conceptual design of the Fast Annihilation Tracking (FACT) detector (see text).

technique has already been demonstrated by members of the AEGIS collaboration with hydrogen atoms [5]. A Moiré deflectometer consisting of two gratings and a position sensitive annihilation detector is used to measure the deflection of the \bar{H} beam in the gravitational field. The downward (or upward!) shift of the Moiré intensity pattern at the detector due to gravity needs to be combined with time of flight and be measured with a vertical precision of $\sigma \simeq 10 \mu\text{m}$. The Zürich group is designing and building (i) the annihilation detector and its readout to characterize the \bar{p}/\bar{H} cloud in the Penning trap and (ii) the position sensitive detector to measure the Moiré pattern.

The AEGIS apparatus, less the Moiré deflectometer, will be installed for the AD runs in 2012. Objectives are to produce \bar{H} -atoms, measure their temperature and demonstrate the production of the \bar{H} -beam by means of Stark acceleration. The goal of our group is to commission the Fast Annihilation Cryogenic Tracking (FACT) detector designed and constructed in 2011/2012.

Depending on temperature, a large fraction of the \bar{H} -atoms annihilate by hitting the confinement walls within $\sim \mu\text{s}$. The detector must therefore be very fast, but only needs to be active for 1 ms every 100 s between AD pulses. The operating conditions are challenging as the detector occupies a cylindrical volume around the trap with an inner radius of 78 mm and outer radius of 103 mm in

a 1T magnetic field, and must operate at 4K. A further complication is the strong 511 keV γ background produced by positrons hitting the positronium target. This occurs a few μs before the first \bar{H} annihilations.

We have opted for a scintillating fiber detector with silicon photomultiplier readout. The FACT detector consists of four layers of 1 mm diameter scintillating fibers¹ coupled to clear fibers of the same diameter which direct the optical signal from the cryogenic region onto arrays of 1 mm diameter silicon photomultipliers (MPPC)². Each layer consists of 200 scintillating fiber loops aligned orthogonal to the beam axis. A sketch is shown in Fig. 2.2. A vertex resolution along the longitudinal axis of 2.5 mm is expected from simulations, which is sufficient for our requirements.

The readout electronics for the 800 fibers must be fast enough to measure the speed (temperature) of the \bar{H} -atoms. The output of the MPPCs is sampled continuously. The principle is shown in Fig. 2.3 for a single channel. The MPPC is connected to a linear amplifier and a fast discriminator feeding the FPGA. The latter controls the MPPC voltage and threshold levels, samples the output of the comparators with a time resolution of ~ 10 ns, and transfers the data to the DAQ system through a USB connection. A single FPGA manages several channels (upper part of Fig. 2.3). The FPGA can be programmed to perform a fast and

¹Kuraray SCSF-78M multi-clad scintillating fibers [6].

²Hamamatsu silicon photomultipliers MPPC S10362-11-100C [7].

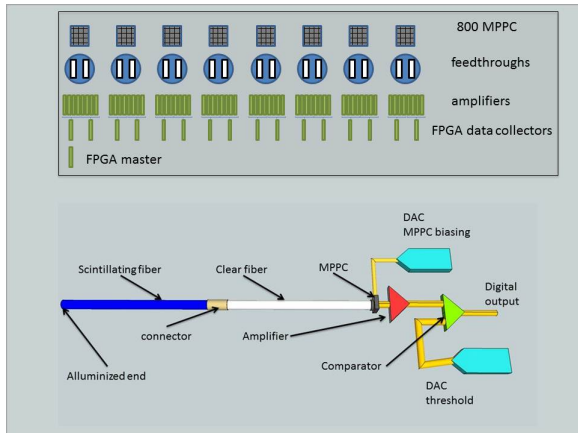


FIG. 2.3 – *Electronics layout for the fiber readout (see text) and readout for one scintillating fiber.*

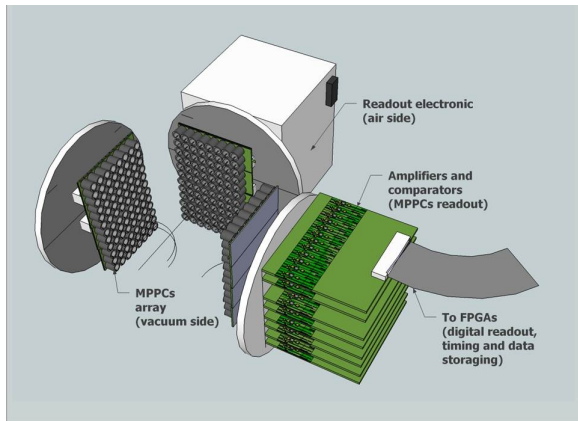


FIG. 2.4 – *MPPCs inside the vacuum region connected by feedthroughs to the readout electronics.*

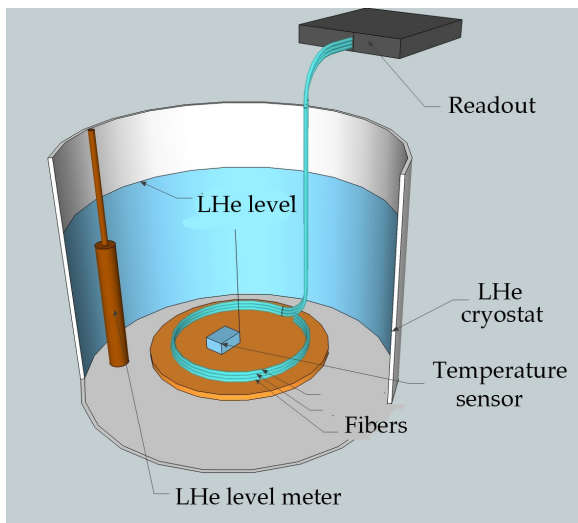


FIG. 2.5 – *Equipment used to measure the performance of scintillating fibers at cryogenic temperatures.*

smart real time readout of all channels. The MPPCs are located inside and the readout electronics outside the AEGIS apparatus (Fig. 2.4).

The scintillating fibers must operate at 4K. Since no data exist we have tested the performance of scintillating fibers with cosmic rays at cryogenic temperatures. The test apparatus consisted of 3 layers of 1 mm diameter Kuraray scintillating fibers arranged in loops at the bottom of a liquid helium cryostat (Fig. 2.5). The light from the scintillating fibers was detected by 3 MPPCs, the outputs of which were amplified and digitized by a LeCroy Wavepro 7100 10 GS/s oscilloscope. The oscilloscope was triggered when the signal of two of the three fibers exceeded 4 photoelectrons and we counted events with a coincidence observed in the third fiber, corresponding to the passage of a cosmic ray through the three fiber layers. The cryostat was filled with liquid helium immersing the fibers for 4 hours during which the detection efficiency was monitored, followed by warm-up to ambient temperature. The rate of events as a function of temperature is shown in Fig. 2.6. We observed a small ($\sim 15\%$) decrease in light yield from room to liquid helium temperature.

We are also investigating (in collaboration with the Albert Einstein Center in Bern) the possibility to use photographic emulsions of the OPERA type to reconstruct more accurately the interference pattern in the gravitation experiment. We would measure the annihilation points of \bar{H} - atoms on the vacuum exit window behind the Moiré de-

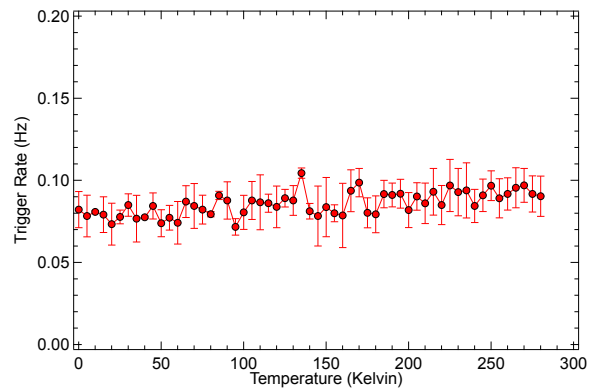


FIG. 2.6 – *Trigger rate of a scintillating fiber from cosmic rays as a function of temperature (see text).*

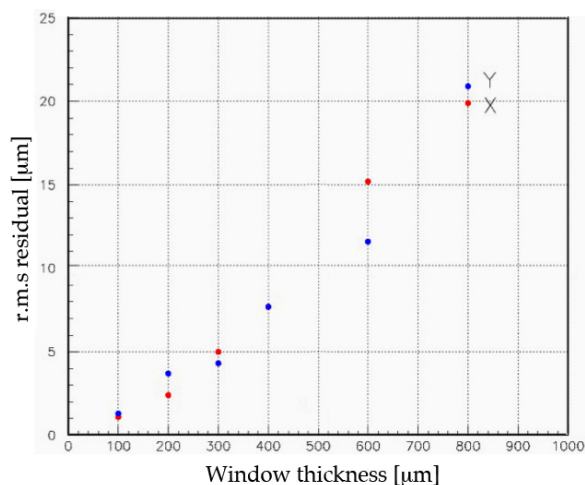


FIG. 2.7 – *R.m.s. position resolution on annihilation tracks as a function of thickness for a titanium vacuum window in which the \bar{H} -atoms annihilate.*

flectometer, using two or more annihilation pions. The emulsion stack would be placed immediately behind a very thin window separating the UHV vacuum from normal vacuum. The time-of-flight and the approximate track positions would be determined by a silicon or scintillating fiber detector

located outside the vacuum enclosure and stored for offline analysis. The emulsions would then be removed periodically and processed in Bern. Figure 2.7 shows the expected vertical resolution on the annihilation point due to multiple scattering as a function of window thickness (neglecting distortions and alignment errors). The Monte Carlo simulation indicates that r.m.s position resolutions of $3 \mu\text{m}$ could be achieved on the annihilation vertex, much better than the required $10 \mu\text{m}$, thus allowing a more accurate measurement of \bar{g} .

However, technical issues such as the performance of emulsions in vacuum (in particular dehydration) need to be investigated first. Also the background rate in the AD hall due to muons from the antiproton production target and from annihilation pions in the AEgIS apparatus need to be measured to assess the frequency at which emulsions would need to be changed. In 2012 we will commission the FACT detector and perform several test with photographic emulsions to plan for the first measurement of \bar{g} after the 2013 maintenance of the CERN accelerators.

- [1] Proposal: <http://doc.cern.ch/archive/electronic/cern/preprints/spsc/public/spsc-2007-017.pdf>
- [2] E. Fischbach and C.L. Talmadge, “The Search for Non-Newtonian Gravity”, Springer (1999).
- [3] M. M. Nieto and T. Goldman, Phys. Rep. **205** (1991) 221.
- [4] M. Charlton, Phys. Lett. **A 143** (1990) 143.
- [5] E. Vliegen F. and Merkt, Phys. Rev. Lett **97** (2006) 033002.
- [6] Kuraray, <http://www.kuraray.co.jp/en/>
- [7] Hamamatsu Photonics, <http://www.hamamatsu.com/>

3 GERDA: Neutrinoless Double Beta Decay in Germanium

L. Baudis, G. Benato, F. Froberg, A. Ferella, K. K. Guthikonda, M. Tarka and M. Walter

in collaboration with: INFN Laboratori Nazionali del Gran Sasso LNGS, Institute of Physics, Jagellonian University Cracow, Institut für Kern- und Teilchenphysik Technische Universität Dresden, Joint Institute for Nuclear Research Dubna, Institute for Reference Materials and Measurements Geel, Max Planck Institut für Kernphysik Heidelberg, Università di Milano Bicocca e INFN Milano, Institute for Nuclear Research of the Russian Academy of Sciences, Institute for Theoretical and Experimental Physics Moscow, Russian Research Center Kurchatov Institute, Max-Planck-Institut für Physik München, Dipartimento di Fisica dell Università di Padova e INFN Sezione di Padova, Physikalisches Institut Eberhard Karls Universität Tübingen

(GERDA Collaboration)

Neutrino oscillations, well established by now, demonstrate that neutrino flavours mix (so lepton flavor is not conserved) and thus that neutrinos have mass. In attempts to explain these observations it is crucial to establish whether neutrinos are Dirac or Majorana particles [1], *i.e.*, whether they exist both as particles and anti-particles or not. The latter option is possible for neutral particles only and even total lepton number would be violated.

The Majorana nature of neutrinos can be tested by studying the neutrinoless double beta decay ($0\nu 2\beta$) which can take place in all isotopes which undergo the allowed double beta decay ($2\nu 2\beta$). Neutrinoless beta decay results in the emission of two monoenergetic electrons sharing the Q -value of the reaction. The decay $2\nu 2\beta$, at the other hand, results in a continuum energy spectrum. Present lower limits on the $0\nu 2\beta$ half lives are of the order 10^{22} years.

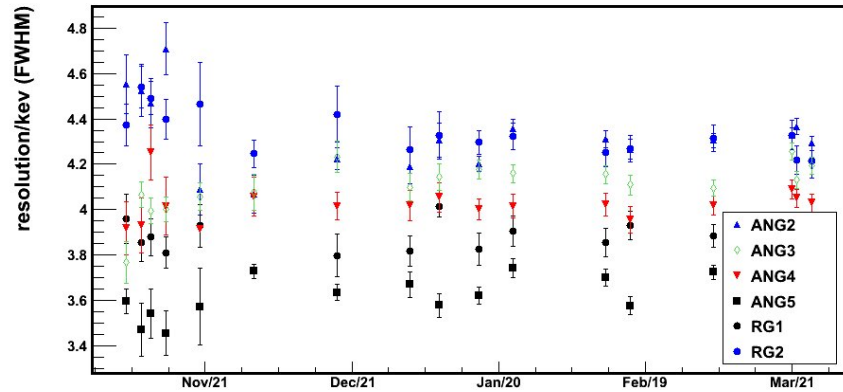
GERDA will search for the $0\nu\beta\beta$ decay in ^{76}Ge ($Q = 2039.006 \pm 0.050$ keV) enriched material which provides at the same time the source and the detector with an energy resolution of $0.1 - 0.2\%$ FWHM at 2 MeV. The construction and commissioning phase of GERDA, located 1400 m underground at the Gran Sasso National Laboratory (LNGS) in Italy has been completed in late 2011. Bare germanium diodes are operated in a 65 m^3 cryostat filled with liquid argon (LAr) and surrounded by a 3m water Cherenkov shield. Figure 3.1 gives a schematic view of the experiment.

A physics run with eight existing enriched ^{76}Ge detectors corresponding to 15.2 kg of ^{76}Ge started in November 2011 and is continuing smoothly. With a background level of $0.017^{+0.007}_{-0.003}$ counts/(keV·kg·y) in the region of interest, GERDA has reached its goal of reducing the background by a factor 10 with respect to the previous experiments which will allow us to scrutinize an earlier claim of a signal [2] using a larger total detector mass and a lower background. First results are expected to become available by the end of this year.



FIG. 3.1 – *Mock-up of the GERDA experiment located underground at LNGS. The physics run with all phase I detectors started in November 2011.*

FIG. 3.2 –
Energy resolution (FWHM) at 583 keV as function of time for the GERDA enriched detectors.



Our group participates actively in the following tasks:

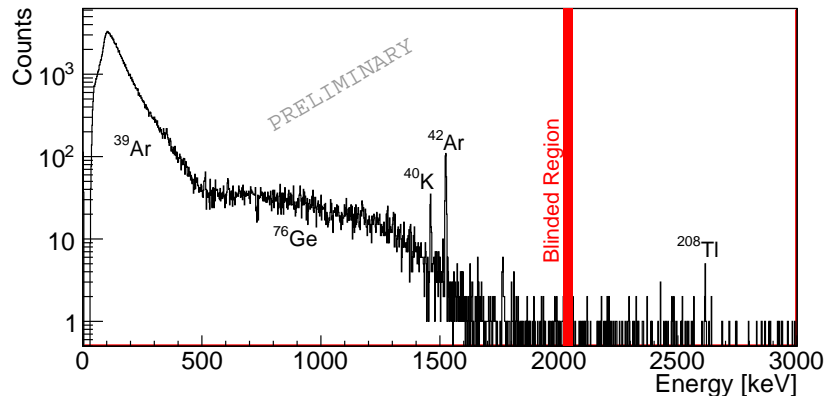
- **Detector calibration**

A new calibration system was constructed, installed and commissioned during the summer of 2011 and it is working as expected. A fully automatic analysis program for the data calibration was made available to the collaboration. One of the aims of the weekly energy calibrations is to test the stability of the detectors and the electronics chain in time. We developed an online database, in which properties such as energy resolution, calibration function, linearity, etc of all detectors are stored and can be displayed as a function of time. As an example, Fig. 3.2 shows the energy resolution at 583 keV at FWHM for all enriched detectors in the period between December 2011 and May 2012.

- **Energy spectrum analysis**

We aim to fully characterize the background of the experiment and determine the half life of the $2\nu 2\beta$ decay. This is a necessary step towards the $0\nu 2\beta$ analysis. We analyze the full energy spectrum (see Fig. 3.3) and compare it with Monte Carlo simulations (MC) of the various potential background sources. A crucial task is the estimation of the active volume of each detector, which is performed by comparing dedicated calibration data to MCs. Since the start of the physics run a 40 keV wide region around the Q-value has been blinded, in order to avoid an unconscious bias. Once all the known background contributions have been identified and quantified, the signal region will be uncovered.

FIG. 3.3 –
Energy spectrum measured by the GERDA detectors in the period November 2011 - April 2012. The $2\nu 2\beta$ decay contribution is clearly visible, as well as the beta spectrum induced by ^{39}Ar decays and several gamma peaks. The blinded region is indicated.



- **Detector pulse shape discrimination**

We are developing a pattern recognition algorithm, based on “Support Vector Machine” (SVM), to distinguish between so-called single site events (SSE) and multi site events (MSE). The two electrons in a double beta decay stop within a short range in the germanium diodes, and thus belong to SSE. On the other hand, a γ -ray depositing the $0\nu 2\beta$ energy in a single germanium detector makes several Compton scatters at well separated locations, yielding a MSE. SSE and MSE have only marginally different pulse shapes and are difficult to distinguish in the present coaxial germanium detectors. Our algorithm is in its test phase, where samples of each type, obtained from calibration data are being used. The goal is to decrease the background in the energy region of interest by a factor 2 - 4.

- **New germanium detectors**

We are active both in the production and the characterization of novel, so-called Broad Energy Germanium detectors (BEGe). About 20 kg of enriched germanium material was supplied to Canberra to grow three first crystals at the end of 2011. The seven BEGe’s made out of this batch are currently characterized in the Hades underground laboratory in Mol, Belgium, with the aim of understanding their intrinsic background and pulse shape discrimination performances. They will be inserted in the GERDA cryostat within a few months from now.

- **LAr instrumentation for Phase II**

A further background reduction can be achieved with the help of the LAr around the diodes. Besides its shielding properties and its use as a coolant for the Ge crystals, LAr is an efficient scintillator. This property will be exploited by installing a light readout system around the argon. The cylindrical side surface will consist of a reflector foil whilst the top and bottom surfaces would be equipped with ultra-low radioactivity photomultiplier tubes. The wave-

length of the LAr scintillation light is 128 nm and it has to be shifted to larger values to better match the photomultipliers. The wavelength shifting is usually performed by a tetraphenyl butadiene (TPB) coating on the reflector. Since current coatings are known to be mechanically unstable, and long term stability is crucial for GERDA, we are searching for an alternative. For this purpose, a liquid argon cell was built in our lab in Zurich, it is currently under commissioning. A first set of reflector foil samples was produced and a preselection has been performed using a fluorescence spectrometer at the MPIK in Heidelberg. These foils will be tested in our LAr cell together with the PMT planned for use in GERDA.

- [1] E. Majorana,
Il Nuovo Cimento B 14, 171-184 (1937).
- [2] H.V. Klapdor-Kleingrothaus *et al.*,
Phys. Lett. B 586, 198-212 (2004).

4 Cold Dark Matter Search with XENON

L. Baudis, A. Behrens, A.D. Ferella, G. Kessler, A. Kish, A. Manalaysay, T. Marrodán Undagoitia, F. Piastra, M. Schumann

in collaboration with:

Columbia University, UCLA, INFN, University of Münster, University of Coimbra, Subatech, The Weizmann Institute of Science, University of Mainz, SJTU, MPIK Heidelberg, Rice University, University of Bologna, Nikhef, Purdue University

(XENON Collaboration)

12

There is overwhelming indirect evidence that a large fraction of the matter content of the universe is dark [1]. Dark matter may be composed of yet unidentified Weakly Interacting Massive Particles (WIMP), a remnant from the early, hot phase of our universe [2]. The XENON program operates time projection chambers (TPCs) filled with liquid xenon (LXe) as target material to detect nuclear recoils from WIMP elastic scatters off xenon nuclei. Operated as two-phase TPCs, as schematically shown in Fig. 4.1, the detectors observe light and charge signals from scintillation and ionization processes, providing a 3-dimensional interaction vertex reconstruction on an event-by-event basis and efficient discrimination against background signals from γ - or β -interactions. The vertex reconstruction allows to define a central, fiducial region of the detector, avoiding background induced in the walls.

We are involved in XENON100, the current phase in this program, which employs a total mass of 161 kg of LXe and in XENON1T, which will use a total mass of ~ 2.4 tons of LXe. The detector is in the design phase, its construction at the *Laboratori Nazionali del Gran Sasso* (LNGS) in Italy will start in late 2012.

XENON100

XENON100 is located in the LNGS interferometer tunnel below an average of 3600 m water equivalent rock overburden, which reduces the muon flux by a factor 10^6 . It uses the passive lead/polyethylene

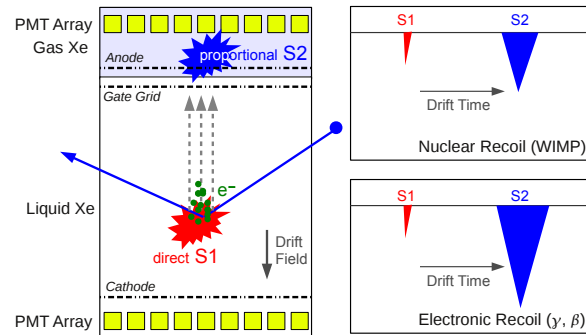


FIG. 4.1 – Working principle of a two-phase TPC: Particle interactions in the liquid xenon target generate prompt scintillation light ($S1$) and ionize the target. The electric field across the detector volume drifts the electrons to the top of the TPC, where they are extracted into the gas phase by a strong extraction field. In the gas phase, they produce a localized proportional scintillation signal ($S2$) which allows to determine the xy -coordinate of the primary interaction. The z -coordinate is derived from the electron drift time, i.e., the time difference between $S1$ and $S2$. The $S2/S1$ amplitude ratio is different for signal (nuclear recoils) and background (electron recoils) [4].

shield of XENON10, with the addition of an inner 5 cm copper layer as well as an outer, 20 cm thick water neutron shield. With 62 kg of liquid xenon in the TPC, XENON100 has a 4.5 times higher target mass than its predecessor, XENON10.

The gamma background was reduced by two orders of magnitude by means of an optimized detector de

sign, as well as screening and selection of radio-pure detector and shield materials [3]. A detail description of the XENON100 instrument is published [4].

In 2011 XENON100 reported results from a 100.9 live days dark matter search [5]. A total of three events were found in the pre-defined signal region, compatible with the background prediction of (1.8 ± 0.6) events. The data was used to constrain the inelastic dark matter model (iDM) [6]. This model overcomes the tension between the annual modulation signal observed by DAMA [8] and the null results of other direct detection experiments. iDM assumes that WIMPs scatter off baryonic matter by simultaneously populating an energy level at δ above the groundstate ($\chi N \rightarrow \chi N^*$). Elastic scattering would be highly suppressed. In contrast to the elastic scattering, where an exponential recoil energy spectrum is expected, the threshold of the inelastic scattering process leads to a peaked recoil spectrum which for xenon ranges from ≈ 10 to ≈ 50 keV_{nr}.

Figure 4.3 shows the parameter space allowed by DAMA and other experiments. The result of XENON100 rules out the iDM interpretation of the DAMA modulation at 90% C.L. [7].

The XENON100 detector is continuously taking science data since March 2011. Compared to the last dark matter run, it has achieved a lower trigger threshold, a higher electronegative purity of the xenon, a lower background due to the ^{85}Kr intrinsic contamination, as well as high-statistics calibration runs with external gamma and neutron sources. About 225 live days of dark matter data have been acquired to date. The data is currently being analyzed, results are expected in early summer.

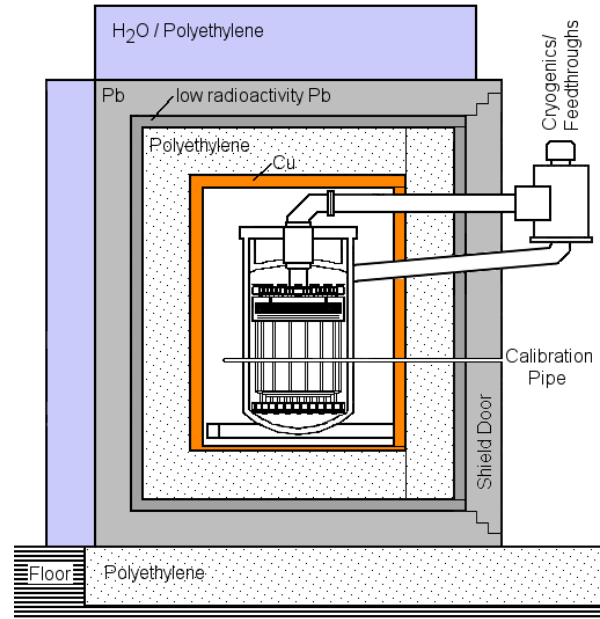


FIG. 4.2 – XENON100 inside its passive shield made of water, lead, polyethylene, and ultra-pure copper, underground at LNGS [4].

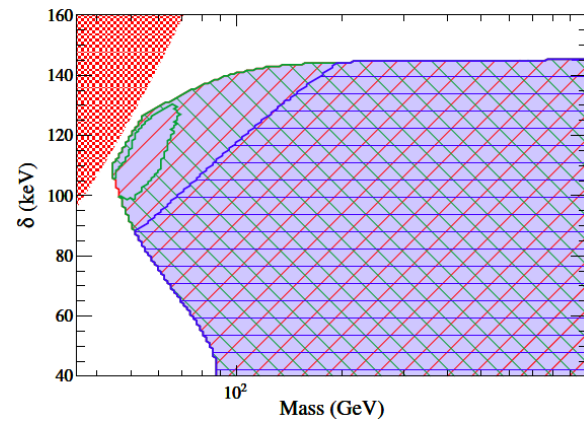


FIG. 4.3 – Parameter space allowed by the DAMA annual modulation signal [8] in the inelastic dark matter model [6] (light blue area), along with the parameter space excluded by CDMS-II (blue horizontal lines) and ZEPLIN-III (green descending lines). XENON100 (red ascending lines) excludes the entire region allowed by DAMA [7].

XENON1T

XENON1T will use about 2.4 tons of LXe in total with 1 ton in the fiducial volume. The xenon tank will be surrounded by a cylindrical 9.6 m × 10 m water Cherenkov shield to reduce the muon induced neutron background to negligible levels. The raw background rate will be 1×10^{-4} events/(keV kg day), hundred times below the one of XENON100 [9] and the sensitivity to the WIMP-nucleon cross section will be pushed to 10^{-47} cm².

14

The XENON1T technical design report was submitted to LNGS in 2010 and in 2011 the project was approved to be installed in Hall B. The design is presently being finalized and construction is expected to start this year.

Our group is responsible for data acquisition and electronics, material screening, design and manufacturing of the inner detector structure, the photosensor calibration system and the tests of new, low-radioactive photomultiplier tubes (PMTs). We are also conducting Monte Carlo simulations targeted at the optimization of the detector design by minimizing the backgrounds from the intrinsic radioactivity of the components, and by improving the light collection efficiency and the vertex resolution. Together with Hamamatsu, the collaboration has developed a new 3-inch low-radioactivity PMT, R11410. Four units are currently being tested in our laboratory for their performance at room and liquid xenon temperatures. Figure 4.4 shows the stability of the gain for one unit over two months of operation in liquid xenon.

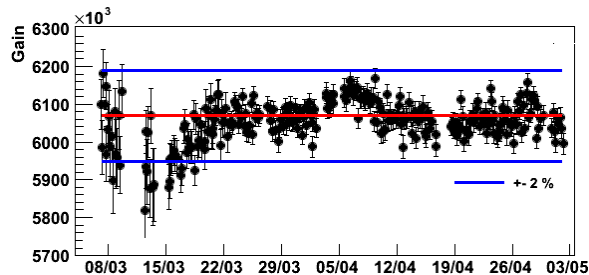


FIG. 4.4 – The gain of one R11410 PMT at liquid xenon temperature measured during two months. The blue lines represent $\pm 2\%$ variation.

Material screening

To screen and select materials for XENON1T, we employ the following techniques:

- Inductively Coupled Plasma Mass Spectrometry (ICP-MS), available at LNGS with a sensitivity down to a few tens of $\mu\text{Bq/kg}$ for ²³⁸U, ²³²Th and ⁴⁰K,
- Neutron Activation Analysis (NAA), available at the Paul Scherrer Institute and at the Johannes Gutenberg University Mainz, with a similar sensitivity as the ICP-MS for the same isotopes,
- High Purity Germanium (HPGe) gamma spectrometers, available both at LNGS (with a sensitivity down to tens of $\mu\text{Bq/kg}$ for ²²⁶Ra, ²²⁸Ra, ²²⁸Th and ⁶⁰Co) and at the Max Planck Institut für Kernphysik (MPIK) (with a sensitivity of $\sim 1\text{mBq/kg}$ for ²²⁶Ra, ²²⁸Ra, ²²⁸Th and ⁶⁰Co),
- ²²²Rn emanation assaying with ultra-low background proportional counters, available at the MPIK Heidelberg.

Our group operates the Gator facility [10] at LNGS, and has access to the ICP-MS and NAA techniques. These are complementary to gamma-ray spectroscopy as they detect the early parts of the ²³⁸U and ²³²Th chains. Gator contains at its core an ultra-low background, 2.2 kg HPGe detector with a relative efficiency of 100.5%, and a measured energy resolution of ~ 3 keV FWHM at 1332 keV. It was extensively used to screen and select materials for XENON100 [3]. A selection of results for XENON1T materials is shown in Table 4.1. Titanium is considered as a material for the cryostat, while torlon is planned to be used inside the TPC, in a small amount. The R11410-10 PMT, with a quantum efficiency of $> 35\%$ at the 178 nm LXe scintillation light wavelength, will be used for the light sensor arrays.

TAB. 4.1 – Results from the radioactivity screening of the XENON1T samples.

Material	Technique	isotope						Unit
		^{238}U	^{226}Ra	^{228}Ra	^{228}Th	^{40}K	^{60}Co	
Ti grade 1	HPGe	30(10)	1.2(4)	< 1.1	< 0.71	< 2.8	< 0.17	mBq/kg
Ti grade 4	HPGe	< 42	< 1.2	2.1(6)	9(1)	< 4.9	< 0.29	mBq/kg
Ti grade 2	HPGe	40(10)	< 0.81	1.9(6)	3.1(3)	< 2.9	< 0.25	mBq/kg
Ti grade 1	NAA	< 650	–	< 110	–	–	–	mBq/kg
Ti grade 1	ICP-MS	25(4)	–	< 8.1	–	< 1600	–	mBq/kg
R11410-10 ^a	HPGe	< 18	< 1.4	< 2.9	< 2.0	17(3)	4.3(4)	mBq/PMT
Torlon	HPGe	< 33	< 2.6	< 5.5	3(1)	< 26	< 11	mBq/kg
Torlon	ICP-MS	4.9(4)	–	0.49(4)	–	11.5(1)	–	mBq/kg

^a 3" PMT

- [1] G. Bertone, D. Hooper, J. Silk,
Phys. Rep. 405, 279 (2005).
- [2] B.W. Lee and S. Weinberg,
Phys. Rev. Lett. 39, 165 (1977).
- [3] E. Aprile *et al.*,
Astropart. Phys. **35**, 43 (2011).
- [4] E. Aprile *et al.*, (XENON100),
Astropart. Phys. 35, 573 (2012).
- [5] E. Aprile *et al.*, (XENON100),
Phys. Rev. Lett. 107, 131302 (2011).
- [6] D. Tucker-Smith and N. Weiner,
Phys. Rev. D 72, 063509 (2005).
- [7] E. Aprile *et al.*, (XENON100),
Phys. Rev. D 84, 061101 (2011).
- [8] C. Savage, G. Gelmini, P. Gondolo and
K. Freese, JCAP 04, 010 (2009).
- [9] E. Aprile *et al.*, (XENON100),
Phys. Rev. D83, 082001 (2011).
- [10] L. Baudis *et al.*, JINST 6, P08010 (2011).
- [11] L. Baudis *et al.*, JINST **6** (2011) P08010.

5 DARWIN: dark matter WIMP search with noble liquids

L. Baudis, A. Behrens, A. Ferella, A. Kish, A. Manalaysay, T. Marrodán Undagoitia, M. Schumann, M. Walter

in collaboration with:

ETHZ, INFN, University of Münster, Subatech, Weizmann Institute, University of Mainz, MPIK Heidelberg, Rice University, University of Bologna, Nikhef, Karlsruhe University, Columbia, UCLA, Princeton

(DARWIN Consortium)

16

Astrophysical observations show that 83% of gravitating matter in our universe is non-luminous and non-baryonic. The dark matter might be in the form of neutral, weakly interacting, stable or long-lived elementary particles, so-called WIMPs, which have eluded direct observation so far. Produced in the early universe, WIMPs would naturally lead to the observed dark matter abundance [1] and are predicted to exist in extensions to the Standard Model of particle physics [2]. Galactic WIMPs may be detected via scatters off atomic nuclei in deep underground experiments [3]. Since expected signal rates are below one interaction per kilogram of target material and year and momentum transfers are around 10 - 100 MeV [4, 5], large detector masses, low energy thresholds and ultra-low backgrounds are essential experimental requirements to directly observe these hypothetical particles.

Experiments using xenon [6–9] and argon [10] as a homogeneous detection medium in a time projection chamber have reached sensitivities of $\sim 10^{-44} \text{cm}^2$ for the spin-independent scattering cross section on nucleons. While a factor of five improvement is predicted with data already in hand [8], ton-scale experiments under commissioning [11] or construction [12] will likely probe the region down to $\sim 5 \times 10^{-47} \text{cm}^2$. Notwithstanding this remarkable leap in sensitivity, and assuming local density and velocity distributions inferred from astronomical observations, significantly larger detectors are requisite to determine WIMP properties, such as its mass, scattering cross section and pos-

sibly spin [13]. To proof the dark matter interpretation of a signal, a measurement of the interaction rate with different target materials is compulsory.

Technologies

The DARWIN study [14–16] is focused on a multi-ton liquid argon and/or xenon experiment rooted in the noble liquid time projection chamber (TPC) technique. The TPCs will record the prompt scintillation light³ created when a particle interacts in the active detector volume along with the few liberated electrons after drifting in a strong electric field⁴ towards the vapor phase residing above the liquid. The prompt light signal will be observed by an array of photosensors immersed in the liquid, the electrons will be detected either directly, or indirectly via proportional scintillation in the gas phase with a second array of photosensors. The time difference between the prompt and delayed signals is determined by the z -position of the primary interaction, the spatial coordinates of the delayed signal reveal its $x - y$ -position. The relative size of the charge and light signals, as well as their time structure will be used to distinguish nuclear recoils, as expected from WIMP scatters, from electronic recoils, which make the majority of the events. The spatial resolution allows to select an inner, low-background region and to reject fast neutrons, which – in contrast to WIMPs – tend to scatter more than once⁵.

³Photon emission from the decay of excited dimers to their dissociative ground state peaks around 128 nm and 178 nm in liquid argon and xenon, respectively [25].

⁴Typical drift fields are 0.5–1 kV/cm, with electron velocities around $\sim 2 \text{ mm}/\mu\text{s}$ [25].

⁵The mean free path of $\sim \text{MeV}$ neutrons is in the range of tens of cm.

DARWIN will immensely benefit from the research and development, and from the construction and operation experience gained with XENON10 [17], XENON100 [18], XENON1T [12], WARP [10], ArDM [11], DarkSide [19], and much of the ongoing work is carried out within the framework of these projects. Here we mention a few studies only, some of these are specific to DARWIN. Other work deals with the cryogenic, gas purification, circulation, storage and recovery systems; with the external water Cerenkov shield and its potential extension with a liquid scintillator (depending on the depth of the underground laboratory – the Gran Sasso Laboratory and the Modane extension are under consideration); with material screening, selection and radon emanation measurements; with high-voltage systems, electrodes and field uniformity simulations; with low-noise, low-power electronics, cables and connectors, trigger schemes, data acquisition and treatment; with Monte Carlo simulations of the expected background noise, of the light collection efficiency and position reconstruction capability; with the design of the time projection chamber, of the cryostat and of the calibration system.

- Light and charge response:

the light and charge yields of noble liquids when exposed to low-energy nuclear recoils (from neutron or potential dark matter interactions) or electronic recoils (from γ - and β -interactions) are studied by several groups participating in DARWIN. A new measurement of the relative scintillation efficiency \mathcal{L}_{eff} in liquid xenon [20] shows an \mathcal{L}_{eff} behavior which is slowly decreasing with energy, with a non-zero value at 3 keV nuclear recoil energy, the lowest measured point. A similar measurement is ongoing for liquid argon [21]. A measurement of the liquid xenon scintillation efficiency for electronic recoils down to 2.3 keV is in progress [22]. A preliminary data analysis indicates that the scintillation yield falls with decreasing energy, as predicted by models of scintillation mechanisms in noble liquids [23]. Nonetheless, the scintillation response at 2.3 keV

is observed to be non-zero, confirming that liquid xenon experiments will have a finite sensitivity at such low interaction energies. Measurements of the charge yields of LAr and LXe within the same energy regime are being planned.

- Signal readout:

the prompt scintillation light is to be observed either with conventional photomultiplier tubes (PMTs) which are low in radioactivity [24] and built to withstand low temperatures and high pressures⁶ or with a new, hybrid photodetector (QUPID [26]), which has an extremely low radioactivity content (<1 mBq/sensor for U/Th/K/Co) [24] and works both in liquid argon and xenon. The delayed signal can be observed directly, using detectors with single electron sensitivity and high spatial granularity (large electron multipliers [27]), or CMOS pixel detectors coupled to electron multipliers (Grid-Pix [28]), or via proportional scintillation in the gas phase, using gaseous photomultipliers without dead zones (GPMs [29]), PMTs or QUPIDs.

Backgrounds and physics reach

DARWIN will be an “ultimate” argon and/or xenon dark matter experiment, before the solar and atmospheric neutrinos become the main, possibly irreducible background. It will directly probe WIMP-nucleon cross sections down to $\sim 10^{-48}$ cm². These cross sections are compatible with recent LHC results, should the dark matter particle turn out to be the neutralino [30–32]. The external background from gammas, muons and neutrons and the background from detector construction materials will be diminished to negligible levels by external shields, the self-shielding of the noble liquids⁷, and the choice of fiducial volumes⁸. More problematic are intrinsic backgrounds from ⁸⁵Kr and ²²²Rn decays in xenon and from ³⁹Ar decays in argon. In xenon, the natural krypton concentration is to be reduced

⁶One example is the Hamamatsu R11410/R11065 3"-tube for LXe/LAr, currently tested for its performance, long-term stability and radioactivity levels at several DARWIN institutions.

⁷The mean free path of 3 MeV gammas is ~ 9 cm and ~ 20 cm in liquid xenon and argon, respectively.

⁸The final choice of the size and target materials are part of the outcome of the study, a baseline scenario is 20 t (10 t) total (fiducial) LAr/LXe mass.

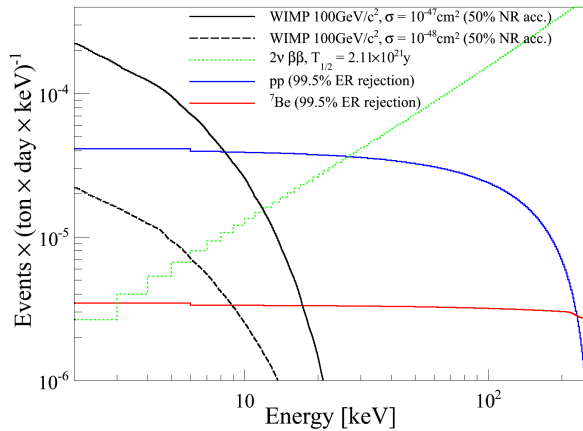


FIG. 5.1 – Expected nuclear recoil spectrum from WIMP scatters in LXe for a spin-independent WIMP-nucleon cross section of 10^{-47} cm^2 (solid) and 10^{-48} cm^2 (dashed) and a WIMP mass of $100 \text{ GeV}/c^2$ (using the standard halo model as in [13]), along with the differential energy spectrum for pp (blue) and ${}^7\text{Be}$ (red) neutrinos, and the electron recoil spectrum from the double beta decay of ${}^{136}\text{Xe}$ (green), assuming the natural abundance of 8.9% and the recently measured half life of $2.1 \times 10^{21} \text{ yr}$ [34]. Other assumptions are: 99.5% discrimination of electronic recoils, 50% acceptance of nuclear recoils, 80% flat analysis cuts acceptance.

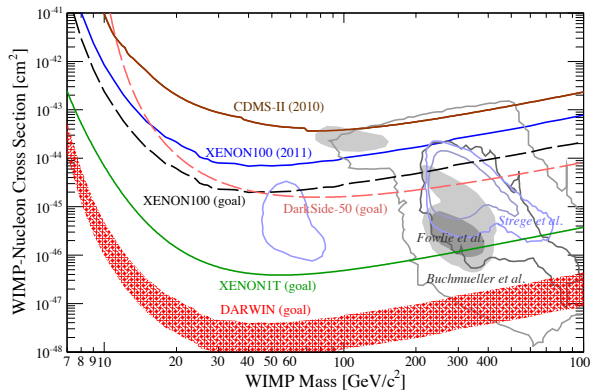


FIG. 5.2 – DARWIN's sensitivity goal for spin-independent WIMP nucleon cross sections, existing limits from XENON100 [8] and CDMS-II [35], future goals and updated theoretical predictions from supersymmetry (closed contours and shaded regions) [30–32].

by cryogenic distillation to $<1 \text{ ppt}$ and the radon level in the liquid is to be kept $<1 \mu\text{Bq}/\text{kg}$. Argon gas that is extracted from deep underground wells is depleted in the radioactive ${}^{39}\text{Ar}$ [33]. Still, a background rejection by pulse-shape analysis of $>10^8$ is required in the case of a liquid argon detector [14, 15]. Figure 5.1 shows the expected nuclear recoil spectrum from WIMP scatters in xenon together with the background from neutrino-electron elastic scatters of solar neutrinos and from the double beta decay of ${}^{136}\text{Xe}$.

In Fig. 5.2 we show the aimed sensitivity of DARWIN, along with existing best upper limits on the WIMP-nucleon cross section, projections for the future and theoretically predicted regions from supersymmetric models.

DARWIN, which was endorsed in recent updates to the European and Swiss roadmaps for astroparticle and particle physics [36, 37], has officially started in 2010. A rough time schedule is the following: a technical design study is to be ready in spring 2013, leading to a letter of intent and engineering studies towards the proposal of a concrete facility in spring 2014, and a technical design report for detector construction by the end of 2014. The shield and detector construction phase is to start in 2015, commissioning in late 2016 with the start of the first physics run by mid 2017.

- [1] B. W. Lee and S. W. Weinberg, *Phys. Rev. Lett.* **39**, 165 (1977).
- [2] J. Feng, *Ann. Rev. Astron. Astrophys.* **48**, 495 (2010).
- [3] M. W. Goodman and E. Witten, *Phys. Rev. D* **31**, 3059 (1985).
- [4] G. Jungmann, M. Kamionkowski, K. Griest, *Phys. Rep.* **267**, 195 (1996).
- [5] J. D. Lewin and P. F. Smith, *Astrop. Phys.* **6**, 87 (1996).
- [6] J. Angle *et al.* (XENON10 Collaboration), *Phys. Rev. Lett.* **100**, 021303 (2008).
- [7] E. Aprile *et al.* (XENON Collaboration), *Phys. Rev. Lett.* **105**,

- 131302 (2010).
- [8] E. Aprile *et al.* (XENON Collaboration), Phys. Rev. Lett. **107**, 131302 (2011)
- [9] V. N. Lebedenko *et al.* (ZEPLIN-III Collaboration), Phys. Rev. D **80**, 052010, (2009); V. N. Lebedenko *et al.*, Phys. Rev. Lett. **103**, 151302, (2009); D.Yu Akimov *et al.*, arXiv:1110.4769 (2011).
- [10] R. Brunetti *et al.* (WARP Collaboration), Astropart. Phys. **28**, 495 (2008).
- [11] A. Rubbia *et al.* (ArDM Collaboration), J. Phys. Conf. Ser. **39**, 129 (2006).
- [12] E. Aprile *et al.* (XENON Collaboration), XENON1T at LNGS, *Proposal*, April (2010) and *Technical Design Report*, October (2010).
- [13] M. Pato, L. Baudis, G. Bertone, R. R. de Austri, L. E. Strigari and R. Trotta, Phys. Rev. D **83**, 083505 (2011).
- [14] L. Baudis (DARWIN Consortium), PoS(IDM2010)122 (2010), arXiv:1012.4764v1 [astro-ph.IM].
- [15] M. Schumann (DARWIN Consortium), arXiv:1111.6251v1 [astro-ph.IM].
- [16] <http://darwin.physik.uzh.ch>
- [17] E. Aprile *et al.* (XENON10 Collaboration), Astroparticle Physics **34**, 679-698 (2011).
- [18] E. Aprile *et al.* (XENON Collaboration), arXiv:1107.2155v1 [astro-ph.IM].
- [19] A. Wright (DarkSide), arXiv:1109.2979 (2011).
- [20] G. Plante *et al.*, Phys. Rev. C **84**, 045805 (2011).
- [21] C. Regenfus, talk presented at TAUP2011 (2011).
- [22] A. Manalaysay, talk presented at TAUP2011 (2011).
- [23] M. Szydagis *et al.*, JINST **6** P10002 (2011).
- [24] E. Aprile *et al.* (XENON Collaboration), Astropart. Phys. **35**, 43 (2011).
- [25] E. Aprile, A.E. Bolotnikov, A.I. Bolozdynya, and T. Doke, Noble Gas Detectors, WILEY-VCH (2006).
- [26] A. Teymourian, D. Aharoni, L. Baudis, P. Beltrame *et al.*, Nucl. Instr. Meth. A **A 654**, 184 (2011).
- [27] A. Badertscher *et al.*, Nucl. Instr. Meth. A **641**, 48 (2011).
- [28] V. Blanco Carballo *et al.*, JINST **5**, P02002 (2010).
- [29] S. Duval *et al.*, arXiv:1110.6053 (2011).
- [30] A. Fowlie, A. Kalinowski, M. Kazana, L. Roszkowski, Y.-L. Sming Tsai, arXiv:1111.6098v1 [hep-ph].
- [31] O. Buchmueller, *et al.*, arXiv:1110.3568v1 [hep-ph], arXiv:1112.3564v1 [hep-ph].
- [32] C. Strege, G. Bertone, D. G. Cerdano, M. Fornasa, R. Ruiz de Austri, R. Trotta, arXiv:1112.4192v1 [hep-ph].
- [33] D. M. Mei, Z. B. Yin, J. Spaans, M. Koppang, *et al.*, Phys. Rev. C **81**, 055802 (2010).
- [34] N. Ackerman *et al.*, Phys Rev Lett. **107**, 212501 (2011).
- [35] Z. Ahmed *et al.*, Science, 1186112 (2010).
- [36] www.aspera-eu.org/images/stories/roadmap/SAC-Roadmap-Nov-1-2011-final.pdf
- [37] www.chipp.ch/documents/roadmap.pdf

6 Very High Energy Gamma Ray Astronomy with CTA

D. Florin, A. Gadola, R. Gredig, B. Huber, A. Manalaysay, S. Steiner, U. Straumann, A. Vollhardt

in collaboration with: ETH Zürich, Jagiellonian University Cracow, MPI für Kernphysik Heidelberg, University of Leeds, Universität Tübingen.

The full CTA collaboration consists of 115 institutes from 23 countries.

(CTA)

20

The Cherenkov Telescope Array (CTA) is a planned next generation array of Imaging Atmospheric Cherenkov Telescopes (IACTs), and is the successor to the current generation of IACTs including MAGIC [1], H.E.S.S [2], and VERITAS [3]. These telescopes are used to detect Very High Energy (VHE) gamma ray photons, in the range of tens of GeV to tens of TeV, emitted from exotic (i.e. non-thermal) astrophysical sources such as quasars, supernovae and their remnants, gamma-ray bursts, and dark matter annihilations. See our contribution to the previous annual report for further details on the motivation for CTA.

Active Mirror Control

Current and future imaging air Cherenkov telescopes use large primary mirrors that are composed of multiple mirror “facets” pieced together to form a much larger mirror. This design facilitates an easier construction of the primary mirror to high optical tolerances, compared with a single large mirror. Each mirror facet is attached to the telescope structure at three fixation points. Between the telescope structure and each fixation point is a rod of adjustable length. Varying the length of individual rods on a single mirror facet allows the orientation of the facet to be fine-tuned.

We have developed a system of wirelessly controlled mechanical actuators that attach to the mirror fixation points that allow the facet orientations to be adjusted remotely, as part of an Active Mirror Control (AMC) system. A fixed rod is attached to one of the three fixation points, while movable actu-

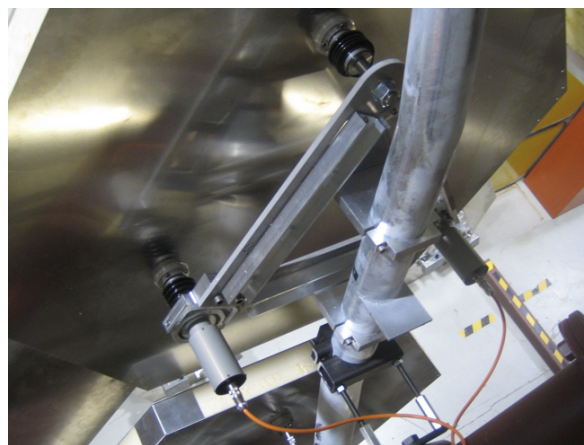


FIG. 6.1 –
Two UZH AMC actuators mounted on the prototype telescope quarter dish in DESY Zeuthen.

ators are attached to the other two fixation points. Prototype models of the actuators were produced in the middle of 2009 and have been under continuous outdoor tests since then, completing so far nearly three million full cycles of extension and retraction.

The Medium-size Telescopes (MST) planned for CTA will be constructed after a series of two prototype structures. The first prototype is a quarter section of the full telescope, for which construction has already begun at DESY Zeuthen, in Germany. The quarter dish is outfitted with “dummy” mirrors (to simulate the size and mass of the real mirror facets), two of which are attached via UZH actuators. Figure 6.1 shows two of the UZH actuators attached to the quarter dish and powered in Zeuthen, assembled in June of 2011.

A full MST prototype will be constructed in Berlin in late of 2012. For the purpose of this proto-



FIG. 6.2 –
AMCs during mass production at UZH, to be used in the full Medium-size Telescope CTA prototype.

type, we have mass-produced 200 AMC actuators. Figure 6.2 shows a sample of these devices during assembly at UZH. Along with the actuators, the rotatable gimbals that fix the actuator to the telescope frame, and the power cables and power distribution system have been produced.

FlashCam

FlashCam is a proposed possible camera design for CTA that focuses on using a fully digital data and trigger pathway. It differs from more traditional

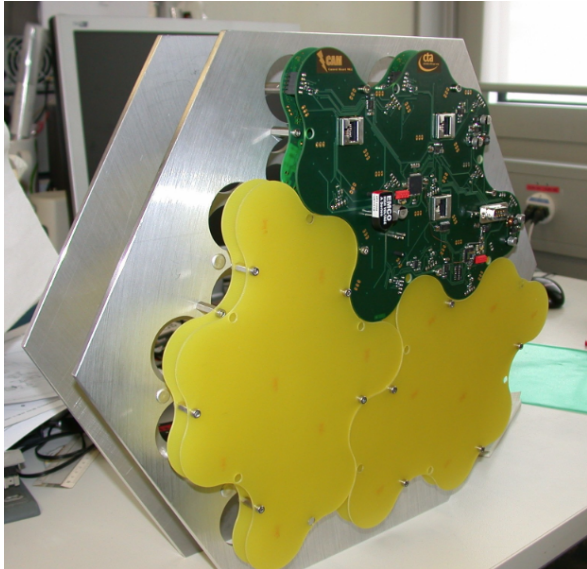


FIG. 6.3 – *Prototype of a section of the full FlashCam mechanics.*

IACT camera designs in that data is digitized continuously, as opposed to having first an analog trigger pipeline that is then used to decide when to digitize the stored analog data. Traditional techniques typically feature an effective sampling rate of around 2 GS/s. However, creating a continuously digitized 2 GS/s pathway is prohibitive both in terms of cost and power consumption for an array of cameras that each consist of thousands of channels. Interestingly, our collaborators at the Max Planck Institute for Nuclear Physics (MPI-K) in Heidelberg, Germany have shown that adequate instrumental and timing resolution can be achieved by using a system that samples at a rate of 250 MS/s. A telescope array of such digitizers is feasible, and is currently being prototyped.

A prototype model is being constructed at UZH that includes the full electronics chain of the real camera, with only twelve pixels. Figure 6.3 shows the mechanical structure of the prototype with two sets of dummy boards and one set of production electronics. Two boards are used in this case; the first board, closest to the photomultiplier tubes (PMTs), contains the high voltage divider and signal preamp. The second board contains the high voltage generation and slow control devices. Figure 6.4 shows the assembled twelve-pixel group from the front, with production PMTs from Hamamatsu Photonics specially designed for CTA. This device allows each PMT to be tested separately.



FIG. 6.4 – *Assembled twelve-pixel group of the FlashCam photon detection plane.*

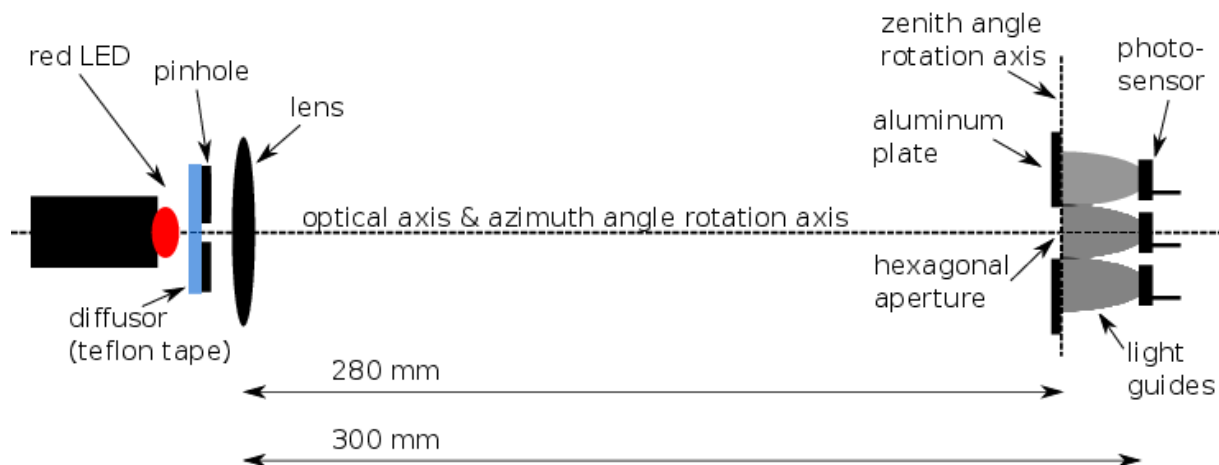


FIG. 6.5 – Schematic of the test setup used for measuring the optical properties of the solid light concentrators used in the G-APD camera.

Solid Light Concentrators

Individual pixels of IACT cameras are in general equipped with special light concentrators that focus incident light onto the entrance area of the photosensors. With the aid of light concentrators, the sensitive area per pixel is increased and a nearly borderless full coverage of the full camera area is achieved.

In conjunction with the FACT group at the ETH-Zurich, our group has contributed extensively to

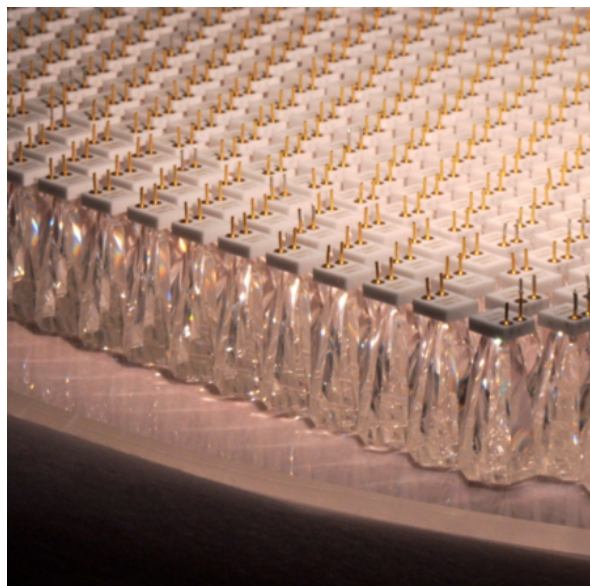


FIG. 6.6 – Installed solid light cones with G-APDs optically glued to the exit aperture of the cones.

the development of parabolic solid light concentrators made from injection-molded polymethyl methacrylate, and to the assembly of the FACT optical front plane. The light concentration is based on total internal reflection. The exit area is tailored to the sensitive area of commercial $3 \times 3 \text{ mm}^2$ Geiger-mode avalanche photodiodes (G-APDs). The design and fabrication of these devices has gone through three production iterations, starting from machined Plexiglas to the final injection molded pieces mentioned above. A test setup (Fig. 6.5) has been produced at UZH to measure the optical properties of each prototype design, including transmission efficiency and angular acceptance roll-off. Additionally, the performance of the optical coupling between light concentrator and G-APD has been extensively studied with this setup. The full set of final light cones have been produced and assembled into the optical front plane of FACT, seen in Figure 6.6, which is now in operation.

- [1] J. A. Coarasa *et al.* (MAGIC Collaboration), *J. Phys. Soc. Jap. Suppl* **77B**, 49 (2008).
- [2] B. Opitz *et al.* (HESS Collaboration), *AIP Conf. Proc.* **1223** 140 (2010).
- [3] D. Hanna *et al.* (VERITAS Collaboration), *J. Phys. Conf. Ser.* **203** 012118 (2010).

7 Testing lepton universality: the $\pi \rightarrow e\bar{\nu} / \pi \rightarrow \mu\bar{\nu}$ branching ratio

P. Robmann, A. van der Schaaf and P. Truöl

in collaboration with: University of Virginia, Charlottesville, USA; Institute for Nuclear Studies, Swierk, Poland; JINR, Dubna, Russia; PSI, Villigen, Switzerland and Rudjer Bošković Intitute, Zagreb, Croatia

(PEN Collaboration)

The measured value of the $\pi \rightarrow e\bar{\nu} / \pi \rightarrow \mu\bar{\nu}$ branching ratio ($1.2312(37) \times 10^{-4}$ [1]), even if 20 years old by now, still gives the best constraint on deviations from the SM assumption of a universal (flavour independent) coupling of W bosons to leptons. Two new experiments [2] are underway which aim at improvements in accuracy by almost one order of magnitude.

Precision measurements of this kind require great care in proper handling of systematic errors. Precise knowledge of the probability density functions (pdf's) of the various observables entering the likelihood analysis has to be based primarily on the measured data with minimal support by simulation in regions where processes can't be isolated sufficiently well. Of particular importance in this respect is the low-energy tail of the $\pi \rightarrow e\bar{\nu}$ positron energy pdf.

Detection efficiencies depend slightly on positron energy, mainly since the mean energy deposited in the MWPC tracking detectors rises with energy in combination with the fixed thresholds of the read-out electronics.

Pion beam

PEN took data during the years 2008 – 2010 at the π E1 beam line at PSI and has been working on the analysis ever since [3]. Charged particles produced in the E target by 590 MeV protons are transported to the experimental area by a series of quadrupole and dipole magnets. The beam line can be thought of as two magnetic spectrometers in a row followed by a focusing magnet triplet. The first spectrometer directs particles in the selected momentum band to a 2 mm thick carbon degrader.

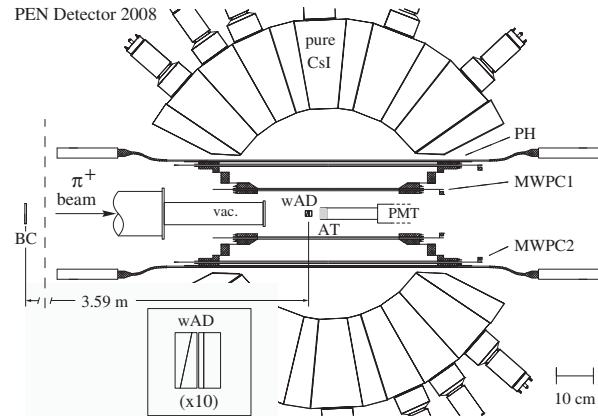


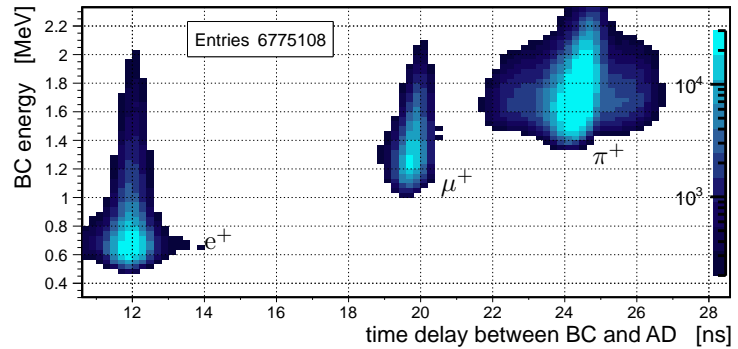
FIG. 7.1 – *PEN as used in the year 2008. The pion beam is focused on beam counter BC and then again 3.59 m further downstream on the active degrader wAD (see inset) which consists of two pairs of wedge-shaped plastic scintillators for a rough position measurement.*

Decay e^+ 's emitted from the active target AT are detected in a 240 element 3π Sr CsI calorimeter preceded by two MWPCs and a plastic hodoscope PH consisting of twenty slabs.

Heavier particles lose more momentum than lighter particles so in the focal plane of the second spectrometer the beam is split up depending on the particle mass and with the help of a collimator pions are separated from muons and positrons.

Figure 7.1 shows a cross-section through the PEN setup as used in 2008. For the chosen beam momentum around 75 MeV/c the pions stop 8 ± 1 mm deep inside the active target AT. All beam counters are read out both with high-performance (2 GHz bandwidth and sampling frequency) waveform digitizers and with long-range multi-hit TDC's which are useful to find extra beam signals in the preceding few μ s which give an enhanced probability for accidental coincidences.

FIG. 7.2 – Distribution of energy loss in the first beam counter (BC) versus time delay between BC and the degrader/tracker (wAD) situated 3.59 m downstream.



24

With the help of BC and wAD remaining beam contaminations can be removed (see Fig. 7.2) ⁹.

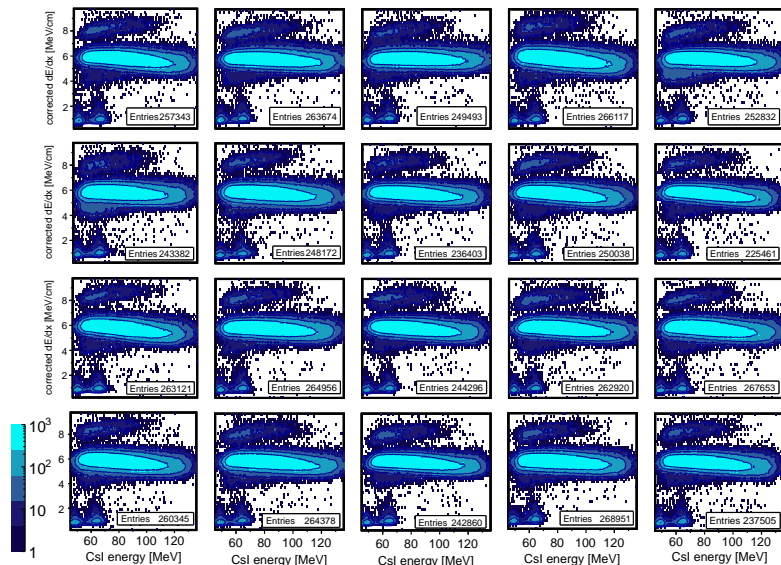
Pions are not only well separated from remaining positrons and muons but the pion velocity (and thus its energy) at the wAD entrance can be determined for each individual event. The trigger for data readout required a delay of 22 – 26 ns characteristic for pions. In order to show all beam contaminations events were selected with at least one additional beam particle. The observed tails in the pion distribution (cut by the trigger) result from pion decay shortly before wAD (see discussion below). Note that (i) larger π or μ energy loss gives slower particles, (ii) pions move with half the speed

of light and (iii) about half of the π 's reaching BC decay before reaching wAD .

Pion reactions

In the past year the emphasis has shifted from merely isolating the two signal processes to understanding all recorded events. About one third of the data are explained by pion reactions in the target which result mostly in the prompt emission of protons and deuterons with relatively high energies. These events are easily recognized (see Fig. 7.3) and very few enter the final samples.

FIG. 7.3 – Distributions of dE/dx versus E of prompt processes for the twenty individual PH plastic scintillators. The energy loss has been corrected to result in “horizontal” distributions for protons (the dominant contribution). The correction factor is equal to 1 at 100 MeV kinetic energy. Note at larger dE/dx the deuteron bands and at the low end the $\mu \rightarrow e\nu\bar{\nu}$ and $\pi \rightarrow e\bar{\nu}$ positrons.



⁹results presented in this report are from the full 2008 data set only

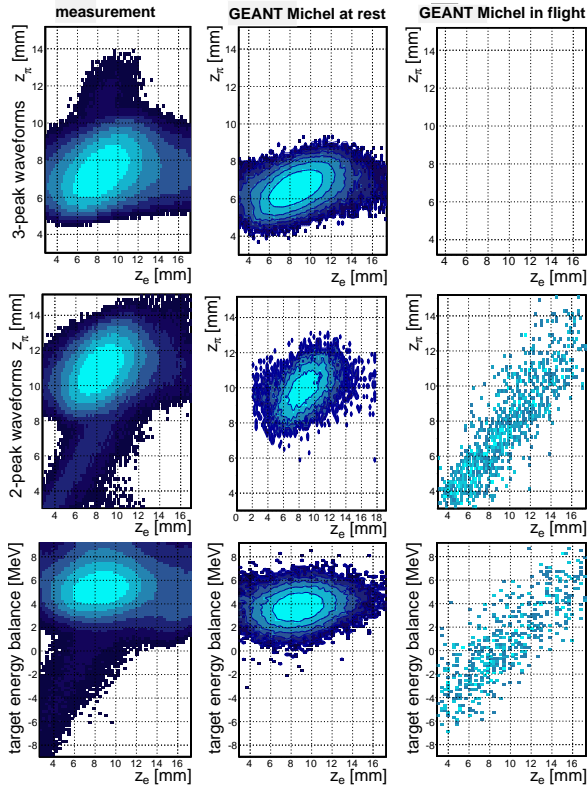


FIG. 7.4 – Evidence for $\pi \rightarrow \mu \bar{\nu}$ decay shortly before the pion would have come to rest. Measured distributions (left) for e^+ final states between 30 and 50 MeV are compared with the corresponding results for simulated $\pi - \mu - e$ sequences (Michel events). The latter are separated in two groups depending on the μ^+ energy at decay (known to the SIMULATOR). Events with muons decaying at rest are shown in the middle, decays in flight in the right panels.

The top two rows show events with well separated signals in the target waveform, either three (typical for $\pi - \mu - e$) or just two (as expected for decay in flight). The bottom row shows all events.

z_e : starting position coordinate of the e^+ along the beam line (from MWPCs).

z_π : final position coordinate of the π^+ along the beam line (from π^+ energy deposited in the target).

The target energy balance is the total target energy minus the predicted energies of π^+ and e^+ . See the text for further explanations.

Pion decay before stopping

Much more problematic are events in which the pion decays shortly before it would have stopped. Such processes can not always be distinguished, in particular when the pion energy at decay time approaches zero, and are thus included in the likelihood analysis. It takes $O(0.1)$ ns for a pion to stop in the active target so a few permille of them decay before stopping. When the resulting muon stops in the target the event may become a $\pi \rightarrow \mu \bar{\nu}$ candidate but no $\pi \rightarrow e \bar{\nu}$. As illustrated in Fig. 7.4 such events show two peaks rather than three in the target waveform and also exhibit a characteristic tail in the distribution of the target energy balance versus decay location along the beam line. The target energy balance is the observed total target energy corrected for the contributions expected for the incoming pion and the outgoing positron. The energy deposited by the pion can be predicted event by event based on the observed pion velocity over the final 3.59 m and the energy loss observed in the preceding beam tracker wAD . The expected positron signal is based on the path length in the target deduced from the positron trajectory. For $\pi \rightarrow e \bar{\nu}$ the energy balance peaks at zero, for $\pi - \mu - e$ it peaks at the 4 MeV muon energy. With the help of the simulation $\pi \rightarrow \mu \bar{\nu}$ in flight can be accounted for with minimal systematic uncertainties.

As shown in Fig. 7.5 $\pi \rightarrow e \bar{\nu}$ in flight was observed too which came as a surprise since we hadn't given it much thought. The process has a weird distribution in the two main observables since energy is Doppler broadened and decaytime is quasi-prompt.

Conclusions

In conclusion we can say that progress has been slow but steady. As so often many complications were “forgotten” in the proposal but so far no real show stopper has been found.

Unfortunately for PEN two key collaborators from Virginia have finished their PhD projects [4, 5] and will move on to post-doc positions elsewhere. This means that the load on the few remaining workers

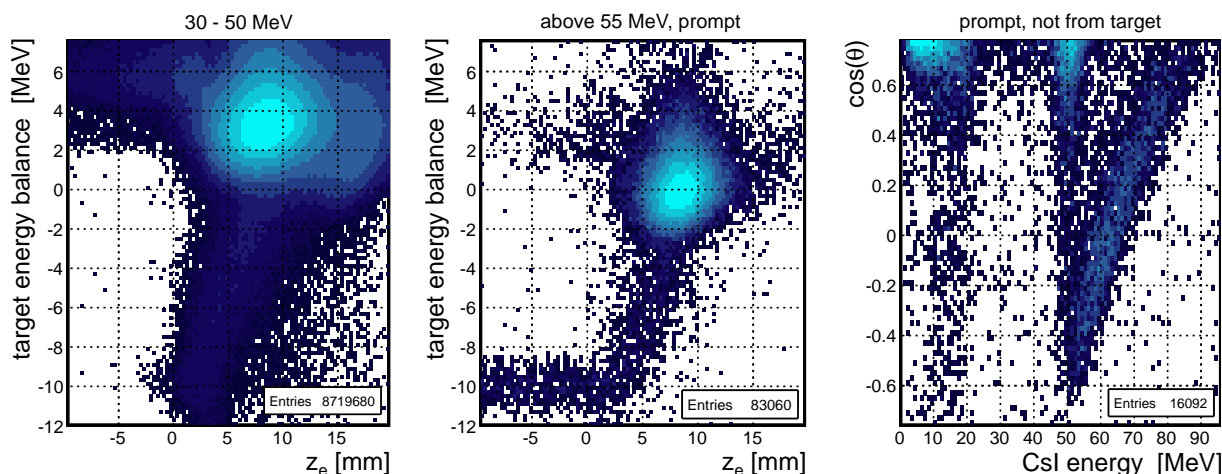


FIG. 7.5 – Evidence for $\pi \rightarrow e\bar{\nu}$ decay in flight. The left panel shows the $\pi \rightarrow \mu\bar{\nu}$ distribution from Fig. 7.4 for comparison. The energy offset has been corrected in this figure. $\pi \rightarrow e\bar{\nu}$ in flight requires no stopping material and may thus lead to decay vertices in front of the target without any target signal (horizontal band around -10 MeV in the middle panel populated by events without the expected ≈ 10 MeV pion signal). The right panel shows a clean signal of such events for which the e^+ energy shows a dependence on polar emission angle θ characteristic for Lorentz broadening. Additional, mostly forward contributions are from scattered beam (below 20 MeV) and decays of μ^+ stops in the degrader system. The energy region below 50 MeV was pre-scaled 1:64 in the trigger for data readout.

will increase even further. In this respect we are extremely happy to mention the bachelor work of Raphael Nydegger who optimized the reconstruction routines of the mini TPC used as beam tracker after 2008 and managed to improve the position resolution by a factor 2.

- [1] G. Czapek *et al.*, Phys. Rev. Lett. **70** (1993) 17; D. I. Britton *et al.*, Phys. Rev. Lett. **68** (1992) 3000.
- [2] PEN Collaboration, PSI experiment R-05-01 (2005), D. Pocanic and A. van der Schaaf, spokespersons; PIENU Collaboration, TRIUMF proposal 1072 (2006), D. Bryman and T. Numao, spokespersons.

- [3] see previous annual reports for details: www.physik.uzh.ch/reports.shtml
- [4] Anthony Palladino Jr., *Investigating Lepton Universality via a Measurement of the Positronic Pion Decay Branching Ratio*, PhD Dissertation (2012), The University of Virginia. http://pen.phys.virginia.edu/references/palladino_dissertation.pdf
- [5] Loreto Peter Alonzi III, *Measuring the Pion Substructure with Radiative Positronic Pion Decays*, PhD Dissertation (2012), The University of Virginia. http://pen.phys.virginia.edu/references/alonzi_dissertation.pdf

8 Study of Coulomb-bound πK pairs

C. Amsler, A. Benelli, and J. Rochet

in collaboration with:

CERN, Czech Technical University, Institute of Physics and Nuclear Physics Institute ASCR (Czech Republic), Laboratori Nazionali di Frascati, Messina University, Trieste University, KEK, Kyoto Sangyo University, Tokyo Metropolitan University, IFIN-HH (Bucharest), JINR (Dubna), Skobeltsin Institute for Nuclear Physics (Moscow), IHEP (Protvino), Santiago de Compostela University, Bern University.

(DIRAC Collaboration)

In 2007 we have observed for the first time electromagnetically bound $\pi^\mp K^\pm$ -pairs ($\pi^\mp K^\pm$ -atoms) [1, 2]. The $\pi^+ K^-$ -atom is unstable and decays through the strong force into $\pi^0 \bar{K}^0$ (while $\pi^- K^+$ -atoms decay into $\pi^0 K^0$). The mean life τ , which we intend to measure, is related to the S-wave πK -scattering lengths a_1 and a_3 in the isospin 1/2 and 3/2 states, respectively. The πK -scattering length is of interest to test chiral perturbation theories extended to the s -quark. From the 2007 data sample we reported the observation of 173 ± 54 πK -pairs [1, 2]. This result led to a lower limit for the mean life of πK -atoms of 0.8 fs in the $1s$ -state, which could be translated into an upper limit of the difference in scattering lengths $|a_1 - a_3| < 0.58 m_\pi^{-1}$.

The DIRAC experiment was initially designed to study $\pi^+ \pi^-$ -atoms. Final results for $\pi^+ \pi^-$ have been published recently [3]. From a sample of 21'227 $\pi^+ \pi^-$ atomic pairs the difference in the isospin 0 and 2 scattering lengths could be measured with a 4% accuracy, $|a_0 - a_2| = 0.2533 \pm 0.0109 m_\pi^{-1}$. The corresponding mean life is 3.15 ± 0.28 fs. An overview of the DIRAC experiment can be found in ref. [4].

A sketch of the DIRAC spectrometer to collect πK (and also more $\pi\pi$) data is shown in Fig. 8.1. Details can be found in previous annual reports and also in ref. [5]. The 24 GeV/c proton beam from the CERN-PS passes through a thin (100 μm) Ni-target. The secondary particles traverse a scintillation fiber detector (SFD) and a ionization hodoscope (IH) with which the opening angle between pairs of secondaries can be measured. The pions and kaons are analyzed in a double-arm magnetic

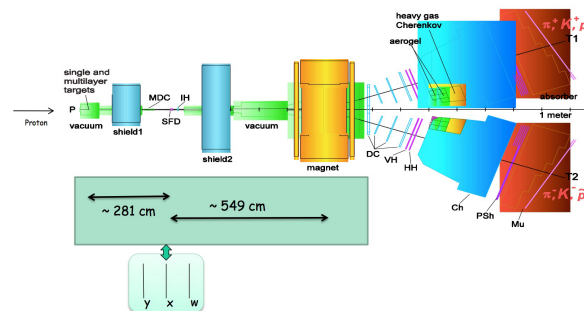


FIG. 8.1 – Sketch of the upgraded DIRAC-II spectrometer, showing the locations of the Čerenkov counters to identify electrons, pions and kaons. MDC: microdrift chambers, SFD: scintillator fiber detector, IH: ionization hodoscope, DC: drift chambers, VH, HH: vertical and horizontal scintillation hodoscopes, CH: N_2 -Čerenkov counter, PSh: preshower, Mu: muon counters.

spectrometer measuring the momentum vectors of two oppositely charged hadrons. Positive particles are deflected into the left arm, negative ones into the right arm. The spectrometer is slightly tilted upwards with respect to the proton beam. Electrons and positrons are vetoed by the N_2 -Čerenkov detectors and muons by their signals in scintillation counters behind steel absorbers. Kaons are separated from pions and protons by heavy gas (C_4F_{10}) Čerenkov counters (which fire on pions) and by aerogel Čerenkov counters (which fire on both pions and kaons, but not on the more numerous protons). Our group has developed and built the 37 ℓ aerogel Čerenkov counter [6] and the gas system for the C_4F_{10} counters [7]. The signal from πK -atoms is observed for πK -pairs with a very small relative momentum (typically $|Q_L| < 3$ MeV/c is the c.m.s system).

In 2007 we used only the detectors downstream of the magnet, but the scintillation fiber detector (SFD) was available for the 2008 – 2010 run to determine the interaction point in the production target with much better precision. The SFD (Fig. 8.2) consists of 3 planes of 205 μm scintillating fibers. Two planes (x - and y -planes) are made of 8 layers each with 480 fibers while the third (w -plane) contains 3 layers of 320 fibers. The fibers are read out in columns of 8, respectively 3 fibers by 30×16 Hamamatsu H6568 photomultipliers. The area covered by each plane is about $10 \times 10 \text{ cm}^2$ and contributes only 1% radiation length. The timing resolution is 460 ps. Tracks are measured with good resolution ($\sigma = 60 \mu\text{m}$) and high efficiency (98%). This leads to a substantial improvement in the resolution on the transverse momentum Q_T (from 3 MeV/c to 1 MeV/c) and also reduces the background.

During 2010 we tuned the Monte Carlo simulation of the SFD and compared with data. A substantial improvement has been achieved (for more details see ref. [8]). Noise, cross-talk between fibers, efficiency and background tracks have been inserted into the simulation. The simulated data were then submitted to the same analysis code as the experimental data. To study the performance of the SFD we used in turn two planes (e.g. y and w). The reconstructed tracks were then extrapolated to the third plane (e.g. x , see Fig. 8.3) and the measured hits compared with the predicted ones.

The excellent agreement between data and Monte Carlo is illustrated in Fig. 8.4 showing both the probability to find a hit within $\pm 1 \text{ mm}$ from the extrapolated trajectories and the probability to find both hits in the third plane if two tracks are found in the first two planes. The loss in the center is due to a hardware suppression algorithm of fiber cross-talks. The ionization hodoscope can be used to reduce background and select true double hits. From these plots one obtains track resolutions for the 2008-9-10 data of $\sigma = 220 \mu\text{m}$ for single tracks and $550 \mu\text{m}$ for double tracks.

Thus the SFD performed as expected from simulations and we could proceed with the analysis of the data using the three planes. We obtain a Q_x

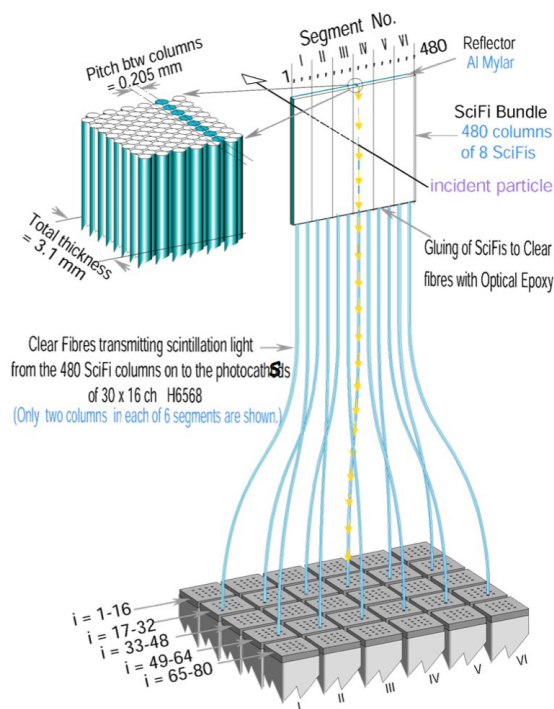


FIG. 8.2 – Sketch of the SFD (x - and y -planes).

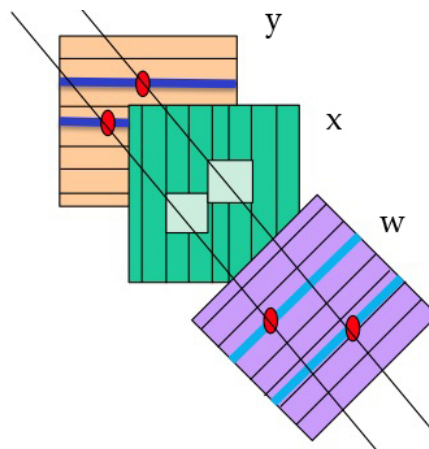


FIG. 8.3 – Measurement of the SFD performance with 2 out of 3 planes.

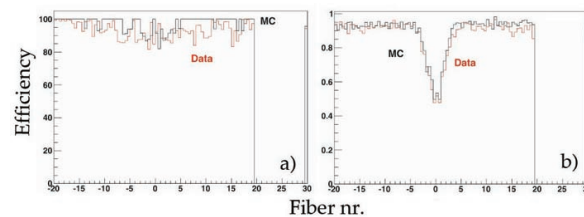


FIG. 8.4 – a) Probability to find one hit in the x -plane around the extrapolated track; b) probability to find both hits for two tracks.

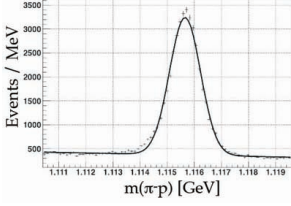


FIG. 8.5 – $\pi^- p$ mass distribution showing the Λ signal.

and Q_y resolution better than 0.5 MeV/c and reconstruct the momentum transfer Q between the kaon and the pion with a resolution of 1 MeV/c. As a calibration tool and momentum resolution measurement we reconstruct Λ decays into $\pi^- p$. The mass distribution shown in Fig. 8.5 confirms the correct energy scale, the value for the Λ mass 1115.7 ± 0.5 MeV being fully compatible with the PDG value (1115.683 ± 0.006 MeV).

Clean πK events are selected by the SFD and IH detectors to resolve the ambiguity of single and double tracks in the upstream part of the apparatus (Fig. 8.1). Particle identification is performed using the heavy gas and aerogel Čerenkov detectors. The precise time difference between the two tracks from the atomic candidates pairs is achieved using the VH. Events with muons or electrons are eliminated using the nitrogen Čerenkov and muon detectors. We finally select events with relative transverse and longitudinal momenta between the two mesons of $Q_T < 4$ MeV/c and $|Q_l| < 20$ MeV/c, respectively. Figure 8.6 (left) shows the preliminary distribution of $\pi^- K^+ + \pi^+ K^-$ events as a function of relative momentum Q (points with error bars).

The fit results are shown in red (atomic pairs), blue (Coulomb pairs), magenta (non-Coulomb pairs). The sum of Coulomb and non Coulomb pairs is displayed in black. The contribution from atomic pairs is shown in red in Fig. 8.6 (right). We find 277 ± 52 atomic pairs to be compared with 173 ± 54 from the 2007 run. However, in 2007 our goal was the first observation of πK -atoms and hence a target was chosen (Pt) for which the production cross section was high. The breakup probability for πK -atoms as a function of mean life (53% for 3.7 fs) is flattening off above ~ 4 fs. Therefore we could only give a lower limit for the mean life of πK -atoms.

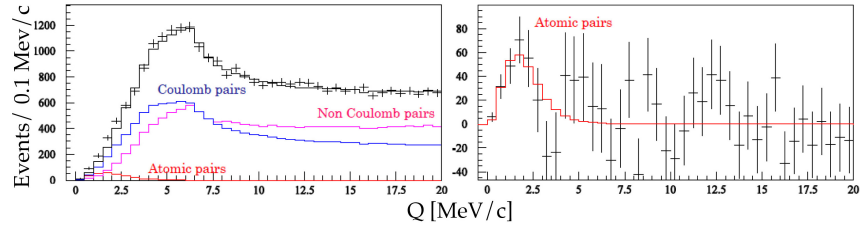


FIG. 8.6 – $\pi^- K^+ + \pi^+ K^-$ events as a function of relative momentum Q . The enhancement at low Q in the right plot is due to πK atomic pairs.

In 2008-9-10 we used a Ni-target which produces fewer atoms but for which the dependence between breakup probability and mean life is described by a steeper function, thus allowing a more accurate measurement of the mean life.

The final analysis of the 2008 – 2010 data is in progress. Due to a slow degradation of the light ($n = 1.008$) aerogel with time (probably due to humidity), we could only use the $n = 1.015$ aerogel and had therefore to restrict the maximum kaon momentum to 5.5 GeV/c, thus unfortunately reducing statistics. Also, a recalibration of the preshower detector (Psh) is required to suppress background from electron-positron pairs which is significant in the new data. Data taking for the DIRAC experiment will be completed in autumn 2012.

- [1] B. Adeva *et al.* (DIRAC Coll.), Phys. Lett. **B 674** (2009) 11.
- [2] Y. Allkofer, PhD Thesis, University of Zurich (2008).
- [3] B. Adeva *et al.* (DIRAC Coll.), Phys. Lett. **B 704** (2011) 24.
- [4] J. Schacher, CERN courier, March 2012, p. 24.
- [5] B. Adeva *et al.* (DIRAC Coll.), Nucl. Instrum. Methods in Phys. Res. **A 515** (2003) 467.
- [6] Y. Allkofer *et al.*, Nucl. Instr. Meth. in Phys. Res. **A 582** (2007) 497; Y. Allkofer *et al.*, Nucl. Instr. Meth. in Phys. Res. **A 595** (2008) 84. C. Amsler, Proc. of Science PoS EPS-HEP (2009) 078.
- [7] S. Horikawa *et al.*, Nucl. Instr. Meth. in Phys. Res. **A 595** (2008) 212.
- [8] A. Benelli, dirac.web.cern.ch/DIRAC/talk/talk1101.pdf.

9 Particle Physics at DESY/HERA (H1)

K. Müller, P. Robmann, U. Straumann, and P. Truöl

in collaboration with:

C. Grab, Institut für Teilchenphysik der ETH, Zürich; S. Egli, M. Hildebrandt, and R. Horisberger, Paul-Scherrer-Institut, Villigen, and 39 institutes outside Switzerland

(H1 - Collaboration)

Figure 9.1 taken from an article in the April 2012 issue of the CERN-Courier illustrates which domains in the (x, Q^2) plane are accessible to the LHC-, HERA- and fixed-target experiments, with Bjorken- x designating the longitudinal fraction of the incoming proton's momentum that is carried by the interacting parton (quark or gluon), and Q^2 marking the square of the four-momentum exchanged in the hard scattering process. Uncertainties in the parton-density functions (PDFs), i.e. the probability density for finding a parton with longitudinal momentum fraction x at momentum transfer Q^2 in the available kinematic regions dominate the precision of all theoretical predictions of cross sections at the LHC, extending now to next-to-next-to-leading order in QCD. The improved extraction of the PDFs from the HERA data therefore remains a central topic of the ongoing analyses of the data collected until 2007.

The two lines of approach to augment the precision of the PDFs are well documented through the preliminary data presented recently [1, 2]. On the one hand the H1-collaboration fine tunes the analysis in order to reduce the systematic errors of their HERA-II as well as their HERA-I data [3–5]. On the other hand a mixed team from both the H1- and the ZEUS-collaboration continues to combine the data in a systematic way considering correlated and uncorrelated errors, and adds successively also exclusive channels [6, 7].

An example of the former approach is an alternative method to determine the integrated luminosity by using elastic QED Compton scattering $e^+p \rightarrow e^+p\gamma$ events [5]. This process is characterized by a small momentum transfer at the proton vertex with both the electron and the photon hav-

ing significant transverse momentum and can be calculated at high precision in perturbative quantum electrodynamics (QED). The results compare favorably with the default measurements of the integrated luminosity using Bethe-Heitler events.

The second approach started in the year 2009 by combining the H1 and ZEUS measurements of the inclusive deep inelastic ep scattering (DIS) cross sections. Both neutral current (NC) and charged current (CC) unpolarized results from the HERA-I period 1994-2000 were considered [8]. The data span six orders of magnitude in Q^2 and x and correspond to twice 63 pb^{-1} . A next-to-leading order (NLO) QCD analysis was performed which determined a new set of parton distributions, HERA PDF1.0,

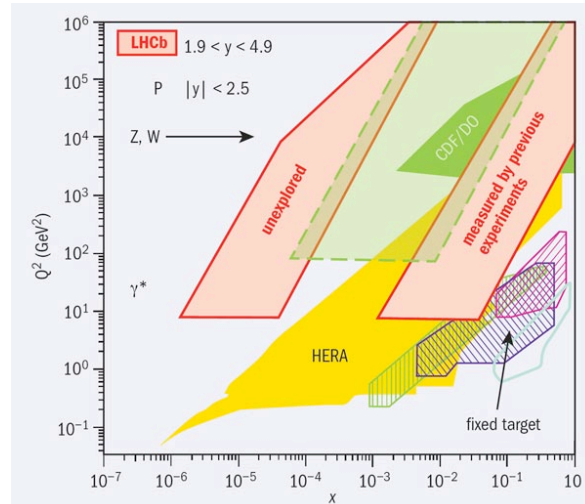


FIG. 9.1 – Domains in the (x, Q^2) -plane accessible to the three experiments Atlas, CMS and LHCb at the LHC in (p, p) collisions, to the two experiments H1 and ZEUS at HERA in (e, p) collisions and to various fixed target experiments. Source: CERN-Courier, April 2012.

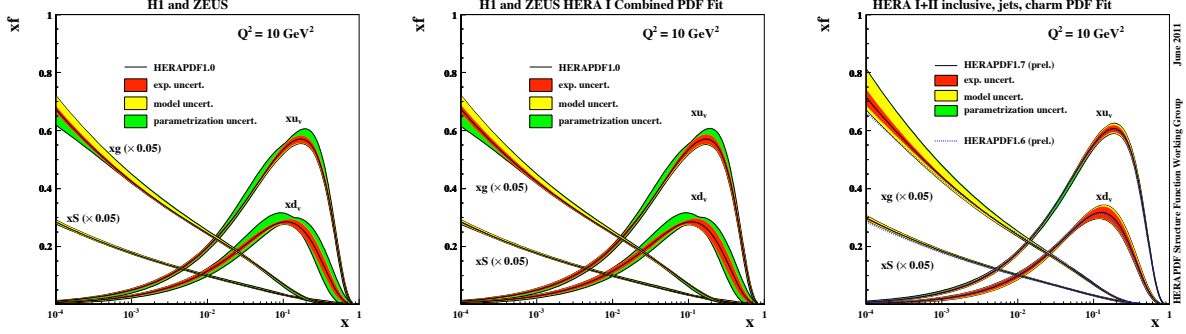


FIG. 9.2 – Evolution of the PDFs determined from the combined H1- and ZEUS-data, from HERA PDF 1.0, to HERA PDF 1.5 and HERA PDF 1.7 for $Q^2 = 10 \text{ GeV}^2$.

with small experimental uncertainties. As an example the PDFs are shown for $Q^2 = 10 \text{ GeV}^2$ in Fig. 9.2. The structure functions F_2 , F_L and F_3 which appear in the general expression for the neutral current cross section (Y_{\pm} are kinematical functions and y is the energy loss of the electron or positron)

$$\frac{d^2 \sigma_{\text{NC}}^{\pm}}{dx dQ^2} = \frac{2\alpha\pi^2}{xQ^4} (Y_+ F_2 \mp Y_- x F_3 - y^2 F_L)$$

are sensitive to the quark (antiquark) $q(\bar{q})$ and gluon g distribution functions:

$$\begin{aligned} F_2 &\propto \sum_i e_i^2 (xq_i + x\bar{q}_i) \\ xF_3 &\propto \sum_i e_i^2 (xq_i - x\bar{q}_i) \\ F_L &\propto \alpha_s \times g. \end{aligned}$$

The gluon distribution is obtained either from the scaling violation of F_2 or from F_L at NLO. Similar expressions hold for the charged current cross section yielding a flavor decomposition:

$$\begin{aligned} \frac{d^2 \sigma_{\text{CC}}^-}{dx dQ^2} &= \frac{G_F^2}{2\pi} \frac{M_W^2}{M_W^2 + Q^2} (u + c + (1 - y^2)(\bar{d} + \bar{c})) \\ \frac{d^2 \sigma_{\text{CC}}^+}{dx dQ^2} &= \frac{G_F^2}{2\pi} \frac{M_W^2}{M_W^2 + Q^2} (\bar{u} + \bar{c} + (1 - y^2)(d + c)) \end{aligned}$$

The PDF-fits use typically parametrisations such as

$$xu(x) = Ax^B(1-x)^C(1+Ex^2)$$

for the distribution of the valence up-quarks (A, B, C are different for d, g, \bar{u}, \bar{d} , $E = 0$ for all except u).

In July 2010 the preliminary HERA-II results have been included. The experiments contribute $\approx 500 \text{ pb}^{-1}$ each and were in very good agreement. An example of the resulting PDF-set HERA 1.5 is shown in Fig. 9.2 [6].

Next, jet and charm production cross sections were included in the analysis enhancing the sensitivity to the gluon PDF. The resulting present best set HERA 1.7 (see also Fig. 9.2) is based on 674 NC and CC data points, 41 data points probing the charm content in the proton, 106 inclusive-jet data points and 224 low proton energy data points. The charm quark mass was fixed at 1.5 GeV from a scan and the strong coupling constant at $\alpha_s = 0.119$ [7]. The analysis indicates a steeper rise of $g(x)$ and demonstrates the consistency of the HERA-data, even though some input data are still preliminary.

Other subjects which have been addressed in the articles published last year include:

- Extension of the structure function measurements to high inelasticity and direct assessment of the longitudinal component using also data from the runs with lower energy proton beams [9];
- Search for contact interactions, leptoquarks and lepton flavor violation [10–12];
- Heavy flavour photo- and electroproduction [13, 14];
- Various aspects of diffraction studied either inclusively or exclusively (through specific final states) [15–19].

Lastly, new results on normalized inclusive jet, di-jet and trijet differential cross sections in DIS have been presented [20]. The regularized unfolding procedure extends an earlier analysis [21]. Detector effects like acceptance and migrations as well as statistical correlations between the multi-jets and the inclusive DIS events are taken into account this way. A phase space of $150 < Q^2 < 15000 \text{ GeV}^2$ and $0.2 < y < 0.7$ was covered. The jets are reconstructed in the Breit frame of reference using the k_T jet algorithm within the laboratory pseudorapidity range $-1.0 < \eta_{\text{lab}} < 2.5$ and the Breit frame transverse momentum range $7 < P_T < 50 \text{ GeV}$ ($5 < P_T < 50 \text{ GeV}$ for di- and trijet), and the invariant mass of the two leading jets larger than 16 GeV . Compared to a previous publication on normalized multi-jet cross sections, the new analysis extends the range in pseudorapidity and reduces the hadronic energy scale uncertainty to 1%. The unfolded cross sections are compared to QCD calculations at NLO and values for the strong coupling $\alpha_s(M_Z)$ are extracted.

- [1] Europhysics Conference on High Energy Physics 2011, Grenoble, France, July 20-27, 2011;
- [2] International Workshop on Deep-Inelastic Scattering and Related Subjects (DIS 2012), Bonn, March 26-30, 2012;
- [3] *Combined Electroweak and QCD Fit of Inclusive Neutral and Charged Current Data with Polarized Lepton Beam* presentation 364 by E. Rizvi [1].
- [4] *High Q^2 Neutral and Charged Current in Polarised Collisions at HERA II* presentation 973 by S. Habib [1].
- [5] *Luminosity Measurement at HERA with Elastic QED Compton Events* presentation 109 by S. Schmitt [2].
- [6] *Combined Measurement and QCD Analysis of the Inclusive ep Scattering Cross Section at HERA (H1 and ZEUS)* presentation 993 by V. Chekelian [1].
- [7] *NLO QCD analysis of inclusive, charm and jet data from HERA (HERA PDF1.7)* presentation 35 by K. Nowak [2].
- [8] F.D. Aaron *et al.* [H1, ZEUS], JHEP **1001** (2010), 109.
- [9] F.D. Aaron *et al.* [H1], Eur. Phys. J. C **71** (2011), 1579.
- [10] F.D. Aaron *et al.* [H1], Phys. Lett. B **701** (2011), 10.
- [11] F.D. Aaron *et al.* [H1], Phys. Lett. B **705** (2011), 52.
- [12] F.D. Aaron *et al.* [H1], Phys. Lett. B **704** (2011), 388.
- [13] F.D. Aaron *et al.* [H1], Eur. Phys. J. C **71** (2011), 1769.
- [14] *Measurement of Inclusive and Dijet D^* Meson Cross Sections in Photoproduction at HERA* F.D. Aaron *et al.* [H1], DESY 11 – 248, arXiv:1203.1170 [hep-ex], Eur. Phys. J. C (2012), in print.
- [15] F.D. Aaron *et al.* [H1], Eur. Phys. J. C **71** (2011), 1771.
- [16] F.D. Aaron *et al.* [H1], Eur. Phys. J. C **71** (2011), 1836.
- [17] F.D. Aaron *et al.* [H1], Eur. Phys. J. C **72** (2012), 1910.
- [18] *Measurement of Dijet Production in Diffractive Deep-Inelastic Scattering with a Leading Proton at HERA* F.D. Aaron *et al.* [H1], DESY 11 – 166, arXiv:1111.0584 [hep-ex], Eur. Phys. J. C (2012), in print.
- [19] *Inclusive Measurement of Diffractive Deep-Inelastic Scattering at HERA* F.D. Aaron *et al.* [H1], DESY 12 – 041, arXiv:1203.4495 [hep-ex], Eur. Phys. J. C (2012), in print
- [20] *Normalised Multi-jet Cross Sections using Regularised Unfolding and Extractions of $\alpha_s(M_Z)$ in Deep-Inelastic Scattering at high Q^2 at HERA* presentation 163 by D. Britzger [2].
- [21] *Jet Production at HERA and determination of α_s* presentation 987 by A. Bagdasarian [1].

10 Particle Physics with LHCb

J. Anderson, R. Bernet, A. Bursche, A. Büchler (until November 2011), N. Chiapolini, M. De Cian, Ch. Elsasser, K. Müller, Ch. Salzmann, S. Saornil, N. Serra, St. Steiner, O. Steinkamp, U. Straumann, M. Tobin, M. Tresch, A. Vollhardt

The full LHCb collaboration consists of 54 institutes from Brazil, China, France, Germany, Ireland, Italy, the Netherlands, Poland, Romania, Russia, Spain, Switzerland, Ukraine, the United Kingdom and the United States of America.

(LHCb - Collaboration)

LHCb is the smallest of the four experiments at the Large Hadron Collider (LHC). Its main goal is the indirect search for New Physics (NP) through precision measurements of CP violating phases and rare heavy-quark decays. The measurements are complementary to direct searches also performed at LHC by CMS and ATLAS. Of particular interest are processes that are strongly suppressed in the Standard Model (SM), such as flavour-changing neutral current $b \rightarrow s$ transitions. Since CP violating asymmetries are generated by diagrams that involve internal loops with virtual particles, they can be very sensitive to NP contributions.

10.1 The LHCb detector

The LHCb detector[1] is a single-arm forward spectrometer exploiting best the forward peaked $b\bar{b}$ production cross section at the LHC. The detector covers polar angles between 15 and 300 mrad in the bending plane of the spectrometer magnet and up to 250 mrad in the non-bending plane. This acceptance corresponds to a pseudorapidity coverage in the range 1.9 to 4.5. The detector has an excellent vertex and momentum resolution needed to separate primary and secondary vertices, provides good invariant mass resolution, and is able to trigger on particles with transverse momentum, p_T , down to a few GeV only. Two RICH detectors allow discrimination between pions and kaons over a wide momentum range. The detector and its performance have been described in previous annual reports [2].

10.1.1 Detector performance and operation

LHCb was designed to operate at a centre-of-mass energy $\sqrt{s} = 14$ TeV, 2622 colliding bunches and an average instantaneous luminosity of $2 \times 10^{32} \text{cm}^{-2} \text{s}^{-1}$. Under these conditions the events are dominated by a single pp interaction per bunch crossing giving an average number of visible interactions, μ , equal to 0.4. However, the data collected in 2011 was taken at $\sqrt{s} = 7$ TeV and luminosities up to $4 \times 10^{32} \text{cm}^{-2} \text{s}^{-1}$ leading to $\mu \simeq 1.6$. These conditions were achieved using a process called *luminosity levelling*: the luminosity delivered to LHCb was kept constant throughout the length of a fill by gradually reducing the beam separation in the vertical plane around the LHCb interaction point. This automatic procedure allowed LHCb to record most of the data at a luminosity around $4 \times 10^{32} \text{cm}^{-2} \text{s}^{-1}$ which is twice the design value. A total of around 11 billion events were collected in 2011 for physics analysis.

The experiment recorded around 1.1fb^{-1} of pp collisions during the 2011 run with a global operation efficiency over 90%. The polarity of the LHCb spectrometer magnet was reversed several times to minimise possible systematic effects due to detector asymmetries. The LHC will run at a higher centre-of-mass energy, $\sqrt{s} = 8$ TeV, during 2012 and the target integrated luminosity for LHCb is 1.5fb^{-1} .

An excellent vertex resolution is required for the high level trigger and for many physics analyses. The LHCb vertex detector has an internal alignment better than $5 \mu\text{m}$ and a single hit position resolution of $4 \mu\text{m}$ has been achieved for

the innermost readout strips. High momentum and invariant mass resolutions are essential for the suppression of combinatorial backgrounds. Measured spatial resolutions in the tracking system are close to the values expected from simulation. The invariant mass resolution obtained for $J/\Psi \rightarrow \mu^+\mu^-$ decays is $12.7 \text{ MeV}/c^2$ close to the simulated $12.1 \text{ MeV}/c^2$. The particle identification performance has been studied using tag-and-probe methods on $\phi \rightarrow K^+K^-$, $K_s^0 \rightarrow \pi^+\pi^-$ and $\Lambda \rightarrow p\pi$ decays and agrees with the results from the simulation over the full momentum range.

10.1.2 Tracker Turicensis: operation and performance

N. Chiapolini, C. Salzmann, S. Saornil, M. Tobin
The Tracker Turicensis (TT) was designed and built at the Physics Institute and has been described in previous annual reports [2]. Modules that originally had a problem with broken bond wires were successfully repaired during the winter shutdown 2010. During 2011 99.8% of the 143360 detector channels were operating which is the highest reliability figure of any silicon tracking detector at the LHC. The continued stable and efficient operation of the TT and the monitoring of its performance including ageing effects are the responsibility of S. Saornil and M. Tobin. The software alignment of the detector is performed by N. Chiapolini and C. Salzmann.

10.2 Physics Results

10.2.1 CP violation in B decays

Mixing in the $B_s - \bar{B}_s$ system is described by the mass difference Δm_s , the decay width difference $\Delta\Gamma_s$, and a single CP violating phase ϕ_s . All three observables can substantially deviate from SM predictions if NP contributes. The LHCb experiment recently extracted the present most accurate values for Δm_s [3] by studying $B_s \rightarrow D_s(3)\pi$ and for the

¹⁰For all the results the first uncertainty is statistical and the second systematic.

other two parameters from $B_s \rightarrow J/\psi\phi$ [4]:

$$\begin{aligned}\Delta\Gamma_s &= 0.116 \pm 0.018 \pm 0.006 \text{ ps}^{-1} \\ \phi_s &= -0.001 \pm 0.101 \pm 0.027 \text{ rad}\end{aligned}$$

in agreement with SM predictions ($\Delta\Gamma_s^{SM} = 0.087 \pm 0.021 \text{ ps}^{-1}$ [5] and $\phi_s^{SM} = 0.036 \pm 0.02 \text{ rad}$ [6])¹⁰. The 5σ deviation of $\Delta\Gamma_s$ from 0 represents the first significant observation of its non-zero value. In addition, a long-standing sign ambiguity in $\Delta\Gamma_s$ has been resolved by separating the S-wave and P-wave contributions to the decay $B_s \rightarrow J/\psi K^+K^-$ [7].

In the B_d system the mixing phase is sizeable and can be associated with the angle β of the Unitarity Triangle, while the width difference is small. At present there is a striking discrepancy between the measured values of $\sin 2\beta$ using $B_d \rightarrow J/\psi K_S^0$ and the branching ratio $\mathcal{B}(B \rightarrow \tau\nu)$ [8, 9]. In the SM these observables can be related through the CKM matrix element V_{ub} . To understand this tension, it will be important to control the contribution of doubly Cabibbo-suppressed penguin diagrams in the $B_d \rightarrow J/\psi K_S^0$ decay. Its U-spin partner, the decay $B_s \rightarrow J/\psi K_S^0$, can be used to measure these effects. LHCb recently found $\mathcal{B}(B_s \rightarrow J/\psi K_S^0) = (3.29 \pm 0.51 \pm 0.33) \times 10^{-5}$ [10].

The photon polarisation in $b \rightarrow s\gamma$ transitions can be determined by CP asymmetry measurements. This observable probes extensions of the SM involving right-handed currents. Important milestones in this measurement are the determination of the ratio of the branching ratios [11]

$$\frac{\mathcal{B}(B_d \rightarrow K^*\gamma)}{\mathcal{B}(B_s \rightarrow \phi^*\gamma)} = 1.12 \pm 0.08_{-0.09}^{+0.11}$$

and the world's most precise measurement of direct CP asymmetry in the decay $B_d \rightarrow K^*\gamma$ [12].

A precise determination of the angle γ of the Unitarity Triangle from tree level decays is another crucial ingredient to test the CKM paradigm. The angle γ is the weak phase between the elements of the CKM matrix V_{cb} and V_{ub} and has been studied by LHCb in the decay $B^+ \rightarrow D^0 K^+$, where the D^0 meson subsequently decays

in CP-eigenstates or where the D^0 meson decays in the Cabibbo-favoured $K^-\pi^+$ and in the doubly Cabibbo-suppressed $K^+\pi^-$ states. LHCb has observed the doubly Cabibbo-suppressed decay $B^+ \rightarrow (K^-\pi^+)_D K^+$ with 10σ significance and has established the CP violation in $B^+ \rightarrow D^0 K^+$ at 5.8σ [13].

The angle γ can also be determined from the loop mediated decays $B_{d,s} \rightarrow h^+h^-$, where h stands for a kaon or a pion. A significant difference in the value of γ from tree level and loop dominated decays would be a clear sign of NP. An important milestone in the determination of γ from loop processes is the first measurement of the time-dependent CP asymmetry in the decay $B_s \rightarrow K^+K^-$, leading to the determination of the direct and mixing asymmetries [14]:

$$\begin{aligned} A_{KK}^{\text{dir}} &= 0.02 \pm 0.18 \pm 0.04, \\ A_{KK}^{\text{mix}} &= 0.17 \pm 0.18 \pm 0.05. \end{aligned}$$

10.2.2 CP violation in Charm

Mixing in the D^0 meson is induced by down-type quarks contributing to the box diagrams, which leads to a strong cancellation; therefore this mixing process is strongly suppressed. Mixing induced and direct CP asymmetries in charm decays are expected to be small, but can be highly enhanced by NP contributions. CP violation in D^0 mixing can be measured by comparing the effective lifetimes of D^0 and \bar{D}^0 decaying in CP eigenstates. The asymmetry of the lifetimes defines A_Γ . This analysis has been performed with a fraction of the data, leading to the result [15]

$$A_\Gamma = (-5.9 \pm 5.9 \pm 2.1) \times 10^{-3}.$$

For the moment no sign of CP violation in this measurement has been observed. The difference in the CP asymmetry of $D^0 \rightarrow \pi^+\pi^-$ and $D^0 \rightarrow K^+K^-$ has also been measured [16]:

$$\Delta A_{CP} = (-8.1 \pm 2.1 \pm 1.1) \times 10^{-3},$$

which is the first evidence of CP violation in the charm sector. The traditional view that CP violation in these channels does not exceed 10^{-3} in the

SM has been questioned recently [17–19] and it is not yet clear if this level of CP violation can be accommodated in the SM.

10.2.3 Rare decays

Searches for the total lepton number violating decay $B^+ \rightarrow h^-\mu^+\mu^+$, where h is a pion, a kaon or a D meson, resulted in today's world's best upper limits [20, 21].

The decays $B_{s,d} \rightarrow \mu^+\mu^-\mu^+\mu^-$ have branching ratios below 10^{-10} in the SM but could be enhanced in models involving exotic scalar particles. Searches for these decays have been performed at LHCb for the first time, leading to [22]:

$$\begin{aligned} \mathcal{B}(B_s \rightarrow \mu^+\mu^-\mu^+\mu^-) &< 1.3 \times 10^{-8} \\ \mathcal{B}(B_d \rightarrow \mu^+\mu^-\mu^+\mu^-) &< 5.4 \times 10^{-9} \end{aligned}$$

at 95% CL. The world's best limit $\mathcal{B}(D^0 \rightarrow \mu^+\mu^-) < 1.3 \times 10^{-8}$ (95% CL) has also been set [23].

The $b \rightarrow dll$ transitions are suppressed by a factor $|V_{td}/V_{ts}|$ with respect to $b \rightarrow sll$. Transitions $b \rightarrow dll$ have been observed for the first time at $\mathcal{B}(B^+ \rightarrow \pi^+\mu^+\mu^-) = (2.4 \pm 0.6 \pm 0.2) \times 10^{-8}$ in agreement with the SM prediction. This is to date the rarest B -decay ever observed.

10.2.4 The very rare decays $B_s^0 \rightarrow \mu^+\mu^-$ and $B^0 \rightarrow \mu^+\mu^-$

A. Büchler, Ch. Elsasser, N. Serra and O. Steinkamp

Our group is deeply involved in this key LHCb measurement. In the decays $B_s^0 \rightarrow \mu^+\mu^-$ and $B^0 \rightarrow \mu^+\mu^-$ NP contributions might be of the same order of magnitude as the contributions from the SM. Hence, lowering the experimental uncertainties in these branching fractions largely reduces the allowed parameter space in various NP models.

The first LHCb results, based on the 2010 data set [24], came already close to the known upper limits set by CDF [25]. In the case of $B_s^0 \rightarrow \mu^+\mu^-$ the limit was still an order of magnitude above the SM prediction $(3.2 \pm 0.2) \times 10^{-9}$ [26].

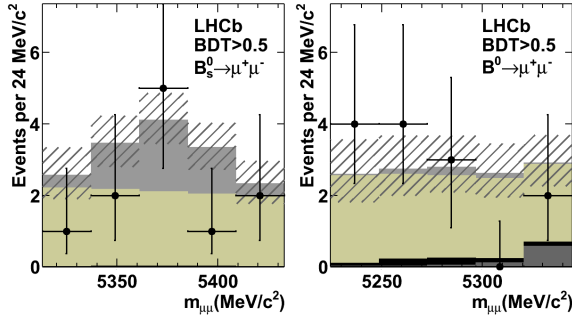


FIG. 10.1 – Distribution of selected candidates (black points) in the (left) $B_s^0 \rightarrow \mu^+\mu^-$ and (right) $B^0 \rightarrow \mu^+\mu^-$ mass window, and expectations for, from the top, $B^0 \rightarrow \mu^+\mu^-$ SM signal (gray), combinatorial background (light gray), $B^0 \rightarrow h^+h'^-$ background (black), and cross-feed of the two modes (dark gray). The hatched area depicts the uncertainty on the sum of the expected contributions.

The analysis was repeated on the full 2011 data set which corresponds to 1 fb^{-1} . Figure 10.1 shows as a result the mass distribution of the selected $B_s^0 \rightarrow \mu^+\mu^-$ and $B^0 \rightarrow \mu^+\mu^-$ candidates which gave the following limits at 95% C.L.[27] :

$$\begin{aligned} \mathcal{B}(B_s^0 \rightarrow \mu^+\mu^-) &< 4.5 \times 10^{-9} \\ \mathcal{B}(B^0 \rightarrow \mu^+\mu^-) &< 1.0 \times 10^{-9} . \end{aligned}$$

As the results are still in agreement with the SM predictions, they heavily constrain NP models [28].

The main activity of our group in this analysis is the calibration of the di-muon invariant mass which is the main variable distinguishing signal from background. The invariant mass resolution for B_s^0 and B^0 was determined by Ch. Elsasser by interpolating between the values for the resonances J/ψ , $\psi(2S)$, $\Upsilon(1S)$, $\Upsilon(2S)$ and $\Upsilon(3S)$ and by considering the resolution of the exclusive $B_{(s)}^0 \rightarrow h^+h^-$ decays where h^\pm is a kaon or a pion. These two results are in perfect agreement. An alternative method, which determines an event-by-event invariant mass error was developed by A. Büchler. It propagates the errors on the muon momenta and the opening angle between the two muons obtained from the track and vertex fit to a mass error.

Ch. Elsasser is also determining the effective masses of B_s^0 and B^0 as well as the impact of final state radiation on the invariant mass distribution. Finally, exclusive $B_{(s)}^0 \rightarrow h^+h^-$ decays are also used to estimate systematic uncertainties in a classifier based on kinematical and topological variables, which is used as an alternative discriminator between signal and background.

10.2.5 Other very rare B -decays

Ch. Elsasser, N. Serra and O. Steinkamp

Thanks to the high momentum resolution and the efficient particle identification as well as the large number of B -mesons LHCb reaches an unprecedented sensitivity to other very rare B -decays such as $B_{(s)}^0 \rightarrow \tau^+\tau^-$ and to Lepton Flavour Violating decays such as $B_{(s)}^0 \rightarrow e^\pm\mu^\mp$ and $B_{(s)}^0 \rightarrow \mu^\pm\tau^\mp$ which are practically forbidden in the SM but can be accommodated in several NP scenarios. In the Pati-Salam model [29], for example, leptoquark exchange mediates these decays already at tree level. The decay $B_{(s)}^0 \rightarrow \tau^+\tau^-$ is less helicity suppressed than $B_{(s)}^0 \rightarrow \mu^+\mu^-$ because of the higher lepton mass.

Our group will study these decay channels, profiting from the experience gained in the $B_{(s)}^0 \rightarrow \mu^+\mu^-$ analysis. In a first stage the focus lies on the study of the τ -reconstruction and -selection using Monte Carlo simulations and more frequent decays into τ 's such as $Z \rightarrow \tau^+\tau^-$.

10.2.6 $B^0 \rightarrow K^*\mu^+\mu^-$

M. De Cian, N. Serra and M. Tresch

The rare decay $B^0 \rightarrow K^*\mu^+\mu^-$ proceeds via flavour-changing neutral currents which makes it of particular interest as its angular distributions and differential branching fraction are sensitive to many potential NP contributions. The forward-backward asymmetry A_{FB} , described by the opening angle between the μ^- and the B^0 in the $\mu^+\mu^-$ rest frame, has attracted special attention. In the SM A_{FB} changes sign at a well defined value of q^2 , the di-muon invariant mass squared. This zero-crossing point is essentially free of hadronic uncer-

tainties and can therefore be very well predicted theoretically. With the full 2011 dataset, LHCb performed an angular analysis and a measurement of the differential branching fraction, which yield the worlds most precise results of all observables involved [30] in good agreement with the SM values. The experimental precision is still statistically limited and not yet sensitive to NP contributions.

Our group is responsible for the determination of the zero-crossing point of A_{FB} , which was measured for the first time [30] (see Fig. 10.2). The result was extracted using a novel "unbinned counting" technique which avoids biases introduced by the range in which the zero-crossing point is looked for or by strong assumptions on the shape of A_{FB} . This shape is in good agreement with the result from a simple counting analysis of the same data. The uncertainty on the zero-crossing point was estimated using a data-driven approach. The result is fully compatible with predictions from the SM.

To account for possible biases introduced by detector acceptance and reconstruction effects, a correction procedure was developed. Correction factors are determined using simulated events, which

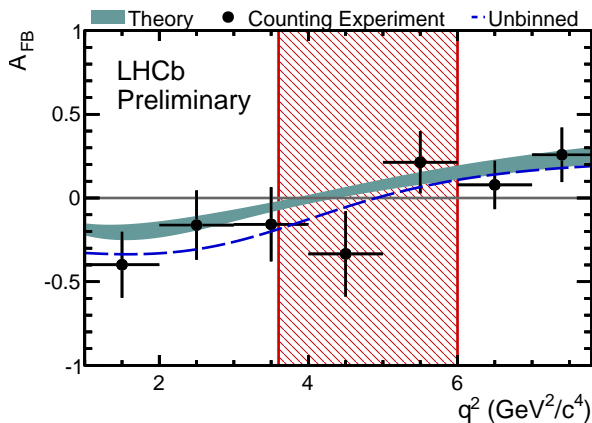


FIG. 10.2 – A_{FB} as a function of q^2 . The dashed blue line corresponds to the "unbinned counting" experiment, the turquoise band is the theoretical prediction [31]. The data points represent the result of counting forward and backward events showing the statistical uncertainty only. The red hatched region shows the observed 68% confidence interval for the zero-crossing point.

have been corrected for known discrepancies between measurement and simulation. Ch. Salzmann played an important role in evaluating the agreement between measurement and simulation in the kinematically similar decay $B^0 \rightarrow J/\Psi(\mu^+\mu^-)K^*$. This decay shares the final state with $B^0 \rightarrow K^*\mu^+\mu^-$ but is more abundant by a factor of 50. He studied several techniques to correct the simulated distributions and, together with M. De Cian, also determined efficiencies for particle identification. The measurement of tracking efficiencies using a tag-and-probe approach, which was developed independently, was needed as a further input for the efficiency studies [32].

Due to limited statistics of the 2011 dataset, not all possible observables could be accessed in the angular analysis. The remaining ones can be measured using a technique similar to the one developed for A_{FB} . Our group is investigating how to extract these quantities which are well predicted in the SM.

10.2.7 W , Z and low mass Drell-Yan production

J. Anderson, A. Bursche, N. Chiapolini, and K. Müller

Measurements of W , Z and low mass Drell-Yan production in the forward region constitute a test of QCD at LHC energies and will provide valuable input to the knowledge of the parton density functions (PDF) of the proton in a kinematic region uniquely accessible by LHCb. Measurements at LHCb are sensitive to Bjorken- x values as low as 8×10^{-6} where x is the momentum fraction carried by the struck quark. Perturbative QCD predictions are available at next-to-next-to-leading order (NNLO).

- W and Z production

W and Z production cross sections and their ratios have been measured by LHCb using the $W \rightarrow \mu\nu$ and $Z \rightarrow \mu\mu$ decay channels. Results have already been presented at conferences and are being published [33].

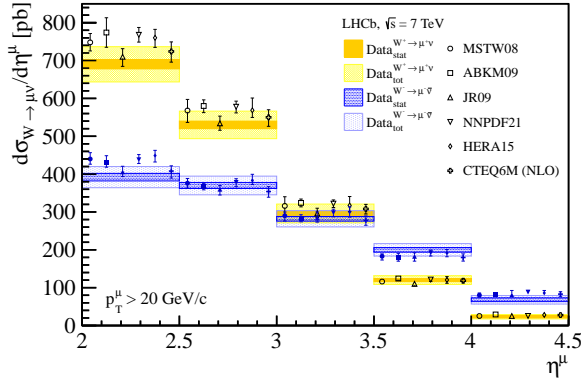


FIG. 10.3 – Pseudorapidity dependence of the $W \rightarrow \mu\nu_\mu$ production cross-section. The dark shaded bands correspond to the statistical uncertainties, the light hatched band to the statistical and systematic uncertainties added in quadrature. The superimposed NNLO (NLO) predictions are displaced horizontally for better presentation.

Our group was largely involved in these measurements by determining the detection efficiencies, estimating background contaminations, and determining theoretical predictions. While the analysis of the Z decaying into two muons is almost background free, there is significant background to the $W \rightarrow \mu\nu_\mu$ analysis since only one muon is observed. Backgrounds from semileptonic heavy flavour decays or pions or kaons misidentified through decay-in-flight or punch-through (QCD backgrounds) are reduced by requiring the muon to be isolated. Further background arises from electroweak processes. The $W \rightarrow \mu\nu_\mu$ signal yield has been determined from fits to the p_T^μ spectra of positive and negative muons.

Figure 10.3 shows the differential W^+ and W^- cross section as a function of the muon pseudorapidity. The inclusive cross-section for W^+ is larger than for W^- , explained by the excess of u over d quarks in the proton. The W cross-sections strongly vary as a function of the pseudorapidity of the charged lepton, and at high pseudorapidities the W^- is larger than the W^+ cross-section as expected from the different helicity dependences. The results are in agreement with theoretical predictions calculated at NNLO with the program DYNLO [34] with six recent parametrisations for

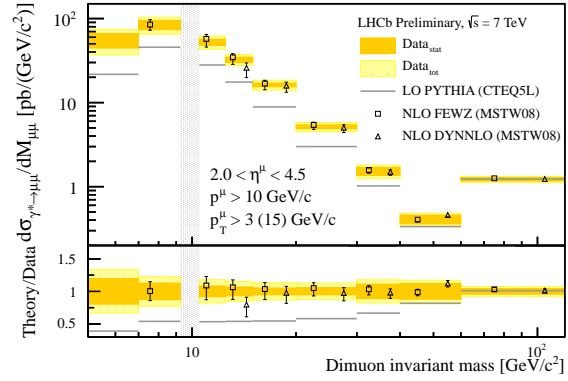


FIG. 10.4 – Differential cross-section for $\gamma^* \rightarrow \mu\mu$ as a function of $M_{\mu\mu}$. The dark shaded (orange) bands correspond to the statistical uncertainties, the light shaded (yellow) band to the statistical and systematic uncertainties added in quadrature. Superimposed are the PYTHIA predictions and two NLO predictions.

the PDFs. Most systematic uncertainties cancel in the ratio $R_W \equiv \sigma(W^+)/\sigma(W^-)$ which is measured with a precision of 1.7% which is below the theoretical uncertainty.

The analysis of electroweak boson production is being extended to events containing jets in the final state (A. Bursche). These events are sensitive to the gluon content in the proton. The dominant uncertainty originates in the jet energy scale. The study of jets is new for LHCb and A. Bursche contributed significantly to their definition and calibration.

- Low mass Drell-Yan production

Drell-Yan cross-sections are measured in the dimuon channel [35]; the analysis is performed by the Zurich group (J. Anderson, N. Chiapolini, K. Müller). While the high $M_{\mu\mu}$ region is very clean, towards low masses QCD backgrounds set in. At low masses there is an additional contribution from the radiative tail of the Υ . The signal yield is extracted from a fit to the muon isolation distribution which is defined as the fraction of the transverse momentum of the jet which contains the muon, carried by the muon. Whereas templates for the heavy flavour and misidentification backgrounds are extracted from data, the signal and the Υ background shapes are taken from simulation. The signal yield

varies between 7% in the lowest and more than 99% in the highest mass bin.

Figure 10.4 compares the measured differential cross-section as a function of the di-muon invariant mass with Monte Carlo predictions from PYTHIA and NLO calculations. The NLO predictions agree well with the measurement but PYTHIA predictions are too low. Using the full 2011 dataset will lead to a large reduction of the systematic uncertainties at low masses.

10.3 Summary and Outlook

The LHCb experiment has performed very well throughout the 2011 LHC run. About 1 fb^{-1} of data have been recorded, with a data taking efficiency exceeding 90%. Key performance parameters match or are close to expectations from simulation studies. The LHCb detector produces high quality results which is reflected in more than 30 publications and many more conference contributions to various physics topics in the past year. LHCb has already shown some world best and world first measurements of B -hadron branching ratios and considerably reduced the parameter space for many models beyond the SM.

- [1] A. A. Alves Jr. *et al.* [LHCb collaboration], JINST 3 S08005 (2008).
- [2] Physik-Institut, University of Zürich, Annual Reports 1996/7 ff.; available at <http://www.physik.uzh.ch/reports.shtml>.
- [3] R. Aaij *et al.* [LHCb collaboration], *Measurement of the $B_s^0 - \bar{B}_s^0$ oscillation frequency Δm_s in $B_s^0 \rightarrow D_s^- (3)\pi$ decays*, arXiv:1112.4311 [hep-ex].
- [4] LHCb collaboration, *First observations and branching fraction measurements of \bar{B}_s^0 to double-charm final states*, LHCb-CONF-2012-002.
- [5] A. Lenz and U. Nierste, JHEP **0706** (2007) 072.
- [6] J. Charles *et al.*, Phys. Rev. D **84** (2011) 033005.
- [7] R. Aaij *et al.* [LHCb collaboration], *Determination of the sign of the decay width difference in the B_s system*, arXiv:1202.4717 [hep-ex].
- [8] J. Charles *et al.*, Eur.Phys.J. C41, 1 (2005).
- [9] M. Ciuchini *et al.*, JHEP 07, 013 (2001).
- [10] LHCb collaboration, *Measurement of the $B_s^0 \rightarrow J/\psi K_s^0$ branching fraction*, LHCb-CONF-2011-048.
- [11] R. Aaij *et al.* [LHCb collaboration], *Measurement of the ratio of branching fractions $\mathcal{B}(B^0 \rightarrow K^{*0}\gamma)/\mathcal{B}(B_s^0 \rightarrow \phi\gamma)$* , arXiv:1202.6267 [hep-ex].
- [12] LHCb collaboration, *First observations and branching fraction measurements of \bar{B}_s^0 to double-charm final states*, LHCb-CONF-2012-004.
- [13] R. Aaij *et al.* [LHCb collaboration], *Observation of CP violation in B^+ to DK^+ decays*, arXiv:1203.3662 [hep-ex].
- [14] LHCb collaboration, *Measurement of time-dependent CP violation in charmless two-body B decays*, LHCb-CONF-2012-007.
- [15] LHCb collaboration, *Measurement of the CP Violation Parameter A_Γ in Two-Body Charm Decays*, LHCb-CONF-2011-046.
- [16] LHCb collaboration, *A search for time-integrated CP violation in $D^0 \rightarrow hh^+$ decays*, LHCb-CONF-2011-061.
- [17] I. Bigi, A. Paul and S. Recksiegel, JHEP 1106 089 (2011).
- [18] A. N. Rozanov and M.I. Vysotsky, *$(\Delta A_{CP})_{LHCb}$ and the fourth generation*, arXiv:1111.6949 [hep-ph].
- [19] H. Cheng and C. Chiang, Phys.Rev. D85 034036 (2012).
- [20] R. Aaij *et al.* [LHCb collaboration], *Searches for Majorana neutrinos in B^- decay*, arXiv:1201.5600 [hep-ex].
- [21] R. Aaij *et al.* [LHCb collaboration], Phys. Rev. Lett. 108 101601 (2012).
- [22] LHCb collaboration, *Search for the rare decays $B_s^0 \rightarrow \mu^+\mu^-\mu^+\mu^-$ and $B_d^0 \rightarrow \mu^+\mu^-\mu^+\mu^-$* ,

- LHCb-CONF-2012-010.
- [23] LHCb collaboration, *Search for the $D^0 \rightarrow \mu^+ \mu^-$ decay with 0.9 fb^{-1} at LHCb*, LHCb-CONF-2012-005.
- [24] R. Aaij *et al.* [LHCb Collaboration], *Physics Letters* **B699** (2011) 330.
- [25] CDF collaboration, *Search for $B_s^0 \rightarrow \mu^+ \mu^-$ and $B_d^0 \rightarrow \mu^+ \mu^-$ Decays in 3.7 fb^{-1} of $p\bar{p}$ Collisions with CDFII*, CDF Public Note 9892.
- [26] A. Buras, *Acta Phys. Polon.* **B41** (2010) 2487.
- [27] R. Aaij *et al.* [LHCb Collaboration], *Strong constraints on the rare decays $B_s \rightarrow \mu^+ \mu^-$ and $B^0 \rightarrow \mu^+ \mu^-$* , submitted to *Phys. Rev. Lett.*, arXiv:1203.4493 [hep-ex].
- [28] N. Mahmoudi, *Direct and indirect searches for New Physics*, Talk at 47th Rencontres de Moriond on Electroweak Interactions and Unified Theories, 10 - 17 Mar 2012, La Thuile, Italy.
- [29] J. Pati and A. Salam, *Phys. Rev.* **D10** (1974), 275.
- [30] R. Aaij *et al.*, *First observations and branching fraction measurements of \bar{B}_s^0 to double-charm final states*, LHCb-CONF-2012-008.
- [31] C. Bobeth *et al.*, *More Benefits of Semileptonic Rare B Decays at Low Recoil: CP Violation*, arXiv:1105.0376 [hep-ex].
- [32] A. Jaeger *et al.*, *Measurement of the track finding efficiency*, LHCb-PUB-2011-025.
- [33] R. Aaij *et al.* [LHCb Collaboration], *Inclusive W and Z production in the forward region at $\sqrt{s} = 7 \text{ TeV}$* , accepted by JHEP, arXiv:1204.1620 [hep-ex].
- [34] S. Catani *et al.*, *Phys. Rev. Lett.* **103** (2009) 082001.
- [35] LHCb collaboration, *Inclusive Drell-Yan production in the forward region at $\sqrt{s} = 7 \text{ TeV}$* , LHCb-CONF-2012-013.

11 Particle physics with CMS

E. Aguiló, C. Amsler, S. de Visscher, M. Ivova, B. Millán Mejías, P. Otyugova, M. Rebero[‡], P. Robmann, and A. Schmidt,

V. Chiochia, C. Favaro, H. Snoek, S. Tupputi, and M. Verzetti

in collaboration with: the CMS Collaboration

[‡] CERN summer student

In 2011 the Large Hadron Collider delivered an integrated luminosity of 5.7 fb^{-1} at 7 TeV (Fig. 11.1) while at most 1 fb^{-1} had been expected at the beginning of the run operation back in March. During this long run CMS recorded 5.2 fb^{-1} of data with its subdetectors performing at an efficiency of 98.5%. The silicon barrel pixel detector, the innermost component of the CMS experiment, was developed in and commissioned by our group (in collaboration with PSI). It allows a precise reconstruction of charged particle tracks and the identification of secondary vertices from long-lived particles. This device is crucial for our research using b -quarks. Details can be found in earlier annual reports.

More than one hundred refereed journal articles have been published by the CMS collaboration in 2011. One of us (V. C.) co-chaired the B -physics analysis group, that has so far released twelve journal articles on quarkonium, B hadron decays and b -quark production measurements. H. S. convened the pixel calibration and reconstruction group, S. d.V. coordinated the simulation in the standard model (SM) physics group. Here we report on the analysis results achieved by the Zurich group on heavy baryons, B_s decays, Higgs searches in τ -lepton pairs and $b\bar{b}$ angular correlations.

11.1 Study of Λ_b and Σ_b

The spectroscopy of b -baryons provides valuable information to test QCD models. Baryon production mechanisms and dynamics of heavy quark decay can be studied from polarization measurements in b -baryon decays. Our group is studying the Λ_b polarization in the decay $\Lambda_b \rightarrow J/\psi (\rightarrow \mu^+ \mu^-) \Lambda (\rightarrow p \pi^-)$ (Fig. 11.2). To select clean Λ_b

candidates large transverse momenta and narrow windows around the Λ and J/ψ masses are chosen, and tight vertex cuts chosen for the daughter particles. The J/ψ Λ invariant mass distribution is

41

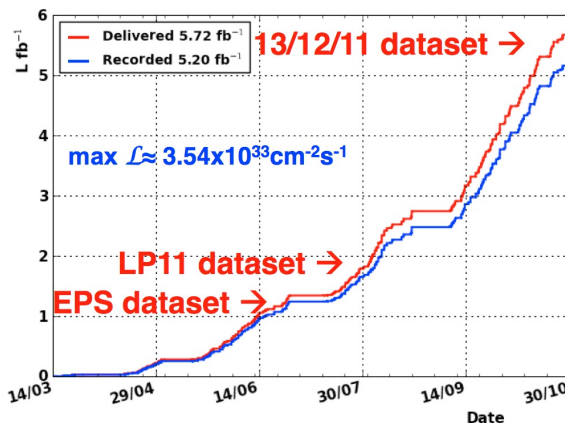


FIG. 11.1 – Integrated luminosity in the 2011 LHC run at $\sqrt{s} = 7 \text{ TeV}$.

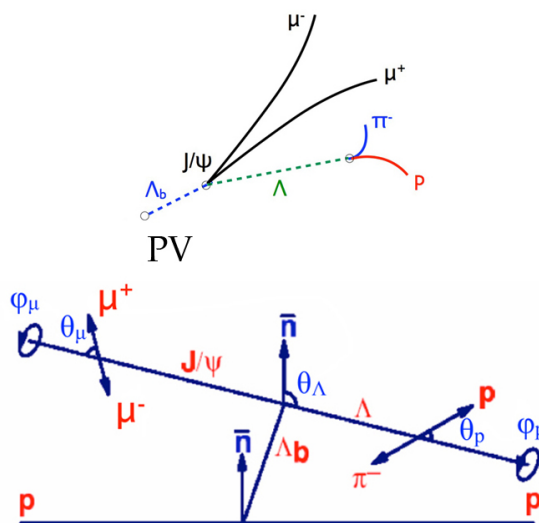


FIG. 11.2 – Decay $\Lambda_b \rightarrow J/\psi (\rightarrow \mu^+ \mu^-) \Lambda (\rightarrow p \pi^-)$ and angles used in the Λ_b polarization analysis.

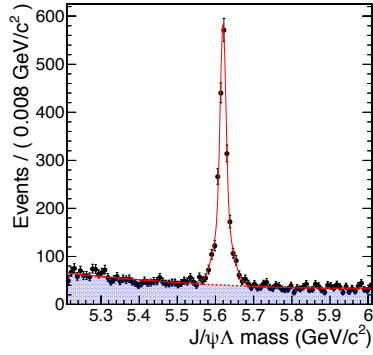


FIG. 11.3 – J/ψ Λ invariant mass distribution with Λ_b fit (red).

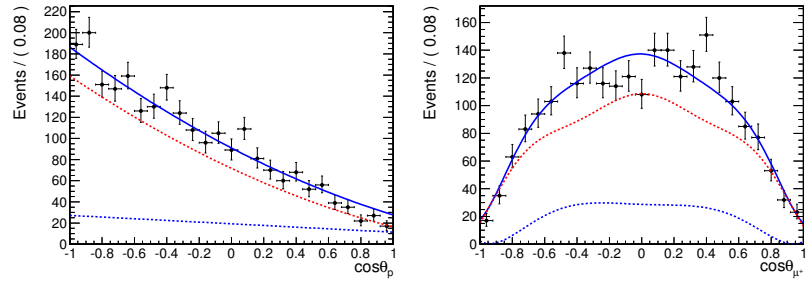


FIG. 11.4 – $\cos\theta_p$ (left) and $\cos\theta_\mu$ (right) distributions in the Λ and J/ψ rest frames with the results of a multidimensional likelihood fit (blue line). The dashed lines show the fits to the Λ_b signal (red) and the background contribution (blue).

42

shown in Fig. 11.3 from 5 fb^{-1} of integrated luminosity, leading to 1929 ± 54 Λ_b -baryons.

We use the angles θ_Λ , θ_p and θ_μ , the polar angles of the Λ , the proton and the μ^+ in the respective rest frames of Λ_b , Λ and J/ψ (Fig. 11.2). The Λ_b polarization manifests itself by a slope in the $\cos\theta_\Lambda$ distribution that can be extracted by analyzing the angular correlations between the daughter particles [1]. The distortions in the angular distributions due to acceptance and cuts are taken into account by Monte Carlo simulation. Sidebands of the Λ_b mass peak are used to estimate the contamination from background. A maximum likelihood fit is then performed. Figure 11.4 shows for instance a preliminary distribution of $\cos\theta_p$ and $\cos\theta_\mu$ together with fits. Work on this analysis is in progress [2].

The Λ_b candidates are also used to reconstruct the four states $\Sigma_b^{(*)\pm} \rightarrow \Lambda_b \pi^\pm$ where the Σ_b or Σ_b^* decays strongly at the primary vertex. Tight require-

ments are applied on the soft pion to suppress the large combinatorial background from other tracks. Figure 11.5 shows the distributions of the Q -values of the decays. The reconstructed candidates can be used to measure Σ_b cross-sections relative to those for Λ_b .

11.2 Observation of a new strange bottom baryon

The Ξ_b^- (5790), a dbs -baryon, and its Ξ_b^0 isospin partner, a ubs -baryon, have been observed at the Tevatron [3]. However, there are two other ground state pairs of baryons in the SU(4) classification, the Ξ_b' with spin 1/2 and the Ξ_b^* with spin 3/2, which can both be negatively charged (dsb) or neutral (usb). Theory (e.g. ref. [4])

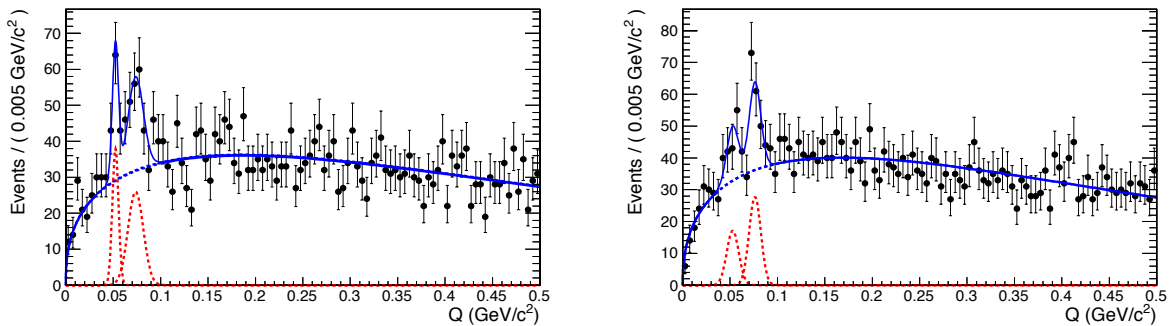


FIG. 11.5 – Q -value distributions for the $\Sigma_b^{(*)}$ decays, where $Q = M(\Lambda_b \pi) - M(\Lambda_b) - M(\pi)$. Left: Σ_b^+ and Σ_b^{*+} . Right: Σ_b^- and Σ_b^{*-} .

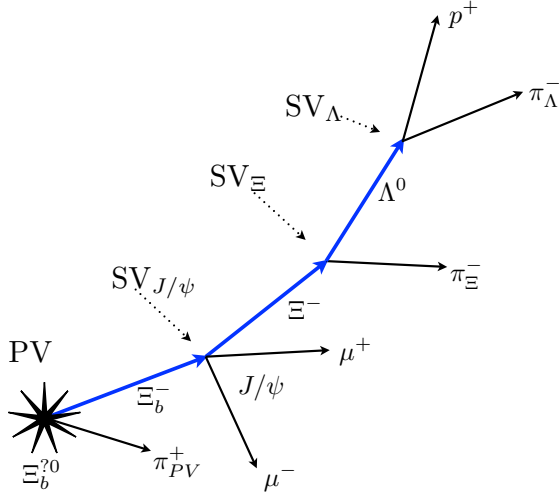


FIG. 11.6 – Decay chain of the new baryon (marked Ξ_b^{*0} at the primary vertex PV). Charge conjugation (baryons and antibaryons) is implicitly assumed.

predicts the mass difference between the Ξ_b' and the Ξ_b to be smaller than the mass of the pion, which forbids the decay $\Xi_b' \rightarrow \Xi_b \pi$. In contrast, the Ξ_b^* would be heavy enough to decay (strongly) into the Ξ_b by pion emission.

We have observed a new usb -baryon decaying into $\Xi_b^- \pi^+$ using 5.0 fb^{-1} of data. We reconstruct the decay $\Xi_b^- \rightarrow J/\psi \Xi^-$, with $J/\psi \rightarrow \mu^+ \mu^-$ and $\Xi^- \rightarrow \Lambda \pi^-$, $\Lambda \rightarrow \pi^- p$ (Fig. 11.6). The events were collected with a trigger requiring a secondary vertex (SV) displaced from the primary (PV), from which two muons emerge with transverse momenta

larger than $3 \text{ GeV}/c$ and invariant mass compatible with the J/ψ (for details on additional selection cuts see ref. [5]). The Λ (or $\bar{\Lambda}$) decays into two opposite charges. The higher momentum track is assumed to be the proton. The two tracks are required to form a vertex displaced from the beamline. The candidate Ξ^- (or $\bar{\Xi}^-$) is reconstructed by combining the Λ with an additional track. A kinematic vertex fit is performed in which the track is assumed to be a pion and the Λ mass constrained to its known value. Figure 11.7 shows the $\Lambda \pi^-$ invariant mass distribution with the Ξ^- signal. The Ξ^- s are then combined with the J/ψ with a kinematic vertex fit, constraining the Ξ^- - and J/ψ -masses to their known values. The resulting $J/\psi \Xi^-$ invariant mass distribution with the Ξ_b^- peak (108 ± 14 events) is displayed in Fig. 11.8 after all selection cuts. The measured mass is in good agreement with the known value.

We then combine the Ξ_b^- baryon with an additional track assumed to be a π and emerging from the PV with charge opposite to the π from Ξ^- (or $\bar{\Xi}^-$) decay, and search for narrow resonances in the mass difference distribution (Fig. 11.9). We observe 29 candidates (with a background of 6.6 ± 2.6) and obtain a mass of $5944.9 \pm 2.8 \text{ MeV}$. This state is thus 154 MeV heavier than the spin $1/2$ Ξ_b^- . Unfortunately the data sample is too small to determine its spin from the decay angular distributions. According to predictions this new baryon would be the Ξ_b^{*0} with spin $3/2$.

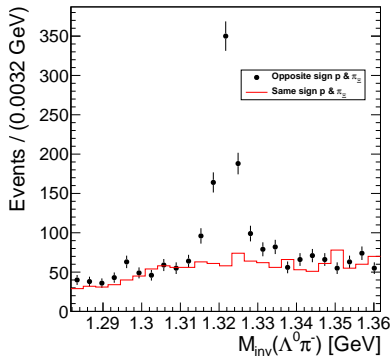


FIG. 11.7 – $\Lambda \pi^-$ invariant mass distribution showing the Ξ^- .

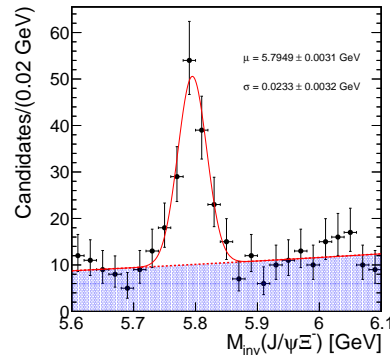


FIG. 11.8 – $J/\psi \Xi^-$ invariant mass distribution showing the Ξ_b^- signal with fit.

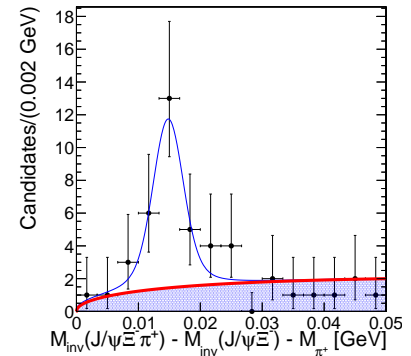


FIG. 11.9 – Q -value distribution of the reaction $\Xi_b^- \pi^+ \rightarrow J/\psi \Xi^- \pi^+$ showing the new Ξ_b^{*0} with fits.

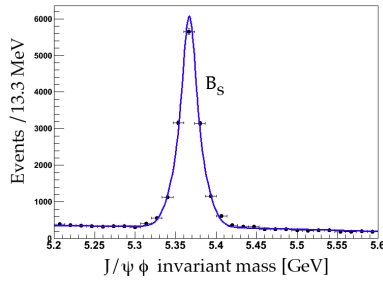


FIG. 11.10 – $J/\psi \phi$ invariant mass showing the B_s (15'000 events).

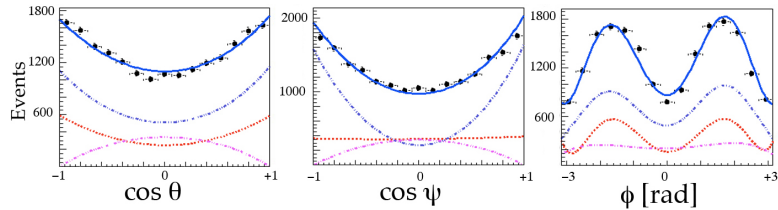


FIG. 11.11 – Measured angular distributions. The dark blue line is the fit, the dotted blue line is the CP -even component, the magenta line the CP -odd component. The red curve shows the background contribution.

44

11.3 Lifetime of the B_s -meson

We are measuring the width difference $\Delta\Gamma_s = \Gamma_L - \Gamma_H$ of the two CP -Eigenstates of the B_s -meson, B_L ($CP = +1$) and B_H ($CP = -1$) in the decay $B_s \rightarrow J/\psi (\rightarrow \mu^+\mu^-) \phi (\rightarrow K^+K^-)$. Three angles are needed to describe this decay. The angles θ and ϕ give the flight direction of the μ^+ in the J/ψ rest frame while ψ is the azimuthal angle of the K^+ with respect to the flight direction of the J/ψ . Since the B_s is pseudoscalar, while the J/ψ and ϕ are vectors, the angular momentum between the two decay products is $L = 0$, or 2 for B_L and $L = 1$ for B_H . Hence the angular distributions are different for the two states (for details see e.g. ref. [6]).

During 2011 we collected 15'000 $B_s \rightarrow J/\psi (\rightarrow \mu^+\mu^-) \phi (\rightarrow K^+K^-)$ events at $\sqrt{s} = 7$ TeV with an integrated luminosity of 4.6 fb^{-1} . Our B_s are “untagged”, which means that we do not distinguish between B_s and \bar{B}_s . The muons pairs are selected with a trigger on displaced J/ψ decay point with respect to the primary vertex. Various cuts are applied, in particular the muons and kaons are required to have transverse momenta larger than 4, respectively 0.7 GeV/c. An additional cut on the decay length reduces the prompt J/ψ background from the primary vertex. The $B_s \rightarrow J/\psi \phi$ peak is shown in Fig. 11.10.

Side band subtraction is applied to determine the contribution from background. Efficiency and acceptance corrections are calculated by Monte Carlo simulation. The results of the likelihood fit taking into account the mass, decay length and angular

distributions are shown in Fig. 11.11. The dark blue line is the fit, the dotted blue (magenta) line is the contribution from the CP even (odd) component. Fitted mass and mean life are in excellent agreement with the known values (5366 MeV and 1.43 ps). This work is still in progress [7] and we obtain a preliminary value for $\frac{\Delta\Gamma_s}{\Gamma_s}$ of 0.107 ± 0.019 , where the error is statistical only. This is compatible with the prediction from the SM: 0.147 ± 0.060 .

11.4 Searches for the Higgs boson in $\tau^+\tau^-$ decays

An important goal of the LHC physics program is to ascertain the mechanism of electroweak symmetry breaking, through which the W and Z^0 bosons obtain mass, while the photon remains massless. In the SM this is achieved via the Higgs mechanism which predicts the existence of a scalar Higgs boson. The minimal supersymmetric standard model (MSSM) contains two Higgs doublets, giving rise to five physical states: a light neutral CP -even state (h), a heavy neutral CP -even state (H), a neutral CP -odd state (A), and a pair of charged states (H^\pm).

A search for the neutral Higgs boson decaying into τ -pairs was performed using an integrated luminosity of 4.6 fb^{-1} [8]. Three independent τ -pair final states were studied with one (or both) τ -leptons decaying leptonically. The distribution of the τ -pair invariant mass for all channels combined is shown in Fig. 11.12 for the MSSM search. The spec-

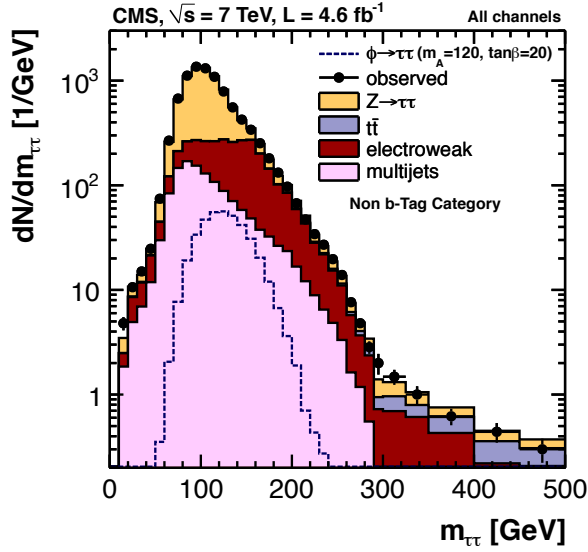


FIG. 11.12 – τ -pair invariant mass distribution in the MSSM Higgs boson search for data (full dots) and simulation (stacked histograms).

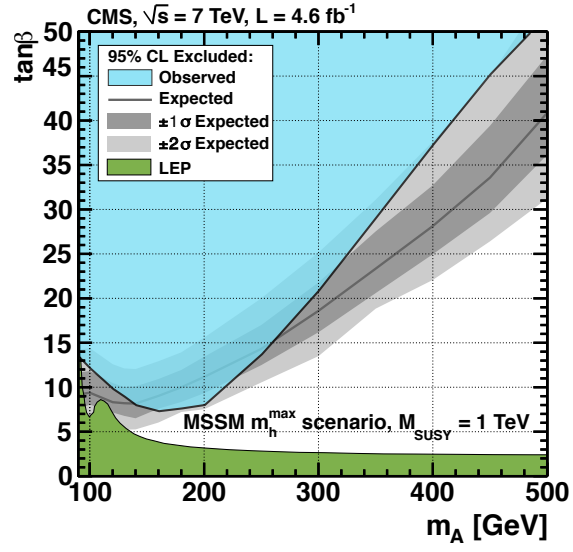


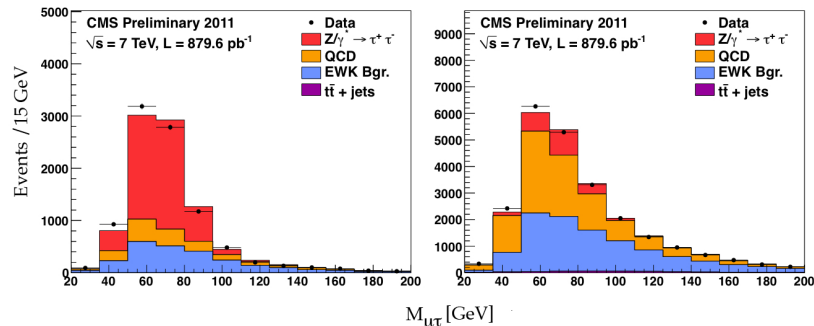
FIG. 11.13 – Region in the $\tan\beta$ vs. m_A parameter space excluded at 95% CL in the MSSM m_h^{\max} scenario.

tra show no evidence for a Higgs boson in both MSSM and SM searches. Upper bounds (95% CL) on the Higgs boson cross section times the branching fraction into τ -pairs are shown in Fig. 11.13. We exclude a Higgs boson with mass $m_H = 125$ GeV with a production cross section 4.4 times that predicted by the SM. The MSSM search excludes previously unexplored regions of the parameter space, reaching as low as $\tan\beta = 7.1$ at $m_A = 160$ GeV.

These Higgs searches rely on the precise estimate of the reconstruction efficiency for the τ hadronic decay, which was measured by our group using a *tag-and-probe* technique [9]. This method exploits the decay $Z^0 \rightarrow \tau_\mu \tau_{\text{had}}$, where τ_μ is a τ decaying into a μ while τ_{had} represents a τ decay into

charged hadrons. The events are required to have exactly one isolated μ and a jet of opposite sign. The events are divided into those surviving a tight cut and those failing the cut, and a simultaneous fit of the visible τ -pair invariant mass is performed in the signal and background regions (Fig. 11.14). The measured τ identification efficiency is typically 60% and agrees well with Monte Carlo simulation. The overall precision of the measurement is 6% (including systematic errors). With the higher instantaneous luminosity in 2012 we will further quantify the performance of hadronic τ reconstruction in an environment characterized by a larger number of simultaneous pp collisions. We are also responsible for the development of the software monitoring the performance of τ -lepton identification.

FIG. 11.14 – τ -pair invariant mass distribution with various signal and background processes for events passing the identification cut (left) and for those failing the identification cut (right).



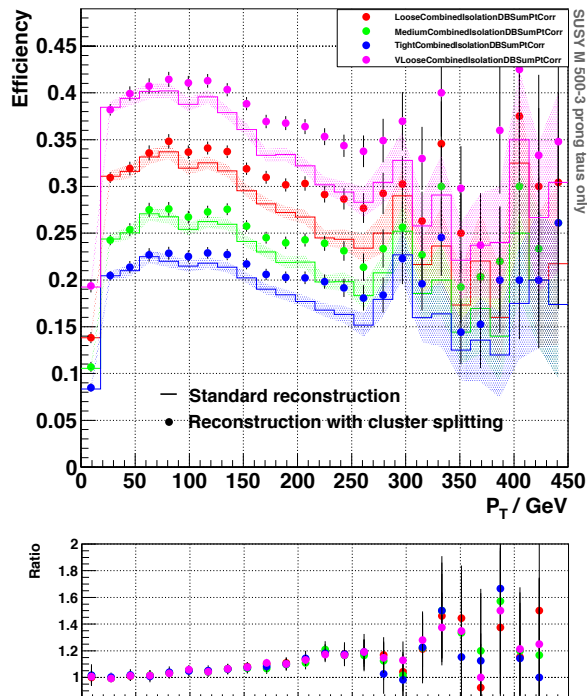


FIG. 11.15 – τ identification efficiency as a function of transverse momentum for Higgs decays. The dots show the improved hit reconstruction based on pixel hit splitting compared to the standard case (histograms). The colors represent the various τ identification procedures. The lower plot shows the relative improvement.

tum, the more collimated the three tracks, which makes them at some point inseparable. In the innermost pixel layer this effect starts to occur for opening angles between the two trajectories of about 5 mrad. For a typical 3-prong τ decay this corresponds to a transverse momentum of 150 GeV/c. The merging of clusters deteriorates the measurement of the particle trajectories and the reconstruction of the τ -lepton.

The charge measured for each cluster, together with an estimate of the track impact angle, can be used to discriminate merged clusters from isolated clusters. We have developed an algorithm for splitting merged pixel clusters, now deployed in the CMS software. The performance improvement in the τ reconstruction was verified on a simulated sample of 500 GeV MSSM Higgs bosons decaying into τ -pairs. Figure 11.15 shows the τ identification efficiency for 3-prong decays as function of τ transverse momentum. Our algorithm improves the identification efficiency by $\sim 20\%$ for $p_T(\tau) > 200$ GeV/c for the four τ identification procedures in CMS (Fig. 11.15, bottom).

11.5 Improvements to the pixel hit reconstruction

We are developing a novel hit reconstruction technique to improve the spatial disentanglement in a dense charged track environment. The implementation of this technique in the CMS software will affect all analyses that depend on the reconstruction of high energetic jets, such as b or τ jets. A fraction of 65% of the τ decay hadronically. The transverse momentum of the τ being large compared to its mass, the tracks in the jet are close to each other. Therefore, excellent spatial resolution is needed for τ reconstruction.

A significant amount of the hadronic τ decays are produced in three charged tracks accompanied by the (invisible) neutrino. The higher the τ momen-

11.6 Studies of B hadron correlations associated to Z^0 bosons

A measurement of the b -quark production associated with a Z^0/γ^* is an important test of QCD and is of great experimental relevance for various searches. The process constitutes a background to the SM Higgs production decaying to $b\bar{b}$, associated with vector bosons. In addition, in models with extended Higgs sector (such as the two-Higgs doublet models), a discovery channel would be $\phi_1 \rightarrow Z^0\phi_2$ with $\phi_2 \rightarrow b\bar{b}$, where $\phi_{1,2}$ are neutral Higgs bosons. Finally, the description of the b -quark dynamics remains difficult, in particular in the soft-collinear region, where the gluon splitting contribution to $q\bar{q}$ -pairs is not well known.

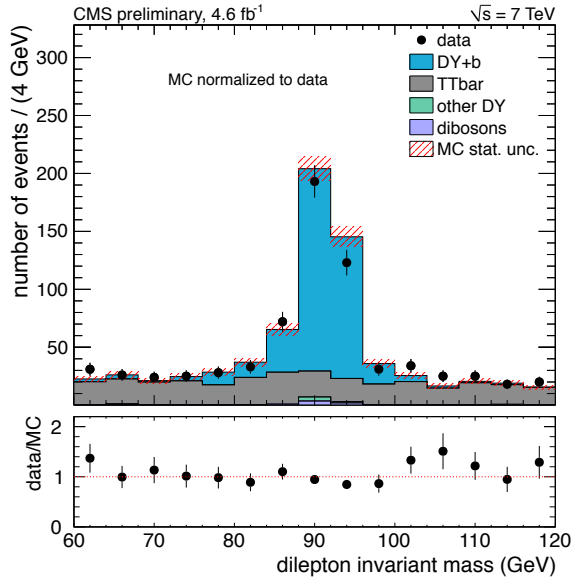


FIG. 11.16 – Dilepton invariant mass distribution.

Our group has performed a measurement of the normalized differential cross-section $pp \rightarrow Z^0/\gamma^* + b\bar{b}$ as a function of B -hadron angular separation [10] for an integrated luminosity of 4.6 fb^{-1} . Leptonic decays of the Z^0 into two leptons (e or μ) of opposite charges are selected (Fig. 11.16). The B -hadron pairs are identified by the Inclusive Vertex Finder (IVF) algorithm, based on the reconstruction of displaced secondary vertices from B decays,

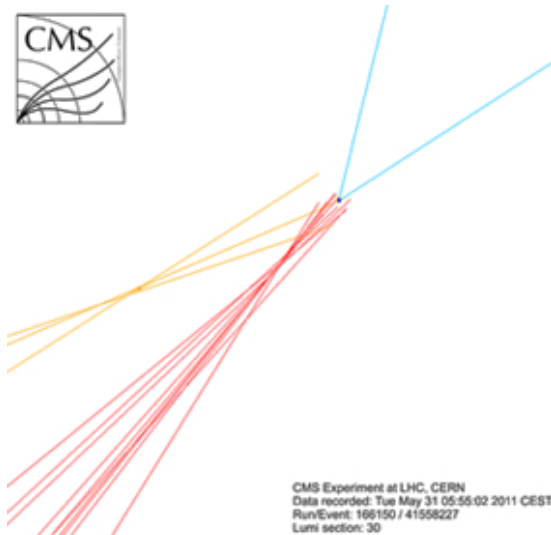


FIG. 11.17 – Event with two displaced vertices from B -hadron decays (red and yellow tracks) and two leptons from a Z^0 boson (blue tracks).

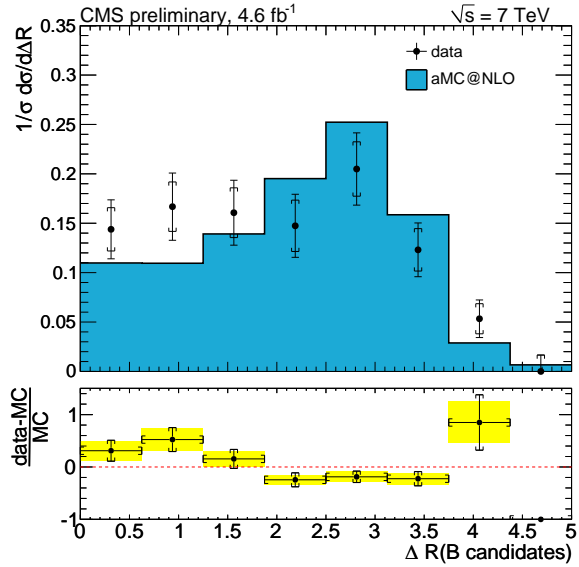


FIG. 11.18 – Normalized production cross section as a function of the angular variable $\Delta R = \sqrt{\Delta\eta^2 + \Delta\phi^2}$. The measured distribution (solid dots) is compared to aMC@NLO prediction.

independently on jets. This allows to resolve B -hadron pairs even at small opening angles (see Fig. 11.17) for which decay products merge into single jets, the standard b -jet tagging techniques then becoming useless.

The observed distribution is compared to the the NLO expectation obtained with aMC@NLO (Fig. 11.18). The data agree reasonably well with simulation within experimental errors, although data suggest a flatter angular distribution at small ΔR . Additional investigations and larger data samples in 2012 will help establishing which theoretical model provides the best description of the data [11].

We are also working on the implementation of the jet matching techniques for the MADGRAPH Monte Carlo simulation which will allow to efficiently produce exclusive samples of $pp \rightarrow Z^0/\gamma^* + b\bar{b}$ events with additional partons. We are implementing the simulation of massive b -quarks in MADGRAPH.

Our group has furthermore improved the b -jet identification in the High Level Trigger (HLT). The reconstruction of the primary vertex is crucial for the application of b -tagging algorithms. To limit CPU time the standard HLT reconstruction per-

forms only a fast 1D estimate of the primary vertex position in the direction of the beam axis, while the coordinates of the online beam spot are used as estimates for the transverse vertex position. The efficiency of the trigger can be improved with an event-by-event estimate of the 3D vertex position at the trigger level. We have assessed the performance of the 3D primary vertex reconstruction using a simulated sample of jet events and an average event pileup of 10, and have established that the algorithm can be successfully applied at trigger level.

48

- [1] M. Kramer and H. Simma, Nucl. Phys. **B 50** (1996) 125.
- [2] M. Ivova Rikova, PhD-thesis, Universität Zürich (in preparation).
- [3] V. M. Abazov *et al.*, Phys. Rev. Lett. **99** (2007) 052001; T. Aaltonen *et al.*, Phys. Rev. Lett. **99** (2007) 052002.
- [4] M. Karliner *et al.*, arXiv:0706.2163 [hep-ph] (2007).
- [5] E. Aguiló, CMS-PAS-BPH-12-001 (to be published).
- [6] L. Wilke, PhD-Thesis, University of Zurich (2009).
- [7] B. Millán Mejías, PhD-thesis, Universität Zürich (in preparation).
- [8] CMS Collaboration, submitted to Phys. Lett. B, prep. arXiv:1202.4083 [hep-ex] (2012).
- [9] M. Verzetti, PoS (EPS-HEP2011) 417 (2011).
- [10] CMS Collaboration, CMS-PAS-EWK-11-015 (to be published).
- [11] C. Favaro, PhD-thesis, Universität Zürich (in preparation).

12 Superconductivity and Magnetism

M. Bendele, S. Bosma, Z. Guguchia, L. Howald (since May 2011), H. Keller, A. Maisuradze, S. Siegrist, E. Stilp, S. Weyeneth

Visiting scientists: D. Di Castro, M. V. Eremin, B. I. Kochelaev, R. Puzniak, A. Shengelaya

Emeritus members: K. A. Müller (Honorarprofessor), T. Schneider (Titularprofessor), M. Mali, J. Roos

in collaboration with:

ETH Zürich (J. Karpinski, N. D. Zhigadlo), Paul Scherrer Institute (K. Conder, R. Khasanov, E. Morenzoni), Polish Academy of Sciences (R. Puzniak), Tbilisi State University (A. Shengelaya), MPI Stuttgart (J. Köhler, A. Bussmann-Holder), Kazan State University (M. V. Eremin, B. I. Kochelaev), EPFL Lausanne (H. Berger), IFW Dresden (P. Pahlke, B. Holzapfel), Università di Roma Tor Vergata (D. Di Castro), BAdW Garching, (A. Erb), University of Geneva (Ø. Fischer).

49

We report on research projects in the field of high-temperature superconductors (HTS's) and materials with novel electronic properties. Our studies involve various complementary techniques, such as muon-spin rotation (μ SR), electron paramagnetic resonance (EPR), nuclear magnetic resonance (NMR), nuclear quadrupole resonance (NQR), and standard magnetometry techniques. Recent investigations on various interesting iron-based superconductors as well as first results obtained for magneto-electric Cu_2OSeO_3 are presented.

12.1 Pressure Effects in Iron-Chalcogenides

With the discovery of superconductivity in $\text{LaFeAsO}_{1-x}\text{F}_y$ [1], a new family of iron-based superconductors was found. Its simplest member is FeSe_{1-x} , consisting of a stack of FeSe layers. The superconducting properties of FeSe_{1-x} [2] and $\text{Fe}_{1+y}\text{Se}_x\text{Te}_{1-x}$ [3] point to multigap superconductivity. We investigated the phase diagrams of FeSe_{1-x} as a function of hydrostatic pressure [4] and of $\text{Fe}_y\text{Se}_{1-x}\text{Te}_x$ as a function of Te substitution [5] and amount of interstitial Fe [6] by means of muon-spin rotation (μ SR), AC and DC magnetometry, and neutron diffraction. FeSe_{1-x} is known to exhibit a large pressure effect on the superconducting transition temperature T_c . In addition, the pressure dependence $T_c(p)$ is non-uniform [4].

Unexpectedly, besides superconductivity coexisting magnetic order appears with pressure p , which is characterized by a magnetic transition temperature T_N much higher than T_c . As seen in Fig. 12.1

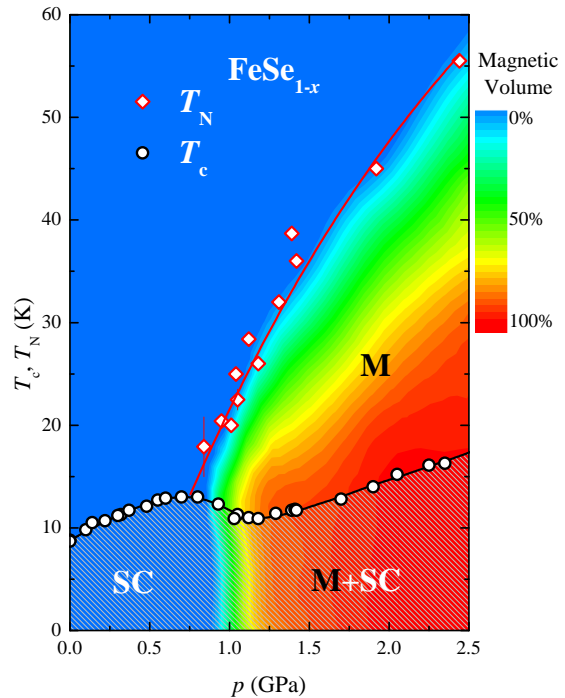


FIG. 12.1 – Pressure dependence of T_c , T_N , and the superconducting and magnetic volume fractions in FeSe_{1-x} . The lines are guides to the eyes. SC and M denote the superconducting and magnetic states of the samples [7].

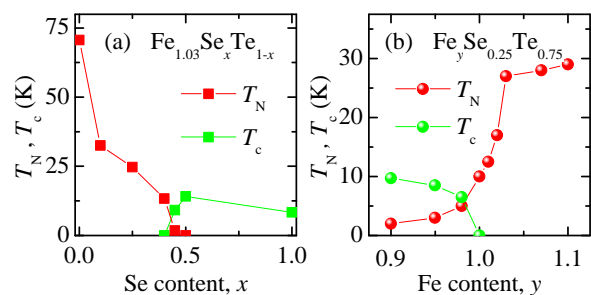


FIG. 12.2 – Phase diagram of $\text{Fe}_y\text{Se}_x\text{Te}_{1-x}$ as a function of x (a) and y (b).

50

magnetism and superconductivity are found to coexist microscopically for $T < T_c$ [4, 7]. Interestingly, substitution of Se by isovalent Te in the system $\text{Fe}_y\text{Se}_x\text{Te}_{1-x}$ has a similar effect. First, $T_c(x)$ increases, then superconductivity and magnetism coexist, and finally the material remains magnetic [5]. Recently, it turned out, that the superconducting and magnetic properties of $\text{Fe}_y\text{Se}_x\text{Te}_{1-x}$ not only depend on the Se-Te ratio x , but also strongly on the Fe content y [6, 8]. Upon fixing $x = 0.25$ and varying y one is able to tune the system from a coexistence region of magnetism and superconductivity to a state where the system is magnetic only (apart from traces of superconductivity, see Figs. 12.2 and 12.3). It was shown by us, that the

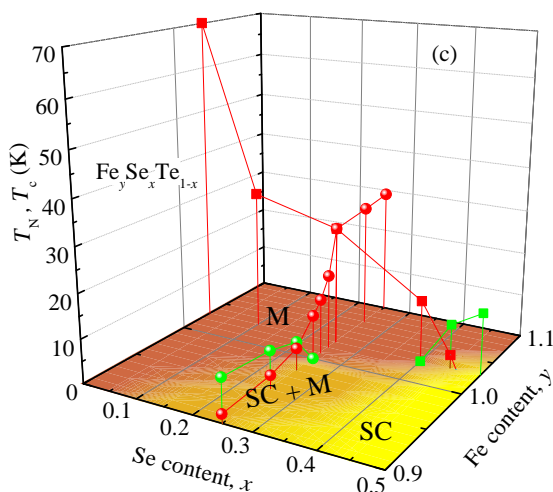


FIG. 12.3 – Combination of panels (a) and (b) of Fig. 12.2 in a tentative three dimensional phase diagram. M and SC denote the magnetic and superconducting phases, respectively [6].

magnetic correlation length decreases with decreasing amount of Fe. This rises the question whether Fe acts as an isolated moment that destroys superconductivity, or is an electron donor that suppresses superconductivity and induces weakly localized electronic states [6].

- [1] Y. Kamihara *et al.*, J. Am. Chem. Soc. **130**, 3296 (2008).
- [2] R. Khasanov *et al.*, Phys. Rev. Lett. **104**, 087004 (2010).
- [3] M. Bendele *et al.*, Phys. Rev. B **81**, 224520 (2010).
- [4] M. Bendele *et al.*, Phys. Rev. Lett. **104**, 087003 (2010).
- [5] R. Khasanov *et al.*, Phys. Rev. B **80**, 140511(R) (2009).
- [6] M. Bendele *et al.*, Phys. Rev. B **82**, 212504 (2010).
- [7] M. Bendele *et al.*, Phys. Rev. B **85**, 064517 (2012).
- [8] R. Viennois *et al.*, J. Sol. St. Chem. **183**, 769 (2010).

12.2 Magnetic torque study of single-crystal $\text{Rb}_x\text{Fe}_{2-y}\text{Se}_2$

A high $T_c \simeq 30$ K is also observed in the related iron-selenide family $A_x\text{Fe}_{2-y}\text{Se}_2$ by intercalating alkali atoms between the FeSe layers [1]. Many reports [2, 3] indicate a coexistence of antiferromagnetism and superconductivity, with the antiferromagnetic domains corresponding to iron vacancy ordering. However, still no consensus for the values of the magnetic penetration depth λ and the magnetic penetration depth anisotropy γ_λ is found in literature.

We performed magnetic torque investigations on a single crystal of $\text{Rb}_x\text{Fe}_{2-y}\text{Se}_2$ for various

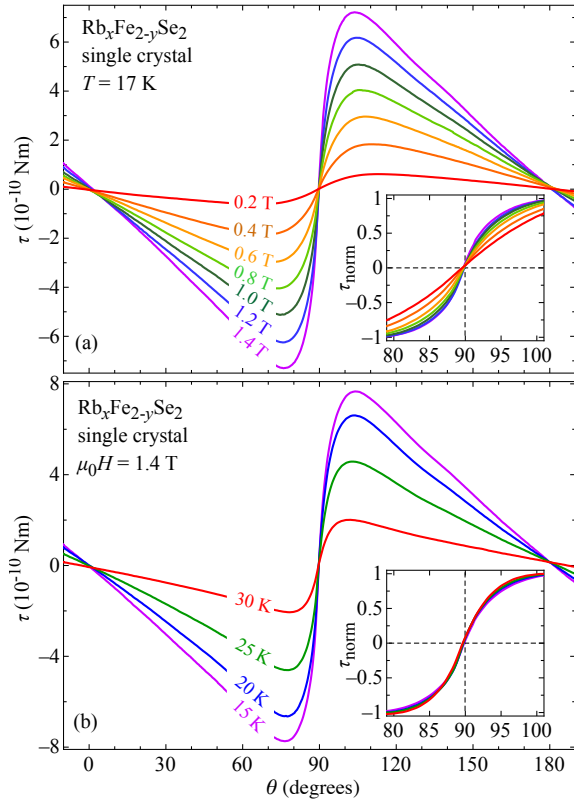


FIG. 12.4 – Angular dependence of the superconducting component of the magnetic torque of $Rb_xFe_{2-y}Se_2$. (a) Magnetic torque at 17 K for various magnetic fields. (b) Magnetic torque at 1.4 T for various temperatures. The insets in both panels show the evolution of $\tau_{\text{norm}} = \tau/\tau_{\text{max}}$ close to the ab -plane [4].

temperatures T and magnetic fields H applied with an angle θ with respect to the crystallographic c -axis of tetragonal $Rb_xFe_{2-y}Se_2$. A change of the slope of torque near the ab -plane ($\theta \sim 90^\circ$) qualitatively reflects a change of γ_λ . Such a change of slope is evident from the torque data shown in Fig. 12.4, indicating that γ_λ depends on field, but not on temperature.

A detailed analysis of these data yields estimates for $\gamma_\lambda(T, H)$ and the effective magnetic penetration depth $\lambda_{\text{eff}}(T, H)$. A summary of these results is shown in Fig. 12.5. The extrapolated value of $\lambda_{\text{eff}}(0) \simeq 1.8 \mu\text{m}$ is surprisingly large compared to other iron-based superconductors. However, measurements on the isotropic lower critical field H_{c1}

are in good agreement with a rather large magnetic penetration depth in $Rb_xFe_{2-y}Se_2$. Intriguingly, microscopic techniques yield typical values of $\lambda \simeq 300 \text{ nm}$ [5]. It is possible that due to phase separation [3] in these materials, macroscopic techniques probing the effective magnetic penetration depth λ_{eff} yield substantially different values for λ than microscopic techniques.

A field dependent γ_λ may be associated with a complex band structure, since in the case of multiple superconducting gaps originating from different bands the superconducting screening currents, related to λ_{ab} and λ_c , may give rise to an unusual behavior of γ_λ . However, if a 2D-3D band scenario were the origin of the field dependence of γ_λ of $RbFe_{2-y}Se_2$, it should be temperature dependent as well [6] which is not the case according to Fig. 12.5d.

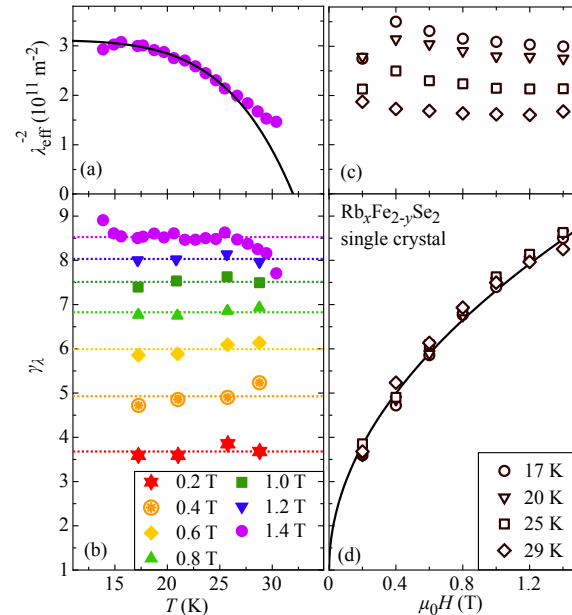


FIG. 12.5 – Summary of all the results obtained from the torque data of $RbFe_{2-y}Se_2$. (a) Temperature dependence of $\lambda_{\text{eff}}^{-2}$. The line is a power law fit to the data at 1.4 T. (b) Temperature dependence of γ_λ for various fields, showing that γ_λ is strongly increasing with H , but is almost independent of T . The dotted lines represent the average γ_λ for each field. (c) Field dependence of $\lambda_{\text{eff}}^{-2}$ for various temperatures. (d) Field dependence of γ_λ for various T . The black line is a guide to the eye [4].

A superconductor coexisting with an antiferromagnetic phase is expected to behave in a peculiar way. Varying the magnetic field can change the domain structure and the coupling between superconducting areas. This could result in variations of the averaged effective anisotropy. As was shown for various iron-based superconductors, the lattice parameters, in particular the pnictogen height in the iron-pnictides, are directly related to superconductivity [7]. Importantly, such scaling also works for the iron-selenide layer [7, 8]. It is possible that magnetostrictive effects, which are expected to increase with magnetic field, may influence the lattice parameters and consequently the anisotropy of the system.

- [1] J. Guo *et al.*,
Phys. Rev. B **82**, 180520 (2010).
- [2] V. Ksenofontov *et al.*,
Phys. Rev. B **84**, 180508 (2011).
- [3] A. Ricci *et al.*,
Phys. Rev. B **84**, 060511 (2011).
- [4] S. Bosma *et al.*,
Phys. Rev. B **85**, 064509 (2012).
- [5] Z. Shermadini *et al.*,
Phys. Rev. B **85**, 100501 (2012).
- [6] M. Angst *et al.*,
Phys. Rev. Lett. **88**, 167004 (2002).
- [7] Y. Mizuguchi *et al.*,
Supercond. Sci. Tech. **23**, 054013 (2010).
- [8] A. Krzton-Maziopa *et al.*,
J. Phys.: Condens. Matter **23**, 052203 (2011).

12.3 Anisotropic magnetic order in $\text{EuFe}_{2-x}\text{Co}_x\text{As}_2$ single crystals

Among the iron-based pnictide HTS's, the family $\text{EuFe}_{2-x}\text{Co}_x\text{As}_2$ is particularly interesting since Eu^{2+} is a rare-earth ion with a $4f^7$ electronic configuration and a total electron spin of $7/2$. This compound is built up by Fe_2As_2 layers, separated

by layers of magnetic Eu^{2+} ions [1]. EuFe_2As_2 exhibits both a spin density wave (SDW) ordering of the Fe moments and an antiferromagnetic ordering of the localized Eu^{2+} moments below 190 K and 19 K, respectively [1, 2]. In contrast to related systems, where the substitution of Fe by Co leads to superconductivity [3], the compounds containing Eu^{2+} exhibit the onset of a superconducting transition, but seem to be hindered to reach zero resistivity at ambient pressure due to the AFM ordering of the Eu^{2+} spins [4, 5]. It is well established that the SDW state of the Fe moments is suppressed as a result of Co doping. However, at present there is no clear picture how the ordering of the Eu spins develops with increasing Co concentration. Thus, it is important to compare the magnetic properties of the Eu sublattice in $\text{EuFe}_{2-x}\text{Co}_x\text{As}_2$ without and with Co doping in order to study the correlation between the ordering of the Eu^{2+} moments and the magnetism of the Fe sublattice. This is crucial to understand the interplay between magnetism of localized moments and superconductivity in $\text{EuFe}_{2-x}\text{Co}_x\text{As}_2$.

A combination of magnetic susceptibility, magnetization, and magnetic torque experiments were performed on single crystals of $\text{EuFe}_{2-x}\text{Co}_x\text{As}_2$ ($x = 0, 0.2$) [6]. The goal of this study is to investigate the macroscopic magnetic properties of the Eu sublattice. Magnetic susceptibility and magnetization investigations provide information on the magnetic structure of a single-crystal sample in magnetic fields applied along the principal axes. In addition, the evolution of the magnetic structure as a function of the tilting angle of the magnetic field and a crystallographic axis can be studied by magnetic torque. The results are summarized in Fig. 12.6 and 12.7. They are discussed in terms of the phase diagram of the Eu^{2+} magnetic sublattice of EuFe_2As_2 and $\text{EuFe}_{1.8}\text{Co}_{0.2}\text{As}_2$ for $H \perp c$ and $H \parallel c$. For the parent compound EuFe_2As_2 four different magnetic phases were identified (see Fig. 12.6a and b): a paramagnetic (PM), an antiferromagnetic (AFM), a canted antiferromagnetic (C-AFM), and a ferromagnetic (FM) phase. The present experiments suggest a C-AFM order of the Eu^{2+} spins in EuFe_2As_2 in the temperature range

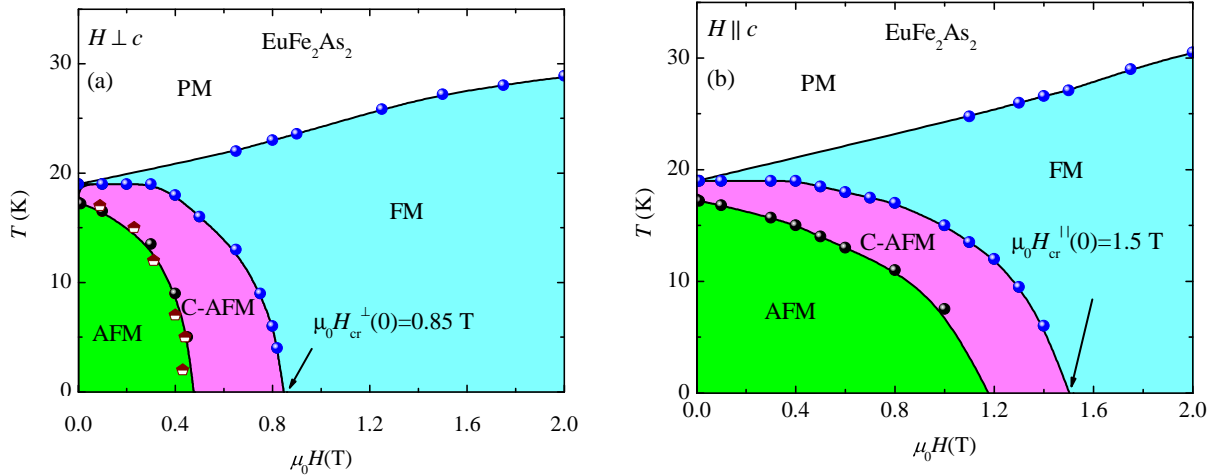


FIG. 12.6 – Magnetic phase diagrams of single-crystal EuFe_2As_2 for $H \perp c$ and for $H \parallel c$. The various phases in the diagrams are denoted as: paramagnetic (PM), antiferromagnetic (AFM), canted antiferromagnetic (C-AFM), ferromagnetic (FM). The spheres and red&white symbols are from the susceptibility and field dependent magnetization measurements, respectively. Solid lines are guides to the eye [6].

between 17 K and 19 K, while below 17 K an AFM structure is proposed. We also propose that at low temperatures the system can be well described by a uniaxial model with an easy plane and A-type AFM order. By applying a magnetic field within the AFM phase, a transition from AFM order via a canted configuration to a FM structure is observed. The corresponding magnetic phase diagrams for Co doped $\text{EuFe}_{1.8}\text{Co}_{0.2}\text{As}_2$ are shown in Fig. 12.7a and b. The magnetic ordering temperature of $\simeq 17$ K is only about 2 K lower as compared to the parent compound. However, in the Co doped $\text{EuFe}_{1.8}\text{Co}_{0.2}\text{As}_2$, no signatures of a low-field and low-temperature AFM state of the Eu^{2+} moments was found. Only a C-AFM phase (with a FM component in the ab -plane) is present at low fields and low temperatures. The ordering temperature $T_{\text{C-AFM}}$ decreases with increasing magnetic field, similar to the parent compound (see Fig. 12.7a and b). The critical magnetic field H_{cr} at which the Eu magnetic ordering is saturated was determined for different temperatures, and the extrapolated zero-temperature values were found to be strongly reduced with Co doping.

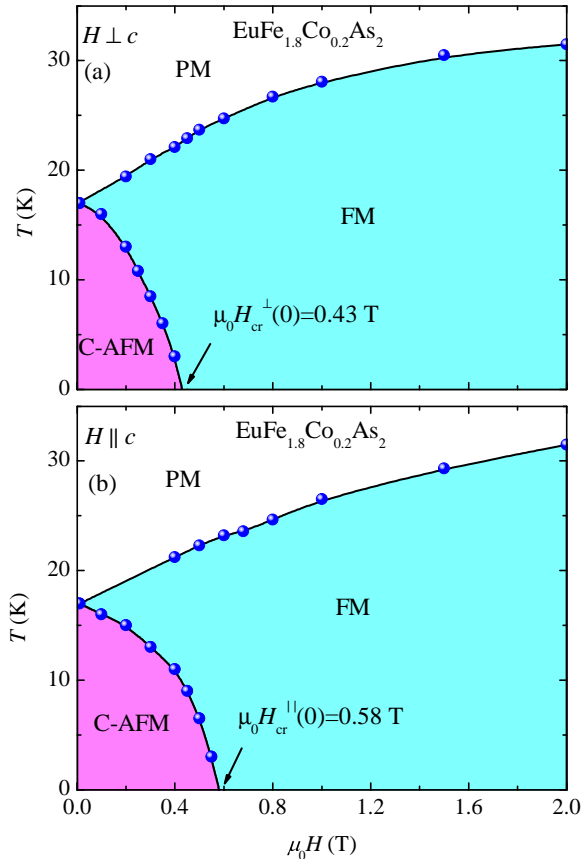


FIG. 12.7 – Magnetic phase diagrams of single-crystal $\text{EuFe}_{1.8}\text{Co}_{0.2}\text{As}_2$ for $H \perp c$ and for $H \parallel c$. The meaning of the symbol is as in Fig. 12.6 [6].

The present investigations reveal that the magnetic configuration of the Eu moments is strongly influenced by the magnetic moments of the Fe sublattice, where superconductivity takes place for a certain range of Co doping. This gives rise to a complex and sophisticated interplay of magnetic phases in $\text{EuFe}_{2-x}\text{Co}_x\text{As}_2$. A detailed knowledge of the interplay between the Eu^{2+} moments and magnetism of the Fe sublattice is important to understand the role of magnetism of the localized Eu^{2+} moments for the occurrence of superconductivity in $\text{EuFe}_{2-x}\text{Co}_x\text{As}_2$.

- [1] H. Raffius *et al.*,
J. Phys. Chem. Solids **54**, 135 (1993).
- [2] Y. Xiao *et al.*,
Phys. Rev. B **80**, 174424 (2009).
- [3] A. S. Sefat *et al.*,
Phys. Rev. Lett. **101**, 117004 (2008).
- [4] Y. He *et al.*,
J. Phys.: Condens. Matter **22**, 235701 (2010).
- [5] Z. Guguchia *et al.*,
Phys. Rev. B **83**, 144516 (2011).
- [6] Z. Guguchia *et al.*,
Phys. Rev. B **84**, 144506 (2011).

12.4 μSR study of the magnetoelectric coupling in Cu_2OSeO_3

Multiferroic and magnetoelectric materials are in the focus of research activities in recent years [1, 2]. The coupling between magnetic and electric parameters increases the degrees of freedom of the ordered ground state, making these materials good candidates for the study of new phenomena in highly correlated electronic systems. Strong magnetoelectric coupling is rather rare in solid state physics, since usual microscopic mechanisms for magnetic and electric polarization are mutually exclusive. Magnetism requires strong exchange interactions related to a strong hybridization of the transition ion electrons leading to conductivity.

Conductivity, on the other hand, is inconsistent with the presence of an electric polarization in a sample [2]. The presence of large magnetic and electric polarizations is an important condition for strong magnetoelectric coupling, making ferro- or ferrimagnetic materials favorable candidates [1].

The ferrimagnetic magnetoelectric compound Cu_2OSeO_3 was recently discovered [3], and single crystals were successfully grown soon after [4]. The compound is piezoelectric and undergoes a ferrimagnetic transition below 60 K, exhibiting magnetoelectric coupling as revealed by magneto-capacitance studies on a polycrystalline sample [3]. An abrupt change of the dielectric constant below the ferrimagnetic transition was later confirmed by infrared studies [5, 6].

In this study we investigated the magnetic properties and the magnetoelectric coupling in Cu_2OSeO_3 by means of zero field and transverse field μSR in combination with alternating electric fields. A careful analysis of the electrostatic and magnetic field distributions in the lattice unit cell allowed us to identify possible muon stopping sites and corresponding local magnetic fields probed by the muon [7]. The obtained μSR spectra were found to be consistent with the ferrimagnetic structure below $T_C = 57.0(1)$ K [3]. In the low temperature limit an internal magnetic field $B_{\text{int}}(0) = 85.37(25)$ mT was detected at the interstitial muon stopping site. The temperature dependence of the internal magnetic is well described by the relation $B_{\text{int}} = B(0)(1 - (T/T_C)^2)^\beta$ with an effective exponent $\tilde{\beta} \simeq 0.39(1)$ which is close to the critical exponent $\beta \simeq 1/3$ for a three dimensional (3D) magnetic system (see Fig. 12.8). Just above T_C the muon relaxation rate follows the power law $\lambda(T) \propto (T/T_C - 1)^{-\tilde{\omega}}$ with $\tilde{\omega} = 1.06(9)$, which is characteristic for 3D ferromagnets. Measurements of $B_{\text{int}}(T)$ with and without an applied electrostatic field $E = 1.66 \times 10^5$ V/m suggest a electric field effect of magnitude $\Delta B_V = B_V(0 \text{ V}) - B_V(500 \text{ V}) = -0.4(4)$ mT [7].

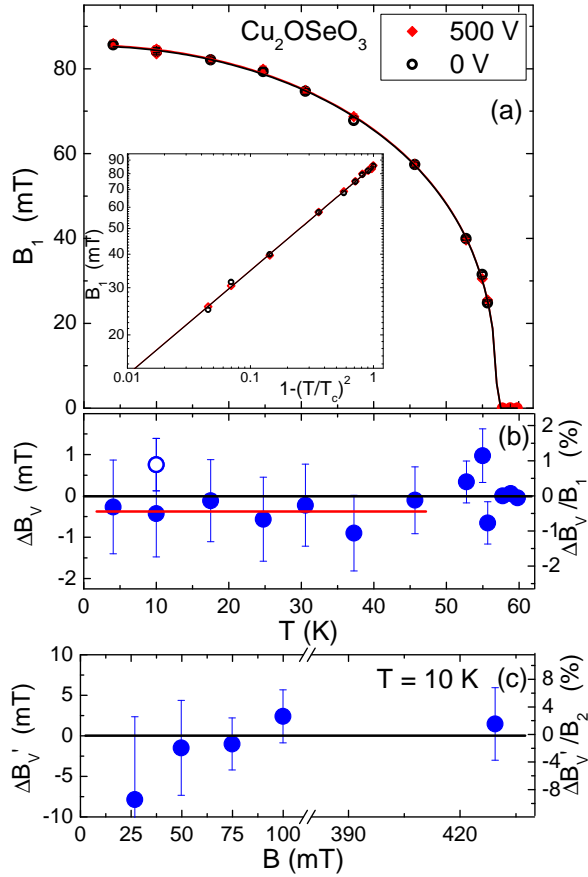


FIG. 12.8 – (a) Temperature dependence of the mean internal B_1 field in single crystal Cu_2OSeO_3 for zero and applied electrostatic field E . The solid lines are power law fits to the data. The insert shows B_1 vs $(1 - (T/T_C)^2)$ on a log-log scale. (b) Electric field shift $\Delta B_V = B_1(0 \text{ V}) - B_1(500 \text{ V})$ as a function of temperature. The solid red line corresponds to the mean value of $\overline{\Delta B_V} \simeq -0.4(4)$ mT below 50 K. (c) Electric field shift $\Delta B'_V = \hat{B}_2(0 \text{ V}) - \hat{B}_2(800 \text{ V})$ as a function of magnetic field measured by transverse field μSR at 10 K [7].

- [1] M. Fiebig, J. Phys. D: Appl. Phys. **38**, R123 (2005).
- [2] N. A. Hill, J. Phys. Chem. B **104**, 6694 (2000).
- [3] J.-W. G. Bos *et al.*, Phys. Rev. B **78**, 094416 (2008).
- [4] M. Belesi *et al.*, Phys. Rev. B **82**, 094422 (2010).
- [5] K. H. Miller *et al.*, Phys. Rev. B **82**, 144107 (2010).
- [6] V. Gnezdilov *et al.*, Fiz. Nizk. Temp. **36**, 688 (2010).
- [7] A. Maisuradze *et al.*, Phys. Rev. B **84**, 064433 (2011).

13 Phase transitions and superconducting photon detectors

A. Aeschbacher, F. von Rohr, H. Grundmann, O. Bossen, K. Inderbitzin, S. Siegrist, A. Engel and A. Schilling

in collaboration with: University of Bern (K. Krämer), EPF Lausanne (L. Forró), Tohoku University (N. Toyota), McMaster University (H. Dabkowska), Karlsruhe Institut für Technologie (K. Il'in), ETH Zürich (A. Imamoglu), Deutsches Zentrum für Luft- und Raumfahrt (H.-W. Hübers, A. Semenov), FIRST Lab ETH Zürich, ESRF Grenoble (C. Mazzoli), PSI Villigen (M. Medarde).

56

13.1 Superconducting nanowire single-photon detectors for optical and X-ray photons

In this report period we could demonstrate that it is possible to make fast single-photon detectors from TaN, which show improved detection efficiencies in the infrared spectral range compared to traditional detectors made from NbN. Moreover, in experiments with X-rays ($\approx 6\text{--}50\text{ keV}$) we successfully transferred the detection principle into the keV region while preserving the fast recovery times.

13.1.1 TaN superconducting nanowire single-photon detectors

In the previous annual report we already reported preliminary results of superconducting nanowire single-photon detectors (SNSPD) sensitive in the optical and near-infrared range made from TaN thin films [1] instead of the common NbN material. These efforts were motivated by the expectation that materials with a lower critical temperature T_c compared to NbN should detect low-energy photons in the infrared with a higher detection efficiency. An extensive and detailed comparison with a similar sized NbN-SNSPD confirmed our expectations [2]. At high bias currents the detection efficiency as a function of the photon wavelength λ shows a well defined plateau extending well into the infrared range followed by the typical roll-off beyond the cut-off wavelength (Fig. 13.1). The improvement compared to a similarly sized NbN SNSPD becomes obvious when the relative detection efficiency $DE_{\text{TaN}}/DE_{\text{NbN}}$ for equal reduced bias current I_b/I_c is plotted versus λ as shown in

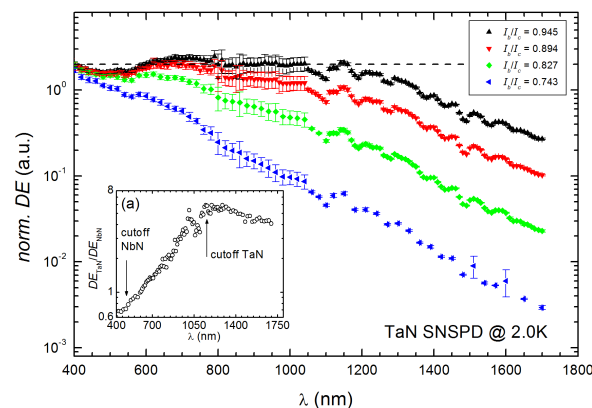


FIG. 13.1 – Detection efficiency of the TaN SNSPD as a function of photon wavelength for different bias currents. In the inset we plotted the relative detection efficiencies for a TaN and NbN detector. The 5 to 6-fold increase of the detection efficiency in the infra-red is clearly visible.

the inset of Fig. 13.1. For $\lambda > 1100\text{ nm}$ the detection efficiency of the TaN detector is 5 to 6 times higher than for the NbN detector.

This improvement has been achieved without compromise in the speed of the detector—its main advantage compared to competing technologies. In Fig. 13.2 voltage traces recorded for both detectors are shown. The pulses are almost identical for both detectors. Especially the rise time is for both detectors $\sim 200\text{ ps}$, given by the 2 GHz bandwidth of our readout electronics. This is already indicating a very small timing jitter for the detection of photons, important for time-correlation experiments. This was confirmed by time-correlation measurements in a setup in the group of Prof. Imamoglu at ETH Zürich, from which we could determine a timing jitter of $\sim 80\text{ ps}$, comparable to standard NbN SNSPD.

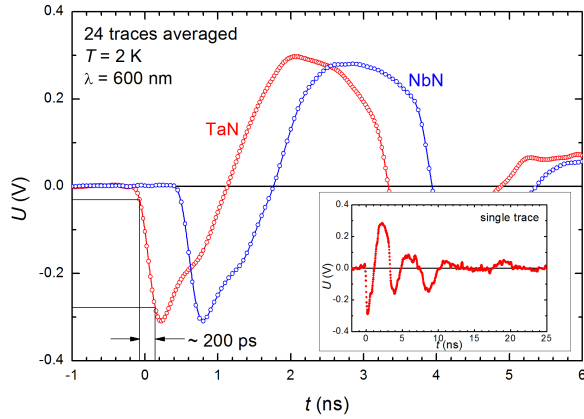


FIG. 13.2 – Amplified and scaled voltage traces of photon counts. In the main figure voltage traces averaged over 24 individual events for a TaN SNSPD (red) and a reference NbN SNSPD (blue) are plotted as a function of time. The rise time of about 200 ps is about the same for both detectors and effectively given by the 2 GHz bandwidth of our readout electronics. The inset shows a longer time interval for a single trace.

13.1.2 X-ray superconducting nanowire single-photon detectors

More than a decade before the successful development of SNSPD for the optical and near-IR wavelength range, serious efforts were undertaken to use this detection principle for X-ray photons with keV-energies [3]. However, these preliminary X-ray detectors struggled with problems after photon detection, making it difficult to operate them in a continuous detection mode. Recently, SNSPDs were used in time-of-flight spectrometry of molecules [4]. For this purpose, a SNSPD from 5 nm thin NbN was successfully tested for X-ray detection in a feasibility study [5]. However, the absorptivity of thin NbN films for X-ray photons and therefore the quantum efficiency of the detectors, are low.

In order to enhance the absorptivity of the superconducting detector, we fabricated an X-ray superconducting nanowire single-photon detector (X-SNSPD) from 100 nm thick niobium (Fig. 13.3a). The detector geometry was designed for a kinetic inductance large enough to significantly reduce the above mentioned problem with

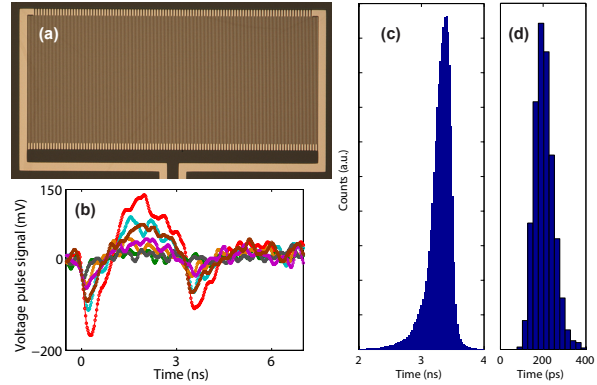
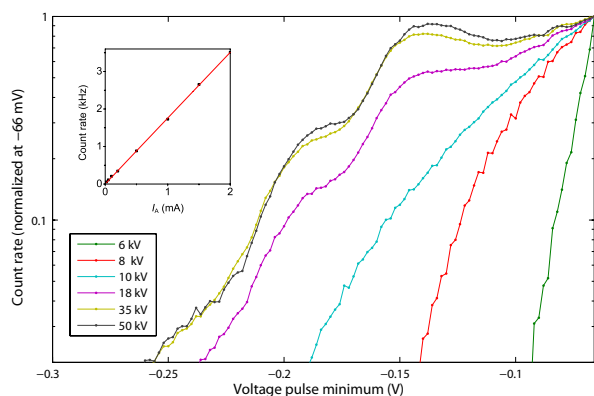


FIG. 13.3 – (a) Optical image of examined X-SNSPD from 100 nm thick niobium, (b) typical voltage pulses after X-ray photon absorption, (c) pulse length histogram and (d) pulse rise time histogram (time spans between 15% and 85% of voltage minimum)

continuous photon detection, and small enough for ultrafast pulse recovery times. We report on the detection of X-ray photons with keV-energies with an ultrafast pulse recovery time of less than 4 ns (Fig. 13.3b and c) and an average pulse rise time of about 200 ps (Fig. 13.3d), again limited only by our electronics setup. In contrast to optical photon-detection in thin-film SNSPDs, X-ray photon detection was possible even at bias currents smaller than 1% of the critical current.

Most remarkably, we observed that the average X-SNSPD signal amplitude depends significantly on the acceleration voltage of the photon emitting X-ray tube. Figure 13.4 shows the corresponding normalized pulse amplitude histograms at different acceleration voltages between 6 kV and 50 kV. Since the detector operates in a single-photon detection mode (inset Fig. 13.4), the variation of the average signal amplitude can be attributed to the variation of the average photon energies at different X-ray tube settings. This phenomenon, which is new for SNSPDs, is explained by the orders-of-magnitude smaller resistance of the normal conducting domains as compared to the situation in thin-film SNSPDs.

Moreover, no dark count events were triggered in over four hours of measurement, even with bias currents very close to the critical current.



58

FIG. 13.4 – Histograms of voltage pulse minima for different X-ray tube acceleration voltages (indicated in the legend). The acceleration voltage determines the maximum energy of the emitted photons. The inset shows that the detector photon count rate is proportional to the photon flux, which was varied by the X-ray tube anode current.

Our results show that ultrafast dark-count-free X-SNSPDs can be fabricated which can operate in a large spectral range. They could find applications where very high count rates, precise timing, a good signal-to-noise ratio and response in a wide spectral range for photon counting are required.

13.2 Experiments on $\text{Ba}_{3-x}\text{Sr}_x\text{Cr}_2\text{O}_8$

We have revived an old idea (see, e.g., JB 2006/07) to examine possibilities to directly prove the existence or the absence of macroscopic phase coherence in a condensate of triplon quasiparticles. We have realized that the time scale for a corresponding measurement is determined by the expected lifetime of phase coherence and was chosen much too long in earlier corresponding magnetic resonance experiments [6].

In an alternative approach we have recently suggested that two interacting triplon condensates with different chemical potentials (i.e. critical fields H_c) should show an a.c. Josephson effect (similar to that observed in superconducting junctions) if they are placed into a common external magnetic field exceeding both critical fields. This effect would manifest itself in a change in the respective energy spectra. To account for the limited quasi-

particle lifetime ($> 10^{-11}$ s [6]) we expect a corresponding experiment to be successful in a junction composed of two weakly coupled compounds with critical fields $\mu_0 H_c$ differing by at least 0.5 T, and with a low enough intrinsic exchange-interaction anisotropy ($< 4 \mu\text{eV}$). As a result of the coupling, certain ESR (electron-spin resonance) active modes should split enough to be observable [6] (i.e., by $\omega_{\text{a.c.}} \approx 10^{11} \text{ s}^{-1}$), which can be investigated in a corresponding high-resolution ESR experiment.

13.2.1 Synthesis of $\text{Ba}_{3-x}\text{Sr}_x\text{Cr}_2\text{O}_8$ as a prototype material

As a first preliminary study we have attempted to synthesize samples within the solid solution $\text{Ba}_{3-x}\text{Sr}_x\text{Cr}_2\text{O}_8$. The reason for this choice is *a*) the relatively low exchange-interaction anisotropy of $\text{Ba}_3\text{Cr}_2\text{O}_8$ and $\text{Sr}_3\text{Cr}_2\text{O}_8$ ($\approx 1 \mu\text{eV}$), *b*) the relatively low critical field of $\text{Ba}_3\text{Cr}_2\text{O}_8$ ($\mu_0 H_c \approx 12$ T [7], which is accessible in standard superconducting laboratory magnets), and *c*) the existence of isostructural $\text{Sr}_3\text{Cr}_2\text{O}_8$ with a $\mu_0 H_c \approx 30$ T [8]. Up to now, the solid solution $\text{Ba}_{3-x}\text{Sr}_x\text{Cr}_2\text{O}_8$ has not yet been reported in the literature, and our aim was not only to show that it exists, but also to explore its physical properties later on.

These synthesis experiments were carried out by the PhD student Henrik Grundmann at the UZH and at McMaster University in Hamilton, Canada, with the help of Dr. Hanna Dabkowska. Although these experiments in an optical floating zone furnace did not yield strictly single-crystalline samples, the re-solidified material contained several, relatively large, well oriented crystallites, which was confirmed by Laue diffraction experiments.

The lattice constants were estimated from the Debye-Scherrer-spectra of reground crystallites (see Fig. 13.5 for a comparison of simulated Debye-Scherrer spectra for $\text{Ba}_3\text{Cr}_2\text{O}_8$ and $\text{Sr}_3\text{Cr}_2\text{O}_8$ with experimental data for $\text{Ba}_{1.5}\text{Sr}_{1.5}\text{Cr}_2\text{O}_8$). The numerical values listed in Tab. 13.1 are close to what is expected according to Vegard's law, based on the lattice constants of $\text{Ba}_3\text{Cr}_2\text{O}_8$ [7] and $\text{Sr}_3\text{Cr}_2\text{O}_8$ [8]. A more precise structural refinement of all prepared compounds is in progress.

TAB. 13.1 – Lattice parameters a and c^a of the prepared $\text{Ba}_{3-x}\text{Sr}_x\text{Cr}_2\text{O}_8$ samples.

material	literature value		from powder spectra		expected from Vegards law	
	a	c	a	c	a	c
$\text{Ba}_3\text{Cr}_2\text{O}_8$	5.742 Å	21.389 Å [7]	-	-	-	-
$\text{Ba}_{2.9}\text{Sr}_{0.1}\text{Cr}_2\text{O}_8$	-	-	5.709 Å	21.367 Å	5.734 Å	21.350 Å
$\text{Ba}_{1.5}\text{Sr}_{1.5}\text{Cr}_2\text{O}_8$	-	-	5.67 Å	20.8 Å	5.5613 Å	20.805 Å
$\text{Sr}_3\text{Cr}_2\text{O}_8$	5.562 Å	20.221 Å [8]	-	-	-	-

^anotation according to Ref. [8]

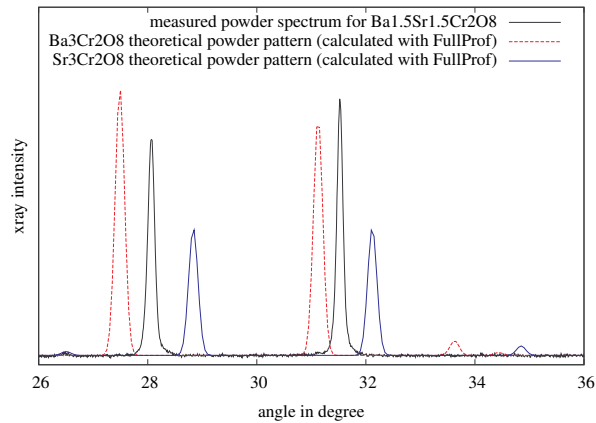


FIG. 13.5 – Comparison of Debye-Scherrer measurements for $\text{Ba}_{1.5}\text{Sr}_{1.5}\text{Cr}_2\text{O}_8$ with simulated powder spectra for $\text{Ba}_3\text{Cr}_2\text{O}_8$ and $\text{Sr}_3\text{Cr}_2\text{O}_8$.

13.2.2 Investigation of the ESR/EPR linewidths in $\text{Ba}_3\text{Cr}_2\text{O}_8$

In a second preliminary study we wished to examine whether the intrinsic line widths in the high-field EPR spectra of $\text{Ba}_{3-x}\text{Sr}_x\text{Cr}_2\text{O}_8$ would allow for the detection of the expected line splitting or not. Measurements on powdered $\text{Ba}_3\text{Cr}_2\text{O}_8$ were carried out at the high-field EPR setup in the group of Prof. László Forró at the EPFL, Lausanne. We found that the width of the ESR line corresponding to transitions between neighbouring triplet branches in $\nu = 210$ GHz is smaller than 0.2 T below room temperature (see Fig. 13.6, lowest panel). Therefore, from the instrumental point of view, it should be possible in principle to detect a line splitting of 0.5 T in this material.

However, below $T \approx 80$ K, an additional line showed up (see Fig. 13.6, upper panels), with an in-

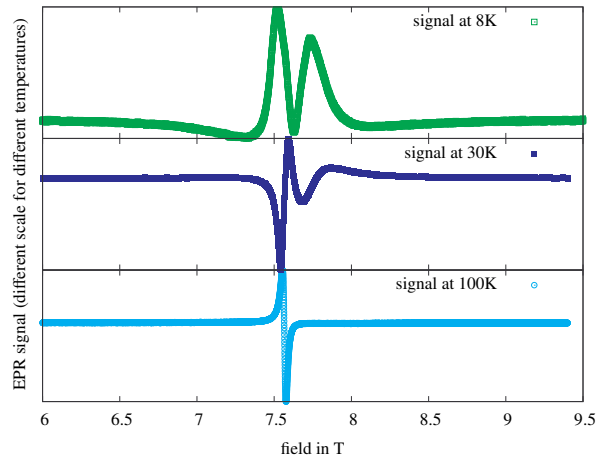


FIG. 13.6 – EPR signal ($\nu = 210$ GHz) at different temperatures.

tensity that increases with decreasing temperature. Up to now it is not clear if this can be attributed to a structural phase transition that occurs around this temperature [9] or if it is due to another phenomenon. We will perform additional EPR measurements on single crystalline samples of $\text{Ba}_3\text{Cr}_2\text{O}_8$ and the solid solutions $\text{Ba}_{3-x}\text{Sr}_x\text{Cr}_2\text{O}_8$ to clarify this issue.

13.3 LC-circuit calorimetry

In conventional calorimetric a.c. methods, a heat capacity is calculated from the amplitude of an imposed temperature oscillation. It is known that the statistical error of such a measurement decreases with measuring time t as $t^{-1/2}$. If an oscillator could be built in which the heat capacity C acts like an electrical capacitance together with a known electrical inductance L , C could be calculated from the resulting resonance frequency ω according to

$C = 1/(L\omega^2)$. Alternatively, L could be a (hypothetical) “thermal inductor”. Rife and Boorstyn [10] have shown that the measurement error for frequency measurements under white noise conditions depends on the measuring time as $t^{-3/2}$, as opposed to $t^{-1/2}$ for measurements of the amplitude. Therefore, a device measuring a frequency that is determined by the heat capacity would maintain most of the advantages of all other a.c.-calorimetry-methods, but the accuracy would be greatly improved.

60

We have successfully constructed such a device in our laboratory with an “effective thermal inductance” by using Peltier elements connected to an electrical inductance L . When the Peltier elements are coupled to a sample and equipped with suitable amplification, we reach autonomous LC -circuit oscillations with a frequency that depends on the heat capacity C as

$$\omega = \frac{1}{\sqrt{\Pi\alpha LC}}, \quad (13.1)$$

where Π and α are the Peltier and Seebeck coefficients of the Peltier element, respectively.

The detailed electrical set up is shown in Fig. 13.7. An inductance of $L \approx 10$ H is realized in the form of an electrical gyrator circuit. The sample is sandwiched between two Peltier elements placed inside a PPMS cryostat (Physical Property Measurement System, Quantum Design Inc.), to control the temperature and magnetic field. The first Peltier element essentially converts variations in the thermal current into corresponding changes in an electrical current. This induces a voltage across L that creates a temperature difference at the Peltier element, thereby counteracting the thermal current. The element is therefore acting as an “effective thermal inductor”. The second sensing Peltier element is used together with an amplifier to provide compensation for electrical and thermal losses.

The performance of the setup was verified with a sample of 45.2 mg of Gadolinium, a ferromagnet with a Curie temperature of $T_C \approx 290$ K. We show in Fig. 13.8(a) the oscillation frequency of the thermal LC circuit that varies with temperature, together with the calculated heat capacity

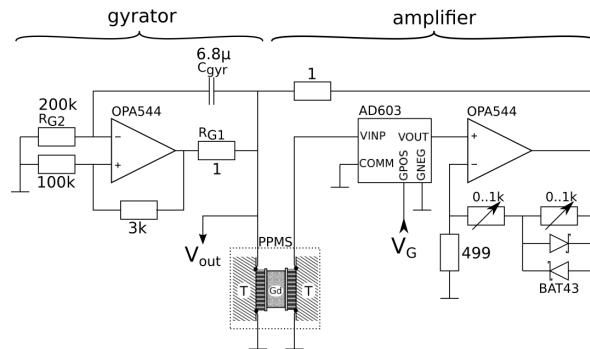


FIG. 13.7 – Schematic of the oscillator circuit. On the left side an electrical gyrator of $L \approx 10$ H forms a resonant circuit with the Gd sample coupled through a Peltier element, while the right side acts as an amplifier to compensate for electrical and thermal losses.

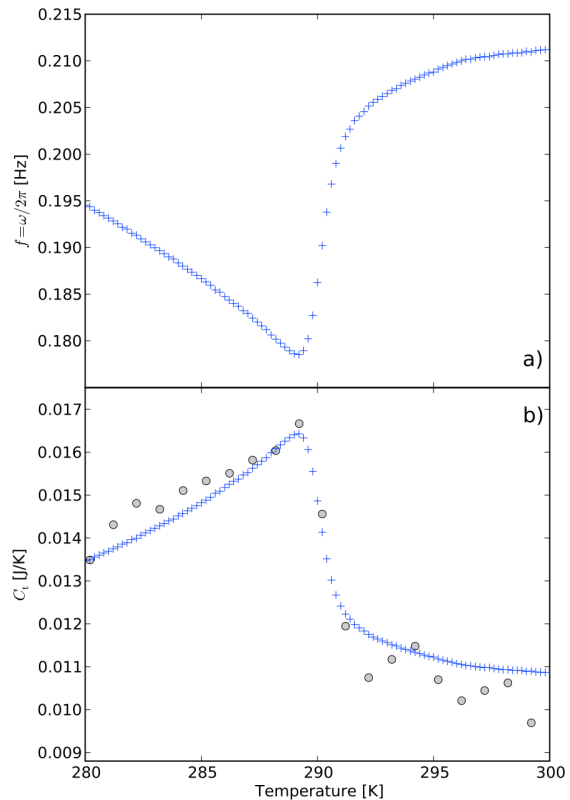


FIG. 13.8 – a) Frequency of the thermal oscillations and b) calculated heat capacity of the test sample (both blue), compared with heat capacity data of the same sample measured with a commercial PPMS option (grey circles).

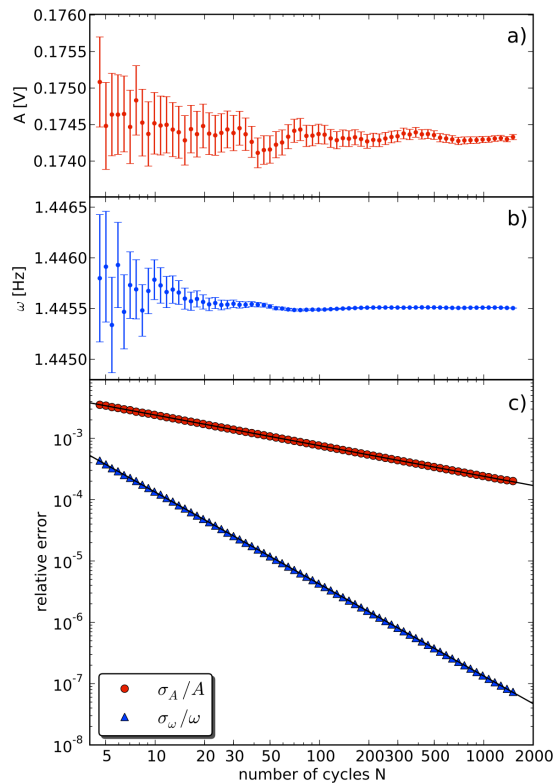


FIG. 13.9 – Results of fits to data taken for an increasing number of measurement cycles N (i.e., increasing measuring time t) for a selected data point from Fig. 13.8. The statistical error in the amplitude A of the temperature oscillation decreases as $N^{-1/2}$, while the corresponding error in frequency and therefore in C decreases as $N^{-3/2}$ as expected.

(Fig. 13.8(b)) in comparison with the data obtained from the commercial heat-capacity option of the PPMS. A plot of the statistical errors of amplitude A and frequency ω obtained from Levenberg-Marquardt fits to the respective temperature oscillations confirms the theoretical predictions for the evolution of the statistical errors with time (see Fig. 13.9) [11, 12].

Autonomous temperature oscillations have now been achieved down to 87 K, thereby demonstrating the feasibility of this technique also at lower temperatures. It remains to be seen, however, if sufficient accuracy improvements and robustness to noise in “vortex-shaking” experiments can be achieved to perform measurements on superconductors and at even lower temperatures.

- [1] K. Il'in *et al.*, published online in *J. Low Temp. Phys.*, (2011)
<http://dx.doi.org/10.1007/s10909-011-0424-3>.
- [2] A. Engel *et al.*,
Appl. Phys. Lett., 100 (2012) 062601
- [3] A. Gabutti *et al.*, *Nucl. Instrum. Methods A*, 278 (1989) 425-430; *ibid.*, 312 (1992) 475-482; L. Parlato *et al.*, *Nucl. Instrum. Methods A*, 348 (1994) 127-130.
- [4] K. Suzuki *et al.*, *J. Low Temp. Phys.*, 151, (2008) 766-770; K. Suzuki *et al.*, *Appl. Phys. Express*, 1, (2008) 031702; N. Zen *et al.*, *Appl. Phys. Letters*, 95, (2009) 172508.
- [5] D. Perez de Lara *et al.*,
J. Low Temp. Phys., 151, (2008) 771-776.
- [6] A. Schilling *et al.*,
accepted by *J. Phys.: Conf. Ser.*,
<http://arxiv.org/abs/1107.4335>;
A. Schilling and H. Grundmann,
accepted by *Ann. Phys. (NY)*,
<http://arxiv.org/abs/1101.1811>
- [7] A. A. Aczel *et al.*, *Journal of Crystal Growth*, 310 (2008) 870; M. Kofu *et al.*, *Phys. Rev. Lett.*, 102 (2009) 177204.
- [8] E. Cuno and H. Müller-Buschbaum,
Z. anorg. allg. Chemie, 572 (1989) 95;
A. A. Aczel *et al.*, *Phys. Rev. Lett.*, 103 (2009) 207203.
- [9] M. Kofu *et al.*,
Phys. Rev. Lett., 102 (2009) 037206.
- [10] D. C. Rife and R. R. Boorstyn,
IEEE Trans. Inf. Theory IT-20, (1974) 591.
- [11] O. Bossen and A. Schilling,
Rev. Sci. Instrum., 82 (2011) 094901.
- [12] *Nature Physics*, 7, (2011) 743.

14 Surface Physics

T. Greber, M. Hengsberger, J. H. Dil, F. Matsui, H. Ma, R. Westerström, L. Castiglioni, H. Cun, D. Leuenberger, B. Slomski, S. Roth, A. Hemmi, G. Landolt, M. Greif, C. Janssen, P. Donà, S. Muff, R. Stania, C. Bernard, E. Eisenring, T. Kälin, J. Osterwalder

The group investigates surface and interface phenomena at the atomic level. For this purpose the surface physics laboratory is well equipped for the preparation and characterization of clean single-crystalline surfaces, metal and molecular monolayer films, as well as covalently bonded single layers, using a wide variety of experimental techniques. Moreover, we currently operate two photoemission spectrometers at the nearby Swiss Light Source (SLS), one for spin- and angle-resolved photoemission spectroscopy (SARPES) and one for photoelectron diffraction and holography. Moreover, the group is participating actively in the buildup of the new SLS beamline PEARL (PhotoEmission and Atomic Resolution Laboratory).

The research carried out during the report period can be grouped into four topics:

- Monolayer films of hexagonal boron nitride (*h*-BN) and graphene on metal surfaces

Over the last several years the group has built up a considerable expertise in the growth and characterization of sp^2 -bonded monolayers on transition metal surfaces. The current studies are motivated by two different guiding principles. The first one is related to the chemical functionality of the adlayers: on Rh(111) and Ru(0001) surfaces, the large lattice misfit induces strongly corrugated sp^2 layers that exhibit also a corrugation in the electrostatic potential landscape that can be exploited for templating molecular adsorbates [1–4]. We have come to a rather complete understanding of the structure of these layers (see Section 14.1). These layers are very inert and can be brought in contact with air, water and many organic solvents, and they are thus amenable to ex-situ experiments. Within a Sinergia project of the Swiss National Science Foundation, funding a consortium of four different groups, we have

built up a growth chamber for handling wafer-size samples, where *h*-BN or graphene films can be grown on four-inch Si(111) wafers covered with monocrystalline Rh(111) films. The chamber is placed in a dedicated clean-room, which enables us to process these samples in a dust-free environment. First experiments involve the manipulation of the surface energy of such films by hydrogen intercalation, monitored by contact angle measurements, and the preparation of organic light-emitting diodes (OLEDs) where the electrons are injected via a well defined *h*/BN/Rh(111) interface.

The second line of research is directed towards the synthesis of epitaxial layers of graphene and *h*-BN with a view on future electronic devices based on graphene. Due to its insulating properties and similar crystal structure and lattice constant, *h*-BN appears to be the ideal 'gate oxide'. We have had first successes in growing graphene layers on top of single-layer *h*-BN on Cu(111) and determining the resulting registry of the two sp^2 lattices. Moreover, based on the progress in the wafer-scale growth of sp^2 layers, making large amounts of samples available, we are currently working on peel-off methods for producing freestanding monolayer films on the centimeter scale.

- Molecular adsorbates and molecular monolayers

The focus on endofullerenes was continued in our endeavour to study monolayer films of magnetic molecules. In a project 'Resonant X-ray Photoelectron Diffraction (RXPD)' funded by the SNF, films of $DySc_2@C_{80}$ molecules, obtained from L. Dunsch of the IWF Dresden, were prepared from minute quantities. They were characterized for their magnetic properties by x-ray magnetic circular dichroism and SQUID (group of H. Keller), and the sam-

ples show long spin relaxation times at a temperature of 2K. The future PEARL beamline at the SLS will permit us to study these molecules in monolayers, using RXPd for combined structural information with sensitivity to magnetism. A first proof-of-principle experiment based on a clean Ni(111) crystal has been published last year [5].

- Spin-resolved photoemission and momentum mapping

Our spin-resolved photoemission chamber (COPHEE) at the SLS has continued to be in high demand as a general user instrument due to its unique performance. In collaboration with several other groups, the ternary compound PbBi_4Te_7 , a three-dimensional topological insulator, was characterized in terms of its electronic and spin structure [6]. Moreover, the studies of the Rashba effect in ultrathin Pb films on Si(111) were continued (see Sec. 14.2). Further studies included the compound BiTeI, which exhibits a giant Rashba effect in the bulk band structure due to its non-centrosymmetric structure [7], and a homologous series of topological insulators of the composition $\text{GeBi}_{4-x}\text{Sb}_x\text{Te}_7$ (in collaboration with the group of A. Schilling).

- Ultrafast processes at surfaces

Within the NCCR 'Molecular Ultrafast Science and Technology' (MUST), our group has built and commissioned a compact angle-resolved photoemission chamber, which will be moved to various ultrashort pulsed light sources available within the consortium. It is currently stationed at ETH (laboratory of U. Keller), being readied for first attosecond photoemission experiments on self-assembled diamondoid monolayers, which show negative electron affinity. Earlier experiments in our group had provided some clues on the mechanism leading to efficient, largely monochromatic electron emission [8]. Last years activities included a pump-probe time-resolved photoemission study of the Bi(114) surface, where the coherent excitation of a surface-related phonon mode is clearly observed (see Sec. 14.3).

- [1] S. Berner *et al.*,
Angew. Chem. Int. Ed. 46, 5115 (2007).
- [2] J. H. Dil *et al.*, Science 319, 1824 (2008).
- [3] T. Brugger *et al.*,
Phys. Rev. B 79, 045407 (2009).
- [4] A. J. Pollard *et al.*,
Angew. Chem. Int. Ed. 49, 1794 (2010).
- [5] M. Morscher *et al.*,
Phys. Rev. B 84, 140406 (2011).
- [6] S. V. Eremeev *et al.*,
Nature Commun. 3, 635 (2012).
- [7] K. Ishizaka *et al.*, Nature Mat. 10, 521 (2011).
- [8] S. Roth *et al.*,
Chem. Phys. Lett. 495, 102 (2010).

In the following, three highlights of last year's research are presented in more detail.

14.1 The unit cell of graphene on ruthenium

In collaboration with: Marcella Iannuzzi, Jürg Hutter, Physikalisch Chemisches Institut, Universität Zürich; Irakli Kalichava, Steven J. Leake, Oliver Bunk, Phil Willmott, Swiss Light Source, Paul Scherrer Institut, 5232 Villigen; Haitao Zhou, Geng Li, Yi Zhang, and Hongjun Gao, Institute of Physics, Chinese Academy of Sciences, Beijing, 100190, China.

A single layer of sp^2 hybridized carbon on the (0001) surface ruthenium (g/Ru) forms a corrugated superstructure (see Fig. 14.1) that is related to the mismatch of the two lattice constants. The unit cell corresponds to a coincidence lattice of 25×25 graphene units (1250 atoms) on top of 23×23 ruthenium unit cells and comprises *four* protrusions [1]. These hills are surrounded by *lateral* electric fields that are imposed by the corrugation of the graphene layer [2]. These fields are important for the templating functionality for adsorbed molecules [3], and for understanding scanning tunneling spectroscopy data measured on the hills in terms of local resonances, implying the scenario of graphene based quantum dot arrays [4].

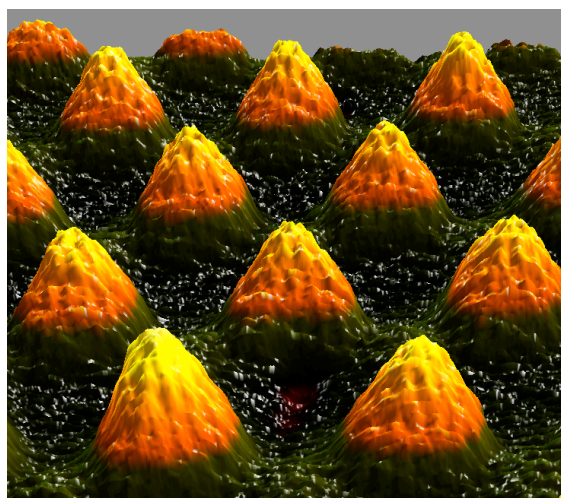


FIG. 14.1 – Three-dimensional representation of low-temperature scanning tunneling microscopy data of the g/Ru superstructure with atomic resolution. The height of the hills is 0.12 nm, their distance is about 3 nm. The corrugation is of crucial importance for the understanding of this structure and its functionality. Data from H.G. Zhang, cover of *J. Phys: Condens Matter* 22 No. 30 (2010).

An earlier surface x-ray diffraction study had concluded that the four hills in the unit cell are not equivalent [1]. An extensive density functional theory (DFT) calculation on the $25\text{-on-}23$ unit cell now shows four hills with very similar heights. The corrugation of 120 pm is in line with a recent DFT calculation on a 11×11 super cell, assuming a 12×12 graphene on 11×11 Ru(0001) coincidence lattice [5]. However, the four hills do not have the same registry of their summit positions with respect to the graphene lattice. The theoretical prediction is one hill with a tetrahedral (Y) apex consisting of four carbon atoms, and three omega (Ω) peaks with carbon six-rings on the crest (see Fig. 14.2). In atomically resolved large scale scanning tunneling microscopy (STM) images it is possible to distinguish the two types of hills within the unit cell. When the structure taken from the DFT calculations is used to model the surface x-ray diffraction data, a better R-factor is obtained without adjustment of any parameters. Moreover, a lower graphene straining (Keating) energy results in comparison with the earlier structural model [6].

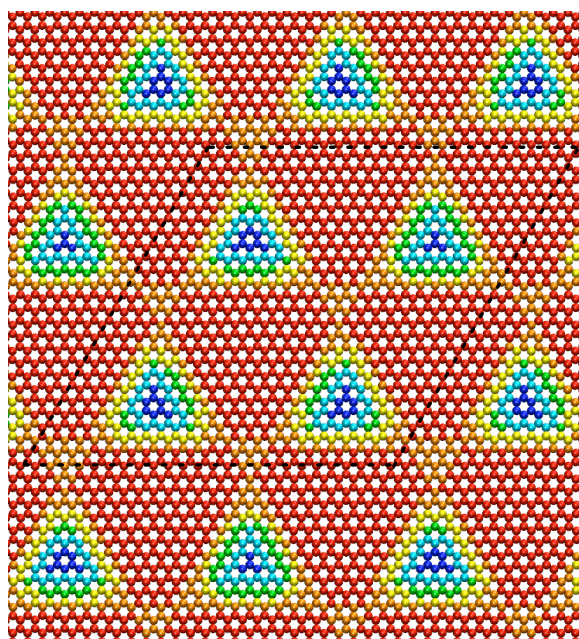


FIG. 14.2 – Theoretical result for the arrangement of the 1250 carbon atoms in the $25\text{-on-}23$ $g/Ru(0001)$ structure (dashed parallelogram). The color indicates the height of the C atoms above the Ru substrate and ranges from 325 pm (blue) to 209 pm (red). Note the two different types of hills: one Y -type hill with one carbon atom on the apex and three Ω -type hills with six carbon atoms centered around the crest of the peak.

- [1] D. Martoccia, *et al.*, *Phys. Rev. Lett.* 101, 126102 (2008).
- [2] T. Brugger, *et al.*, *Phys. Rev. B* 79, 045407 (2009).
- [3] A. J. Pollard *et al.*, *Angew. Chem. Int. Ed.* 49, 1794 (2010).
- [4] H.G. Zhang *et al.*, *J. Phys.: Condens. Matter* 22, 302001 (2010).
- [5] D. Stradi *et al.*, *Phys. Rev. Lett.* 106, 186102 (2011).
- [6] D. Martoccia *et al.*, *New J. Phys.* 12, 04302 (2010).

14.2 Rashba effect in Pb quantum well states

In collaboration with: Gustav Bihlmayer, Peter Grünberg Institut and Institute for Advanced Simulation, Forschungszentrum Jülich and JARA, 52425 Jülich, Germany; Luc Patthey, Swiss Light Source, Paul Scherrer Institute, 5232 Villigen.

When the thickness of a metal layer on a semiconductor is reduced to the coherence length of the conduction electrons, quantum confinement between the semiconductor band-gap and the image potential outside the metallic surface results in the formation of quantum well states (QWS) with quantized energy levels. These confined electrons, while bouncing back and forth between the metal-substrate and metal-vacuum interface, are free to move within the film plane, thus forming a prototypical two-dimensional electron gas (2DEG). The asymmetric confinement of the 2DEG results in the lifting of the spin degeneracy of the electronic states via the spin-orbit interaction (SOI), described by the Rashba effect [1]. The spin texture of a Rashba system consists of tangentially aligned spins of opposite direction on the spin split concentric Fermi circles centered around the $\bar{\Gamma}$ point, forming two spin vortices in momentum space.

This scenario was confirmed experimentally for QWS in ultrathin Pb films on Si(111) [2]. The study yielded two unexpected results: (i) the degree of spin splitting did not depend on the film thickness, and (ii) the helicity of the spin vortices was reversed when compared to the surface state on Au(111). Finding (i) suggested that the Rashba effect arises from contributions within the entire Pb layer rather than from the interfaces only. This is consistent with the understanding that the Rashba-type spin splitting is produced by the local asymmetry of the wave functions close to the Pb nuclei, where the Coulomb potential gradient is very strong [3]. In this model both, the metal-substrate and the metal-vacuum interfaces play a significant role by inducing an asymmetric wave function envelope due to the different penetration depths into the confinement barriers. To test this model we have grown ultra-thin Pb layers on different interfaces while keeping the metal-vacuum interface constant [4].

Figure 14.3(a) shows the measured momentum dependent spin splittings for samples where the Pb quantum films were grown on a preformed $\sqrt{3} \times \sqrt{3}$ -R30° reconstructed surface induced by either Pb, Bi or Ag. Compared with the Pb interface, we find a reduction of the Rashba effect by almost 50 % on

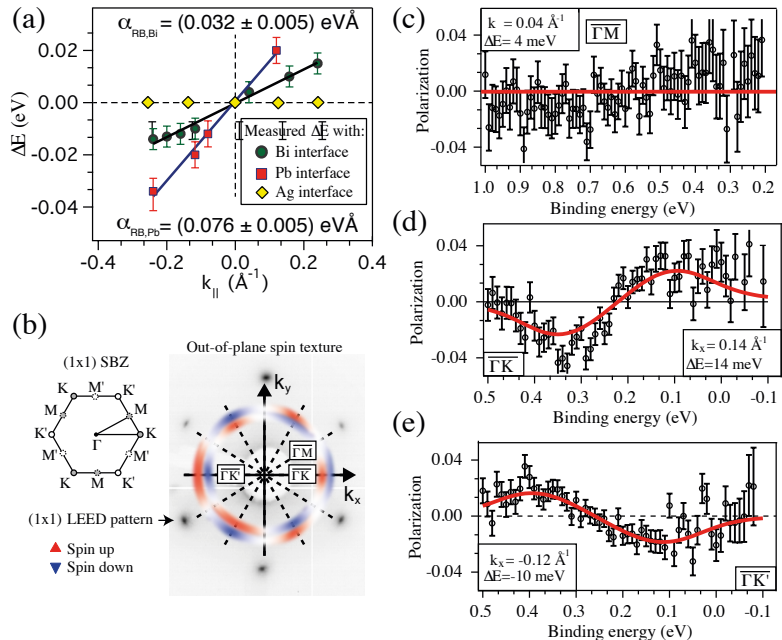
65

FIG. 14.3 –

(a) Measured spin splittings of Pb QWS for different interfaces between the Pb film and the Si(111) substrate, plotted at different in-plane momenta. The linear fit is used to obtain the Rashba parameter.

(b) Out-of-plane spin texture in Pb/Bi/Si(111).

(c-e) Spin polarization data of the z-component taken at different high symmetry directions [4].



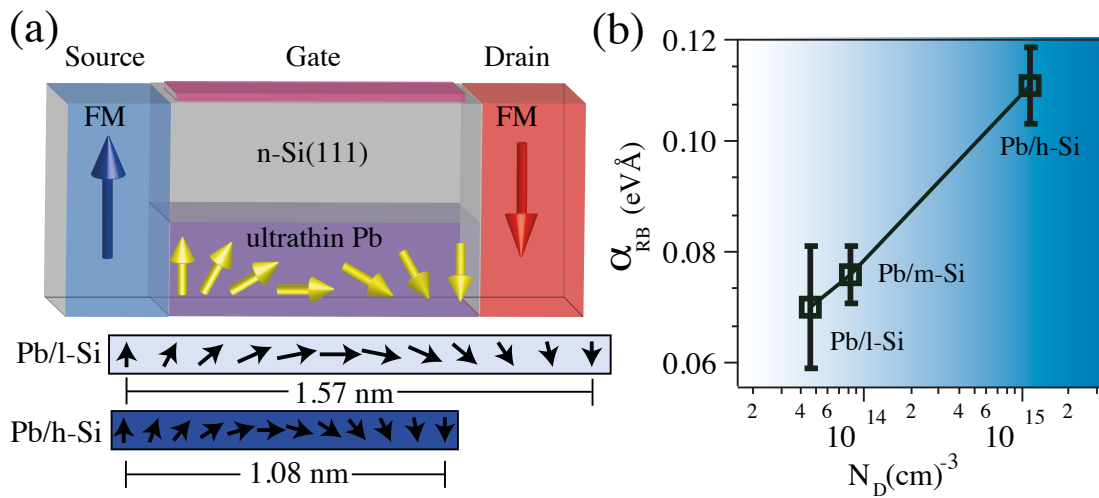


FIG. 14.4 – (a) Schematic drawing of a spin-field-effect transistor with expected 180° spin rotation lengths in a lightly ($\text{Pb/l-Si}(111)$) and heavily ($\text{Pb/h-Si}(111)$) n -doped system. (b) shows the dependence of the experimentally determined Rashba parameters on the n -Si substrate doping.

the Bi-reconstructed Si(111), while on the Ag interface the spin splitting drops below the resolution of our spin detector. It is concluded that the strength of the SOI can be manipulated through interface engineering, and that the Ag interface induces an almost symmetric charge distribution within the Pb film. Moreover, we have measured an out-of-plane spin polarization in the Pb/Bi/Si(111) system, which follows the three-fold symmetry of the lattice. This is seen in Fig. 14.3(b-e): along the $\bar{\Gamma}$ - \bar{M} direction of the (1x1) surface the spin polarization is fully in-plane, i.e. the z -polarization is zero, while it points out-of-plane along $\bar{\Gamma}$ - \bar{K} . Since this system is non-magnetic, time-reversal symmetry dictates a reversal of the z -polarization along $\bar{\Gamma}$ - \bar{K}' . This is exactly what we observe.

One of the main goals in the field of *spintronics* is the realization of a spin-based field-effect transistor [5] with the following operating principle (Fig. 14.4(a)): a Rashba system forms a 2D channel between ferromagnetic (FM) source and drain electrodes. Depending on whether the electron spins are aligned parallel or antiparallel with the magnetization direction of the drain after propagating along the channel, a high or low current passes through. The SOI permits to control the momentum splitting, and consequently the degree of spin rotation in the channel, by means of an externally

applied gate voltage rather than through an external magnetic field. A large step towards the realization of such a device is our recent investigation of the dependence of the Rashba effect on the doping level of the n -type Si(111) substrate. As can be seen from Fig. 14.4(b) the strength of the SOI can be tuned effectively: a change in the donor concentration by a factor of ~ 20 raises the Rashba constant by almost a factor of two. We conjecture that the gradient of the band bending at the film-substrate interface is the decisive factor for this effect. This finding opens up the possibility to tune the Rashba-type spin splitting in metallic QWS via an externally applied gate voltage.

- [1] Y. A. Bychkov and E. I. Rashba, J. Phys. C: Solid State Physics, 17, 6039 (1984).
- [2] J. H. Dil *et al.*, Phys. Rev. Lett. 101, 266802 (2008).
- [3] G. Bihlmayer *et al.*, Surf. Sci., 600, 3888 (2006).
- [4] B. Slomski *et al.*, Phys. Rev. B, 84, 193406 (2011).
- [5] S. Datta and B. Das, Appl. Phys. Lett. 56, 665 (1990).

14.3 Electron dynamics in a quasi-one-dimensional topological metal: Bi(114)

A few years ago, a new class of materials called topological insulators was predicted and later on experimentally demonstrated [1], which exhibit spin-polarized and topologically protected surface states owing to strong spin-orbit interaction. More recently, a so-called topological metal was discovered on the Bi(114)-surface, which consists of atomic rows that support a one-dimensional surface state [2]. The Fermi line corresponding to the Fermi surface of the surface state is spin split as shown by spin-resolved photoelectron spectroscopy [2] and circular dichroism in the angular distribution [3].

We performed time-resolved photoelectron spectroscopy experiments on the Bi(114) surface. The electron-electron scattering rates are found to be extremely low due to the low density of states close to the Fermi level and due to the spin structure of the surface states, resulting in picosecond lifetimes. In contrast to the weak electron-electron scattering, electron-phonon interaction is quite strong in bismuth owing to its rhombohedral crystal structure, in which slight deviations from the simple cubic structure cause huge changes in the electronic density of states.

Surprisingly, the complex interplay of electronic and phonon degrees of freedom can be cast into a simple model involving three coupled rate equations for electrons, the bath of weakly coupled phonons, referred to as the *lattice*, and a subset of strongly coupled phonons, which dominates the response to the coherent excitation in a way very similar to the case of high-Tc superconductors [4]. The electronic temperature rise after excitation can be extracted from our spectra by fitting a Fermi-Dirac distribution or by evaluating the excess energy in the electron gas. The results of fitting the three differential equations to the electronic temperature data are shown in Fig. 14.5. The resulting coupling parameter indicates a strong coupling and a high occupation by several quanta of each single mode.

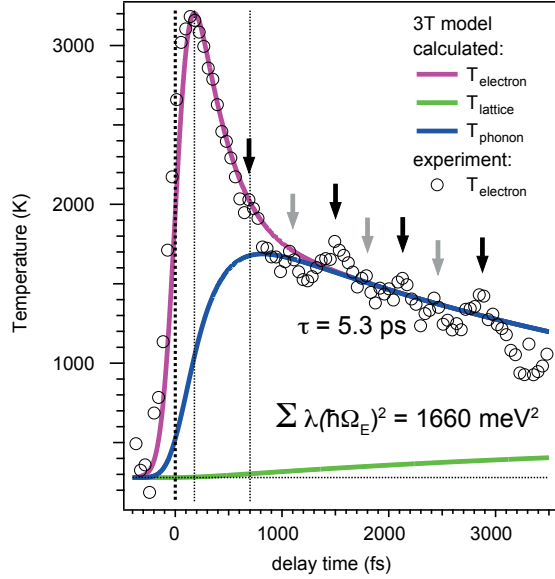


FIG. 14.5 – Evolution of the electronic temperature after absorption of the laser (pump) pulse at time delay zero (open symbols). The rise and subsequent decay on two distinct timescales can be fitted by using different temperatures for electrons (purple line), for a subset of strongly coupled phonons (blue line), and for the general lattice (green line). The term $\sum \lambda(\hbar\Omega_E)^2$ indicates the coupling strength between electrons and the particular phonon subset summed over all modes. The arrows mark maxima in the electronic spectra, which are caused by excitation of coherent phonon modes. These oscillations were ignored in the three-temperature analysis.

Moreover, the spectra of the hot electron gas exhibit energy and intensity oscillations due to the excitation of coherent phonon modes [5, 6], as shown in Fig. 14.6. The Fourier transforms of the transients can be used for identifying the involved phonon modes by comparing the frequencies with calculated phonon band structures for bismuth [7]. We deduce from our data that a transverse optical phonon mode with a frequency of 0.72 THz and a maximum density of states close to the X-point of the bulk Brillouin zone drives the observed intensity and binding energy oscillations of the electronic states at the Fermi level. Since the X-point corresponds to a standing wave along the direction of the atomic chains on Bi(114), the strong suscep-

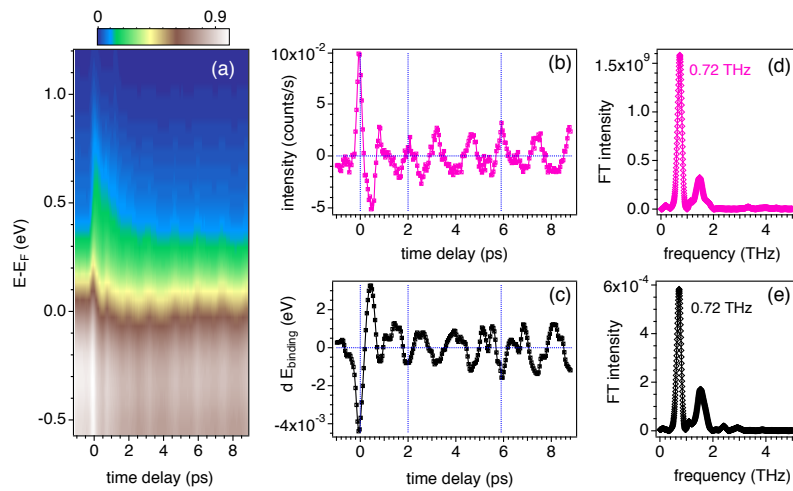


FIG. 14.6 – (a) Time-resolved photoemission data on a false-color scale as function of delay and binding energy. Close to delay zero unoccupied states above the Fermi energy are populated; the excited states decay and show intensity and energy modulations. Center panels show the measured oscillations in intensity (b) and energy (c), and (d, e) the corresponding Fourier transforms.

68

tibility of the quasi-one-dimensional electron gas in the chains to perturbations could explain why this particular phonon mode had never been observed so far in time-resolved experiments.

- [1] D. Hsieh *et al.*, Science 323, 919 (2009).
- [2] J. Wells *et al.*, Phys. Rev. Lett. 102, 096802 (2009).
- [3] D. Leuenberger, Ph.D. thesis, University of Zurich (2011).
- [4] L. Perfetti *et al.*, Phys. Rev. Lett. 99, 197001 (2007).
- [5] M. Hase *et al.*, Phys. Rev. Lett., 88 (2002).
- [6] D. Fritz *et al.*, Science, 315 (2007).
- [7] E.D. Murray *et al.*, Phys. Rev. B 75, 184301 (2007).

15 Physics of Biological Systems

Conrad Escher, Hans-Werner Fink, Patrick Helfenstein, Alina Horwege, Tatiana Latychevskaia, Jean-Nicolas Longchamp, Mirna Saliba, Flavio Wicki (since December 2011).

in collaboration with:

Ian Cox, Photek Ltd (Great Britain); Prof. Philippe Dumas, CNRS Strasbourg (France); Eugen Ermantraut, Clondiag Chip Technologies GmbH (Germany); Prof. Bruno Klaholz, University of Strassbourg (France); Prof. John Miao, University of California at Los Angeles (USA); Prof. Jannik C. Meyer, University of Vienna (Austria); Dr. Iлона Müllerová and Dr. Luděk Frank, Institute of Scientific Instruments, Brno (Czech Republic); Dr. Soichiro Tsujino, PSI (Switzerland); Dr. Fabio Lamattina, EMPA Dübendorf (Switzerland); Stephan Fässler, Sinar AG (Switzerland).

The structural investigation of individual biological objects by employing coherent low-energy electrons is the primary goal of our research. It involves in-line holography with low energy electrons, Fourier transform holography as well as coherent diffraction imaging and is assisted by micro-structuring techniques using a focused gallium ion beam device as well as a focused helium ion beam available to us at the at the Swiss Federal Laboratories for materials science and technology (EMPA) in Dübendorf. Our current activities are divided in the following interconnected individual projects:

- **Electron Holography and Coherent Diffraction**

Major experimental challenges are to improve the interference resolution, establish methods for creating free standing thin films of graphene transparent for low-energy electrons as well as appropriate techniques to present a single protein to the coherent electron wave front. Next to these experimental issues, a second, equally important aspect for achieving high resolution structural information is the reconstruction of the electron holograms, respectively iterative phase retrieval, in coherent diffraction. This is achieved by employing newly developed numerical algorithms to solve the integrals governing these coherent optics problems.

- **Lens-less Imaging by Fourier Transform Holography (FTH)**

FTH with low-energy electrons is a high resolution lens-less imaging method based on the

use of an extended reference where a specimen of biological or non-biological nature is non-destructively imaged. The recording is performed by illuminating the specimen and reference object or pinhole with a parallel beam of low-energy electrons. The result of the interference between the wave scattered by the specimen and the reference wave results in an intensity distribution, or holographic diffraction pattern, whose Fourier transform represents the autocorrelation of the transmission function of the specimen under study.

- **Electron and Ion Point Sources**

Field Ion Microscopy and related techniques are employed for fabricating and applying novel electron and ion point sources. In collaboration with the PSI, field emitter arrays are characterized and specified for their use as bright electron sources for the X-Ray Free Electron Laser (XFEL) project.

- **DNA and Proteins in the Liquid Phase**

The aim of this project is to directly observe the dynamics of single DNA molecules in liquids by video fluorescent microscopy. In combination with molecular anchoring techniques, adopted from Clondiag Chip Technologies in Jena, we also address the energetics of a single DNA molecule. Appropriate DNA modifications for attaching fluorescent proteins are also designed by and shall serve us in our efforts to obtain structural information about proteins by electron holography and coherent diffraction. Thermal desorption spectroscopy of water from

fluorescent proteins shall help us to judge under what thermal conditions proteins are still in their native state in a vacuum environment.

Most of the protein structural information available today has been obtained from crystallography experiments by means of averaging over many molecules assembled into a crystal. Since biological molecules exhibit different conformations, averaging smears out structural details. That is why a strong desire to gain structural data from just a single molecule is emerging. We are working towards the objective of deriving atomic structure information from experiments carried out on just one individual molecule subject to the interaction with a coherent low-energy electron wave. Meanwhile, it has been thoroughly established that electrons with kinetic energies below 200 eV are the only radiation known today where elastic scattering dominates. Radiation damage-free imaging of a single biological molecule is thus possible by recording holograms and coherent low-energy electron diffraction patterns [1].

Retrieval of the Phase of the Scattered Wave - When Holography Meets Coherent Diffraction

The phase problem is inherent to crystallographic, astronomical and optical imaging where only the intensity of the scattered signal is detected and the phase information is lost and must somehow be recovered to reconstruct the object's structure. Modern imaging techniques at the molecular scale rely on utilizing novel coherent light sources like X-ray free electron lasers for the ultimate goal of visualizing such objects as individual biomolecules rather than crystals [2]. Here, unlike in the case of crystals where structures can be solved by model building and phase refinement, the phase distribution of the wave scattered by an individual molecule must directly be recovered. There are two well-known solutions to the phase problem: holography and coherent diffraction imaging (CDI). Both techniques have their pros and cons. In holography, the reconstruction of the scattered complex-valued

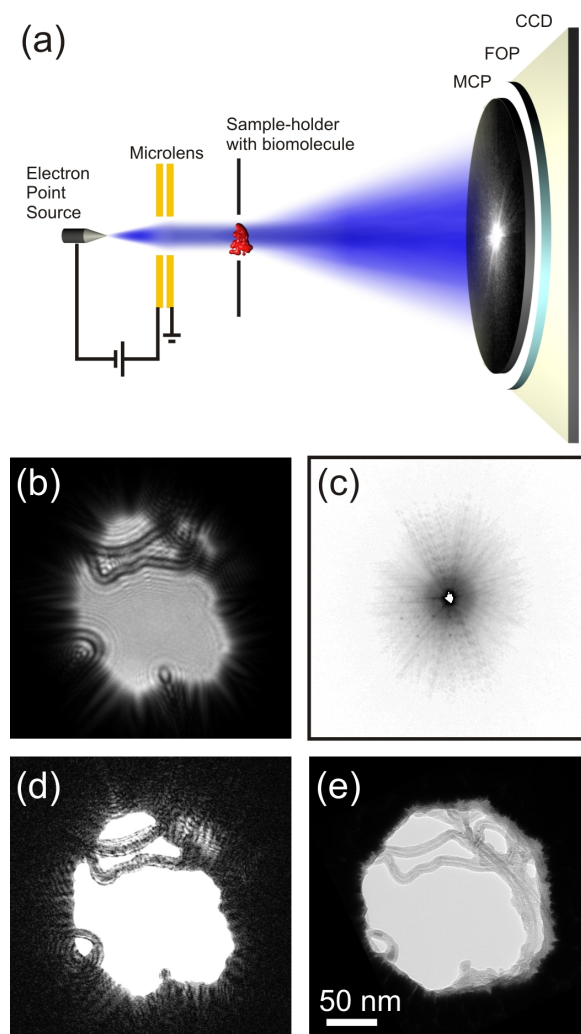


FIG. 15.1 – HCDI reconstructions of a coherent low-energy electron diffraction pattern of individual carbon nanotubes. (a) Schematics of the low-energy electron microscope, the distance between electron source and detector amounts to 68 mm. The detector components are: micro-channel plate (MCP), fiber optical plate (FOP) and CCD chip. (b) Hologram recorded with electrons of 51 eV kinetic energy. (c) Diffraction pattern recorded with electrons of 145 eV kinetic energy. (d) Reconstructed amplitude distribution using HCDI. (e) TEM image recorded with 80 keV electrons. In (b) and (d) the central parts of the images, with 600x600 pixels are shown.

object wave is directly provided by a well-defined reference wave that must cover the entire detector area which often is an experimental challenge. CDI

provides highest possible, only wavelength limited, resolution, but the phase recovery is an iterative process which requires some pre-defined information about the object and whose outcome is not always uniquely-defined. Moreover, the diffraction patterns must be recorded under oversampling conditions, a pre-requisite to be able to solve the phase problem. We have shown how holography and CDI can be merged into one superior technique: holographic coherent diffraction imaging (HCDI). An inline hologram can be recorded by employing a modified CDI experimental scheme. We demonstrated that the amplitude of the Fourier transform of an inline hologram is related to the complex-valued visibility, thus providing information on both, the amplitude and the phase of the scattered wave in the plane of the diffraction pattern. With the phase information available, the condition of oversampling the diffraction patterns becomes obsolete, and the phase problem can be solved in a fast and unambiguous manner. We demonstrated the reconstructions of various diffraction patterns of objects recorded with visible light as well as with low-energy electrons as shown in Fig. 15.1 [3].

Non-destructive Imaging of an Individual Protein

The mode of action of proteins is to a large extent given by their ability to adopt different conformations. This is why imaging single biomolecules at atomic resolution is one of the ultimate goals of biophysics and structural biology. The existing protein database has emerged from X-ray crystallography, NMR or cryo-TEM investigations. However, these tools all require averaging over a large number of proteins and thus over different conformations. This of course results in the loss of structural information. Likewise it has been shown that even the emergent X-FEL technique will not get away without averaging over a large quantity of molecules.

We have recently obtained the first recordings of a protein at sub-nanometer resolution obtained from one individual ferritin by means of low-energy electron holography. One single protein could be im-

aged for an extended period of time without any sign of radiation damage. Since ferritin exhibits an iron core, the holographic reconstructions could also be cross-validated against TEM images of the very same molecule by imaging the iron cluster inside the molecule while the protein shell is decomposed.

The protein of interest needs to be free-standing in space when exposed to the low-energy electron beam. Therefore the protein is attached to a carbon nanotube suspended over a hole. Strictly speaking, arrays of small holes of 240 nm in diameter are milled in a carbon coated silicon nitride membrane by means of a focused gallium ion beam. The nanotube-ferritin complex is kept in aqueous solution of which a droplet is applied onto the holey membrane. Once the droplet has dried out some of the nanotubes remain across holes providing free-

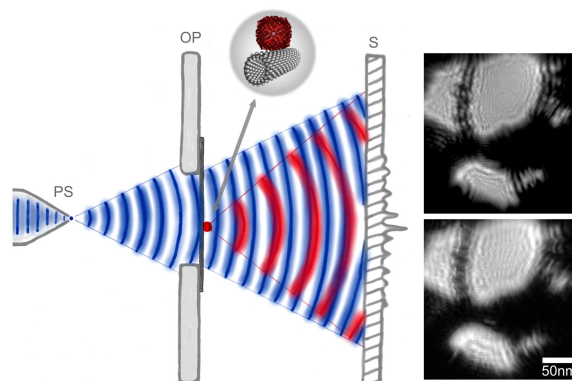


FIG. 15.2 – *Left: Scheme for recording the low-energy electron hologram of a protein. Conduction electrons confined in a pointed $W(111)$ single crystal wire are field emitted into vacuum at an atomic-sized emission area providing a coherent low-energy electron point source (PS). At the less than 1 micron distant object-plane (OP), part of the coherent electron wave is scattered by a ferritin attached to a carbon nanotube constituting the object wave indicated in red. At a distant detector screen (S), the far-field interference pattern between object- (red) and reference-wave (blue) - the hologram - is recorded and its digital record is subject to the numerical reconstruction of the protein. Right: A hologram (top) and its reconstruction (bottom) show individual ferritins attached to a carbon nanotube.*

standing ferritin molecules. These molecules can then be examined in our low-energy electron microscope.

Prior to the described preparation procedure the carbon nanotubes undergo acid treatment in order to form carboxyl groups on the outer wall and hence disperse efficiently in ultra highly purified water. Adding a buffered solution of proteins, the latter eventually bind to the nanotubes by dipole forces, as schematically illustrated in the inset of Fig. 15.2. This preparation does not rely on specific features of ferritin and hence is applicable to a large class of biomolecules [4].

72

Recent Achievements in Coherent Diffraction Microscopy

We have decided to use the damage-free radiation provided by coherent low-energy electrons to realize coherent diffraction imaging of single molecules. The overall setup of our coherent electron diffraction imaging microscope is sketched in Fig. 15.3 (left) together with a recently achieved coherent diffraction pattern of free-standing graphene recorded in the transmission mode with a 8000x6000 pixels CCD chip. A sharp W-tip acts as an electron point source emitting a coherent spherical electron wave with kinetic energies between 50 and 300 eV. A micro-lens placed a few microns away from the electron emitter forms

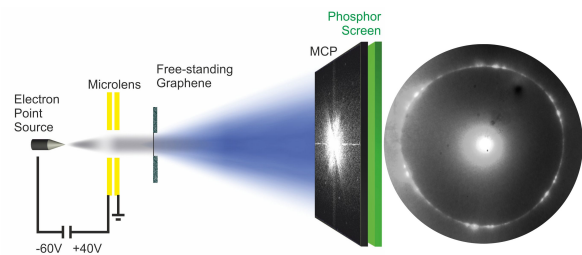


FIG. 15.3 – *Left: Schematic representation of the coherent electron diffraction microscope for imaging individual biomolecules. Right: Coherent diffraction pattern of a free-standing graphene flake mounted on a micro machined holey silicon nitride membrane. With a kinetic energy of 400 eV, the highest order diffraction signal corresponds to a resolution below 2 Å in real space.*

a coherent parallel wave that impinges onto a molecule attached to a micro-structure some distance behind the lens in a field-free region. At a distant detector, the intensity of the diffraction pattern corresponding to the amplitude-square of the Fourier transform of the object is recorded with high spatial resolution. In order to sample this pattern with sufficiently high frequency to match the oversampling requirement, the object must be surrounded by a no-density region.

Lens-less Imaging by Fourier Transform Holography: Nano-Patterning Using the Helium Ion Microscope

The Orion helium ion microscope, see Fig. 15.4, at the EMPA in Dübendorf allows structuring of thin films in the nanometer regime. FTH is a lens-less imaging method based on the use of a reference scatterer [5–8]. If coherent low-energy electrons are used, FTH turns into a high-resolution imaging technique where a specimen of biological or non-biological nature is non-destructively imaged.

The recording is performed by illuminating the specimen and reference scatterer with a parallel beam of electrons whose energy range is 50-200 eV. The interference between the wave scattered by the specimen and the reference wave results in an intensity distribution, or holographic diffraction pattern, whose Fourier transform represents the auto-

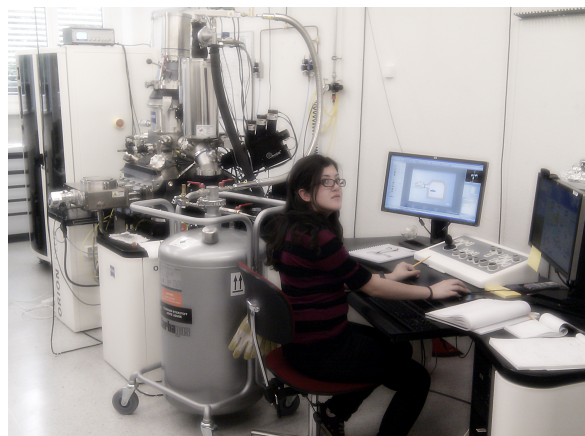


FIG. 15.4 – *Mirna Saliba working on the helium ion microscope at the EMPA in Dübendorf.*

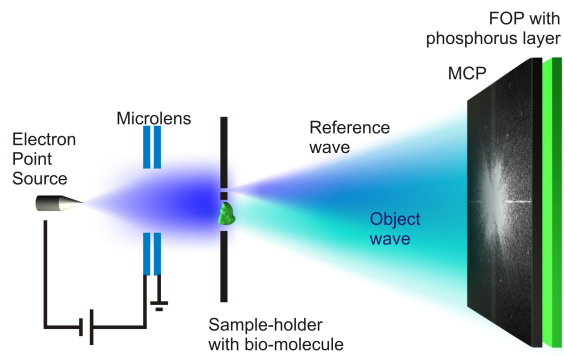


FIG. 15.5 – Schematic of FTH: From left to right: a divergent beam of low-energy electrons impinges on an electrostatic micro-lens which collimates the beam. It is incident on the sample plane that includes a specimen and a pinhole.

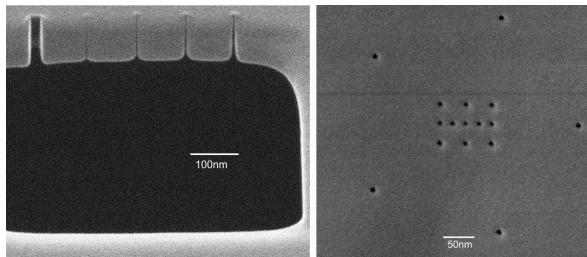


FIG. 15.6 – Left: 1 pixel width lines milled with varying doses across a structure. The line on the far right clearly shows a width below 5 nm. Right: Patterning of a mask suitable for Fourier transform holography: the object to be reconstructed consists of an array of 7 nm holes surrounded by 5 pinholes to serve as reference scatterers.

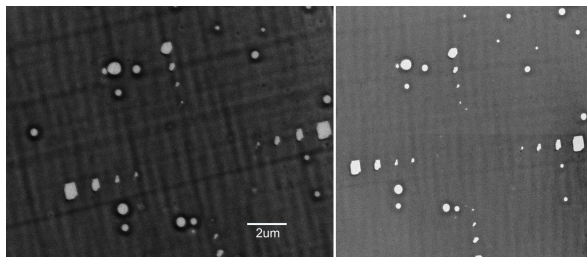


FIG. 15.7 – Left: Helium ion micrograph in transmission mode of several milled holes in a 15 nm thin carbon membrane. Right: Transmission electron micrograph of the same region at 120 kV.

correlation of the transmission function of the specimen under study. FTH (see Fig. 15.5) highlights the most advantageous aspects of both holography and coherent diffraction imaging, i.e. it is a hybrid technique that naturally encrypts the phase information by the use of a reference scatterer and yields high resolution complex-valued images of the specimen of interest in a single computational step.

FTH with low-energy electrons requires the fabrication of pinholes with just 5-20 nm diameter serving as reference scatterers. The latter is achieved by a Helium Ion Microscope (HIM) [9]. Obtaining the minimal pinhole size (5 nm) with the HIM is crucial to push the resolution limit, i.e the smaller the milled pinhole, the higher the resolution of the reconstructed image. So far, nano-patterning has been routinely achievable using the HIM¹¹. The milling has been performed in metal coated silicon nitride substrates as well as in free-standing carbon membranes, as shown in Figs. 15.6 and 15.7

- [1] M. Germann, T. Latychevskaia, C. Escher, and H.-W. Fink, Phys. Rev. Lett. 104, 095501 (2010).
- [2] J. Miao *et al.*, Phys. Rev. B 67 (2003).
- [3] T. Latychevskaia, J. N. Longchamp, and H.-W. Fink, arXiv, 1106.1320 (2011), under review in PRX.
- [4] J.-N. Longchamp, T. Latychevskaia, C. Escher, and H.-W. Fink, arXiv, 1201.4300 (2011), under review in PRL.
- [5] G. W. Stroke *et al.*, J. Opt. Soc. Am. 55, 1327-1328 (1965).
- [6] I. McNulty *et al.*, Science 256, 1009-1012 (1992).
- [7] S. Eisebitt *et al.*, Nature 432, 885-888 (2004).
- [8] M. Guizar-Sicairos, and J. R. Fienup, Opt. Express 15, 17592-17612 (2007).
- [9] M. Ananth *et al.*, Proc. SPIE 8036 (2011).

¹¹We kindly acknowledge the support of Ivan Shorubalko and Fabio Lamattina with the Orion helium ion microscope at the EMPA in Dübendorf

16 Physical Systems Biology and non-equilibrium Soft Matter

C.M. Aegerter, D. Assmann, G. Ghielmetti, U. Nienhaus, M. Schindlberger (Master Student) till 10.11, and T. Schluck

in collaboration with: Institute of Molecular Life Sciences (K. Basler, T. Aegerter-Wilmsen, C. Lehner, S. Luschnig), ETH Zürich (E. Hafen, I. Sbalzarini, P. Koumoutsakos), EPF Lausanne (P. Renaud, D. Floreano), University of Lausanne (S. Bergmann), Biozentrum Basel (M. Affolter), University of Strasbourg (N. Rivier), University of Fribourg (A. Jazwinska), University of Konstanz (G. Maret, W. Bühner, T. Sperling, N. Isert), New York University (C.C. Maass), Deutsches Luft- und Raumfahrtzentrum (M. Sperl), University of Twente (A. Mosk), Université Joseph Fourier Grenoble (S. Skipetrov, F. Graner), Technion Haifa (E. Akkermans).

74

Work in the group of physical systems biology and non-equilibrium soft-matter is concerned with the study of developmental biology using physical techniques and study of light transport in turbid media. This is both in light of fundamental processes as well as applications for imaging in turbid media in particular biological systems. Moreover, the group works on the study of inherent non-equilibrium systems that can be tracked physically, such as driven granular gases. In the last year, we have made considerable progress in several of these areas, two of which are discussed in detail below. These subjects concern the transport of light in turbid media and the transition to Anderson localisation of light and the development of a method for three dimensional microscopy behind extremely turbid layers.

16.1 Localization of light

The quest for the experimental demonstration of Anderson localisation [1] in a three dimensional disordered medium has a very long history [2–7] and clear-cut evidence for that transition has only been shown very recently by our group using time-resolved transmission experiments [8, 9]. The main hindering property of extremely turbid samples is that absorption is always dominating the transport through thick and turbid samples [6, 7]. This can be resolved with time dependent measurements since localisation and absorption have different signatures in the time dependent transmission through a sample. However, a direct study

of the mean square spread of the photon cloud $\langle r^2 \rangle = \sigma^2$ transported through a sample presents a much clearer measure for the transport properties of a sample [10]. For instance, because all photons measured in this way have spent the same amount of time inside the sample, meaning that they are all equally affected by absorption. Thus a determination of the mean square width of the transmitted light is completely independent of absorption and presents a direct measure of the transport mechanism. For turbid samples (all samples discussed here are TiO_2 nanoparticles with diameters in the range of 200 nm), this transport is diffusive, which means that the width σ^2 increases linearly with time for all times [10]. This can be seen in Fig. 16.1, where the time dependence of σ^2 is shown for a diffusive sample with a turbidity of $kl^* = 6.8$. Note that for these samples the absorption length as determined from static transmission measurements is shorter than the sample thickness, but the measured width can exceed the thickness.

The width of the photon distribution is determined using a pulsed laser system and an ultra-fast gated CCD camera. The incoming pulsed laser (pulse duration 100 fs) is focused on the surface of the sample and the transmitted light is imaged onto the CCD camera. The camera is coupled to an image intensifier, with a gate that can be opened on a very short time scale (1 ns). This opening can be scanned with a time resolution of 250 ps. Due to the repetition rate of the laser of 80 MHz, many different laser pulses impinge onto the sample dur-

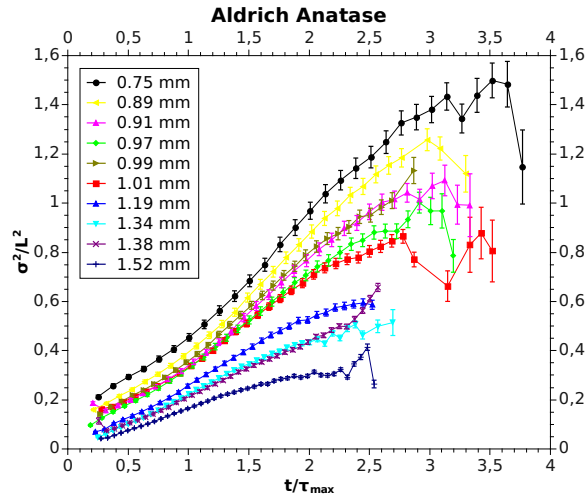


FIG. 16.1 – The mean square width scaled with the sample size $\frac{\sigma^2}{L^2}$ for a diffusive sample with a scattering strength of $kl^* = 6.8$. The time axis is scaled with the diffusion time $\tau_{max} \propto L^2/D$. The width increases linearly over the whole time window, also exceeding the thickness of the sample. This shows that absorption does not play a role in the determination of the width. The slope of the curve corresponds directly to the diffusion coefficient of light in the sample.

ing a measurement of the CCD with a given setting of the opening, such that an image of very fast processes can be taken. Thus we obtain snapshots of the light distribution behind the samples at different times.

This is shown in Fig. 16.2, where also the contours of a Gaussian fit determining the width is shown. In the sample shown, the width increases at early times, but then stays constant. This behaviour is expected for extremely turbid samples, where localisation of light sets in, corresponding to a limiting length scale of the localisation length [10].

This is shown in more detail in the time and thickness dependence of the width of an even more turbid sample (R700) shown in Fig. 16.3. Here again the width as determined from the intensity measurements as described before are shown. Initially, the width increases linearly as expected for a diffusive process. However at later times, the width saturates and remains constant for thick samples. Such behaviour of light in a random medium means

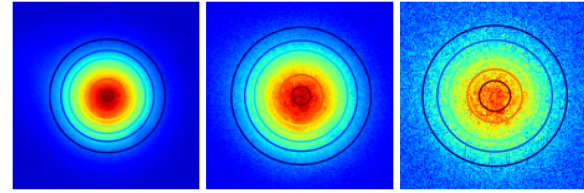


FIG. 16.2 – A section of the raw data (with the fit displayed via contours) of a R104 sample that features a plateau. From left to right the time-stamps are 4, 6 and 8 ns after the initial laser-pulse. From 4 to 6 ns one can see a broadening in the profile width, whereas from 6 to 8 ns no further increase can be seen. This constant profile width is the signature of Anderson localisation.

that the transport of light by diffusion has been limited to the corresponding length scale. This localisation length can only be observed for extremely turbid samples with $kl^* \simeq 1$ [11], in three dimensional media [12]. In this case, light traveling on closed loops interferes with itself, leading to a breakdown of transport on scales bigger than

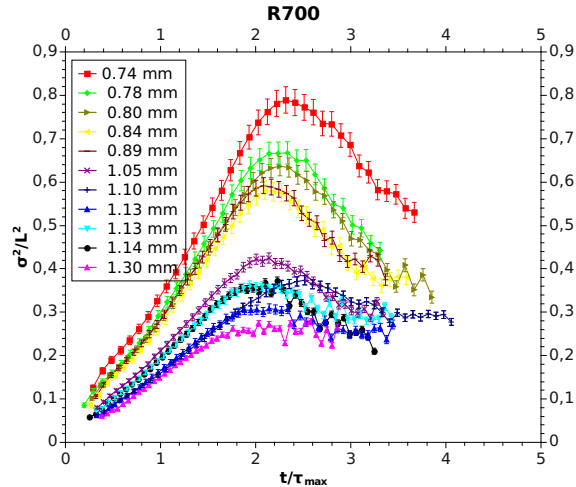


FIG. 16.3 – The mean square width scaled with the sample size $\frac{\sigma^2}{L^2}$ for the sample with the highest turbidity $kl^* = 2.7$, R700. For this sample, the spread of the photon cloud comes to a halt at a length scale corresponding to the localisation length. This plateau can be clearly seen in the samples with the biggest thickness. When the sample thickness becomes comparable to the localization length, additional effects come into play which lead to an effective reduction of the width as a function of time.

these loops. In Fig. 16.3, one can also observe that for thinner samples, the width can even decrease with time, which is not expected. This can, however, be understood in a statistical picture of localisation, where a range of localisation lengths corresponding to differently sized loops exist. For thin samples, only the smaller loops can be populated at long times leading to a decrease of the average width.

The samples shown in Fig. 16.3 all had the same turbidity and thus the same localisation length. However, as the critical turbidity for the transition to localisation is approached, the localisation length diverges and localisation can no longer be observed when the localisation length becomes comparable to the sample thickness [12, 13]. A way of studying the turbidity dependence of the localisation length is via a change in the wavelength of the incoming light in one and the same sample. Due to a change in scattering cross-section with wavelength, different turbidities are obtained for different wavelengths. The turbidities are determined using coherent backscattering [14, 15]. Such a dependence of the width with incoming wavelength is shown in Fig. 16.4 for a sample as in Fig. 16.3 with a thickness of $L = 0.98\text{mm}$. As the wavelength increases, so does kl^* and we move gradually to the transition to diffusive behaviour. At the highest value of $kl^* = 3.5$, the width does no longer saturate completely, but rather shows a sub-diffusive increase.

This can be observed more clearly in the case of a sample with higher kl^* , ranging from $kl^* = 5$ to 6, as shown in Fig. 16.5. Here at the highest value of kl^* , a linear increase is observed indicating diffusive behaviour, but at lower values of kl^* a slower increase in σ^2 is seen. This corresponds to the mobility edge of the transition, where the transport can still take place however is slowed down due to interference effects. Theory predicts a re-scaling of the diffusivity inversely proportional to the thickness, which is in good agreement with the observed time dependence of the increase of σ^2 [16, 17]. This behaviour has already been observed studying the time dependence of the width of ultra-sound transported through turbid media [18].

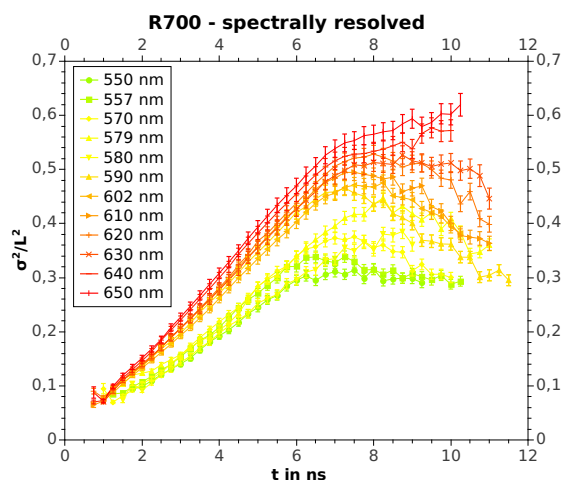


FIG. 16.4 – Spectral measurement of a R700 sample in the range 550 – 650 nm. At larger wavelength the turbidity kl^* increases and localising effects get stronger as can be seen via the lower mean square width σ_∞^2 of the plateaus. For wavelengths above 650 nm one observes starting of a breakdown of localisation to a sub-diffusive behaviour.

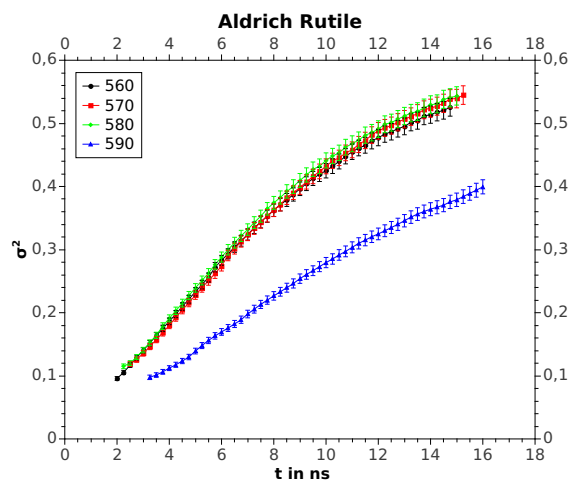


FIG. 16.5 – The spectral measurement of a sample which is diffusive at a wavelength of 590 nm. With decreasing wavelength λ the turbidity kl^* increases, leading to the establishment of sub-diffusive behaviour. However, the width keeps increasing with time indicating that strong localisation of light has not yet been reached for the corresponding turbidities down to $kl^* = 5.4$. However, these data clearly indicate the presence of the mobility edge, where the diffusion coefficient scales inversely with the sample thickness.

16.2 Three dimensional microscopy in turbid media

- [1] P.W. Anderson, Phys. Rev. **109**, 5 (1958).
- [2] Y. Kuga and A. Ishimaru, J. Opt. Soc. Am. A **1**, 831 (1984).
- [3] M.P. van Albada, and A. Lagendijk, Phys. Rev. Lett. **55**, 2696 (1985).
- [4] P.E. Wolf, and G. Maret, Phys. Rev. Lett. **55**, 2696 (1985).
- [5] J.M. Drake and A.Z. Genack, Phys. Rev. Lett. **63**, 259 (1989).
- [6] D.S. Wiersma, P. Bartolini, A. Lagendijk, *et al.*, Nature **390**, 671 (1997).
- [7] F. Scheffold, R. Lenke, R. Tweer, *et al.*, Nature **398**, 206 (1999).
- [8] M. Störzer, P. Gross, C.M. Aegerter and G. Maret, Phys. Rev. Lett. **96**, 063904 (2006).
- [9] C.M. Aegerter M. Störzer, and G. Maret, Europhys. Lett. **75**, 562 (2006).
- [10] N. Cherroret, S.E. Skipetrov and B.A. van Tiggelen, Phys. Rev. E **82**, 056603 (2010).
- [11] A.F. Ioffe and A.R. Regel, Progress in Semiconductors **4**, 237 (1960).
- [12] E. Abrahams *et al.*, Phys. Rev. Lett. **42**, 673 (1979).
- [13] R. Berkovits and M. Kaveh, J. Phys. C: Cond. Mat. **2**, 307 (1990).
- [14] P. Gross, M. Störzer, S. Fiebig, M. Clausen, G. Maret, and C. M. Aegerter, Rev. Sci. Instrum. **78**, 033105 (2007).
- [15] S. Fiebig, C.M. Aegerter, W. Bührer, M. Störzer, E. Akkermans, G. Montambaux and G. Maret, EPL **81**, 64004 (2008).
- [16] D. Vollhardt and P. Wölfle, Phys. Rev. B **22**, 4666(1980).
- [17] S.E. Skipetrov and B.A. van Tiggelen, Phys. Rev. Lett. **96**, 043902 (2006).
- [18] H. Hu, A. Strybulevych, J.H. Page, S.E. Skipetrov and B.A. van Tiggelen, Nature Phys. **4**, 945 (2008).

Apart from studies into the fundamental aspects of light transport in turbid media, we are also applying our know-how in this field to create applications in the realm of imaging in turbid media. The main difficulty to image structures in living systems lies in the fact that many tissues are turbid, such that no focus can be formed and thus no image plane can be detected.

Using wave-front shaping, we have invented a technique to overcome this and be able to obtain scanning fluorescence images at optical resolution behind turbid layers that are completely intransparent [1]. This was already described in a previous annual report and rests on principles of wave-front shaping to create a focus [2] and the memory effect [3–5]. The same principle has been used subsequently to obtain optical resolution images behind turbid layers where the focus is created via phase conjugation of the outgoing light [6]. We have now expanded the technique to be able to obtain three dimensional fluorescence images behind similarly turbid screens [7]. To understand the principles of this we quickly review the basics of the memory effect and how this is used to scan a focus.

The memory effect leads to a retention of correlation of the phase over an angular scale determined by the thickness of the turbid medium. This is because the light transport through the turbid medium is confined to a cone with a width corresponding to the thickness of the medium. This is for a point illumination. When considering different channels through the turbid medium as illuminated by different point sources, then a change of the incoming phase remains correlated within this cone. Thus, phase changes of the order of $qL \simeq 1$ remain conserved, where $q = \theta k$ is the overall scattering vector with $k = 2\pi/\lambda$ and L is the thickness of the layer [3–5]. In the application for a scanning microscope, the angle θ corresponds to the angle covering the field of view of the microscope. For the experiments presented here with a layer of thickness $L = 15\mu\text{m}$ and a wavelength of $\lambda = 488\text{nm}$, this angle is $\theta \simeq 5 \cdot 10^{-3}$.

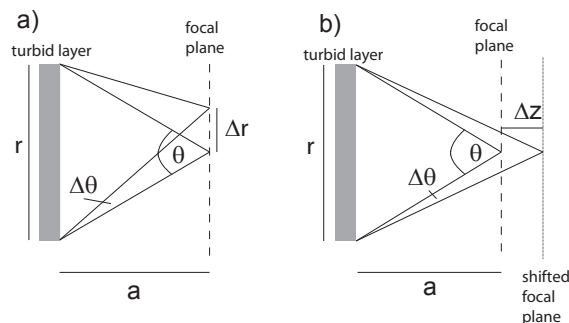


FIG. 16.6 – Geometry of scanning in the different directions. The change in angle is limited by the memory effect. a) shows the situation for two-dimensional scanning in the $x-y$ plane. The change in angle here is given by $\Delta\theta = \Delta r/a$. In the z -direction in contrast, the change in angle is given by $\Delta\theta = r\Delta z/a^2$.

For two-dimensional scanning in the $x-y$ plane, the angle determines directly the field of view together with the distance from the scattering layer a via $\Delta r = a\Delta\theta$. Thus, for a shift in the focal position, the phase of the incoming light must be changed by an amount corresponding to $\phi = kr \cdot \frac{\Delta r}{a}$. This change in phase is achieved by a tilting of the wave front by the galvo-scanner discussed above. In the geometry of our experiment, the intensity of the focus is halved over a distance of $\Delta r_{max} \simeq 5\mu m$, thus indicating the spatial resolution. For scanning in the z direction, the situation is slightly different, as illustrated in Fig. 16.6. The angle change now not only depends on the distance a , but also on the radial component. The shift in position is now given by $\Delta z = a^2\Delta\theta/r$, where the memory effect still correlates paths within the cone of angle $\theta \simeq 1/(kL)$. Again, this corresponds to a phase change of the incoming light of $\phi = kr^2 \cdot \frac{\Delta z}{a^2}$. This change in phase is obtained by adding a curvature to the incoming light field by adding a parabolic shift to the SLM, where the radius of curvature, R , corresponds to $1/R = \frac{\Delta z}{a^2}$.

Again, for the geometry of the experiment described here, this yields a scanning range of

$\Delta z_{max} \simeq 60\mu m$. Thus, for this geometry, the field of view obtained in the z -direction can be increased with respect to that in the $x-y$ plane. This is true as long as the size of the illumination is smaller than the distance of the structure of interest from the scattering layer. However, this difference also leads to an anisotropy in the size of the focal spot. In the z -direction, the focal spot will be larger by a factor of a/r as compared to the $x-y$ direction. This is because of the difference in path lengths in the different directions causing the interference based focus. With the geometry described above, we expect a resolution in the $x-y$ plane given by half the wavelength of the light used, i.e. 250 nm and a resolution in the z -direction of $3\mu m$.

Fig. 16.7 shows a sequence of cuts through a fluorescent bead hidden behind a screen with a thickness of more than 10 mean free paths. Such a screen is completely intransparent and conventional imaging is impossible. Each cut shown in the figure is obtained by scanning the $x-y$ plane using a tilting of the incoming wave-front. The different cuts are made by adding a parabolic phase field to the SLM, leading to a shift of the focus in the z direction. The distance between successive cuts is $2\mu m$ for all images except between parts d,e and f, which are centered about the middle of the particle and are spaced by $1\mu m$. As can be seen from the different intensities of the article, the focus scans through the whole structure, but the resolution is worse than in the $x-y$ plane as discussed above. A determination of the width of the point-spread function in the z -direction gives a resolution of $3.0(1)\mu m$ in good agreement with the expectation. The scan range is illustrated in Fig. 16.8, where two fluorescent beads are positioned $55\mu m$ apart, both within the plane of observation. The figure shows three cuts through the plane at different depths of $0, 30$ and $55\mu m$. At a distance corresponding to the scan range in the z -direction, the quality of the focus deteriorates, such that the image quality is similarly worsened. However, as seen in Fig. 16.8c, we still observe the position of the second bead.

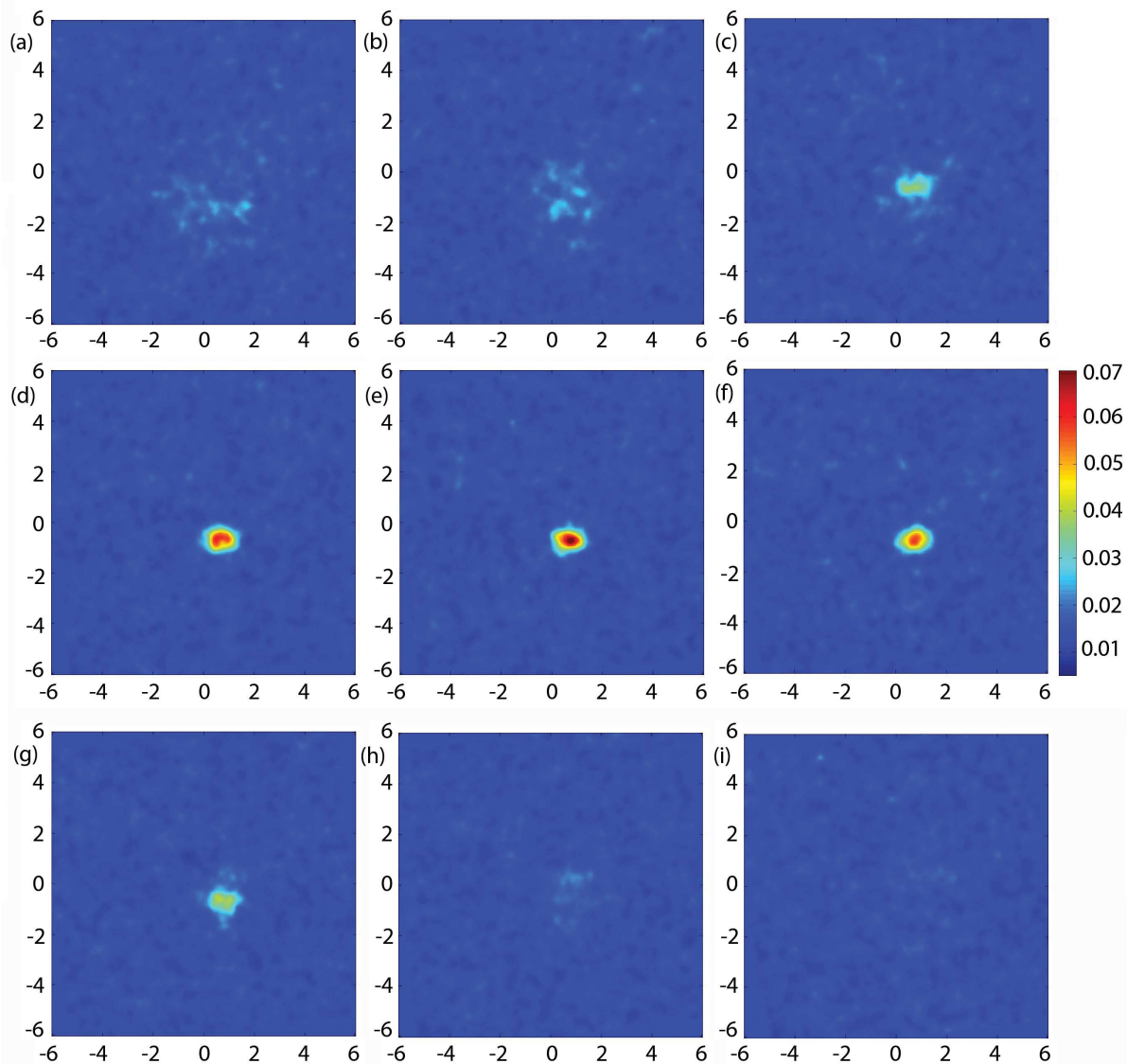
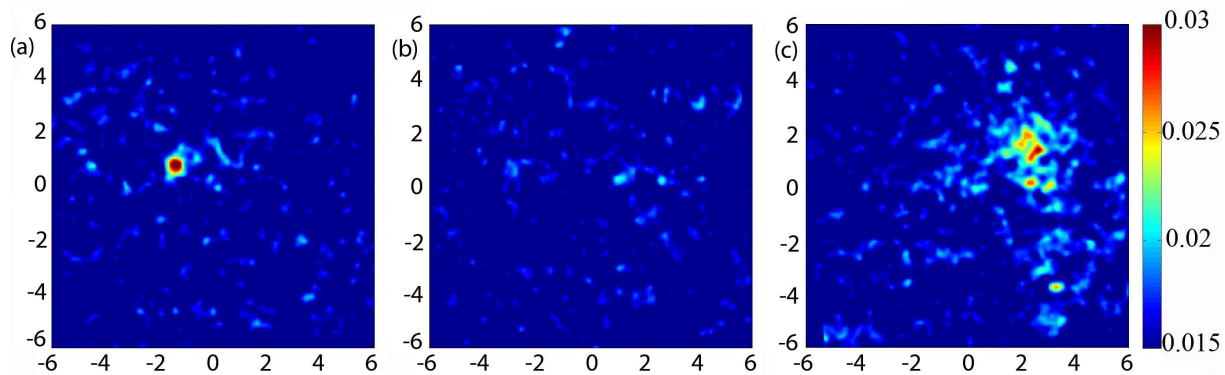


FIG. 16.7 – The fluorescence signal of a single 450 nm diameter fluorescent bead hidden behind a turbid layer. The images show the scattered light fluorescence image of the same bead and on the same intensity scale, while the position of the focal plane differs between the images.

In (a), the position is at $-7 \mu\text{m}$, behind the bead and consecutively moves forward in steps of $2 \mu\text{m}$, until it lies $7 \mu\text{m}$ in front of the bead position in image (i). The center of the bead, which would therefore lie between image (d) and its subsequent image has been added as well in part (e). Thus, the difference in z position between parts (d) and (e) as well as (e) and (f) corresponds to only $1 \mu\text{m}$. The $x - y$ scan range in this case is $12 \times 12 \mu\text{m}^2$.



80

FIG. 16.8 – The fluorescence signal of two 450 nm diameter fluorescent beads hidden behind an intrasparant turbid layer. The two beads are spaced 55 μm apart in the z -direction and are at positions $(-2, -1)$ and $(2, -2)$ respectively in the (x, y) plane. The images show the scattered light fluorescence image on the same intensity scale, at three different depth.

In (a), the position is centered at the first bead, whereas at (b) the position is 30 μm towards the second particle. Figure (c) finally is at a z position of 55 μm corresponding to the position of the second particle. The scan range in this case is a window in the $x - y$ plane of $12 \times 12 \mu\text{m}^2$. As discussed in the text, the z scan-range is 60 μm explaining the deteriorating quality of the image of the second particle. However, the three dimensional structure of the beads' positioning can be clearly seen.

- [1] I. M. Vellekoop and C.M. Aegerter, Opt. Lett. **35**, 1245 (2010).
- [2] I. M. Vellekoop and A. P. Mosk, Opt. Lett. **32**, 2309 (2007).
- [3] D.L. Fried, J. Opt. Soc. Am. **72**, 52 (1982).
- [4] S. Feng, C. Kane, P.A. Lee, and A.D. Stone, Phys. Rev. Lett. **61**, 834 (1988).
- [5] I. Freund, M. Rosenbluh, and S. Feng, Phys. Rev. Lett. **61**, 2328 (1988).
- [6] C. L. Hsieh, Y. Pu, R. Grange, G. Laporte, and D. Psaltis, Opt. Express **18**, 20723-20731 (2010).
- [7] G. Ghielmetti and C.M. Aegerter, Opt. Express **20**, 3744 (2012).

17 Mechanical Workshop

K. Bösiger, B. Lussi, R. Maier, M. Schaffner, S. Scherr, D. Dürst (apprentice), D. Gabrielli (apprentice since August 2011) and T. Naterop (until July 2011)

Besides many projects carried out for research groups, both at our institute and at other institutes of the university, the examinations of the apprentices and the installation of a new turning center draw our attention in this reporting period. We further extended the service provided by the central metal and technical material store maintained by our staff¹². Over thirty institutes and local high schools were supplied with materials and technical support. The large number of attendants at the information meeting organized by us in November 2011, shows that this service is highly appreciated. The income generated by the production of components for outside companies was used for the continuing education of the apprentices and the workshop staff and helped to finance new workshop equipment and the extension of the central store.

In December 2011 a new computer controlled turning center (see Fig. 17.1) was installed. The ma-

chine features two high power spindles with a rotation rate of up to 5500 rpm. The fully integrated y-axis and the turret driving up to sixteen tools, either in radial or axial direction, in combination with an automatic bar loading magazine enables the automated series production of complex parts. SolidWorks 3D design software more and more used by our research groups noticeably improved the accuracy and reliability of the technical drawings.

During four weeks we conducted the basic workshop courses for bachelor students. There were six courses, each with a 35 hours work load. We also directly supported a number of bachelor- and master-theses. In October 2011 we organized two welding courses for physics laboratory assistant apprentices from the ETH. For those interested in a grade as polytechnician we again provided two one-week trial apprenticeships.

81



FIG. 17.1 – Left: new twin turret-turning center with bar loading system. Right: the turret for up to 16 tools and the right spindle.

¹²For a catalogue see <http://www.physik.uzh.ch/groups/werkstatt/>

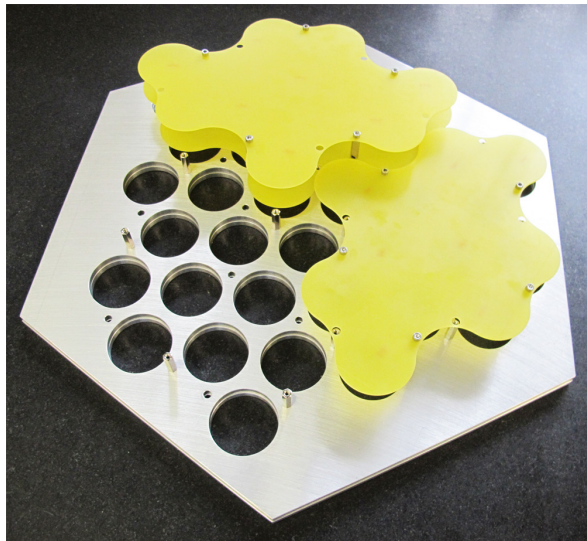


FIG. 17.2 – CTA FlashCam prototype structures.



FIG. 17.3 – Borazon cooler device.

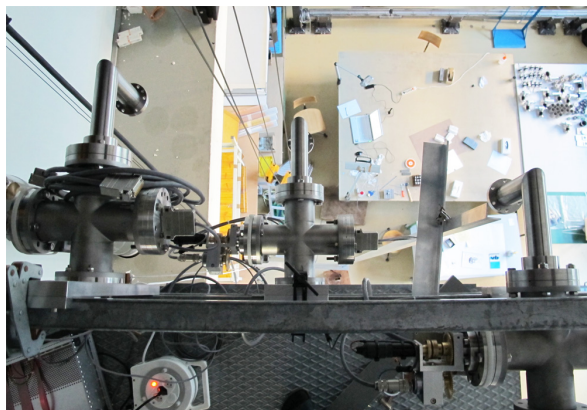


FIG. 17.4 – The GERDA calibration system being tested in the assembly hall.

Below we mention a selection of our activities:

- **CTA Cherenkov Telescope Array (Sec. 6)**

Several test setups were manufactured. We produced a prototype structure for the CTA FlashCam project and modified parts for the Active Mirror Control (AMC) actuators (Fig. 17.2).

- **Surface Physics (Sec. 14)**

We manufactured a custom-built borazon cooler device (Fig. 17.3). Different series of components made out of molybdenum and stainless steel were fabricated.

- **Neutrinoless double betadecay (Sec. 3)**

For the GERDA experiment we designed and manufactured the mechanics of the calibration system. The three complete systems were thoroughly tested in the assembly hall of the workshop (Fig. 17.4) before transportation to the Gran Sasso Underground Laboratory (LNGS). In autumn 2011 we started with the assembly of a freon liquefaction plant.

- **Superconductivity and Magnetism (Sec. 12)**

A very ambitious task was the design and construction of a rotating sample holder with special coils (Fig. 17.5). The device runs inside a low temperature cryostat and the orientation of the probe is computer controlled with very high precision. The requirements for all parts including the gear wheels were very strict. We again produced evaporation masks and high-pressure containers made out of high-tensile materials.

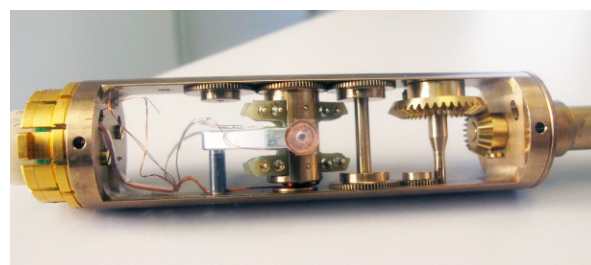


FIG. 17.5 – Probe holder with the precision gear for the sample rotation and the special coil.

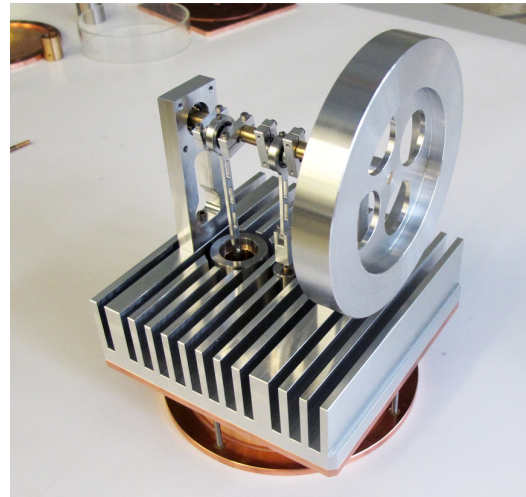
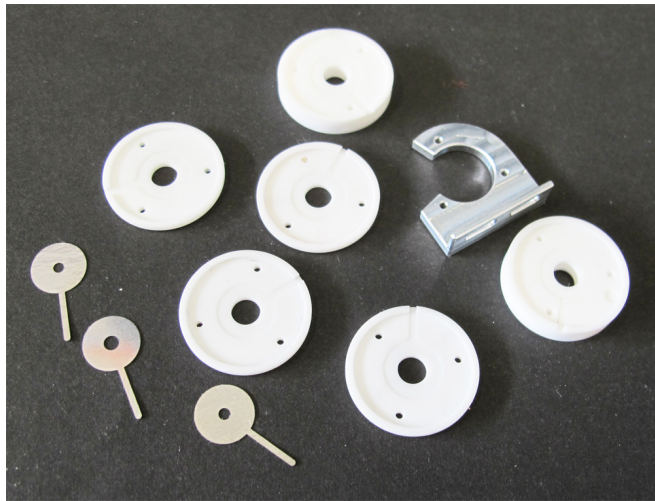


FIG. 17.6 – Left: special working parts made for the low energy electron point source (LEEPS). Right: gamma-type Stirling engine made by an apprentice in his final examination.

- **Physics on the nanometer scale (Sec. 15)**

The special vapour deposition device with six coating stations had to be modified and the water cooling system was improved. We manufactured tiny custom-built high voltage connectors using ceramic and plastic materials which have to work under vacuum. All necessary parts for a low energy electron point source were manufactured (Fig. 17.6 left).

- **Continuing education of the workshop staff**

The workshop staff attended CAD software courses introducing the Catia Tools *Kinematics* and *3DVIA Composer* and the basics of *SolidWorks*. We took welding training courses and went to seminars on new tooling and state of the art machinery techniques and in relation with the education of the apprentices to the regular meetings. Tutorials in programming and operating of the new turning center were organized.

- **Education of the apprentices**

The final and intermediate examinations of the apprentices in May and June 2011 were carried out with great success. In his final work the candidate manufactured all the parts for a Stirling engine (Fig. 17.6 right). In August 2011 a new apprentice started his education. Besides the mandatory Swissmechanic courses the apprentices attended again advanced courses in

computer controlled machine (CNC) programming, pneumatics and electronics.

In this reporting period the demand from other institutes of the university on our laser cutting system has grown notably. This modern machine could be fully exploited:

- **Museum of zoology**

A series of 250 custom-built headphones.



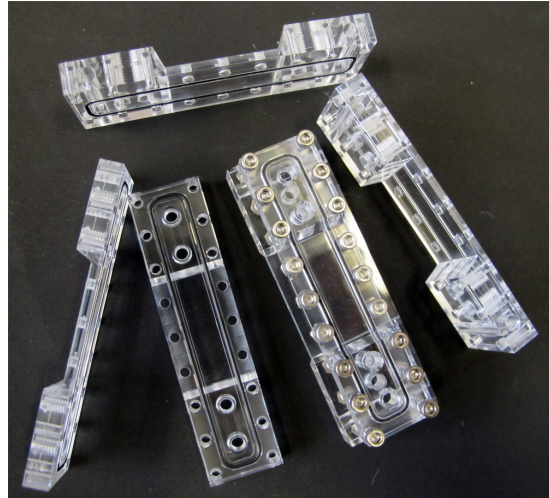
- **Department of geography**

Two special metallic channels for measuring the volumetric flow rate of melt water.

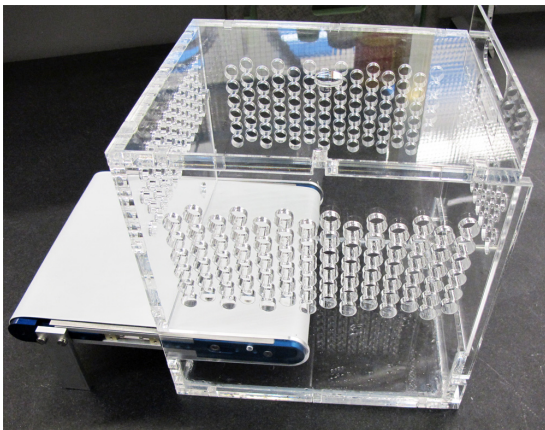


- **Institute of virology**
Small series of parts which are Javel water resistant

- **Institute of physiology**
Dedicated membrane holders made out of plexi-glass.

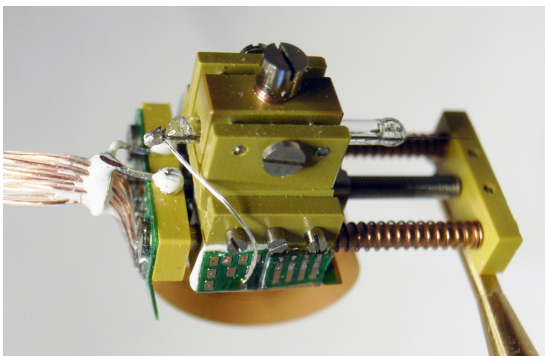


- **Institute of neuroinformatics**
A special plastic box with an integrated conveyor band used to study the behavior of oscine



- **Outside company**
A high performance LED lamp

birds and a miniaturized piezodrive with sensor holder. Note that the diameter of the screws is only 0.8 mm!



18 Electronics Workshop

D. Florin, P. Soland, and A. Vollhardt

In addition to the routine service and support work for the research groups of the institute the electronics workshop also performed some maintenance tasks for the LHCb experiment at CERN during the extended period of beam interrupt. Various setups and devices for the laboratories and demonstration experiments for the undergraduate lectures were improved. For example a battery supported power supply was developed for a sensitive weight comparator used in a measurement of the gravitational constant.

Below we list some of our more interesting projects and activities.

- Phase Transitions, Materials and Applications (Sec. 13)

For the probing of samples inside the helium cryostat, a small printed circuit board based on a low-loss ceramic substrate has been designed and assembled (see Fig. 18.1).

We developed and manufactured a device used to build a thermo-electric oscillator (see Fig. 18.2). The unit allows the measurement of the specific heat of samples with a novel method. The instrument consists essentially of an inductance (gyrator) and an amplifier. To allow high flexibility many of the settings can be adjusted with switches and potentiometers.

- Superconductivity and Magnetism (Sec. 12)

For a rotating sample holder inside the cryostat, the electronic boards (base plate and sample board, see Fig. 18.4) were designed and mounted in collaboration with the mechanical workshop.

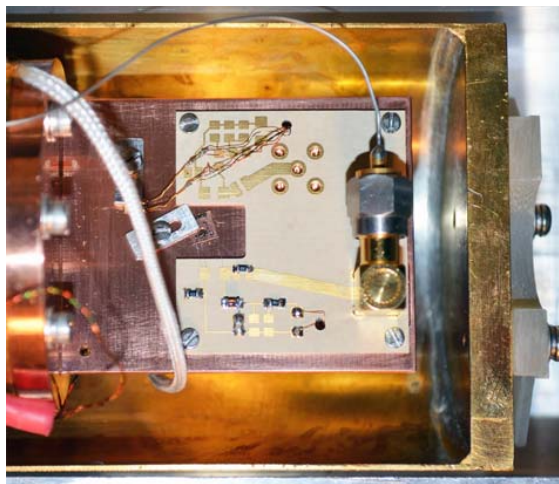


FIG. 18.1 – Sample holder with low-loss ceramic substrate printed circuit board.



FIG. 18.2 – Thermo electronic oscillator device.



FIG. 18.3 – Electronics of the thermo electronic oscillator.

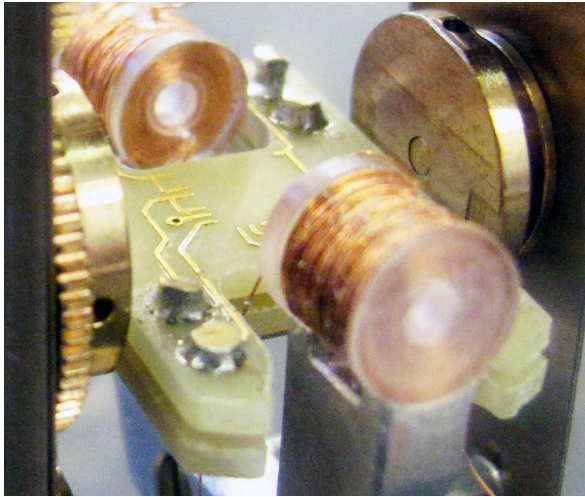


FIG. 18.4 – Sample board installed on the sample holder.

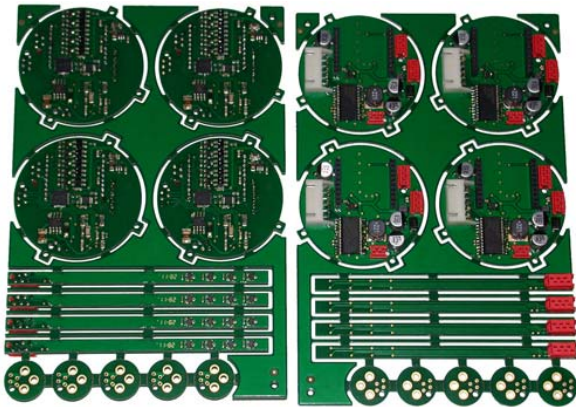


FIG. 18.5 – Active mirror control printed circuit boards.

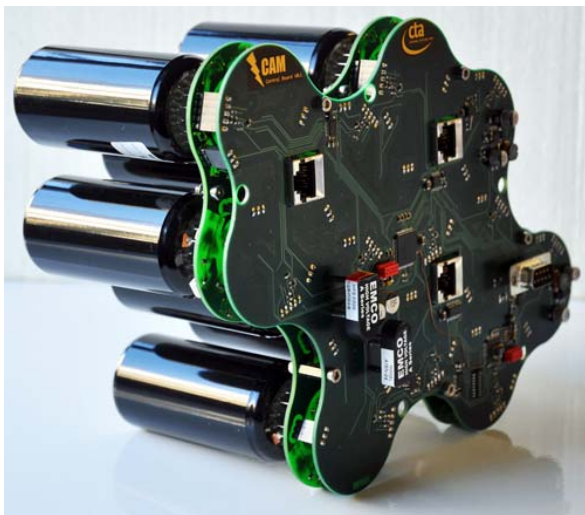


FIG. 18.6 – Complete FlashCam module.

- Electronics for the Cherenkov Telescope Array (CTA) experiment (Sec. 6)

The controllers for the Active Mirror Control (AMC) actuators (see Fig. 18.5) have been exchanged and a bootloader software was implemented allowing the complete firmware to be uploaded remotely via the wireless interface.

For the FlashCam project a 12-channel photomultiplier readout board has been designed (see Fig. 18.6). Special features are the low-power design which includes the PMT bias supply and the on-board preamplifier which prepares the PMT signals for transmission over three differential CAT-6 cables. Individual control of the bias voltage of all 12 channels as well as voltage and current monitoring is done via a commercial fault-tolerant CAN-bus.

For the FlashCam photomultipliers a compact DC/DC power supply with +5 V input voltage and adjustable (-500 V / -1500 V) high voltage outputs was developed. To minimize the influence of higher order parasitic signals the transformation is based on Royer converters.

- Neutrinoless double beta decay (Sec. 3)

For the precise positioning of the calibration sources in the GERDA experiment we produced a motor control system (hard- and software, see Figs. 18.7 through 18.10). The unit houses three identical blocks allowing the independent vertical positioning of three different radioactive sources. A DC-motor coupled to a planetary gear set moves the source container fixed to a perforated stainless steel band with a velocity of 10 mm/s and a precision of about 1 mm over the full range of 7 m.

For the position determination of the source two independent sensors are used to make the system redundant. Optical incremental encoders measure the position using the perforation of the steel band. The upper end position is determined by a micro end switch which also defines the absolute reference position. The second system consists of a multi-turn magnetic absolute encoder which is fixed to the axis of the planetary gear. The motor controller logic evaluates the signals of the end switches and the

position encoders and performs different consistency tests.

The controller can be connected to a computer through an RS-232/422 interface allowing computer controlled operation. Alternatively the front panel of the control unit can be used for local operation. LCD displays indicate the actual source positions as well as status and error messages.

In connection with other astroparticle physics experiments we also designed a printed circuit board using surface mounted devices which serves as a universal photomultiplier base.



FIG. 18.7 – Motor control unit (front view).

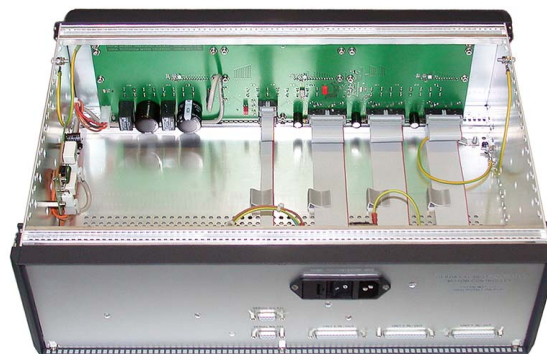


FIG. 18.8 – Motor control unit (inside view).

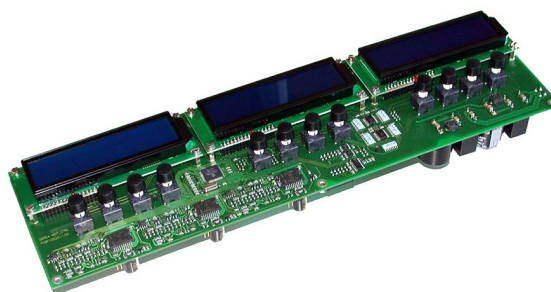


FIG. 18.9 – Main printed circuit board of the motor control system.

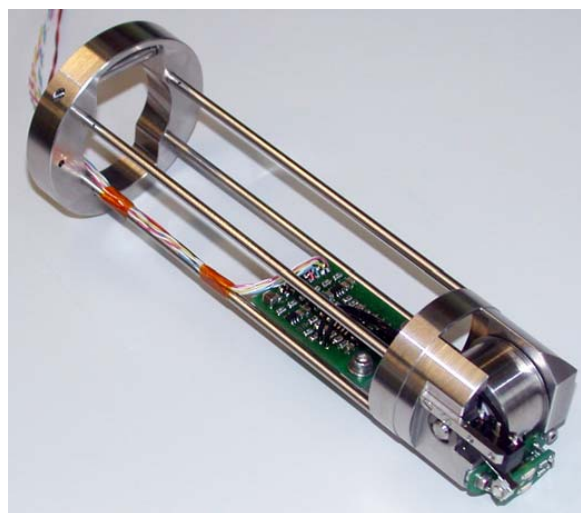


FIG. 18.10 – Deviation roller with incremental encoder, end switch and control electronics.

19 Publications

19.1 Elementary particles and their interactions

19.1.1 Dark Matter

Articles in press

- **Search for WIMPs in liquid argon**
C. Amsler, Proceedings of the WIN \tilde{O} 11 Conference, Cape Town (2011), arXiv.org/abs/1105.4524.
- **Study of nuclear recoils in liquid argon with monoenergetic neutrons**
C. Regenfus, Y. Allkofer, C. Amsler, W. Creus, A. Ferella, J. Rochet, M. Walter, Journal of Physics: Conference Series, arXiv:1203.0849v1

88

Lecture

- C. Regenfus: Study of nuclear recoils in liquid argon
12th Int. Conf. on Topics in Astroparticle and Underground Physics (TAUP 2011), Munich, Germany, 8 September 2011.

19.1.2 ATHENA, AEGIS

Articles

- **Towards the production of an ultra cold antihydrogen beam with the AEGIS apparatus**
J. W. Storey, Hyperfine Interact, DOI 10.1007/s10751-011-0401-x.
- **The AEGIS experiment at CERN, measuring the free fall of antihydrogen**
A. Kellerbauer *et al.* (AEGIS Collaboration), Hyperfine Interact, DOI 10.1007/s10751-012-0583-x.
- **Off-axial plasma displacement suitable for antihydrogen production in AEGIS experiment**
C. Canali *et al.* (AEGIS Collaboration), Eur. Phys. J. **D 65** (2011) 499.

Lectures

- J. Storey: Towards the production of an ultra cold antihydrogen beam with the AEGIS apparatus
10th international conference on Low Energy Antiproton Physics (LEAP 11), Vancouver, Canada, 29 April 2011.
- J. Storey: AEGIS : Measuring the fall of antihydrogen (with a detour through antihydrogen physics
Laboratoire Leprince-Ringuet, Palaiseau, France, 16 May 2011.

19.1.3 CDMS

Articles

- **Combined Limits on WIMPs from the CDMS and EDELWEISS Experiments**
Z. Ahmed *et al.* (CDMS, EDELWEISS Collaborations), Phys. Rev. D 84, 011102(R) (2011).

Lectures

- S. Arrenberg: Search for Inelastic Dark Matter with the CDMS experiment
SPS Meeting 2011, Lausanne, June 16th, 2011.

PhD thesis

- **Searching for Dark Matter with the Cryogenic Dark Matter Search Experiment**
S. Arrenberg, PhD Thesis, Physik-Institut, Universität Zürich, 2011.

89

19.1.4 GERDA

Articles

- **Production and characterization of a custom-made ^{228}Th source with reduced neutron source strength for the Borexino experiment**
Maneschg, L. Baudis, R. Dressler, K. Eberhardt, R. Eichler, H. Keller, R. Lackner, B. Praast, R. Santorelli, J. Schreiner, M. Tarka, B. Wiegel, A. Zimbal, Nucl. Instr. and Meth. A 54372, (2011).

Lecture

- F. Froberg: The GERDA Experiment - A Search for Neutrinoless Double Beta Decay
TeVPA 2011, Stockholm, Sweden, August 5th, 2011.

19.1.5 XENON

Articles

- **Limits on the release of Rb isotopes from a zeolite based 83m-Kr calibration source for the XENON project**
V. Hannen, E. Aprile, F. Arneodo, L. Baudis, M. Beck, K. Bokeloh, A.D. Ferella, K. Giboni, R.F. Lang, O. Lebeda, H.-W. Ortjohann, M. Schumann, A. Spalek, D. Venos, C. Weinheimer, JINST 6 P10013 (2011).
- **The XENON100 Dark Matter Experiment**
E. Aprile *et al.* (XENON100 Collaboration), Astropart.Phys. 35 (2012) 573-590.

PUBLICATIONS

- **Implications on Inelastic Dark Matter from 100 Live Days of XENON100 Data**
E. Aprile *et al.* (XENON100 Collaboration), Phys. Rev. D 84, 061101 (2011).
- **Search for light dark matter in XENON10 data**
J. Angle *et al.* (XENON10 Collaboration), Phys. Rev. Lett. 107, 051301 (2011).
- **Dark Matter Results from 100 Live Days of XENON100 Data**
E. Aprile *et al.* (XENON100 Collaboration), Phys. Rev. Lett. 107, 131302 (2011).
- **Material screening and selection for XENON100**
E. Aprile *et al.* (XENON100 Collaboration), Astropart. Phys. 35:43-49, 2011.
- **Characterization of the Quartz Photon Intensifying Detector (QUPID) for use in Noble Liquid Detectors**
A. Teymourian, D. Aharoni, L. Baudis, P. Beltrame, E. Brown, D. Cline, A.D. Ferella, A. Fukasawa, C.W. Lam, T. Lim, K. Lung, Y. Meng, S. Muramatsu, E. Pantic, M. Suyama, H. Wang, K. Arisaka, Nucl. Instr. and Meth. A 654 (2011), 184-195.
- **Gator: a low-background counting facility at the Gran Sasso Underground Laboratory**
L. Baudis, A.D. Ferella, A. Askin, J. Angle, E. Aprile, T. Bruch, A.Kish, M. Laubenstein, A. Manalaysay, T. Marrodan Undagoitia, M. Schumann, JINST 6 P08010, 2011.
- **Likelihood Approach to the First Dark Matter Results from XENON100**
E. Aprile *et al.* (XENON100 Collaboration), Phys. Rev. D 84, 052003 (2011).

Lectures

- L. Baudis: Direct detection of particle dark matter: where do we stand, where are we going?
Physics Colloquium Oxford University, January 27, 2012.
- L. Baudis: Dark matter: new results from direct detection
Physics Colloquium Bethe Forum, Bonn University, November 19, 2011.
- L. Baudis: Direct searches for dark matter in the Milky Way
TU Darmstadt, November 4, 2011.
- L. Baudis: Dark matter: new results from direct detection
PANIC, MIT, July 25, 2011.
- L. Baudis: Dark Matter: New Results from Direct Detection
Origin of Mass 2011, CP3-Origins, Ondense, May 13, 2011.
- L. Baudis: Recent results on direct WIMP searches: the XENON100 experiment
University of California, Irvine, May 4, 2011.
- L. Baudis: XENON100: new results
APS meeting Anaheim, May 2, 2011.
- L. Baudis: Dark matter: new results from direct detection
IceCube Inauguration Workshop, University of Wisconsin, Madison, April 29, 2011.
- L. Baudis: Recent results on direct WIMP searches: the XENON100 experiment
University of Chicago, April 27, 2011.

- M. Schumann: Direct Dark Matter Search with Noble Liquids
Rencontres de Moriond 2012, Cosmology Session, La Thuile, Italy, March 14th, 2012.
- M. Schumann: XENON
Bethe Forum 2011, Bonn, Germany, November 15th, 2011.
- A. Manalaysay: Measurements of the low-energy response of liquid xenon
TAUP 2011, Munich, Germany, September 8th, 2011.
- M. Schumann: XENON and DARWIN
CHIPP Meeting 2011, Leysin, Switzerland, September 1st, 2011.
- M. Schumann: Results of XENON100
TeVPA 2011, Stockholm, Sweden, August 3rd, 2011.
- T. Marrodan Undagoitia: Direct Dark Mater Detection and the XENON100 experiment
MPI, Heidelberg, August 1st, 2011.
- T. Marrodan Undagoitia: Mini-review Direct Dark Mater Detection and recent XENON100 results
EPS-HEP 2011, Grenoble, France, July 21st, 2011.
- A. Manalaysay: Probing light WIMPs with liquid xenon
7th PATRAS workshop on axions, WIMPs and WISPs, Mykonos, June 30th, 2011.
- M. Schumann: New Results from the XENON100 Dark Matter Experiment
SPS Meeting 2011, Lausanne, June 18th, 2011
- A. Behrens: Poster: Tests of PMTs for Future Dark Matter Detectors
SPS Meeting 2011, Lausanne, June 16th - 18th, 2011.
- M. Schumann: New Results from the XENON100 Dark Matter Experiment
Physikalisches Institut Universität Heidelberg, June 6th, 2011.
- T. Marrodan Undagoitia: The XENON100 experiment: results from 100d data
Bonn, May 16th, 2011.
- A. Kish: Cosmogenics backgrounds in the XENON100 experiment
CAB workshop by DUSEL, Berkeley LBNL, April 15th, 2011.

91

PhD thesis

- **Dark Matter Search with the XENON100 Experiment**
A. Kish, PhD Thesis, Physik-Institut, Universität Zürich, 2011

Master thesis

- **Kalibrierung von Flüssig-Xenon-Detektoren zur Suche nach dunkler Materie im Universum**
C. Geis, Physik-Institut, Universität Zürich, 2011.

PUBLICATIONS

19.1.6 DARWIN

Lectures

- L. Baudis: DARWIN: dark matter WIMP search with noble liquids
DM 2012, Marina del Rey, February 24, 2012. Physics Colloquium TU Darmstadt, November 4, 2011.
- L. Baudis: DARWIN: dark matter WIMP search with noble liquids
TAUP, Munich, September 8, 2011.
- M. Schumann: DARWIN
7th PATRAS workshop on axions, WIMPs and WISPs, Mykonos, July 1st, 2011.

92

19.1.7 CTA

Articles

- **Design concepts for the Cherenkov Telescope Array CTA: An advanced facility for ground-based high-energy gamma-ray astronomy**
M. Actis *et al.* (CTA Collaboration), *Exper.Astron.* 32 (2011) 193-316.
- **Solid light concentrators for small-sized photosensores used in Cherenkov telescopes**
B. Huber *et al.*, *Proc. 32nd ICRC*, Beijing, China, 2011.

19.1.8 DIRAC

Articles

- **Determination of $\pi\pi$ scattering lengths from measurement of the $\pi\pi$ atom lifetime**
B. Adeva *et al.* (DIRAC Collaboration), *Phys. Lett. B* 704 (2011) 24.

19.1.9 H1

Articles

- **Measurement of the Azimuthal Correlation between the most Forward Jet and the Scattered Positron in Deep-Inelastic Scattering at HERA**
H1 Collaboration, F. D. Aaron *et al.*, *Eur. Phys. J. C* 72 (2012) 1910.
- **Search for lepton flavour violation at HERA**
H1 Collaboration, F. D. Aaron *et al.*, *Phys. Lett. B* 701 (2011) 10.
- **Measurement of Photon Production in the Very Forward Direction in Deep-Inelastic Scattering at HERA**
H1 Collaboration, F. D. Aaron *et al.*, *Eur. Phys. J. C* 71 (2011) 1771.

- **Measurement of $D^{*\pm}$ Meson Production and Determination of $F_2^{c\bar{c}}$ at low Q^2 in Deep-Inelastic Scattering at HERA**
H1 Collaboration, F. D. Aaron *et al.*, Eur. Phys. J. C **71** (2011) 1769.
- **Measurement of the Inclusive $e^\pm p$ Scattering Cross Section at High Inelasticity y and of the Structure Function F_L**
H1 Collaboration, F. D. Aaron *et al.*, Eur. Phys. J. C **71** (2011) 1579.
- **Search for contact interactions in $e^\pm p$ collisions at HERA**
H1 Collaboration, F. D. Aaron *et al.*, Phys. Lett. B **705** (2011) 52.
- **Measurement of the diffractive longitudinal structure function F_L^D at HERA**
H1 Collaboration, F. D. Aaron *et al.*, Eur. Phys. J. C **71** (2011) 1836.
- **Search for first generation leptoquarks in $e^\pm p$ collisions at HERA**
H1 Collaboration, F. D. Aaron *et al.*, Phys. Lett. B **704** (2011) 388.

93

Articles in press

- **Inclusive Measurement of Diffractive Deep-Inelastic Scattering at HERA**
H1 Collaboration, F. D. Aaron *et al.*, Eur. Phys. J. C, arXiv:1203.4495 [hep-ex].
- **Measurement of Dijet Production in Diffractive Deep-Inelastic Scattering with a Leading Proton at HERA**
H1 Collaboration, F. D. Aaron *et al.*, Eur. Phys. J. C, arXiv:1111.0584 [hep-ex].

19.1.10 LHCb

Articles

- **Measurement of b-hadron masses**
LHCb-Collaboration, R. Aaij *et al.*, Phys. Lett. B **708** (2012) 241.
- **Observation of $B_s \rightarrow J/\psi f_2'(1525)$ in $J/\psi K^+ K^-$ final states**
LHCb-Collaboration, R. Aaij *et al.*, Phys. Rev. Lett. **151801** (2012).
- **Measurement of the $B_s^0 - \bar{B}_s^0$ oscillation frequency Δm_s in $B_s^0 \rightarrow D_s^-(3)\pi$ decays**
LHCb-Collaboration, R. Aaij *et al.*, Phys. Lett. B **709** (2012) 177.
- **Measurement of the CP-violating phase ϕ_s in the decay $B_s \rightarrow J/\psi\phi$**
LHCb-Collaboration, R. Aaij *et al.*, Phys. Rev. Lett. **108** (2012) 101803.
- **Measurement of the CP violating phase ϕ_s in $\bar{B}_s^0 \rightarrow J/\psi f_0(980)$**
LHCb-Collaboration, R. Aaij *et al.*, Phys. Lett. B **707** (2012) 49.
- **Search for the rare decays $B_s \rightarrow \mu^+ \mu^-$ and $B^0 \rightarrow \mu^+ \mu^-$**
LHCb-Collaboration, R. Aaij *et al.*, Phys. Lett. B **708** (2012) 55.
- **Evidence for CP violation in time-integrated $D^0 \rightarrow h^- h^+$ decay rates**
LHCb-Collaboration, R. Aaij *et al.*, Phys. Rev. Lett. **108** (2012) 111602.

PUBLICATIONS

94

- **First observation of the decay $B_s^0 \rightarrow K^{*0} \bar{K}^{*0}$**
LHCb-Collaboration, R. Aaij *et al.*, Phys. Lett. B **709** (2012) 50.
- **Measurement of b hadron production fractions in 7 TeV pp collisions**
LHCb-Collaboration, R. Aaij *et al.*, Phys. Rev. D **85** (2012) 032008.
- **Measurement of the effective $B_s^0 \rightarrow K^+ K^-$ lifetime**
LHCb-Collaboration, R. Aaij *et al.*, Phys. Lett. B **707** (2012) 349.
- **Search for CP violation in $D^+ \rightarrow K^- K^+ \pi^+$ decays**
LHCb-Collaboration, R. Aaij *et al.*, Phys. Rev. D **84** (2011) 112008.
- **First observation of the decay $\bar{B}_s^0 \rightarrow D^0 K^{*0}$ and a measurement of the ratio of branching fractions $\mathcal{B}(\bar{B}_s^0 \rightarrow D^0 K^{*0})/\mathcal{B}(\bar{B}^0 \rightarrow D^0 \rho^0)$**
LHCb-Collaboration, R. Aaij *et al.*, Phys. Lett. B **706** (2011) 32.
- **Absolute luminosity measurements with the LHCb detector at the LHC**
LHCb-Collaboration, R. Aaij *et al.*, JINST **7** (2012) P01010.
- **Search for the lepton number violating decays $B^+ \rightarrow \pi^- \mu^+ \mu^+$ and $B^+ \rightarrow K^- \mu^+ \mu^+$**
LHCb-Collaboration, R. Aaij *et al.*, Phys. Rev. Lett. **108** (2012) 101601.
- **Measurements of the Branching fractions for $B_s \rightarrow D_s \pi \pi \pi$ and $\Lambda_b^0 \rightarrow \Lambda_c^+ \pi \pi \pi$**
LHCb-Collaboration, R. Aaij *et al.*, Phys. Rev. D **84** (2011) 092001, [Erratum-ibid. D **85** (2012) 039904].
- **Observation of J/ψ pair production in pp collisions at $\sqrt{s} = 7$ TeV**
LHCb-Collaboration, R. Aaij *et al.*, Phys. Lett. B **707** (2012) 52.
- **Measurement of the inclusive ϕ cross-section in pp collisions at $\sqrt{s} = 7$ TeV**
LHCb-Collaboration, R. Aaij *et al.*, Phys. Lett. B **703** (2011) 267.
- **Measurement of V^0 production ratios in pp collisions at $\sqrt{s} = 0.9$ and 7 TeV**
LHCb-Collaboration, R. Aaij *et al.*, JHEP **1108** (2011) 034.
- **Determination of f_s/f_d for 7 TeV pp collisions and a measurement of the branching fraction of the decay $B_d \rightarrow D^- K^+$**
LHCb-Collaboration, R. Aaij *et al.*, Phys. Rev. Lett. **107** (2011) 211801.
- **Search for the rare decays $B_s \rightarrow \mu \mu$ and $B_d \rightarrow \mu \mu$**
LHCb-Collaboration, R. Aaij *et al.*, Phys. Lett. B **699** (2011) 330.
- **Measurement of J/ψ production in pp collisions at $\sqrt{s} = 7$ TeV**
LHCb-Collaboration, R. Aaij *et al.*, Eur. Phys. J. C **71** (2011) 1645.

Articles in press

- **Measurement of the polarization amplitudes and triple product asymmetries in the $B_s^0 \rightarrow \phi \phi$ decay**
LHCb-Collaboration, R. Aaij *et al.*, Phys. Lett. B, arXiv:1204.2813 [hep-ex]
- **Inclusive W and Z production in the forward region at $\sqrt{s} = 7$ TeV**
LHCb-Collaboration, R. Aaij *et al.*, JHEP, arXiv:1204.1620 [hep-ex]

- **Measurement of the ratio of prompt χ_c to J/ψ production in pp collisions at $\sqrt{s} = 7$ TeV**
LHCb-Collaboration, R. Aaij *et al.*, Journal of High Energy Physics, arXiv:1204.1462
- **Measurement of $\psi(2S)$ meson production in pp collisions at $\sqrt{s} = 7$ TeV**
LHCb-Collaboration, R. Aaij *et al.*, Eur. Phys. Jour. C, arXiv:1204.1258 [hep-ex]
- **Measurements of the branching fractions of the decays $B_s^0 \rightarrow D_s^\mp K^\pm$ and $B_s^0 \rightarrow D_s^- \pi^+$**
LHCb-Collaboration, R. Aaij *et al.*, JHEP, arXiv:1204.1237 [hep-ex]
- **First observation of the decay B_c^+ to $J/\psi \pi^+ \pi^- \pi^+$**
LHCb-Collaboration, R. Aaij *et al.*, Physics Review Letters, arXiv:1204.0079 [hep-ex]
- **Strong constraints on the rare decays $B_s \rightarrow \mu^+ \mu^-$ and $B^0 \rightarrow \mu^+ \mu^-$**
LHCb-Collaboration, R. Aaij *et al.*, PRL, arXiv:1203.4493 [hep-ex]
- **Observation of CP violation in B^+ to DK^+ decays**
LHCb-Collaboration, R. Aaij *et al.*, Physics Letters B, arXiv:1203.3662 [hep-ex]
- **Differential branching fraction and angular analysis of the decay $B^0 \rightarrow K^{*0} \pi^+$**
LHCb-Collaboration, R. Aaij *et al.*, PRL, arXiv:1112.3515v2 [hep-ex]
- **Measurements of the branching fractions and CP asymmetries of B^+ to $J/\psi \pi^+$ and B^+ to $\psi(2S) \pi^+$ decays**
LHCb-Collaboration, R. Aaij *et al.*, Phys Rev X, arXiv:1203.3592 [hep-ex]
- **Measurement of Υ production in pp collisions at $\sqrt{s} = 7$ TeV**
LHCb-Collaboration, R. Aaij *et al.*, EPJC, arXiv:1202.6579
- **Measurement of the ratio of branching fractions $\mathcal{B}(B^0 \rightarrow K^{*0} \gamma) / \mathcal{B}(B_s^0 \rightarrow \phi \gamma)$**
LHCb-Collaboration, R. Aaij *et al.*, Physical Review D, arXiv:1202.6267 [hep-ex]
- **Search for the X(4140) state in B^+ to $J/\psi \phi K^+$ decays**
LHCb-Collaboration, R. Aaij *et al.*, Physical Review D Rapid Communications, arXiv:1202.5087 [hep-ex]
- **Opposite-side flavour tagging of B mesons at the LHCb experiment**
LHCb-Collaboration, R. Aaij *et al.*, Eur. Phys. J. C, arXiv:1202.4979 [hep-ex]
- **Measurement of the B^\pm production cross-section in pp collisions at $\sqrt{s} = 7$ TeV**
LHCb-Collaboration, R. Aaij *et al.*, JHEP, arXiv:1202.4812 [hep-ex]
- **Determination of the sign of the decay width difference in the B_s system**
LHCb-Collaboration, R. Aaij *et al.*, Physical Review Letters, arXiv:1202.4717 [hep-ex]
- **Measurement of the cross-section ratio $\sigma(\chi_{c2}) / \sigma(\chi_{c1})$ for prompt χ_c production at $\sqrt{s} = 7$ TeV**
LHCb-Collaboration, R. Aaij *et al.*, Phys. Lett. B, arXiv:1202.1080 [hep-ex]
- **Searches for Majorana neutrinos in B^- decays**
LHCb-Collaboration, R. Aaij *et al.*, Physics Review D, arXiv:1201.5600 [hep-ex]
- **First observation of the decays $\bar{B}^0 \rightarrow D^+ K^- \pi^+ \pi^-$ and $B^- \rightarrow D^0 K^- \pi^+ \pi^-$**
LHCb-Collaboration, R. Aaij *et al.*, Physical Review Letters, arXiv:1201.4402 [hep-ex]
- **Observation of X(3872) production in pp collisions at $\sqrt{s} = 7$ TeV**
LHCb-Collaboration, R. Aaij *et al.*, Eur. Phys. J. C, arXiv:1112.5310 [hep-ex]

PUBLICATIONS

- **Measurement of charged particle multiplicities in pp collisions at $\sqrt{s} = 7$ TeV in the forward region**
LHCb-Collaboration, R. Aaij *et al.*, EPJ, arXiv:1112.4592 [hep-ex]
- **Measurement of mixing and CP violation parameters in two-body charm decays**
LHCb-Collaboration, R. Aaij *et al.*, JHEP, arXiv:1112.4698 [hep-ex]

Notes and reports

- **Measurement of the track finding efficiency**
A. Jaeger *et al.*, CERN-LHCb-PUB-2011-025.

96

- **Inclusive Drell-Yan production in the forward region at $\sqrt{s} = 7$ TeV**
LHCb collaboration, LHCb-CONF-2012-013
- **Measurement of the relative Z plus jet cross section**
W. Barter and A. Bursche, LHCb-ANA-2012-006
- **Differential branching fraction and angular analysis of the $B^0 \rightarrow K^{*0} \mu^+ \mu^-$ decay**
LHCb collaboration, LHCb-CONF-2012-008
- **Analysis of $B^0 \rightarrow K^{*0} \mu^+ \mu^-$ at LHCb**
LHCb collaboration, LHCb-CONF-2011-038
- **Search for the rare decays $B_s^0 \rightarrow \mu^+ \mu^-$ with 300 pb^{-1} at LHCb**
LHCb collaboration, LHCb-CONF-2011-037
- **Search for the rare decay $B_s^0 \rightarrow \mu^+ \mu^-$ at the LHC with the CMS and LHCb experiments Combination of LHC results of the search for $B_s^0 \rightarrow \mu^+ \mu^-$ decays**
CMS and LHCb Collaborations, LHCb-CONF-2011-047
- **Updated measurements of W and Z production at $\sqrt{s} = 7$ TeV with the LHCb experiment**
LHCb collaboration, LHCb-CONF-2011-039

Conference contributions

- Michel De Cian: Rare electroweak penguin decays at LHCb
LHCb-Theory Workshop: Implications of LHCb measurements and future prospects, CERN, Switzerland, 16 - 18 Apr 2012.
- Katharina Müller: Electroweak results at LHCb
SM@LHC, Copenhagen, Denmark, 10th-13th April 2012.
- Jonathan Anderson: Inclusive low mass Drell-Yan production in the forward region at $\sqrt{s} = 7$ TeV
XX International Workshop on Deep-Inelastic Scattering and Related Subjects (DIS 2012), Bonn, Virginia, Germany, 11 - 15 Apr 2011.
- Albert Bursche: Jet reconstruction with LHCb
XX International Workshop on Deep-Inelastic Scattering and Related Subjects (DIS 2012), Bonn, Virginia, Germany, 11 - 15 Apr 2011.

- Albert Bursche: Elektroschwache Bosonen im LHCb Experiment
Frühjahrstagung der Deutschen Physikalischen Gesellschaft, Göttingen, Deutschland, 27.2. - 2.3. 2012.
- Ulrich Straumann: The LHCb experiment
50. International Winter Meeting on Nuclear Physics, Bormio (Italy), 23-27 January 2012.
- Ulrich Straumann: The LHCb Experiment: Operation, performance and results
ETH Kolloquium, Zurich, 23. November 2011.
- Nicola Serra: Physics at LHCb
Amsterdam Particle Physics Symposium, Amsterdam, Netherlands, 30 Nov-2 Dec 2011.
- Nicola Serra: LHCb Physics
CHIPP plenary meeting, Leysin, 1st September 2011
- Nicola Serra: Flavour physics results
EPS Summary Workshop CERN, 2nd August 2011
- Jonathan Anderson: W and Z production in the forward region with the LHCb experiment
Meeting of the Division of Particles and Fields of the American Physical Society, Providence, Rhode Island, 9-13 Aug 2011
- Olaf Steinkamp: LHCb physics, performance, prospects
7th Patras Workshop on Axions, WIMPs and WISPs, Mykonos, Greece, 26 Jun-1 Jul 2011.
- Jonathan Anderson: W and Z production in the forward region at LHCb
2nd Workshop on Standard Model Benchmarks at Hadron Colliders, Zeuthen, Germany, 15-17 June 2011.
- Nicola Chiapolini: An inquiry into the nature and distribution of proton partons
Joint annual meeting of the OePG/SPS, Lausanne, 15.-17. June 2011
- Albert Bursche: LHCb also likes the flavour of electroweak bosons (Poster)
Joint annual meeting of the OePG/SPS, Lausanne, 15.-17. June 2011
- Michel De Cian: Peak performance at LHCb
Joint annual meeting of the SPS, OePG/SPS, Lausanne, 15.-17. June 2011
- Christophe Salzmann: Searching for new physics in $B \rightarrow K^* \mu\mu$ at LHCb
Phenomenology 2011 Symposium: The Curtain Rises...for Particle Discoveries, Madison, Wisconsin, 9-11 May 2011

19.1.11 CMS

Articles

- **A new CMS pixel detector for the LHC luminosity upgrade**
C. Favaro, Nucl. Instr. and Meth. **A 658** (2011) 41.
- **Performance of the CMS pixel detector from the first LHC collisions**
S. de Visscher, Nuclear Physics B - Proc. Suppl. **215** (2011) 101.

PUBLICATIONS

- **Measurement of exclusive b -hadron production at 7 TeV with the CMS experiment**
E. Aguiló, PoS (BEAUTY 2011) 003.
- **The Alignment of the CMS Silicon Tracker**
E. Aguiló, Nuclear Physics B - Proc. Suppl. **215** (2011) 104.
- **CMS Detector Performance**
H. Snoek, PoS (BEAUTY 2011) 048.
- **Measurement of tau identification efficiency at CMS**
M. Verzetti, PoS (EPS-HEP2011) 417.
- **Performance of track and vertex reconstruction and b -tagging studies with CMS in pp collisions at $\sqrt{s} = 7$ TeV**
A. Schmidt, PoS (Kruger 2010) 032.

98

From the 85 articles signed by the full CMS Collaboration Zürich contributed directly to:

- **Measurement of the B^+ Production Cross Section in pp Collisions at $\sqrt{s} = 7$ TeV**
CMS Collaboration, Phys. Rev. Lett. **106** (2011) 112001.
- **Search for Neutral MSSM Higgs Bosons Decaying to Tau Pairs in pp Collisions at $\sqrt{s} = 7$ TeV**
CMS Collaboration, Phys. Rev. Lett. **106** (2011) 231801.
- **Measurement of the B^0 Production Cross Section in pp Collisions at $\sqrt{s} = 7$ TeV**
CMS Collaboration, Phys. Rev. Lett. **106** (2011) 252001.
- **Search for $B_s^0 \rightarrow \mu^+ \mu^-$ and $B^0 \rightarrow \mu^+ \mu^-$ decays in pp collisions at $\sqrt{s} = 7$ TeV**
CMS Collaboration, Phys. Rev. Lett. **107** (2011) 191802.
- **Measurement of the B_s^0 Production Cross Section with $B_s^0 \rightarrow J/\psi \phi$ Decays in pp Collisions at $\sqrt{s} = 7$ TeV**
CMS Collaboration, Phys. Rev. **D 84** (2011) 052008.
- **Search for Supersymmetry in pp Collisions at 7 TeV in Events with Jets and Missing Transverse Energy**
CMS Collaboration, Phys. Lett. **B 698** (2011) 196.
- **Inclusive b -hadron production cross section with muons in pp collisions at $\sqrt{s} = 7$ TeV**
CMS Collaboration, J. High Energy Phys. **03** (2011) 090.
- **Measurement of $B\bar{B}$ angular correlations based on secondary vertex reconstruction at $\sqrt{s} = 7$ TeV**
CMS Collaboration, J. High Energy Phys. **03** (2011) 136.
- **J/ψ and $\psi(2S)$ production in pp collisions at $\sqrt{s} = 7$ TeV**
CMS Collaboration, J. High Energy Phys. **02** (2012) 011.
- **Prompt and non-prompt J/ψ production in pp collisions at $\sqrt{s} = 7$ TeV**
CMS Collaboration, Eur. Phys. J. **C 71** (2011) 1575.

and these are the remaining CMS publications:

- **Search for Stopped Gluinos in pp collisions at $\sqrt{s} = 7$ TeV**
CMS Collaboration, Phys. Rev. Lett. **106** (2011) 011801.
- **Measurement of the Isolated Prompt Photon Production Cross Section in pp Collisions at $\sqrt{s} = 7$ TeV**
CMS Collaboration, Phys. Rev. Lett. **106** (2011) 082001.
- **Dijet Azimuthal Decorrelations in pp Collisions at $\sqrt{s} = 7$ TeV**
CMS Collaboration, Phys. Rev. Lett. **106** (2011) 122003.
- **Search for Pair Production of First-Generation Scalar Leptoquarks in pp Collisions at $\sqrt{s} = 7$ TeV**
CMS Collaboration, Phys. Rev. Lett. **106** (2011) 201802.
- **Search for Pair Production of Second-Generation Scalar Leptoquarks in pp Collisions at $\sqrt{s} = 7$ TeV**
CMS Collaboration, Phys. Rev. Lett. **106** (2011) 201803.
- **Measurement of Dijet Angular Distributions and Search for Quark Compositeness in pp Collisions at $\sqrt{s} = 7$ TeV**
CMS Collaboration, Phys. Rev. Lett. **106** (2011) 201804.
- **Search for Supersymmetry in pp Collisions at $\sqrt{s} = 7$ TeV in Events with Two Photons and Missing Transverse Energy**
CMS Collaboration, Phys. Rev. Lett. **106** (2011) 211802.
- **Study of Z boson production in PbPb collisions at $\sqrt{s_{NN}} = 2.76$ TeV**
CMS Collaboration, Phys. Rev. Lett. **106** (2011) 212301.
- **Measurement of the Polarization of W Bosons with Large Transverse Momenta in W +Jets Events at the LHC**
CMS Collaboration, Phys. Rev. Lett. **107** (2011) 021802.
- **Indication of suppression of excited states in PbPb collisions at $\sqrt{s} = 2.76$ TeV**
CMS Collaboration, Phys. Rev. Lett. **107** (2011) 052302.
- **Measurement of the t-channel single top quark production cross section in pp collisions at $\sqrt{s} = 7$ TeV**
CMS Collaboration, Phys. Rev. Lett. **107** (2011) 091802.
- **Search for Three-Jet Resonances in pp Collisions at $\sqrt{s} = 7$ TeV**
CMS Collaboration, Phys. Rev. Lett. **107** (2011) 101801.
- **Measurement of the Inclusive Jet Cross Section in pp Collisions at $\sqrt{s} = 7$ TeV**
CMS Collaboration, Phys. Rev. Lett. **107** (2011) 132001.
- **Search for New Physics with a Mono-Jet and Missing Transverse Energy in pp Collisions at $\sqrt{s} = 7$ TeV**
CMS Collaboration, Phys. Rev. Lett. **107** (2011) 201804.
- **Search for Supersymmetry at the LHC in Events with Jets and Missing Transverse Energy**
CMS Collaboration, Phys. Rev. Lett. **107** (2011) 221804.

PUBLICATIONS

100

- **Search for a Vectorlike Quark with Charge 2/3 in $t + Z$ Events from pp Collisions at $\sqrt{s} = 7$ TeV**
CMS Collaboration, Phys. Rev. Lett. **107** (2011) 271802.
- **Search for signatures of extra dimensions in the diphoton mass spectrum at the Large Hadron Collider**
CMS Collaboration, Phys. Rev. Lett. **108** (2012) 111801.
- **Measurement of the Inclusive Upsilon production cross section in pp collisions at $\sqrt{s} = 7$ TeV**
CMS Collaboration, Phys. Rev. **D 83** (2011) 112004.
- **Observation and studies of jet quenching in PbPb collisions at nucleon-nucleon center-of-mass energy = 2.76 TeV**
CMS Collaboration, Phys. Rev. **C 84** (2011) 024906.
- **Measurement of the Differential Cross Section for Isolated Prompt Photon Production in pp Collisions at 7 TeV**
CMS Collaboration, Phys. Rev. **D 84** (2011) 052011.
- **Measurement of the $t\bar{t}$ Production Cross Section in pp Collisions at 7 TeV in Lepton + Jets Events Using b-quark Jet Identification**
CMS Collaboration, Phys. Rev. **D 84** (2011) 092004.
- **Measurement of the weak mixing angle with the Drell-Yan process in proton-proton collisions at the LHC**
CMS Collaboration, Phys. Rev. **D 84** (2011) 112002.
- **Inclusive search for squarks and gluinos in pp collisions at $\sqrt{s} = 7$ TeV**
CMS Collaboration, Phys. Rev. **D 85** (2012) 012004.
- **Measurement of the Rapidity and Transverse Momentum Distributions of Z Bosons in pp Collisions at $\sqrt{s} = 7$ TeV**
CMS Collaboration, Phys. Rev. **D 85** (2012) 032002 .
- **First Measurement of the Cross Section for Top-Quark Pair Production in Proton-Proton Collisions at $\sqrt{s} = 7$ TeV**
CMS Collaboration, Phys. Lett. **B 695** (2011) 424.
- **Search for Microscopic Black Hole Signatures at the Large Hadron Collider**
CMS Collaboration, Phys. Lett. **B 697** (2011) 434.
- **Search for a heavy gauge boson W' in the final state with an electron and large missing transverse energy in pp collisions at $\sqrt{s} = 7$ TeV**
CMS Collaboration, Phys. Lett. **B 698** (2011) 21.
- **Measurement of W^+W^- Production and Search for the Higgs Boson in pp Collisions at $\sqrt{s} = 7$ TeV**
CMS Collaboration, Phys. Lett. **B 699** (2011) 25.
- **First Measurement of Hadronic Event Shapes in pp Collisions at $\sqrt{s} = 7$ TeV**
CMS Collaboration, Phys. Lett. **B 699** (2011) 48.
- **Measurement of the Tau pairs production cross section in proton-proton collisions at $\sqrt{s} = 7$ TeV**
CMS Collaboration, Phys. Lett. **B 700** (2011) 187.

- **Search for a W' boson decaying to a muon and a neutrino in pp collisions at $\sqrt{s} = 7$ TeV**
CMS Collaboration, Phys. Lett. **B 701** (2011) 160.
- **Search for a Heavy Bottom-like Quark in pp Collisions at $\sqrt{s} = 7$ TeV**
CMS Collaboration, Phys. Lett. **B 701** (2011) 204.
- **Measurement of $W\gamma$ and $Z\gamma$ production in pp collisions at $\sqrt{s} = 7$ TeV**
CMS Collaboration, Phys. Lett. **B 701** (2011) 535.
- **Measurement of the Ratio of the 3-jet to 2-jet Cross Sections in pp Collisions at $\sqrt{s} = 7$ TeV**
CMS Collaboration, Phys. Lett. **B 702** (2011) 336.
- **Search for First Generation Scalar Leptoquarks in the $e^?jj$ Channel in pp Collisions at $\sqrt{s} = 7$ TeV**
CMS Collaboration, Phys. Lett. **B 703** (2011) 246.
- **A search for excited leptons in pp Collisions at $\sqrt{s} = 7$ TeV**
CMS Collaboration, Phys. Lett. **B 704** (2011) 143.
- **Search for Physics Beyond the Standard Model Using Multilepton Signatures in pp Collisions at $\sqrt{s} = 7$ TeV**
CMS Collaboration, Phys. Lett. **B 704** (2011) 411.
- **Measurement of the charge asymmetry in top-quark pair production in proton-proton collisions at $\sqrt{s} = 7$ TeV**
CMS Collaboration, Phys. Lett. **B 709** (2012) 28.
- **Combined results of searches for the standard model Higgs boson in pp collisions at $\sqrt{s} = 7$ TeV**
CMS Collaboration, Phys. Lett. **B 710** (2012) 26.
- **Search for the standard model Higgs boson decaying to W^+W^- in the fully leptonic final state in pp collisions at $\sqrt{s} = 7$ TeV**
CMS Collaboration, Phys. Lett. **B 710** (2012) 91.
- **Search for the standard model Higgs boson decaying to bottom quarks in pp collisions at $\sqrt{s} = 7$ TeV**
CMS Collaboration, Phys. Lett. **B 710** (2012) 284.
- **Measurement of isolated photon production in pp and PbPb collisions at $\sqrt{s_{NN}} = 2.76$ TeV**
CMS Collaboration, Phys. Lett. **B 710** (2012) 256.
- **Charged particle multiplicities in pp interactions at $\sqrt{s} = 0.9, 2.36,$ and 7 TeV**
CMS Collaboration, J. High Energy Physics **01** (2011) 079.
- **Measurements of Inclusive W and Z Cross Sections in pp Collisions at $\sqrt{s} = 7$ TeV**
CMS Collaboration, J. High Energy Physics **01** (2011) 080.
- **Search for Heavy Stable Charged Particles in pp collisions at $\sqrt{s} = 7$ TeV**
CMS Collaboration, J. High Energy Phys. **03** (2011) 024.
- **Measurement of the lepton charge asymmetry in inclusive W production in pp collisions at $\sqrt{s} = 7$ TeV**
CMS Collaboration, J. High Energy Phys. **04** (2011) 050.

PUBLICATIONS

102

- **Measurement of Bose-Einstein Correlations in pp Collisions at $\sqrt{s} = 0.9$ and 7 TeV**
CMS Collaboration, J. High Energy Phys. **05** (2011) 029.
- **Strange Particle Production in pp Collisions at $\sqrt{s} = 0.9$ and 7 TeV**
CMS Collaboration, J. High Energy Phys. **05** (2011) 064.
- **Search for Large Extra Dimensions in the Diphoton Final State at the Large Hadron Collider**
CMS Collaboration, J. High Energy Phys. **05** (2011) 085.
- **Search for Resonances in the Dilepton Mass Distribution in pp Collisions at $\sqrt{s} = 7$ TeV**
CMS Collaboration, J. High Energy Phys. **05** (2011) 093.
- **Search for Physics Beyond the Standard Model in Opposite-sign Dilepton Events in pp Collisions at $\sqrt{s} = 7$ TeV**
CMS Collaboration, J. High Energy Phys. **06** (2011) 026.
- **Search for new physics with same-sign isolated dilepton events with jets and missing transverse energy at the LHC**
CMS Collaboration, J. High Energy Phys. **06** (2011) 077.
- **Search for supersymmetry in events with a lepton, a photon, and large missing transverse energy in pp collisions at $\sqrt{s} = 7$ TeV**
CMS Collaboration, J. High Energy Phys. **06** (2011) 093.
- **Measurement of the $t\bar{t}$ production cross section and the top quark mass in the dilepton channel in pp collisions at $\sqrt{s} = 7$ TeV**
CMS Collaboration, J. High Energy Phys. **07** (2011) 049.
- **Long-range and short-range dihadron angular correlations in central PbPb collisions at $\sqrt{s_{NN}} = 2.76$ TeV**
CMS Collaboration, J. High Energy Phys. **07** (2011) 076.
- **Search for Light Resonances Decaying into Pairs of Muons as a Signal of New Physics**
CMS Collaboration, J. High Energy Phys. **07** (2011) 098.
- **Search for Supersymmetry in Events with b Jets and Missing Transverse Momentum at the LHC**
CMS Collaboration, J. High Energy Phys. **07** (2011) 113.
- **Search for Same-Sign Top-Quark Pair Production at $\sqrt{s} = 7$ TeV and Limits on Flavour Changing Neutral Currents in the Top Sector**
CMS Collaboration, J. High Energy Phys. **08** (2011) 005.
- **Charged particle transverse momentum spectra in pp collisions at $\sqrt{s} = 0.9$ and 7 TeV**
CMS Collaboration, J. High Energy Phys. **08** (2011) 086.
- **Measurement of the Inclusive Z Cross Section via Decays to Tau Pairs in pp Collisions at $\sqrt{s} = 7$ TeV**
CMS Collaboration, J. High Energy Phys. **08** (2011) 117.
- **Dependence on pseudorapidity and on centrality of charged hadron production in PbPb collisions at $\sqrt{s_{NN}} = 2.76$ TeV**
CMS Collaboration, J. High Energy Phys. **08** (2011) 141.

- **Search for New Physics with Jets and Missing Transverse Momentum in pp collisions at $\sqrt{s} = 7$ TeV**
CMS Collaboration, J. High Energy Phys. **08** (2011) 155.
- **Search for supersymmetry in pp collisions at $\sqrt{s} = 7$ TeV in events with single lepton, jets, and missing transverse momentum**
CMS Collaboration, J. High Energy Phys. **08** (2011) 156.
- **Measurement of the Underlying Event Activity at the LHC with $\sqrt{s} = 7$ TeV and Comparison with $\sqrt{s} = 0.9$ TeV**
CMS Collaboration, J. High Energy Phys. **09** (2011) 109.
- **Measurement of the Drell-Yan Cross Section in pp Collisions at $\sqrt{s} = 7$ TeV**
CMS Collaboration, J. High Energy Phys. **10** (2011) 007.
- **Measurement of the Inclusive W and Z Production Cross Sections in pp Collisions at $\sqrt{s} = 7$ TeV with the CMS experiment**
CMS Collaboration, J. High Energy Phys. **10** (2011) 132.
- **Measurement of energy flow at large pseudorapidities in pp collisions at $\sqrt{s} = 0.9$ and 7 TeV**
CMS Collaboration, J. High Energy Phys. **11** (2011) 148 .
- **Jet Production Rates in Association with W and Z Bosons in pp Collisions at $\sqrt{s} = 7$ TeV**
CMS Collaboration, J. High Energy Phys. **01** (2012) 010.
- **Exclusive $\gamma\gamma \rightarrow \mu^+\mu^-$ production in proton-proton collisions at $\sqrt{s} = 7$ TeV**
CMS Collaboration, J. High Energy Phys. **01** (2012) 052 .
- **Measurement of the Production Cross Section for Pairs of Isolated Photons in pp collisions at $\sqrt{s} = 7$ TeV**
CMS Collaboration, J. High Energy Phys. **01** (2012) 133 .
- **Measurement of the $t\bar{t}$ Production Cross Section in pp Collisions at $\sqrt{s} = 7$ TeV using the Kinematic Properties of Events with Leptons and Jets**
CMS Collaboration, Eur. Phys. J. **C 71** (2011) 1721.
- **Forward Energy Flow, Central Charged-Particle Multiplicities, and Pseudorapidity Gaps in W and Z Boson Events from pp Collisions at $\sqrt{s} = 7$ TeV**
CMS Collaboration, Eur. Phys. J. **C 72** (2012) 1839 .
- **Missing transverse energy performance of the CMS detector**
CMS Collaboration, Journal of Instrumentation **6** (2011) P09001 .
- **Determination of Jet Energy Calibration and Transverse Momentum Resolution in CMS**
CMS Collaboration, Journal of Instrumentation **6** (2011) P11002.
- **Performance of τ -lepton reconstruction and identification in CMS**
CMS Collaboration, Journal of Instrumentation **7** (2012) P01001.

PUBLICATIONS

Articles in press

- **Heavy flavor physics with the CMS experiment**
V. Chiochia, Proceedings of the 2011 Hadron Collider Physics symposium, Paris (2011),
arXiv.org/abs/1201.6677.

From 17 articles signed by the full CMS Collaboration Zürich contributed directly to:

- **Search for the standard model Higgs boson in the $H \rightarrow ZZ \rightarrow l^+l^-\tau^+\tau^-$ decay channel in pp collisions at $\sqrt{s} = 7$ TeV**
CMS Collaboration, arXiv:1202.3617.
- **Search for neutral Higgs bosons decaying to tau pairs in pp collisions at $\sqrt{s} = 7$ TeV**
CMS Collaboration, arXiv:1202.4083.
- **Inclusive b-jet production in pp collisions at $\sqrt{s} = 7$ TeV**
CMS Collaboration, arXiv:1202.4617.
- **Measurement of the cross section for production of $pp \rightarrow b\bar{b}X$, decaying to muons in pp collisions at $\sqrt{s} = 7$ TeV**
CMS Collaboration, arXiv:1203.3458.
- **Search for $B_s \rightarrow \mu^+\mu^-$ and $B^0 \rightarrow \mu^+\mu^-$ decays**
CMS Collaboration, arXiv:1203.3976.

and these are the remaining CMS publications in press:

- **Centrality dependence of dihadron correlations and azimuthal anisotropy harmonics in PbPb collisions at $\sqrt{s_{NN}} = 2.76$ TeV**
CMS Collaboration, arXiv:1201.3158.
- **Suppression of non-prompt J/ψ , prompt J/ψ , and $Y(1S)$ in PbPb collisions at $\sqrt{s_{NN}} = 2.76$ TeV**
CMS Collaboration, arXiv:1201.5069.
- **Measurement of the inclusive production cross sections for forward jets and for dijet events with one forward and one central jet in pp collisions at $\sqrt{s} = 7$ TeV**
CMS Collaboration, arXiv:1202.0704.
- **Search for a Higgs boson in the decay channel $H \rightarrow ZZ^{(*)} \rightarrow q\bar{q}l^-l^+$ in pp collisions at $\sqrt{s} = 7$ TeV**
CMS Collaboration, arXiv:1202.1416.
- **Search for the standard model Higgs boson decaying into two photons in pp collisions at $\sqrt{s} = 7$ TeV**
CMS Collaboration, arXiv:1202.1487.
- **Study of high- p_T charged particle suppression in PbPb compared to pp collisions at $\sqrt{s_{NN}} = 2.76$ TeV**
CMS Collaboration, arXiv:1202.2554.
- **Search for the standard model Higgs boson in the $H \rightarrow ZZ \rightarrow 2l2\nu$ channel in pp collisions at $\sqrt{s} = 7$ TeV**
CMS Collaboration, arXiv:1202.3478.

- **Search for large extra dimensions in dimuon and dielectron events in pp collisions at $\sqrt{s} = 7$ TeV**
CMS Collaboration, arXiv:1202.3827.
- **Jet momentum dependence of jet quenching in PbPb collisions at $\sqrt{s_{NN}} = 2.76$ TeV**
CMS Collaboration, arXiv:1202.5022.
- **Search for quark compositeness in dijet angular distributions from pp collisions at $\sqrt{s} = 7$ TeV**
CMS Collaboration, arXiv:1202.5535.
- **Search for microscopic black holes in pp collisions at $\sqrt{s} = 7$ TeV**
CMS Collaboration, arXiv:1202.6396.
- **Search for heavy, top-like quark pair production in the dilepton final state in pp collisions at $\sqrt{s} = 7$ TeV**
CMS Collaboration, CERN-PH-EP-2012-081.

105

Reports

- **Angular correlation between B -hadrons produced in association with a Z -boson in pp collisions at $\sqrt{s} = 7$ TeV**
S. de Visscher, C. Favaro, V. Chiochia, A. Schmidt, C. Amsler, P. Bortignon, C. Grab, A. Rizzi, CMS PAS EWK-11-015.
- **Observation of a new Ξ_b -baryon**
E. Aguiló, CMS PAS BPH-12-001.

Lectures

- E. Aguiló: Measurement of exclusive b -hadron production at 7 TeV with the CMS experiment
13th International Conference on B -Physics at Hadron Machines (Beauty2011), Amsterdam, The Netherlands, 5 April 2011.
- E. Aguiló: Recent results from proton-proton collisions at CMS
Laboratoire de Physique des Hautes Energies, EPFL, Lausanne, Switzerland, 31 October 2011.
- E. Aguiló: Heavy Flavour Production at $E_{cm} = 7$ TeV
Rencontres de Moriond on QCD and High Energy Interactions, La Thuile, Italy, 12 March 2012.
- V. Chiochia: Recent heavy flavor measurements at CMS
Physikalisches Institut, Bonn, Germany, 19 May 2011.
- V. Chiochia: BSM flavour physics signatures from ATLAS and CMS
Workshop on Implications of LHC results for TeV-scale physics, CERN, Geneva, Switzerland, 29 August 2011.
- V. Chiochia: Heavy Flavor physics with the CMS experiment
PH Colloquium, CERN, Geneva, Switzerland, 11 October 2011.
- V. Chiochia: Heavy flavour physics with the CMS experiment
INFN Pisa, Italy, 25 October 2011.

PUBLICATIONS

- V. Chiochia: Heavy flavor physics with the CMS experiment
Hadron Collider Physics Symposium 2011 (HCP 2011), Paris, France, 17 November 2011.
- V. Chiochia: Measurements of b -quark production with the CMS experiment
Workshop on New Physics from Heavy Quarks at Hadron Colliders, University of Washington, Seattle, USA, 7 February 2012.
- C. Favaro: Angular correlation between B -hadrons produced in association with a Z -boson
Student's LHCC poster session, CERN, Geneva, Switzerland, 21 March 2012.
- P. Otyugova: Measurements of B - production with the CMS experiment
Physics at LHC 2011 Conference (PLHC2011), Perugia, Italy, 6 June 2011.
- A. Schmidt: Measurements of inclusive b -quark production with CMS
XIX International Workshop on Deep-Inelastic Scattering and Related Subjects (DIS 2011), Newport News, USA, 11 April 2011.
- H. Snoek: CMS detector performance
13th International Conference on B -Physics at Hadron Machines (Beauty2011), Amsterdam, The Netherlands, 4 April 2011.
- S. de Visscher: Recent heavy flavor results from CMS
Phenomenology Symposium, Univ. Wisconsin at Madison, USA, 9 May 2011.
- M. Verzetti: Search for MSSM Higgs decay into tau pairs with the CMS experiment
Swiss Physical Society, EPFL, Lausanne, Switzerland, 15 June 2011.
- M. Verzetti: Tau identification at CMS
International Europhysics Conference on High Energy Physics (EPS 2011), Grenoble, France, 21 July 2011.

106

19.1.12 Miscellaneous

Contributions to the Review of Particle Physics 2012 (to appear)

- **Scalar mesons below 2 GeV**
C. Amsler, S. Eidelman, T. Gutsche, C. Hanhart, S. Spanier and N.A. Törnqvist
- **The $\eta(1405)$, $\eta(1475)$, $f_1(1420)$, and $f_1(1510)$**
C. Amsler and A. Masoni
- **Quark Model**
C. Amsler, T. DeGrand and B. Krusche

Talks

- L. Baudis: The Universe in 45 Minutes
Helvetia Management Forum, St. Gallen, October 27, 2011.

- P. Truöl: Von der Biologie bis zur Teilchenphysik: Aufschlüsseln der Struktur der Materie mit Elektronenmikroskopen
Helvetia Management Forum, St. Gallen, October 27, 2011.

19.2 Condensed matter

19.2.1 Superconductivity and Magnetism

Articles

- **Identifying the Pairing Mechanism in Fe-As Based Superconductors: Gaps and Isotope Effects**
A. Bussmann-Holder, A. Simon, H. Keller, and A. R. Bishop,
J. Supercond. Nov. Magn. **24**, 1099-1103 (2011).
- **Rearrangement of the antiferromagnetic ordering at high magnetic fields in SmFeAsO and SmFeAsO_{0.9}F_{0.1} single crystals**
S. Weyeneth, P. J. W. Moll, R. Puzniak, K. Ninos, F. F. Balakirev, R. D. McDonald, H. B. Chan, N. D. Zhigadlo, S. Katrych, Z. Bukowski, J. Karpinski, H. Keller, B. Batlogg, and L. Balicas,
Phys. Rev. B **83**, 134503-1-9 (2011).
- **The Meissner effect in a strongly underdoped cuprate above its critical temperature**
E. Morenzoni, B. M. Wojek, A. Suter, T. Prokscha, G. Logvenov, and I. Bozović,
Nature Comm. **2**, 272-1-7 (2011).
- **Two-Dimensional Magnetic and Superconducting Phases in Metal-Insulator La_{2-x}Sr_xCuO₄ Superlattices Measured by Muon-Spin Rotation**
A. Suter, E. Morenzoni, T. Prokscha, B. M. Wojek, H. Luetkens, G. Nieuwenhuys, A. Gozar, G. Logvenov, and I. Bozović,
Phys. Rev. Lett. **106**, 237003-1-4 (2011).
- **Strong coupling between Eu²⁺ spins and Fe₂As₂ layers in EuFe_{1.9}Co_{0.1}As₂ observed with NMR**
Z. Guguchia, J. Roos, A. Shengelaya, S. Katrych, Z. Bukowski, S. Weyeneth, F. Murányi, S. Strässle, A. Maisuradze, J. Karpinski, and H. Keller,
Phys. Rev. B **83**, 144516-1-7 (2011).
- **Diamagnetism, Nernst signal, and finite-size effects in superconductors above the transition temperature T_c**
T. Schneider and S. Weyeneth,
Phys. Rev. B **83**, 144527-1-11 (2011).
- **Oxygen Isotope Effect in Cuprates Results from Polaron-induced Superconductivity**
S. Weyeneth and K. A. Müller,
J. Supercond. Nov. Magn. **24**, 1235-1239 (2011).
- **Lanthanoid-Containing Open Wells Dawson Silicotungstates: Synthesis, Crystal Structures, and Properties**
L. Ni, F. Hussain, B. Spingler, S. Weyeneth, and G. R. Patzke,
Inorg. Chem. **50**, 4944-4955 (2011).

- **Isotope and interband effects in a multi-band model of superconductivity**
A. Bussmann-Holder, H. Keller, R. Khasanov, A. Simon, A. Bianconi, and A. R. Bishop,
New J. Phys. **13**, 093009-1-8 (2011).
- **Observation of a first-order phase transition deep within the vortex-solid region of $\text{YBa}_2\text{Cu}_3\text{O}_7$**
M. Reibelt, S. Weyeneth, A. Erb, and A. Schilling,
Supercond. Sci. Technol. **24**, 105019-1-5 (2011).
- **Magnetic torque study of the temperature-dependent anisotropy parameter in overdoped superconducting single-crystal $\text{YBa}_2\text{Cu}_3\text{O}_7$**
S. Bosma, S. Weyeneth, R. Puzniak, A. Erb, A. Schilling, and H. Keller,
Phys. Rev. B **84**, 024514-1-7 (2011).
- **μSR investigation of magnetism and magnetoelectric coupling in Cu_2OSeO_3**
A. Maisuradze, Z. Guguchia, B. Graneli, H. M. Rønnow, H. Berger, and H. Keller,
Phys. Rev. B **84**, 064433-1-6 (2011).
- **Tuning of competing magnetic and superconducting phase volumes in $\text{LaFeAsO}_{0.945}\text{F}_{0.055}$ by hydrostatic pressure**
R. Khasanov, S. Sanna, G. Prando, Z. Shermadini, M. Bendele, A. Amato, P. Carretta, R. De Renzi, J. Karpinski, S. Katrych, H. Luetkens, and N. D. Zhigadlo
Phys. Rev. B **84**, 100501(R)-1-5 (2011).
- **Muon-spin rotation measurements of the magnetic penetration depth in the iron-based superconductor $\text{Ba}_{1-x}\text{Rb}_x\text{Fe}_2\text{As}_2$**
Z. Guguchia, Z. Shermadini, A. Amato, A. Maisuradze, A. Shengelaya, Z. Bukowski, H. Luetkens, R. Khasanov, J. Karpinski, and H. Keller,
Phys. Rev. B **84**, 094513-1-7 (2011).
- **Anisotropic magnetic order of the Eu sublattice in single crystals of $\text{EuFe}_{2-x}\text{Co}_x\text{As}_2$ ($x = 0, 0.2$) studied by means of magnetization and magnetic torque**
Z. Guguchia, S. Bosma, S. Weyeneth, A. Shengelaya, R. Puzniak, Z. Bukowski, J. Karpinski, and H. Keller,
Phys. Rev. B **84**, 144506-1-11 (2011).
- **Interplay of composition, structure, magnetism, and superconductivity in $\text{SmFeAs}_{1-x}\text{P}_x\text{O}_{1-y}$**
N. D. Zhigadlo, S. Katrych, M. Bendele, P. J. W. Moll, M. Tortello, S. Weyeneth, V. Yu. Pomjakushin, J. Kanter, R. Puzniak, Z. Bukowski, H. Keller, R. S. Gonnelli, R. Khasanov, J. Karpinski, and B. Batlogg,
Phys. Rev. B **84**, 134526-1-14 (2011).
- **Mixed state of $\text{La}_{1.83}\text{Sr}_{0.17}\text{CuO}_4$ studied by means of muon-spin rotation and magnetization experiments in a low magnetic field**
B. M. Wojek, S. Weyeneth, S. Bosma, E. Pomjakushina, and R. Puzniak,
Phys. Rev. B **84**, 144521-1-9 (2011).
- **Muon spin rotation investigation of the pressure effect on the magnetic penetration depth in $\text{YBa}_2\text{Cu}_3\text{O}_x$**
A. Maisuradze, A. Shengelaya, A. Amato, E. Pomjakushina, and H. Keller,
Phys. Rev. B **84**, 184523-1-10 (2011).

- **Magnetism, superconductivity, and coupling in cuprate heterostructures probed by low-energy muon-spin rotation**
B. M. Wojek, E. Morenzoni, D. G. Eshchenko, A. Suter, T. Prokscha, H. Keller, E. Koller, Ø. Fischer, V. K. Malik, C. Bernhard, and M. Döbeli,
Phys. Rev. B **85**, 024505-1-9 (2012).
- **New spinel oxide catalysts for visible-light-driven water oxidation**
F. Conrad, M. Bauer, D. Sheptyakov, S. Weyeneth, D. Jaeger, K. Hametner, P.-E. Car, J. Patscheider, D. Günther, and G. R. Patzke,
RSC Adv. **2**, 3076-3082 (2012).
- **Magnetic-Field Tuned Anisotropy in superconducting $\text{Rb}_x\text{Fe}_{2-y}\text{Se}_2$**
S. Bosma, R. Puzniak, A. Krzton-Maziopa, M. Bendele, E. Pomjakushina, K. Conder, H. Keller, and S. Weyeneth
Phys. Rev. B **85**, 064509-1-6 (2012).
- **Coexistence of superconductivity and magnetism in FeSe_{1-x} under pressure**
M. Bendele, A. Ichsanow, Yu. Pashkevich, L. Keller, Th. Strässle, A. Gusev, E. Pomjakushina, K. Conder, R. Khasanov, and H. Keller,
Phys. Rev. B **85**, 064517-1-11 (2012).
- **Absolute value and temperature dependence of the magnetic penetration depth in $\text{Ba}(\text{Co}_{0.074}\text{Fe}_{0.926})_2\text{As}_2$**
O. Ofer, J. C. Baglo, M. D. Hossain, R. F. Kiefl, W. N. Hardy, A. Thaler, H. Kim, M. A. Tanatar, P. C. Canfield, R. Prozorov, G. M. Luke, E. Morenzoni, H. Saadaoui, A. Suter, T. Prokscha, B. M. Wojek, and Z. Salman,
Phys. Rev. B **85**, 060506(R)-1-5 (2012).
- **Muon spin rotation study of the intercalated graphite superconductor CaC_6 at low temperatures**
F. Murányi, M. Bendele, R. Khasanov, Z. Guguchia, A. Shengelaya, C. Baines, and H. Keller,
J. Supercond. Nov. Magn. **25**, 159-163 (2012).

PhD theses

- **Superconductivity and magnetism in cuprate single crystals and thin-film heterostructures**
Bastian Manuel Wojek, PhD Thesis, Physik-Institut, Universität Zürich, 2011
- **The superconducting and magnetic properties of the iron-chalcogenides**
Markus Bendele, PhD Thesis, Physik-Institut, Universität Zürich, 2011

Master theses

- **Si/SiO-Braggspiegel für Scheiben Laser (Vertical External Cavity Surface Emitting Laser)**
Fabian Hobrecker, Master Thesis, Physik-Institut, Universität Zürich, 2011
- **PbTe quantum well vertical external cavity surface emitting laser**
Rosa Maria Rodriguez, Master Thesis, Physik-Institut, Universität Zürich, 2011

Articles in press

- **Isotope and multiband effects in layered superconductors**
A. Bussmann-Holder and H. Keller,
J. Phys.: Condens. Matter.
- **Spin density wave induced disordering of the vortex lattice in superconducting $\text{La}_{2-x}\text{Sr}_x\text{CuO}_4$**
J. Chang, J. S. White, M. Laver, C. J. Howell, S. P. Brown, A. T. Holmes, L. Maechler, S. Strässle, R. Gilardi, S. Gerber, T. Kurosawa, N. Momono, M. Oda, M. Ido, O. J. Lipscombe, S. M. Hayden, C. D. Dewhurst, R. Vavrin, J. Gavilano, J. Kohlbrecher, E. M. Forgan, and J. Mesot,
Phys. Rev. B.
- **Tuning the structural instability of SrTiO_3 by Eu doping: the phase diagram of $\text{Sr}_{1-x}\text{Eu}_x\text{TiO}_3$**
Z. Guguchia, A. Shengelaya, H. Keller, J. Köhler, and A. Bussmann-Holder,
Phys. Rev. B.

Conference reports

- **Intrinsic and structural iron isotope effect on the superconducting transition temperature of FeSe_{1-x}**
M. Bendele, R. Khasanov, K. Conder, E. Pomjakushina, V. Pomjakushin, A. Bussmann-Holder, and H. Keller,
Annual meeting of the Swiss Physical Society, Lausanne, June 15-17, 2011.
- **Magnetic torque study of the temperature dependent anisotropy in $\text{YBa}_2\text{Cu}_3\text{O}_7$**
S. Bosma, S. Weyeneth, R. Puzniak, A. Erb, A. Schilling, and H. Keller,
Annual meeting of the Swiss Physical Society, Lausanne, June 15-17, 2011.
- **Muon-spin rotation measurements of the magnetic penetration depth in the Fe-based superconductors $\text{Ba}_{1-x}\text{Rb}_x\text{Fe}_2\text{As}_2$**
Z. Guguchia, Z. Shermadini, A. Amato, A. Maisuradze, A. Shengelaya, Z. Bukowski, H. Luetkens, R. Khasanov, J. Karpinski, and H. Keller,
Annual meeting of the Swiss Physical Society, Lausanne, June 15-17, 2011.
- **Strong coupling between the Eu^{2+} spins and the Fe_2As_2 layers in $\text{EuFe}_{1.9}\text{Co}_{0.1}\text{As}_2$ as revealed by NMR**
Z. Guguchia, J. Roos, A. Shengelaya, S. Katrych, Z. Bukowski, S. Weyeneth, F. Murányi, S. Strässle, A. Maisuradze, J. Karpinski, and H. Keller,
Annual meeting of the Swiss Physical Society, Lausanne, June 15-17, 2011.
- **μSR investigation of pressure effect on superfluid density in $\text{YBa}_2\text{Cu}_3\text{O}_x$**
A. Maisuradze, A. Shengelaya, A. Amato, K. Conder, E. Pomjakushina, and H. Keller,
Annual meeting of the Swiss Physical Society, Lausanne, June 15-17, 2011.
- **Low-energy μSR investigations of photo induced effects on the magnetic state of $\text{La}_{2-x}\text{Sr}_x\text{CuO}_4$ at low doping ($x < 0.02$)**
E. Stilp, A. Suter, T. Prokscha, H. Keller, E. Morenzoni, Z. Salman, E. Pomjakushina, K. Conder, A. Gozar, I. Bozović, and G. Logvenov,
Annual meeting of the Swiss Physical Society, Lausanne, June 15-17, 2011.
- **Magnetic torque study of the canted antiferromagnetic state of $\text{EuFe}_{2-x}\text{Co}_x\text{As}_2$ single crystals**
S. Weyeneth, S. Bosma, Z. Guguchia, R. Puzniak, A. Shengelaya, Z. Bukowski, J. Karpinski, and

H. Keller,

Annual meeting of the Swiss Physical Society, Lausanne, June 15-17, 2011.

- **Iron isotope effects in FeSe_{1-x}**

M. Bendele, R. Khasanov, K. Conder, E. Pomjakushina, V. Pomjakushin, A. Bussmann-Holder, and H. Keller,

Swiss workshop on Materials with Novel Electronic Properties, Les Diablerets, June 29 - July 1, 2011.

- **Temperature dependent anisotropy in superconducting single-crystal YBa₂Cu₃O₇ studied by torque magnetometry**

S. Bosma, S. Weyeneth, R. Puzniak, A. Erb, A. Schilling, and H. Keller,

Swiss workshop on Materials with Novel Electronic Properties, Les Diablerets, June 29 - July 1, 2011.

- **Muon-spin rotation measurements of the magnetic penetration depth in the Fe-based superconductors Ba_{1-x}Rb_xFe₂As₂**

Z. Guguchia, Z. Shermadini, A. Amato, A. Maisuradze, A. Shengelaya, Z. Bukowski, H. Luetkens, R. Khasanov, J. Karpinski, and H. Keller,

Swiss workshop on Materials with Novel Electronic Properties, Les Diablerets, June 29 - July 1, 2011.

- **NMR investigation of the coupling between the Eu²⁺ spins and the Fe₂As₂ layers in EuFe_{1.9}Co_{0.1}As₂**

Z. Guguchia, J. Roos, A. Shengelaya, S. Katrych, Z. Bukowski, S. Weyeneth, F. Murányi, S. Strässle, A. Maisuradze, J. Karpinski, and H. Keller,

Swiss workshop on Materials with Novel Electronic Properties, Les Diablerets, June 29 - July 1, 2011.

- **Photo persistent effects of La_{2-x}Sr_xCuO₄ at low doping ($x < 0.02$) by Low-energy μ SR**

E. Stilp, A. Suter, T. Prokscha, H. Keller, E. Morenzoni, Z. Salman, E. Pomjakushina, K. Conder, A. Gozar, I. Bozović, and G. Logvenov,

Swiss workshop on Materials with Novel Electronic Properties, Les Diablerets, June 29 - July 1, 2011.

- **Generics of the diamagnetism, Nernst signal, and finite size effects in superconductors above the transition temperature**

S. Weyeneth and T. Schneider,

Swiss workshop on Materials with Novel Electronic Properties, Les Diablerets, June 29 - July 1, 2011.

- **Magnetic-field tuned anisotropy in superconducting Rb_xFe_{2-y}Se₂**

S. Bosma, R. Puzniak, A. Krzton-Maziopa, M. Bendele, E. Pomjakushina, K. Conder, H. Keller, and S. Weyeneth,

E-MRS Fall Meeting, Warsaw, Poland, September 19 - 23, 2011.

- **Strong coupling between the Eu²⁺ spins and the Fe₂As₂ layers in EuFe_{1.9}Co_{0.1}As₂ as revealed by NMR**

Z. Guguchia, J. Roos, A. Shengelaya, S. Katrych, Z. Bukowski, S. Weyeneth, F. Murányi, S. Strässle, A. Maisuradze, J. Karpinski, and H. Keller,

E-MRS Fall Meeting, Warsaw, Poland, September 19 - 23, 2011.

- **Muon-spin rotation measurements of the magnetic penetration depth in the Fe-based superconductors Ba_{1-x}Rb_xFe₂As₂**

Z. Guguchia, Z. Shermadini, A. Amato, A. Maisuradze, A. Shengelaya, Z. Bukowski, H. Luetkens, R. Khasanov, J. Karpinski, and H. Keller,

E-MRS Fall Meeting, Warsaw, Poland, September 19 - 23, 2011.

PUBLICATIONS

- **Diamagnetism, Nernst signal, and finite size effects in superconductors above the transition temperature**
S. Weyeneth and T. Schneider,
E-MRS Fall Meeting, Warsaw, Poland, September 19 - 23, 2011.
- **μ SR investigation of pressure effect on superfluid density in $\text{YBa}_2\text{Cu}_3\text{O}_x$**
A. Maisuradze, A. Shengelaya, A. Amato, E. Pomjakushina, and H. Keller,
Annual meeting of the American Physical Society, Boston, USA, February 27 - March 2, 2012.

Invited lectures

112

- M. Bendele: Pressure induced static magnetic order in superconducting FeSe_{1-x}
12th International Conference on Muon Spin Rotation, Relaxation and Resonance, Cancun, Mexico, May 16-20, 2011.
- H. Keller: Probing fundamental properties of high-temperature superconductors with positive muons
International Conference Resonances in Condensed Matter Devoted to the Century of Prof. S. A. Altshuler, Kazan Federal University, Kazan, Russia, June 21-25, 2011.
- H. Keller: From cuprate to iron-based superconductors - some key signatures of high-temperature superconductivity
7th International Conference on Stripes and High T_c Superconductivity STRIPES 11, Quantum Phenomena in Complex Matter & Quantum Physics of Living Matter, University of Rome "La Sapienza", Rome, Italy, July 10-16, 2011.
- H. Keller: Absence of orbital currents in superconducting $\text{YBa}_2\text{Cu}_4\text{O}_8$ using a Zeeman-perturbed nuclear quadrupole resonance technique
26th International Conference on Low Temperature Physics, Hosted by the Institute of Physics Chinese Academy of Sciences, Beijing, China, August 10-17, 2011.
- H. Keller: From cuprate to iron-based superconductors - some key signatures of high-temperature superconductivity
Leibniz Institute for Solid State and Materials Research Dresden, IFW-Dresden, Dresden, Germany, August 29, 2011.
- H. Keller: Isotope effects in layered high-temperature superconductors
Université de Fribourg, Department of Physics, Fribourg, Switzerland, October 25, 2011.

19.2.2 Phase transitions and superconducting photon detectors

Articles

- **Dynamic stability of organic conducting polymers and its replications in electrical conduction and degradation mechanics**
E. F. C. Chimamkam, T. Schweizer, A. Schilling, J. M. F. Ferreira
Adv. Funct. Mat., 21 (2011) 2240.
- **Coexistence of Magnetism and Superconductivity in the Iron-Based Compound $\text{Cs}_{0.8}(\text{FeSe}_{0.98})_2$**
Z. Shermadini, A. Krzton-Maziopa, M. Bendele, R. Khasanov, H. Luetkens, K. Conder,

E. Pomjakushina, S. Weyeneth, V. Pomjakushin, O. Bossen, and A. Amato
Phys. Rev. Lett., 106 (2011) 117602.

- **Magnetic torque study of the temperature-dependent anisotropy parameter in overdoped superconducting single-crystal $\text{YBa}_2\text{Cu}_3\text{O}_7$**

S. Bosma, S. Weyeneth, R. Puzniak, A. Erb, A. Schilling and H. Keller
Phys. Rev. B, 84 (2011) 024514.

- **Rapid one-step chemical synthesis of polyaniline-manganese ferritenanocomposites without external initiator and mechanical agitation**

E.F.C. Chimamkam, T. Schweizer, A. Schilling, and J.M.F. Ferreira
Nanotech, 1 (2011) 527.

- **LC-Circuit Calorimetry**

O. Bossen and A. Schilling
Rev. Sci. Instrum., 82 (2011) 094901.

- **Observation of a first-order phase transition deep within the vortex-solid region of $\text{YBa}_2\text{Cu}_3\text{O}_7$**

M. Reibelt, S. Weyeneth, A. Erb, A. Schilling
Supercond. Sci. Technol., 24 (2011) 105019.

- **Tantalum nitride superconducting single-photon detectors with low cut-off energy**

A. Engel, A. Aeschbacher, K. Inderbitzin, A. Schilling, K. Il'in, M. Hofherr, M. Siegel, A. Semenov, H.-W. Hübers
Appl. Phys. Lett., 100 (2012) 062601.

Articles in press

- **Experimental tests for macroscopic phase coherence in magnetic-quasiparticle condensates of insulating spin systems**

A. Schilling, H. Grundmann and R. Dell'Amore
J. Phys.: Conf. Ser.

- **Ultra-thin TaN films for superconducting nanowire single-photon detectors**

K. Il'in, M. Hofherr, D. Rall, M. Siegel, A. Semenov, A. Engel, K. Inderbitzin, A. Aeschbacher and A. Schilling
J. Low Temp. Phys.

- **On Josephson effects in insulating spin systems**

A. Schilling, H. Grundmann
Annals of Physics.

Master theses

- **Superconducting Nanowire Single-Photon Detectors based on TaN Thin Films**

Adrian Aeschbacher
Master Thesis, Physik-Institut Universität Zürich, 2011.

- **Mie resonance spectroscopy of single levitated particle**

Yiea-Funk Te
Master Thesis, Physik-Institut Universität Zürich, 2012.

Contributed Conference Presentations

- A. Engel: Evaluation of Superconducting Nanowire Single-Photon Detectors as X-ray Detectors
SPG Jahrestagung, Lausanne, 15.6.2011.
- F. von Rohr: GeBi_4Te_7 : A Novel Topological Insulator (Poster)
Swiss Workshop on Materials with Novel Electronic Properties, Les Diablerets, 29.6.-1.7.2011.
- A. Aeschbacher: Superconducting Nanowire Single-Photon Detectors based on TaN Thin Films (Poster)
Swiss Workshop on Materials with Novel Electronic Properties, Les Diablerets, 29.6.-1.7.2011.
- A. Engel: Fluctuations in Current-biased Superconducting Nanowires
Superconductivity Centennial Conference, Den Haag (Netherlands), 22.9.2011.
- A. Engel: Detection of Soft X-Rays using Superconducting Nanowire Single-Photon Detectors
International Workshop on Nanowire Superconducting Single-Photon Detectors, Eindhoven (Netherlands), 23.9.2011.
- K. Inderbitzin: Ultrafast X-Ray Photon Detection in Thin- and Thick-Film SNSPDs (Poster)
International Workshop on Nanowire Superconducting Single-Photon Detectors, Eindhoven (Netherlands), 23.9.2011.

114

Invited Lectures

- F. von Rohr: Novel Materials for Superconductors and Topological Insulators
Solid State Physics Seminar at University of Zürich, 25.5.2011.
- A. Schilling: The early years of the cuprates - how to escape a research bubble
SPS Jahrestagung Lausanne, 16.06.2011.
- O. Bossen: Realization of a thermal LC-circuit
Swiss Workshop on Materials with Novel Electronic Properties, Les Diablerets, 30.6.2011.
- A. Schilling: Josephson effects in insulating quantum spin systems?
LT 26 Beijing (China), 16.08.2011.

19.2.3 Surface Physics

Articles

- **Strongly enhanced electron-phonon coupling in the Rashba-split state of the Bi/Ag(111) surface alloy**
D. Guan, M. Bianchi, S. Bao, E. Perkins, F. Meier, J. H. Dil, J. Osterwalder, Ph. Hofmann,
Phys. Rev. B 83, 155451:1-6 (2011).
- **Time-resolved photoelectron spectroscopy to probe ultrafast charge transfer and electron dynamics in solid surface systems and at metal-molecule interfaces**

L. Castiglioni, M. Greif, D. Leuenberger, S. Roth, J. Osterwalder, M. Hengsberger, *Chimia* 65, 342-345 (2011).

- **Synthesis of graphene on rhodium from 3-pentanone**
S. Roth, J. Osterwalder, T. Greber, *Surf. Sci.* 605, L17-L19 (2011).
- **Tuning the spin texture in binary and ternary surface alloys on Ag(111)**
I. Gierz, F. Meier, J. H. Dil, K. Kern, C. R. Ast, *Phys. Rev. B* 83, 195122:1-7 (2011).
- **Energy distribution curves of ultrafast laser-induced field emission and their implications for electron dynamics**
H. Yanagisawa, M. Hengsberger, D. Leuenberger, M. Klöckner, C. Hafner, T. Greber, J. Osterwalder, *Phys. Rev. Lett.* 107, 087601:1-5 (2011).
- **Large tunable Rashba spin splitting of a two-dimensional electron gas in Bi₂Se₃**
P. D. C. King, R. C. Hatch, M. Bianchi, R. Ovsyannikov, C. Lupulescu, G. Landolt, B. Slomski, J. H. Dil, D. Guan, J. L. Mi, E. D. L. Rienks, J. Fink, A. Lindblad, S. Svensson, S. Bao, G. Balakrishnan, B. B. Iversen, J. Osterwalder, W. Eberhardt, F. Baumberger, Ph. Hofmann, *Phys. Rev. Lett.* 107, 096802:1-5 (2011).
- **Disentanglement of electron dynamics and space-charge effects in time-resolved photoemission from h-BN/Ni(111)**
D. Leuenberger, H. Yanagisawa, S. Roth, J. Osterwalder, M. Hengsberger, *Phys. Rev. B* 84, 125107:1-9 (2011).
- **Resonant photoelectron diffraction with circularly polarized light**
M. Morscher, F. Nolting, T. Brugger, T. Greber, *Phys. Rev. B* 84, 140406(R):1-4 (2011).
- **Manipulating the Rashba-type spin splitting and spin texture of Pb quantum well states**
B. Slomski, G. Landolt, F. Meier, L. Patthey, G. Bihlmayer, J. Osterwalder, J. H. Dil, *Phys. Rev. B* 85, 193406:1-6 (2011).
- **Atom-specific spin mapping and buried topological states in a homologous series of topological insulators**
S. V. Eremeev, G. Landolt, T. V. Menshchikova, B. Slomski, Y. M. Koroteev, Z. S. Aliev, M. B. Babanly, J. Henk, A. Ernst, L. Patthey, A. Eich, A. A. Khajetoorians, J. Hagemeyer, O. Pietzsch, J. Wiebe, R. Wiesendanger, P. M. Echenique, S. S. Tsirkin, I. R. Amiraslanov, J. H. Dil, E. V. Chulkov, *Nature Commun.* 3, 635:1-7 (2012).
- **Viewpoint: Can spin-polarized photoemission measure spin properties in condensed matter ?**
J. Osterwalder, *J. Phys.: Condens. Matter* 24, 171001:1-3 (2012).
- **Topical Review: Spin-orbit-induced photoelectron spin polarization in angle-resolved photoemission from both atomic and condensed matter targets**
U. Heinzmann, J. H. Dil, *J. Phys: Condens. Matter* 24, 173001:1-30 (2012).

Articles in press

- **Three-dimensional spin rotation at the Fermi surface of a strongly spin-orbit coupled surface system**
P. Höpfner, J. Schäfer, A. Fleszar, J. H. Dil, B. Slomski, F. Meier, C. Loho, C. Blumenstein, L. Patthey, W. Hanke, R. Claessen, *Phys. Rev. Lett.*

PUBLICATIONS

- **Attosecond transversal streaking to probe electron dynamics at surfaces**

L. Castiglioni, D. Leuenberger, M. Greif, J. Osterwalder, and M. Hengsberger, in *Proceedings of the ATTO03 Conference*, Springer Proceedings in Physics Series, Springer.

Book chapter

- **Photoelectron spectroscopy and diffraction**

J. Osterwalder, in *Surface and Interface Science*, edited by Klaus Wandelt, Wiley-VCH, Weinheim 2012, pages 151-214.

PhD thesis

- **Electron dynamics in low-dimensional surfaces studied by time-resolved photoelectron spectroscopy**

Dominik Leuenberger, PhD Thesis, Physik-Institut, Universität Zürich, 2011.

Master thesis

- **Spin-polarisierte Elektronenkanone**

Colette Rosenberg, Master Thesis, Physik-Institut, Universität Zürich, 2012.

Contributed conference presentations

- **Photoelectron diffraction on SnPc/Ag(111) (Poster)**

M. Greif, Swiss Physical Society Meeting, Lausanne, 18.06.11.

- **Controlling the Rashba-type spin splitting in Pb quantum well states**

B. Slomski, Swiss Physical Society Meeting, Lausanne, 18.06.11.

- **Spin structure of three-dimensional topological insulators**

G. Landolt, Swiss Physical Society Meeting, Lausanne, 18.06.11.

- **Spin structure manipulation in three-dimensional topological insulators**

J. H. Dil, Conference on New Generation of strongly correlated electron systems, Santiago de Compostela, Spain, 07.07.11.

- **Transversal attosecond streaking to probe electron dynamics at surfaces and interfaces (Poster)**

Luca Castiglioni, ATTO3 Conference, Sapporo, Japan, 07.07.11.

- **Time-resolved photoelectron diffraction (Poster)**

M. Greif, FEMTO-10 Conference, Madrid, Spain, 12.07.11.

- **Ultrafast electron transfer dynamics in photoemission from negative-electron-affinity layers (Poster)**

M. Hengsberger, FEMTO-10 Conference, Madrid, Spain, 12.07.11.

- **Spin structure of topological insulators in the limit of ultra-thin films**

G. Landolt, Fall Meeting of the European Materials Research Society, Warsaw, Poland, 20.09.11.

- **Spin structure manipulation in three-dimensional topological insulators**
J. H. Dil, International Conference on Atomically Controlled Surfaces, Interfaces and Nanostructures (ACSIN-2011), St. Petersburg, Russia, 07.10.11.
- **Wafer-scale epitaxial h-BN as a substrate for graphene growth: a progress report**
J. Osterwalder, Workshop on Graphene Synthesis and Characterization for Applications, Lake Windermere, U. K., 16.11.11.
- **Time-resolved photoelectron diffraction (Poster)**
M. Greif, NCCR MUST Assembly Meeting, Lenk, 11.01.12.
- **Transversal attosecond streaking to probe electron dynamics at surfaces and interfaces (Poster)**
L. Castiglioni, NCCR MUST Assembly Meeting, Lenk, 11.01.12.
- **Electron dynamics and coherent lattice excitations in the one-dimensional Bi(114) surface(Poster)**
D. Leuenberger, NCCR MUST Assembly Meeting, Lenk, 11.01.12.
- **Graphene on Ru(0001): the four hills in the 25-on-23 structure**
T. Greber, March Meeting of the American Physical Society, Boston, USA, 01.03.12.
- **Self-protecting topological states**
J. H. Dil, PSI-Workshop on Spectroscopy of Novel Materials, Beatenberg, 02.03.12.
- **Manipulating the Rashba-type spin splitting of Pb quantum well states through the substrate charge density**
B. Slomski, PSI-Workshop on Spectroscopy of Novel Materials, Beatenberg, 02.03.12.
- **Coexistence of Rashba-split surface and bulk states in a non-centrosymmetric system**
G. Landolt, PSI-Workshop on Spectroscopy of Novel Materials, Beatenberg, 02.03.12.
- **p- to n-type transition in the three-dimensional topological insulator $\text{Ge Bi}_{4-x}\text{Sb}_x\text{Te}_7$**
S. Muff, PSI-Workshop on Spectroscopy of Novel Materials, Beatenberg, 02.03.12.
- **Hopping and trapping of F4TCNQ molecules on the h-BN nanomesh**
H. Cun, March Meeting of the American Physical Society, Boston, USA, 01.03.12.
- **The four hills of graphene on Ru(0001) '25 on 23'**
T. Greber, Symposium on Surface Science (3S), St. Christoph, Austria, 13.03.12.
- **Self-protecting spin-polarized surface states in ternary topological insulators**
J. H. Dil, Symposium on Surface Science (3S), St. Christoph, Austria, 13.03.12.
- **Time-resolved phototelectron diffraction for measuring structural dynamics at surfaces**
M. Greif, International Conference on Ultrafast Structural Dynamics (ICUSD 2012), Berlin, Germany, 20.03.12.
- **Manipulating the Rashba-type spin splitting through the interface and substrate charge density**
B. Slomski, Frühjahrstagung der Deutschen Physikalischen Gesellschaft, Berlin, Germany, 25.03.12.
- **Photoelectron diffraction on SnPc/Ag(111)**
M. Greif, Frühjahrstagung der Deutschen Physikalischen Gesellschaft, Berlin, Germany, 26.03.12.

PUBLICATIONS

118

- J. H. Dil: Spin-resolved ARPES on three-dimensional topological insulators
IFW-Seminar, Leibniz Institute for Solid State and Materials Research, Dresden, Germany, 04.04.11.
- T. Greber: Nanomesh und seine berühmte Schwester Graphene als Quantenschablonen
Physik-Kolloquium, Technische Universität Ilmenau, Germany, 03.05.11.
- J. H. Dil: Spin-resolved ARPES on three-dimensional topological insulators
NCCR MaNEP Topical Meeting on 'Topological Properties of Electronic Materials', Geneva, 06.05.11.
- J. Osterwalder: Spin matters at surfaces
ARPES Workshop, Diamond Light Source, Didcot, U.K., 08.06.11.
- J. H. Dil: Spin-resolved ARPES on systems with strong spin-orbit interaction
Quantum Many-Body Phenomena Seminar, Universität Würzburg, Germany, 26.05.11.
- T. Greber: Nanomesh and his famous sister graphene as nano-templates
International Workshop on Nanomaterials and Nanodevices, Institute of Physics, Chinese Academy of Sciences, Beijing, China, 02.07.11.
- T. Greber: How photons turn the electrons
International Workshop on Nanomaterials and Nanodevices, Xiantan, China, 04.07.11.
- D. Leuenberger: Disentanglement of electron dynamics and space-charge effects on h-BN/Ni(111)
Seminar, Institut für Angewandte Physik, Universität Bern, Bern, 07.07.11.
- J. H. Dil: Spin-resolved ARPES on systems with strong spin-orbit interaction
Condensed Matter Seminar, Princeton University, Princeton, NJ, USA, 28.07.11.
- T. Greber: Resonant photoelectron diffraction (RXP)
International Conference on the Structure of Surfaces (ICSOS-10), Hong Kong, China, 02.08.11.
- J. H. Dil: Towards spin manipulation in three-dimensional topological insulators
European Conference on Surface Science (ECOSS-28), Wroclaw, Poland, 30.08.11.
- J. H. Dil: Spin-resolved ARPES on three-dimensional topological insulators
Fall Meeting of the European Materials Research Society, Warsaw, Poland, 20.09.11.
- J. Osterwalder: Spin structures of surface states measured by spin-polarized ARPES
International Conference on Atomically Controlled Surfaces, Interfaces and Nanostructures (ACSIN-2011), St. Petersburg, Russia, 07.10.11.
- J. H. Dil: Spin structure manipulation in three-dimensional topological insulators and thin films
PSI-IOP Workshop on Research at Large Scale Facilities, Institute of Physics, Chinese Academy of Sciences, Beijing, China, 20.10.11.
- J. H. Dil: Spin-resolved ARPES on thin films and three-dimensional topological insulators
X. Zhou Group Seminar, Institute of Physics, Chinese Academy of Sciences, Beijing, China, 24.10.11.
- T. Greber: Molecular trapping on boron nitride and carbon based honeycomb superstructures
US-Morocco Workshop on Nanomaterials and Renewable Energies, Al Akhawayn University, Ifrane, Morocco, 18.11.11.

- T. Greber: Boron nitride and graphene based honeycomb superstructures ... bottom-up perspectives for nanodevices
1st Euro-Mediterranean Conference on Materials and Renewable Energies (EMCMRE-1), Marrakech, Morocco, 24.11.11.
- M. Hengsberger: Time-resolved photoelectron spectroscopy from a one-dimensional metal: Bi(114)
Abteilungsseminar Physikalische Chemie, Fritz-Haber-Institut, Berlin, 19.12.11.
- T. Greber: The corrugation of graphene on ruthenium
Symposium on Surface and Nano Science (SSNS'12), Shizukuishi, Japan, 11.01.12.
- J. H. Dil: Spin-resolved ARPES on topological insulators and beyond
Condensed Matter Seminar, University of Geneva, Geneva, 18.01.12.
- D. Leuenberger: Time-resolved experiments on a vicinal Bi(114) surface
I. Matsuda Group Seminar, SPring-8, Japan, 06.02.12.
- J. Osterwalder: Photoemission studies of boron nitride, graphene, Rashba systems and topological insulators
Lecture, Graduate School of Materials Science, Nara Institute of Science and Technology, Nara, Japan, 29.02.12.
- J. Osterwalder: Exploring spin degrees of freedom at nonmagnetic surfaces
16th Hiroshima International Symposium on Synchrotron Radiation, Hiroshima, Japan, 02.03.12.
- J. Osterwalder: Exploring spin degrees of freedom at nonmagnetic surfaces
Seminar, Institute of Solid State Physics, University of Tokyo, Japan, 05.03.12.
- T. Greber: Boron nitride and graphene based honeycombs on transition metals
Seminar, Brookhaven National Laboratory, Brookhaven, NY, USA, 07.03.12.
- T. Greber: Hexagonal boron nitride and carbon on 4d transition metals: corrugated single-layer templates for nanosciences
Materials Group Seminar, PSI, Villigen, 26.03.12.

119

Outreach Activities

- J. Osterwalder, S. Steiner, R. Gredig: Von Science Fiction zur Realität
2x90 min. and 3x30 min. modules taught at the TecDay and TecNight of the Kantonsschule Frauenfeld, 03.11.11.

19.2.4 Physics of Biological Systems

Articles

- **Novel Fourier-domain constraint for fast phase retrieval in coherent diffraction imaging**
T. Latychevskaia, J.-N. Longchamp, and H.-W. Fink, Optics Express 19(20), 19330-39 (2011).
- **Individual filamentous phage imaged by electron holography**
G.B. Stevens, M. Krüger, T. Latychevskaia, P. Lindner, A. Plückthun and H.-W. Fink, Eur. Biophys. J. (2011) 40:1197-1201.

PUBLICATIONS

Conference contributions

- Jean-Nicolas Longchamp: Coherent low-energy electron diffraction of single biomolecules (poster)
Microscopy Conference MC 2011, 28.08-02.09.2011, Kiel, Germany.
- Mirna Saliba: Microlens-assisted Fourier transform holography (poster)
Microscopy Conference MC 2011, 28.08-02.09.2011, Kiel, Germany.
- Tatiana Latychevskaia: Numerical reconstruction of holograms and diffraction patterns of individual biomolecules
Microscopy Conference MC 2011, 28.08-02.09.2011, Kiel, Germany.
- Mirna Saliba: Microlens-assisted Fourier transform holography
25th Rhine-Knee regional Meeting on X-ray crystallography of biomacromolecules, 28.09-30.09.2011, Campus Sursee, Switzerland.
- Tatiana Latychevskaia: Imaging individual biological molecules with coherent low-energy electrons
25th Rhine-Knee regional Meeting on X-ray crystallography of biomacromolecules, 28.09-30.09.2011, Campus Sursee, Switzerland.
- Tatiana Latychevskaia: Coherent diffraction imaging of individual biological molecules using low-energy electrons
ARC Centre of Excellence for Coherent X-ray Science, 6th Annual Workshop, 10.10-12.10.2011 Melbourne, Australia.

120

Master theses

- **Experimental Study of the Binding Properties between Water and DNA**
Flavio Lanfranconi, Physik-Institut, Universität Zürich, June 2011.
- **Design and Implementation of a Miniaturized Electron Column**
Flavio Wicki, Physik-Institut, Universität Zürich, November 2011.

19.2.5 Physical Systems Biology and non-equilibrium Soft Matter

Articles

- **Integrating Mechanical Control Theory into Models of Biological Development**
V. Petrov, and C.M. Aegerter, *Journal of Mechanics in Medicine and Biology* **11**, 713 (2011).
- **Scattered light fluorescence microscopy in three dimensions**
G. Ghielmetti and C.M. Aegerter, *Optics Express* **20**, 3744 (2012).

Articles in press

- **Velocity distributions of uniformly heated three dimensional granular gases**
C.C. Maass, G. Maret, and C.M. Aegerter.

- **Integrating force sensing and signalling pathways in a model for the regulation of size in the wing imaginal disc of *Drosophila***
T. Aegerter-Wilmsen, M.B. Heimlicher, A.C. Smith, C.M. Aegerter, and K. Basler.
- **In-vivo imaging of the *Drosophila* wing imaginal disc over time: novel insights on growth and boundary formation**
U. Nienhaus, T. Aegerter-Wilmsen, and C.M. Aegerter.
- **Direct evidence for localization of light in highly turbid samples**
T. Sperling, W. Bühner, C.M. Aegerter, and G. Maret.

Master thesis

- **Elastic Properties of Two-dimensional Foams**
M. Schindlberger, Master's Thesis, Universität Zürich, 2011.

121

Conference reports

- **In-vivo imaging**
U. Nienhaus and C.M. Aegerter, WingX retreat, Schwarzsee, Switzerland (July 13-15 2011).
- **Photo-elastic properties of the wing imaginal disc of *Drosophila*.**
T. Schluck and C.M. Aegerter, WingX retreat, Murten, Switzerland (March 4-5 2011).
- **Mechanical growth regulation of *Drosophila* wing discs. (poster)**
U. Nienhaus, T. Aegerter-Wilmsen, T. Schluck and C.M. Aegerter, URPP Systemsbiology and functional Genomics conference; Grindelwald, Switzerland (October 3-4, 2011).
- **Mechanical growth regulation of *Drosophila* wing discs. (poster)**
U. Nienhaus, T. Aegerter-Wilmsen, T. Schluck and C.M. Aegerter, SystemsX.ch Systemsbiology conference; Basel, Switzerland (October 24-26, 2011).

Invited lectures

- C.M. Aegerter: Elastic properties of the wing imaginal disc of *Drosophila*.
Colloquium in Plant Sciences, Universität Bern, Switzerland (21.03.2011).
- C.M. Aegerter: Was hat Physik mit Systembiologie zu tun?
Physikalische Gesellschaft Zürich, ETHZ, Switzerland (24.03.2011).
- C.M. Aegerter: Mechanical growth regulation of the wing imaginal disc of *Drosophila*.
Swiss Soft Matter Day, Basel, Switzerland (08.06.2011).
- C.M. Aegerter: Imaging through turbid layers.
Biomedical Photonics Network meeting, Neuchatel, Switzerland (30.11.2011).
- C.M. Aegerter: Imaging through turbid layers
Seminar in Biophotonics, University Hospital Zurich, Switzerland (08.12.2011).
- C.M. Aegerter: Forschung und Lehre in Physik und Biologie an der Universität Zürich
Presentation Lions-Club WInterthur, Switzerland (01.02.2012).